

Coupled Plasmonic Nanostructures Based on Core-Shell Particles

DISSERTATION

Zur Erlangung des akademischen Grades

Doctor rerum naturalium
(Dr. rer. nat.)

vorgelegt

dem Bereich Mathematik und Naturwissenschaften
der Technischen Universität Dresden



von

M. Sc. Yannic Brasse

Geboren am 15.02.1991 in Koblenz

Eingereicht am 27.02.2020

Verteidigt am 25.06.2020

Begutachtet durch:

Prof. Dr. Andreas Fery

Prof. Dr. Nikolai Gaponik

Die Dissertation wurde in der Zeit von Dezember 2015 bis Februar 2020
unter der Betreuung von Prof. Dr. Andreas Fery
am Leibniz-Institut für Polymerforschung Dresden e.V. angefertigt.

„Was ist mit diesem Rätselwort gemeint?“

Faust I - Vers 1337

Contents

ABSTRACT	I
KURZFASSUNG	II
LIST OF PUBLICATIONS	III
LIST OF ABBREVIATIONS	IV
I INTRODUCTION	1
II SYNOPSIS	3
III STATUS OF THE FIELD	9
1 PLASMONIC NANOPARTICLES.....	9
1.1 Colloidal Particles.....	9
1.2 Localized Surface Plasmon Resonances.....	13
1.3 Particle Characterization	17
2 COUPLING OF PLASMONIC PARTICLES	26
2.1 Inter-Particle Coupling	26
2.2 Optical Absorbers	29
2.3 Diffractive Coupling	31
3 PLASMONIC CORE-SHELL SYSTEMS	33
3.1 Inorganic Shells	33
3.2 Polymer Shells	35
4 ASSEMBLY OF COLLOIDAL PARTICLES.....	39
4.1 Interface-Mediated Assembly	39
4.2 Template-Assisted Assembly	42
4.3 Mechano-Tunable Plasmonic Arrays.....	48
IV FLUORESCENCE IN COLLOIDAL PLASMONIC CAVITIES	51
V A SWITCHABLE MAGNETIC LIBRARY	61
VI A TUNABLE ANTI-REFLECTIVE METASURFACE	77
VII PERSPECTIVE: MECHANO-TUNABLE PLASMONIC LATTICES	89
REFERENCES	95
APPENDIX	105
DANKSAGUNG	141
VERSICHERUNG UND ERKLÄRUNG	143

Abstract

Plasmonic nanoparticles feature remarkable optical and electronic properties in consequence of the excitation of conduction band electrons by visible light, which leads to collective oscillations. This so called localized surface plasmon resonance (LSPR) is utilized in the fields of photovoltaics, sensing, catalysis and optoelectronics. Especially, the emergence of optical metasurfaces—subwavelength structured surfaces with properties typically not occurring for homogeneous materials—has attracted significant attention for the applications mentioned above. However, their fabrication is usually complex and the materials often lack *in situ* tunability.

Here, a colloidal approach is demonstrated for the preparation of optical metasurfaces with tunable properties. They are based on plasmonic gold nanoparticles, which were coated with three different shell materials to provide three different functionalities when coupled to plasmonic mirrors: i) Dye-labeled silica coatings exhibit strong enhancement of their fluorescent properties, as shown in this extensive single particle study. ii) Hydrogel shells are applied to receive switchable electric and magnetic properties in response to swelling of the gel. iii) Electrochromic polymer coatings facilitate the preparation of anti-reflective metasurfaces that feature tunable efficiency by changing the pH or applying a voltage.

In addition, mechano-tunable plasmonic lattices are demonstrated. The material is based on self-assembled gold nanoparticles, which are embedded in a transparent elastomer matrix and feature pronounced surface lattice resonances (SLR). These tunable resonances could be applied for lasing, strain sensing, or controlling catalytic reactions.

Kurzfassung

Plasmonische Nanopartikel besitzen bemerkenswerte optische und elektronische Eigenschaften, die sie für Anwendungen in Bereichen der Katalyse, Sensorik, Optoelektronik, sowie der Nanooptik prädestinieren. Ihre Eigenschaften beruhen auf der Anregung von Leitungsbandelektronen zu kollektiven Oszillationen durch sichtbares Licht. Diese sogenannte Oberflächenplasmonenresonanz ist insbesondere für optische Metaoberflächen von Interesse, also Materialien mit strukturierten Oberflächen im Größenbereich unterhalb der sichtbaren Wellenlängen, welche Charakteristika aufweisen, die bei homogenen Materialien typischerweise nicht auftreten. Sie werden allerdings häufig mit aufwendigen Methoden hergestellt und sind *in situ* nicht justierbar.

In dieser Arbeit werden kolloidale Ansätze zur Herstellung plasmonischer Metaoberflächen mit einstellbaren optischen und elektronischen Eigenschaften vorgestellt. Das Konzept basiert auf der Verwendung von plasmonischen Goldkernen, die mit drei unterschiedlichen funktionellen Schalen beschichtet und anschließend mit plasmonischen Spiegeln gekoppelt wurden: i) Farbstoffmarkierte Silicapartikel zeigen starke Fluoreszenz-verstärkung, wie in dieser ausführlichen Einzelpartikelstudie nachgewiesen wird. ii) Hydrogelbeschichtungen werden verwendet um schaltbare elektrische und magnetische Eigenschaften mittels Quellung zu erzeugen. iii) Elektrochrome Polymerhüllen fungieren als Antireflexschicht auf Goldoberflächen, deren Extinktion sich mittels Anlegen einer Spannung oder durch pH-Änderungen einstellen lässt.

Neben diesen Ansätzen werden mechanisch einstellbare plasmonische Gitterstrukturen vorgestellt. Die selbstassemblierten und in transparentem Elastomer eingebetteten Goldnanopartikel weisen eine ausgeprägte Oberflächengitterresonanz auf. Diese kann für sensorische Zwecke in den Bereichen der Mikromechanik und der Katalyse, sowie für abstimmbare Laser verwendet werden.

List of Publications

- [1] “Magnetic and Electric Resonances in Particle-to-Film-Coupled Functional Nanostructures”
Y. Brasse, M. B. Müller, M. Karg, C. Kuttner, T. A. F. König, A. Fery, *ACS Appl. Mater. Interfaces* **2018**, *10*, 3133.
- [2] “Single Particle Spectroscopy of Radiative Processes in Colloid-to-Film-Coupled Nanoantennas”
M. J. Schnepf[#], Y. Brasse[#], F. R. Goßler, A. M. Steiner, J. Obermeier, M. Lippitz, A. Fery, T. A. F. König, *Z. Phys. Chem.* **2018**, *232*(9-11), 1593.
[#]M. J. Schnepf and Y. Brasse contributed equally.
- [3] “Mechanotunable Surface Lattice Resonances in the Visible Optical Range by Soft Lithography Templates and Directed Self-Assembly”
V. Gupta, P. T. Probst, F. R. Goßler, A. M. Steiner, J. Schubert, Y. Brasse, T. A. F. König, A. Fery, *ACS Appl. Mater. Interfaces* **2019**, *11*, 28189.
- [4] „Mechanotunable Plasmonic Properties of Colloidal Assemblies”
Y. Brasse, V. Gupta, H. C. T. Schollbach, M. Karg, T. A. F. König, A. Fery, *Adv. Mater. Interfaces* **2019**, 1901678.
- [5] “A Tunable Polymer-Metal Based Anti-Reflective Metasurface”
Y. Brasse, C. Ng, M. Magnozzi, H. Zhang, P. Mulvaney, A. Fery, D. E. Gómez, *Macromol. Rapid Commun.* **2020**, *41*, 1900415.
- [6] “Plasmonics of Au/Polymer Core/Shell Nanocomposites for Thermoresponsive Hybrid Metasurfaces”
M. Magnozzi, Y. Brasse, T. A. F. König, F. Bisio, E. Bittrich, A. Fery, M. Canepa, *ACS Appl. Nano Mater.* **2020** (Article ASAP).

List of Abbreviations

A	absorbance
A_H	Hamaker constant
a	polarizability
AFM	atomic force microscopy
BC	boundary condition
BIS	N,N' -methylenebisacrylamide
c	concentration
C	capacitance
CAPA	capillarity-assisted particle-assembly
CCD	charged coupled device
CTAB	cetyltrimethylammonium bromide
CM	coupling mode
χ	interaction parameter
d	distance
D_h	hydrodynamic diameter
DLVO	Derjaguin, Landau, Verwey, Overbeek
DM	dipolar mode
Δ	ellipsometric parameter (phase difference)
e	elementary charge
E	energy
EBL	electron beam lithography
EPD	electrophoretic particle deposition
ε	dielectric function / electric permittivity
η	dynamic viscosity
F	force
FLIM	fluorescence lifetime imaging
FDM	finite difference method
FDTD	finite difference time domain
FEM	finite element method
FWHM	full width half maximum
Γ	relaxation rate
k_B	Boltzmann constant
L	inductance
LIL	laser interference lithography
LSPR	localized surface plasmon resonance
λ	wavelength
λ_D	Debye length
n	refractive index

NA	numerical aperture
NIPAM	<i>N</i> -isopropylacrylamide
ν	Poisson's ratio
μ	magnetic permeability
μ_e	electrophoretic mobility
p	absolute value of the periodicity
PANI	polyaniline
PDMS	polydimethylsiloxane
PEG	polyethylene glycol
PNIPAM	poly(<i>N</i> -isopropylacrylamide)
Ψ	ellipsometric parameter (amplitude component)
ψ_0	surface potential
q	absolute value of the scattering vector
Q	quality factor
QE	quantum efficiency
R	radius
R_H	hydrodynamic radius
rpm	revolutions per minute
rcf	relative centrifugal force
SEM	scanning electron microscopy
SDS	sodium dodecyl sulfonate
σ	cross-section
T	temperature
T_λ	transmittance
TCSPC	time correlated single photon counting
TEM	transmission electron microscopy
TEOS	tetraethyl orthosilicate
τ	lifetime
θ	scattering angle
θ_{obj}	maximum half angle of an objective
VPT	volume phase transition
W	work

I Introduction

The emergence of colors has fascinated mankind since ancient times and inspired them to craft precious pieces of art and jewelry.^[1] Spectacular impressions are achieved by using gemstones with colors that originate from effects beyond common absorption. Prominent examples for this are opals, which also represent the origin of the homonymous effect—opalescence.^[2] It describes the phenomenon in which matter appears differently colored, depending on whether the observer *looks at* or *looks through* an object.^[3] Though, opalescence is clearly distinguished from iridescence, which is based on interference.^[4] The common opal, displayed in **Figure 1a**, shows its typical hue due to pronounced scattering of blue light (looked at), whereas the transmitted light (looked through) exhibits the complementary color orange.^[5] The effect occurs because small domains of water are present within a network of silicon dioxide particles.^[2] This could be interpreted as the inverse structure of a colloidal silica dispersion (see **Figure 1b**), which exhibits the same optical effect upon illumination.^[6] Such behavior of turbid media was first explained by Rayleigh^[7] and Mie,^[8] who particularly emphasized these effects occurring in gold colloids. Gold nanoparticles had attracted significant attention over centuries because of their distinctive ruby color.^[9,10] This color arises due to the excitation of conduction band electrons in coinage metal nanoparticles. The resulting localized surface plasmon resonance (LSPR) is characterized by strong absorption and scattering in the visible wavelength range (see **Figure 1c**).^[11]

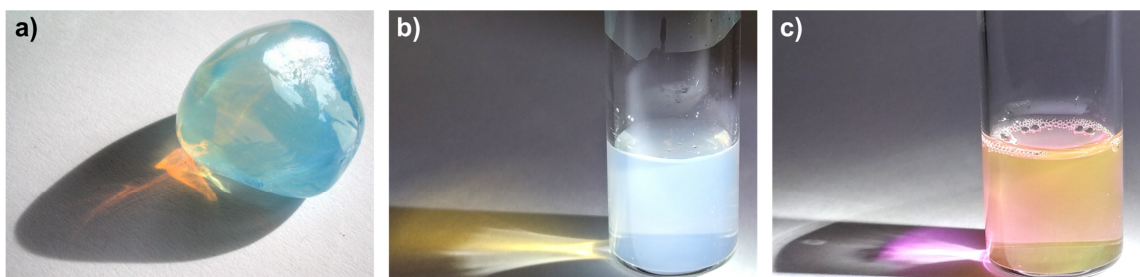


Figure 1. Opalescence of different media. a) The common opal exhibits its typical color due to pronounced scattering of blue light whereas the transmitted rays possess the complementary color orange. b) The same effect is observed in colloidal dispersions of small silica nanoparticles (150 nm). c) Gold nanoparticles dispersions efficiently absorb and scatter light due to excitation of their LSPR. The sample scatters green light whereas the transmission appears reddish, which results in a brownish color of the dispersion. a) Reprinted under the terms of the Creative Commons Attribution-Share Alike 2.0 Generic license.^[12] c) Credit for providing gold nanoparticles goes to Anja Steiner.

Plasmonic nanostructures are nowadays applied in diverse fields such as catalysis,^[13] photovoltaics,^[14] chemical,^[15] and bio-sensing,^[16] optoelectronics,^[17] and nano-optics.^[18] Their benefit lies in the ability of controlled light manipulation. More precisely, the effective optical constants of a material can be modulated by utilization of plasmonic building blocks.^[19] The resulting optical metamaterials feature properties that are typically not observed in nature.^[20] Since the advent of metamaterials in the early 2000s,^[21] various approaches have striven for effects like perfect absorption,^[22] optical

cloaking,^[23] and energy harvesting.^[24] The key feature of these strategies is usually an array of optical resonators. These are represented by coupled plasmonic nanostructures, which are commonly fabricated by lithographic techniques. However, less complex and more facile methods are accessible *via* assembly of colloidal nanoparticles featuring the required plasmonic properties.^[25] In particular, these particles can be configured with shell materials that provide additional functionality to the resulting nanostructure.^[26-28]

This work focusses on the application of plasmonic core-shell particles to create plasmonic metasurfaces, *i.e.*, subwavelength structured plasmonic surfaces,^[29] with unique optical properties. For this purpose, gold nanoparticles were functionalized with three different shell materials and subsequently coupled to plasmonic mirrors: i) A fluorescently doped silica shell is applied to study the influence of plasmonic coupling on radiative processes. The combined structural, morphological, and optical investigation on the single particle level reveals extraordinary *fluorescence enhancement* and *reduced bleaching effects*. ii) Particles with a thermoresponsive shell are examined regarding their local electric and magnetic field enhancement. By simultaneous variation of the particle size and the hydrogel thickness, a library is achieved that features *switchable electric and magnetic properties*, which are triggered by swelling of the gel. iii) Electrochromic polymer coatings are utilized to receive *tunable anti-reflective surfaces* which can be adjusted by applying a voltage or changing pH.

The reported effects are predominantly based on plasmonic near-field coupling, but recent advances in the field of long-range interactions revealed novel methods for light manipulation as well.^[30] The scattering of colloidal particles (as shown in Figure 1) can be utilized to induce collective resonances of superior optical quality.^[31] A prerequisite for these surface lattice resonances (SLRs) is a periodic array of plasmonic nanoparticles, in which the Bragg mode meets the LSPR wavelength.^[32] As a perspective, the application of elastic matrix materials with self-assembled colloidal particles is discussed. The resulting mechano-tunable plasmonic lattices feature *adjustable narrow-band optical feedback*, and thus, are promising structures for nanoscopic strain-sensing^[33], lasing,^[34] and monitoring of catalytic reactions.^[35]

II Synopsis

The content of this chapter is based on several publications [1,2,5] as specified in the 'List of Publications'. For individual contributions, please refer to the respective sections in Chapters IV-VI.

Outline

This chapter will provide an overview of this thesis which contains three major parts: *Chapter III* gives an insight into the present literature concerning colloid science, plasmonics, and nanoparticle assembly—allowing the reader to put this work into context with preceding and current research in these fields. *Chapters IV-VI* represent the essence of this work and highlights different aspects of plasmonic core-shell particles that are coupled to plasmonic mirrors. As depicted in **Figure 2**, three shell materials based on dye labeled silica, hydrogels, and electrochromic polymers will be described. Each coating provides a specific adjustment to the coupling behavior of the plasmonic cores, resulting in various effects on the optical as well as the electronic properties of the systems. Namely, fluorescence enhancement is achieved by application of dye labeled silica shells, while switchable absorbance occurs for hydrogel coated systems, and the reflectance tuning is received by polyaniline coatings. *Chapter VII* discusses perspectives in context of a different coupling mechanism based on particle-particle interactions. The narrow-band collective resonances occurring in plasmonic lattices are proposed to be suitable for monitoring mechanical deformations and catalytic reactions. The results of chapters IV and V are summarized in the following sections.

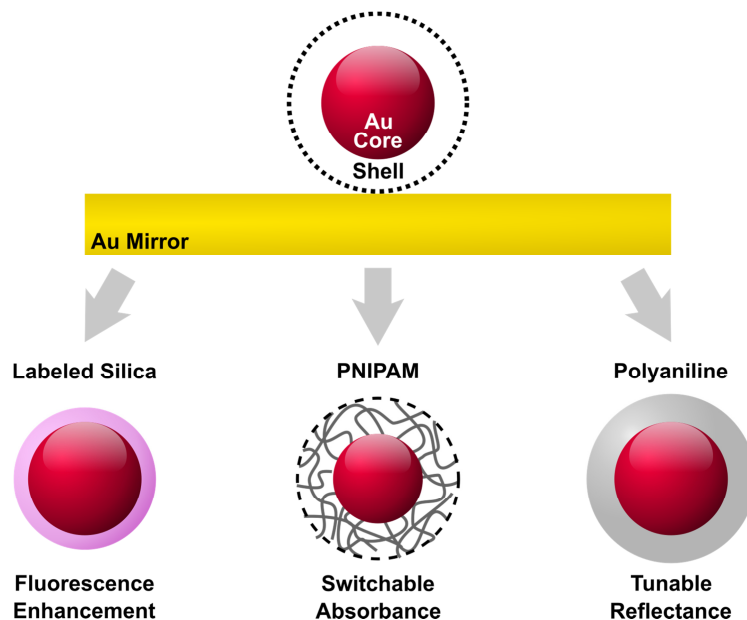


Figure 2. Effects induced by coupling of plasmonic core-shell particles and a gold mirror. The coupling of plasmonic core-shell particles with a plasmonic mirror results in different influences on the optical and electronic properties. The application of labeled silica shells is used to generate fluorescence enhancement while PNIPAM shells result in a switchable absorbance and polyaniline coatings are used for tuning of the reflectance.

Fluorescence in Colloidal Plasmonic Cavities

Quantum emitters are key components in optoelectronic devices such as lasers, light-emitting diodes (LEDs), and optical computers. Their performance is typically limited by their radiative decay rates (k_r) and bleaching effects. This section demonstrates a gold-core/fluorescent-shell system that significantly alters the radiative processes of the incorporated dye molecules (rhodamine B). As depicted in **Figure 3a**, excitation of the rhodamine dye-labeled shell leads to fluorescence emission. The gold core is coupled to a gold mirror, which results in formation of a plasmonic cavity featuring strong field enhancements. This cavity resonance leads to a decrease of k_r in the gap region and thus, strong fluorescent enhancement. These effects are studied on the single particle level by correlating atomic force microscopy (AFM), scanning electron microscopy (SEM), scattering spectroscopy, fluorescence lifetime imaging (FLIM), and time-correlated single photon counting (TCSPC). The core-shell system, on which the effect is based, is shown by a schematic and a TEM micrograph in Figure 3b. In comparison to the reference system with labeled silica on glass, the cavity features a 5-fold increase of the emission rate (see Figure 3c). Hereby, a colloidal gain material is presented that can be combined with existing self-assembly methods to study coherent energy transfer processes.

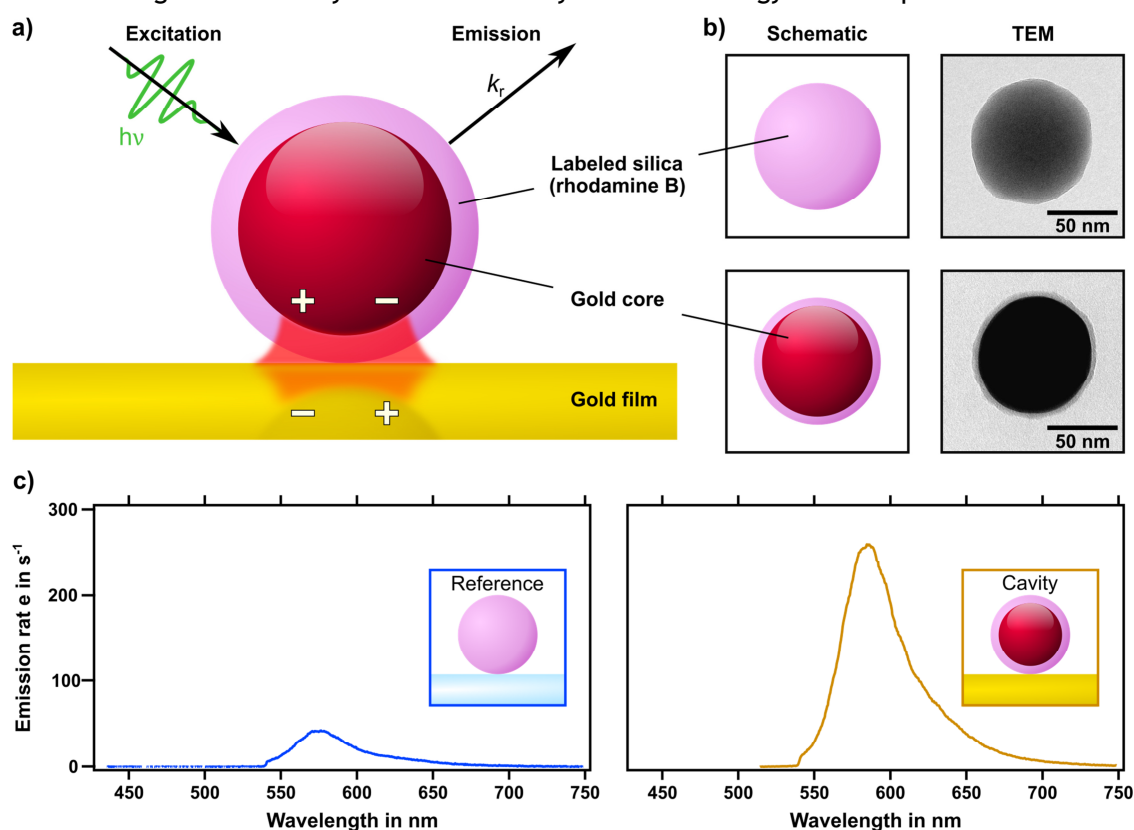


Figure 3. Fluorescence enhancement in a plasmonic cavity. a) Schematic depiction of the cavity system: Excitation of the particle shell leads to fluorescence emission of rhodamine B (radiative decay rate k_r). The plasmonic core induces a mirror charge in the gold film which results in strong field enhancement in the gap region (cavity). The plasmonic cavity leads to a reduction of k_r and thus, an enhanced emission (red halo). b) Structure of a labeled silica particle (top) and a core-shell particles (bottom) including a schematic depiction (left) and a TEM image (right). c) Emission rates of the reference system (silica particle on glass) and the plasmonic cavity (core-shell particle on gold) in dependence on the wavelength. Adapted with permission.^[36] Copyright 2019 by Walter de Gruyter GmbH.

A Switchable Magnetic Library

Film-coupled nanoparticles find application in solar cells, sensing, and photocatalysis. For these purposes, tailored optical properties based on scalable synthesis methods are required. Here, the coupling of gold nanoparticles with continuous gold films is investigated regarding the effects of particle-to-film distance, cavity geometry, and particle size. To efficiently screen these parameters, a particle-to-film coupled functional nanostructure was fabricated with varying particle size and film distance (see Figure 4a). Gold-core/poly(*N*-isopropylacrylamide)-shell (Au-PNIPAM) nanoparticles were used to self-assemble a monolayer of well-separated plasmonic particles. A gradient in nanoparticle size was introduced by an overgrowth process and finally coupling was induced by evaporation of a metal film. The assemblies are characterized using AFM, SEM, and optical spectroscopy to show the effects of localized magnetic and electric field enhancement, which increase with the particle size. The results are in excellent agreement with finite-difference time-domain (FDTD) modelling methods (see Figure 4b) and calculations of the effective permeability and permittivity. Finally, a proof of concept is provided for dynamic tuning of the cavity size by swelling of the hydrogel layer. The switchability of the coupled resonance, combined with the macroscopic self-assembly technique, provides access to a cost-efficient library for magnetic and electric resonances.

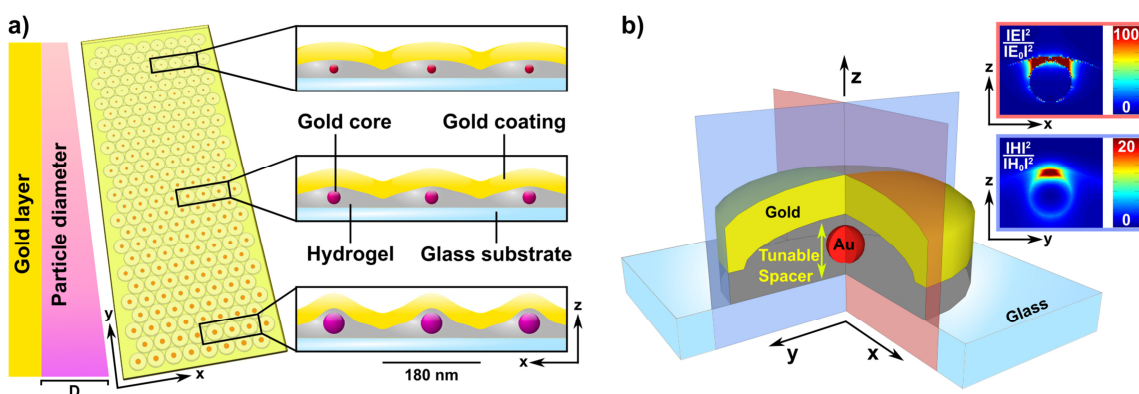


Figure 4. Structure and electronic properties of the switchable library. a) Schematic depiction of the film-coupled library. A microscopy slide is coated with a monolayer of Au-PNIPAM particles with varying particle diameter and covered by a gold layer of continuous thickness. Insets show the cross-section at different positions, *i.e.*, different particle sizes. b) Cross-sectional structure of the cavity including the planes of the electric (red) and the magnetic field (blue). The respective insets show FDTD simulations of the electric and magnetic field enhancement in the gap region. Adapted with permission.^[37] Copyright 2018 by the American Chemical Society.

A Tunable Anti-Reflective Metasurface

Anti-reflective surfaces are of great interest for optical devices, sensing, photovoltaics, and photocatalysis. However, most of the anti-reflective surfaces lack *in situ* tunability of the extinction with respect to the wavelength. This section demonstrates a tunable anti-reflective surface based on colloidal particles comprising a gold-core with an electrochromic polyaniline shell (Au-PANI; see Figure 5a). These particles were randomly deposited on gold films, resulting in a subwavelength structured surface (metasurface), as shown in Figure 5b. Consequently, there is a decrease in the reflectance of up to 99.8% at the localized surface plasmon resonance wavelength (see Figure 5c). This narrowband feature can be tuned by varying the pH or by application of an electric potential, resulting in wavelength shifts of up to 30 nm. The transition is induced by the changing dielectric properties of polyaniline, which influence the plasmonic peak position. It is accompanied by an apparent color transition from red to a greenish color, as displayed in Figure 5d. Furthermore, electrophoretic particle deposition is shown to be an efficient method for controlling the inter-particle distance and optimizing the overall efficiency of the anti-reflective metasurface thereby.

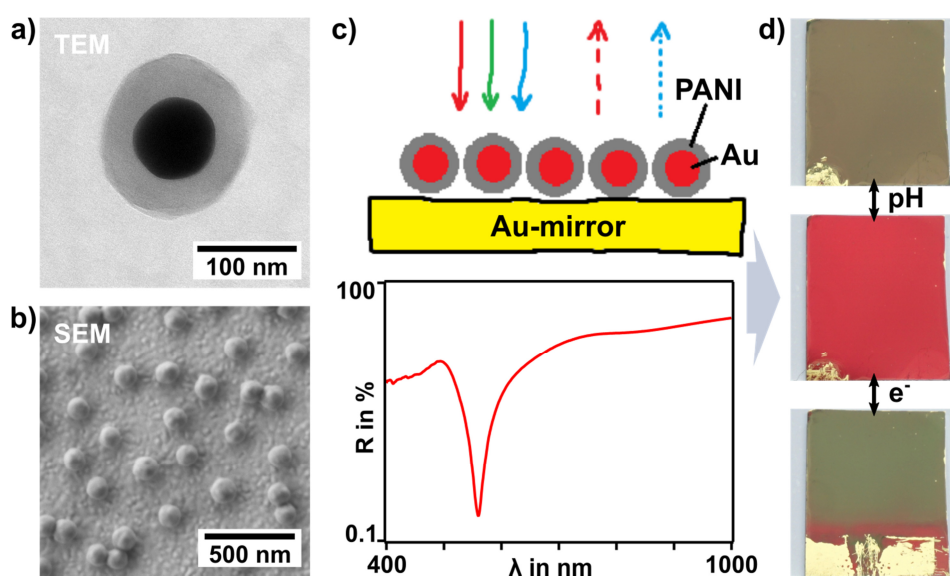


Figure 5. Anti-reflective metasurface based on Au-PANI particles. a) TEM image of a Au-PANI particle. b) SEM image of the gold surface coated with Au-PANI particles. c) Top: schematic depiction of the coated surface evoking a reduced reflectance of green light. Bottom: measured reflectance in dependence on the wavelength. d) Pictures of the sample as prepared (center), after treatment with NaOH-solution (top), and after reduction by applying a negative potential (bottom). Adapted under the terms of the Creative Commons Attribution Non-Commercial License CC BY-NC.^[38] Copyright 2019 by the authors.

Mechano-Tunable Plasmonic Lattices

Plasmonic lattices are promising candidates for integration in photonic devices, as well as devices for strain sensing and chemical detection. Yet, their fabrication is foremost based on lithographic techniques that facilitate elaborate equipment, but advances in colloidal self-assembly allow for the required precision to create plasmonic lattices as well. Here, the properties of mechano-tunable plasmonic lattices are investigated and discussed with respect to their potential for sensing applications. Plasmonic particle lattices evoke coupling between localized and diffractive modes, which results in surface lattice resonances (SLRs). These resonances are characterized by narrow spectral linewidths in consequence of increased resonance lifetimes. Their properties are strongly dependent on the periodicity, the symmetry, and the refractive index surrounding. Hexagonal gold nanoparticle lattices were prepared from Au-PNIPAM particles *via* interface-mediated assembly and transferred to solid substrates (see Figure 6a). After removal of the polymer shell by plasma treatment, the lattice was embedded in polydimethylsiloxane (see Figure 6b). The homogeneous refractive index surrounding gives rise to lattice coupling, as observed in Figure 6c (blue graph). Depending on the orientation, a splitting of this mode was found upon stretching, which gives rise to up to three distinct resonances. The resonance shifts are proposed to be suitable for localized strain sensing and tunable lasing if combined with optical gain materials. Furthermore, partially embedded plasmonic lattices are promising structures for chemical sensing by means of local refractive index changes and their impact on SLRs.

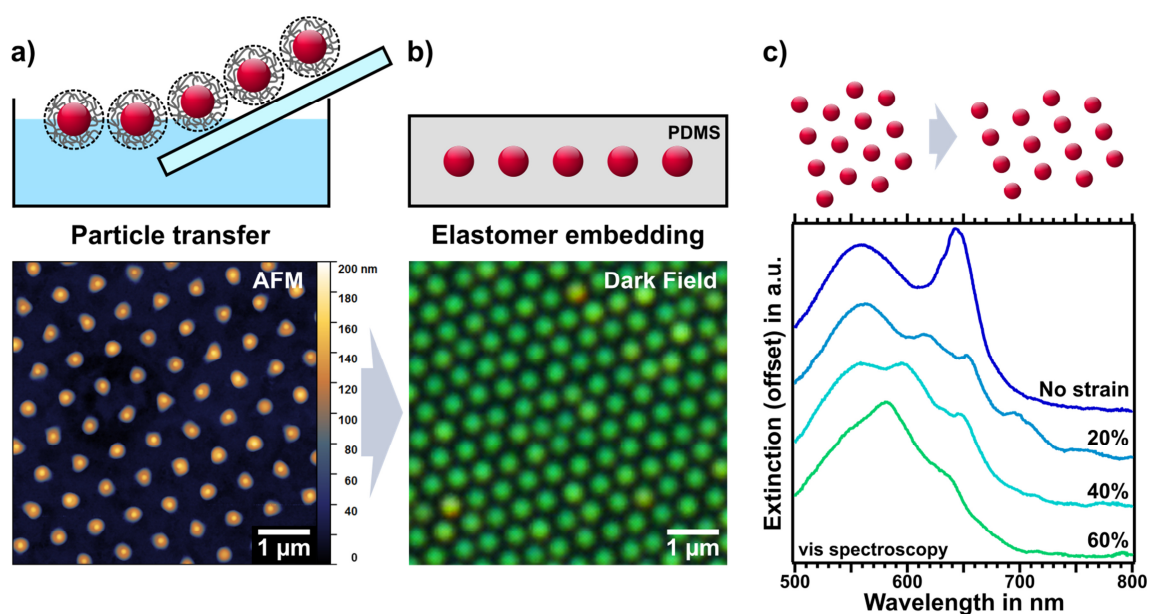


Figure 6. Mechano-Tunable Plasmonic Lattice. a) Schematic depiction of the interface-assisted assembly of Au-PNIPAM particles and a respective AFM image. b) Schematic cross section of gold nanoparticles embedded in PDMS and a corresponding dark field micrograph. c) Schematic transition of a hexagonal lattice under uniaxial strain. The spectroscopic data of such structure reveal splitting of the SLR peak into three distinct modes.

III Status of the Field

1 Plasmonic Nanoparticles

For the understanding of plasmonic nanoparticles—and their assembly in the subsequent chapters—it is important to be familiar with the fundamentals of colloid science and the electronic properties of noble metal particles. Several key questions will be answered in this section:

- What are colloids?
- How are stable colloidal particles defined?
- Why are gold colloids colored but not golden?
- Which methods are used to characterize these particles?

1.1 Colloidal Particles

Colloids were first mentioned over 150 years ago by Thomas Graham. He introduced gelatin as the archetype for this class of substances that is distinguished by their “gelatinous character” and a “low diffusibility”.^[39] Interestingly, this proposal would not include the suspensions of gold particles showing a “ruby colour” that were investigated by Faraday during the same period.^[9] The interpretation of a colloid was mainly influenced by scientists of the early 20th century^[3,8,10] towards the present definition as particles that are dispersed in a medium and have at least in one direction a dimension roughly between 1 nm and 1 μm .^[40] It was Zsigmondy^[41] who first used a technique called ultramicroscopy to study such particles. This method is nowadays established as dark field microscopy and serves as one of the key investigation techniques in this work.

For keeping the definition of colloidal particles comprehensive, the description by size is intentionally vague. A more specific interpretation is found by consideration of *stable* colloidal dispersions. They are characterized by not showing macroscopic phase separation over time as the dispersed phase is subject to Brownian motion.^[42,43] In a colloidal system, different destabilizing forces have to be taken into account. Namely, gravitation and buoyancy can lead to sedimentation or creaming, while attractive forces result in aggregation and coalescence. If these forces are outweighed by counteracting forces, the system can be considered stable. These stabilizing forces are driven by the thermal energy ($\sim k_B T$) and repulsive interactions. A convenient description of the interplay between attractive van der Waals and repulsive electrostatic double layer interactions was given by Derjaguin, Landau, Verwey, and Overbeek (DLVO).^[44,45] **Figure 7** shows the resulting energy of two similar particles in dependence of their distance d .

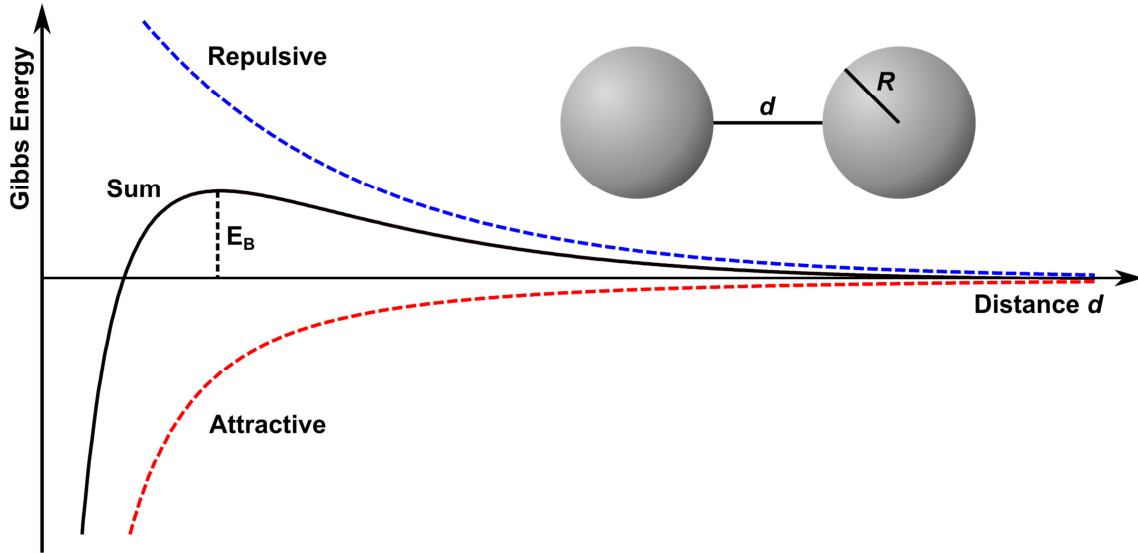


Figure 7. Gibbs energy versus inter-particle distance. For two similar particles, the sum of attractive van der Waals interactions (red) and repulsive electrostatic double layer interactions (blue) results in the DLVO energy profile (black) with an energy barrier E_B that correlates to the colloidal stability.

The attractive van der Waals energy is defined as:^[46]

$$W(d)_{\text{att}} = -\frac{A_H}{12\pi d^2} \quad (1)$$

Here, A_H is the Hamaker constant.

The electric double layers lead to a repulsive interaction energy that results from:^[46]

$$W(d)_{\text{rep}} = 64c_0k_B T \cdot \tanh^2\left(\frac{e\psi_0}{4k_B T}\right) \cdot e^{-\frac{d}{\lambda_D}} \quad (2)$$

With the concentration c_0 of a monovalent salt, the elementary charge e , the surface potential ψ_0 , and the Debye length λ_D . When calculating the sum of these energies, the decisive parts are the proportionalities to $1/d^2$ of the attractive term and to e^{-d} of the repulsive term:

$$W(d)_{\text{DLVO}} = W(d)_{\text{rep}} + W(d)_{\text{att}} \quad (3)$$

A common method for determining the interaction force $F(d)$ from the area-dependent energy $W(d)$ for curved surfaces, e.g. two spheres, is the Derjaguin approximation:^[47]

$$F(d) = 2\pi R_{\text{eff}} \cdot W(d) \quad (4)$$

For two identical spheres, the effective radius results in $R_{\text{eff}} = (R_1^{-1} + R_2^{-1})^{-1} = R/2$. With the van der Waals forces being always attractive (negative sign) the DLVO force is ruled by these attractive interactions at low distances whereas it is dominated by repulsive interactions at intermediate distances.

Since van der Waals forces always rule at low distances, aggregates are formed if the energy barrier E_B can be overcome by the thermal energy, which leads to instable

colloids. Therefore, it is important to take a closer look at the contributions influencing the extent of E_B . As can be seen from $W(d)_{\text{rep}}$, there is a proportionality to the surface potential ψ_0 . Obviously, increasing the surface potential increases the colloidal stability. The decay of the repulsive term is further influenced by the Debye length. λ_D is defined as the distance at which ψ_0 decays to the 1/e-fold:^[46,48]

$$\lambda_D = \sqrt{\frac{\epsilon\epsilon_0 k_B T}{2c_0 e^2}} \quad (5)$$

With ϵ as the permittivity.

Thus, it is a measure for the screening of surface charges by ions dissolved in the dispersant (dependence on c_0). Unfortunately, the experimental determination of ψ_0 and λ_D is difficult due to the electrical double layer. However, the potential can be quantified indirectly by calculating the ζ -potential from measurements of the electrophoretic mobility of particles. It describes the charge at the slipping plane—thus includes the electrical double layer. A common rule of thumb considers particles with a ζ -potential exceeding ± 30 mV as stable.^[48,49] This value becomes significant if compared to $k_B T/e$, that is, the required potential to compete with the thermal energy, which is 25 mV at room temperature.^[50]

To generate a sufficient surface potential for stabilization of a colloidal dispersion, different synthetic strategies are available. Introducing surface charges is a common method to enhance the repulsion between colloidal particles. This is typically achieved by adding small, charged molecules or surfactants. For instance, the Turkevich^[51] synthesis uses citrate to reduce Au^{+III} to Au^0 , but at the same time, the Au-nuclei are stabilized by the negatively charged citrate molecules. Similarly, surfactants like sodium dodecyl sulfonate (SDS) can be used as stabilizing agents. However, repulsive charge interactions are not exclusively responsible for the colloidal stability.

Another method for stabilizing nanoparticles is the application of polymers as stabilizing agents. The resulting particle interactions, partially going beyond classical DLVO forces, are often referred to as steric interactions. Before considering these interactions, it is necessary to examine the nature of the polymer-nanoparticle binding. Physisorbed polymers like polyethylene glycole (PEG) on gold particles are typically in a dynamic equilibrium with their dissolved state whereas chemisorbed polymers like the thiol-functionalized PEG-SH feature a strong binding to the particle surface. Hereby, the accessible polymer conformation (e.g. coils or brushes) and the stability of the shell are determined. The mentioned steric interactions are usually of repulsive nature as they are entropic. When the polymeric shells of two colloidal particles start overlapping, an osmotic pressure arises.^[47] The extent of these interactions, as well as counteracting attractive forces, are dependent on the interplay between polymer-polymer, polymer-solvent, and solvent-solvent interactions that are described by the Flory-Huggins theory.^[52,53] An interesting quantity for their evaluation is the polymer-solvent interaction parameter χ . Values < 0.5 describes that polymer-solvent interactions are

more favorable than polymer-polymer interactions and thereby indicates good solvent conditions. For values >0.5 , polymer-polymer interactions are energetically preferred, which means these bad solvent conditions lead to more compact polymer coils.^[54] This means, steric interactions are less extended and additional attractive interactions between the polymer chains have to be taken into. Thus, good solvent conditions are generally favorable in polymer-stabilized colloids. Since the χ -parameter is temperature-dependent, a polymer-solvent system may cross the border between good and bad solvent conditions. This is referred to as theta condition and is of special interest for polymer-coated colloidal particles. As the stabilizing forces arising from steric repulsion are significantly altered at the theta temperature, responsive systems can be created. A popular example is poly(*N*-isopropylacrylamide) (PNIPAM), a temperature responsive polymer that undergoes a significant volume phase transition (VPT).^[55,56] Further information on the application as coating for nanoparticles is given in section 3.2.

It is important to note that particle interactions are mostly combinations of different forces. In that sense, repulsive steric interactions are often accompanied by DLVO forces. Popular examples for the interplay of both forces are polyelectrolytes.^[47] In their case, a single polymer chain carries multiple ionic groups. Together with the steric interactions, the repulsive charge interactions contribute to the stability of polyelectrolyte coated gold particles.^[57] On the contrary, charged conductive polymers provide insufficient repulsive interactions if applied as particle coatings because they are insoluble in water. Polyaniline (PANI) is an example of such polymers that can be applied as particle coatings but require further agents such as SDS to provide sufficient colloidal stability.^[28,58] Still, these coatings are relevant due to their redox- and pH-responsive behavior (section 3.2). Furthermore, this behavior comes along with changes of the permittivity that, in turn, influences the optical properties of metallic nanoparticles as described in the following section.

1.2 Localized Surface Plasmon Resonances

Inorganic pigments have been used since ancient times to create intense colors.^[59,60] The combination of these pigments with glass is particularly fascinating, as it allows to create objects that are not only colored themselves, but also influence the color of transmitted light (see Figure 8a). Metal salts are commonly applied for the preparation of stained glass, as they provide the required thermal stability and a defined absorption without bleaching over time. However, during processing, some salts are reduced to their metallic state—but without revealing their typically known colors. The Lycurgus Cup shown in Figure 8b is probably the most popular example of metallic gold exhibiting an intense ruby color.

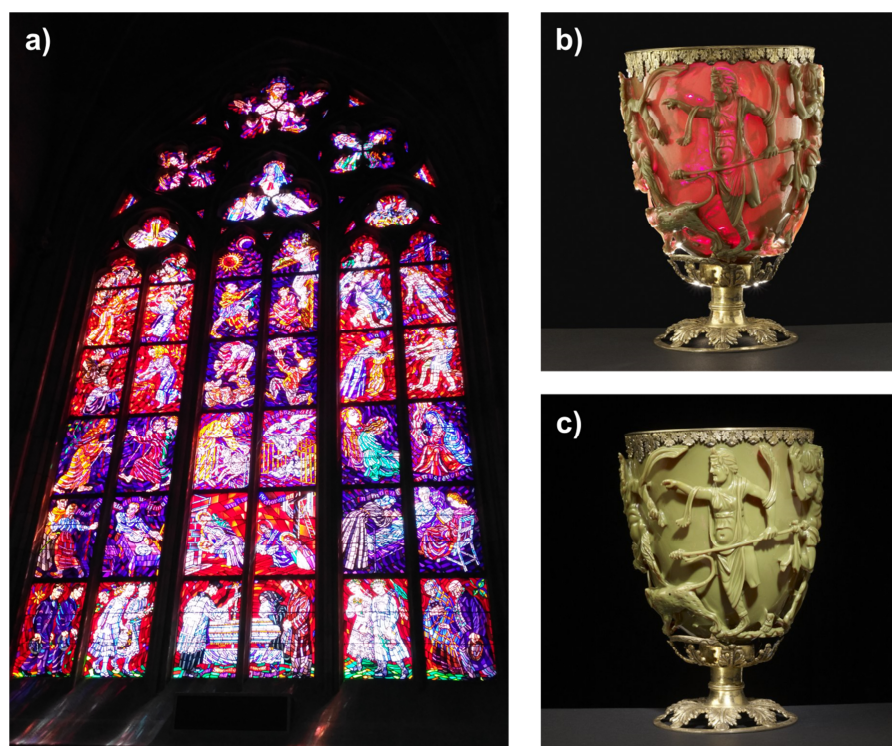


Figure 8. Artworks from stained glass. a) Window in the Holy Sepulcher Chapel (St. Vitus Cathedral, Prague) designed by Karel Svoboda. b/c) The Lycurgus Cup: a Roman drinking cup from the 4th century. b) Picture taken with illumination from inside of the cup (transmission). c) Picture with illumination from outside (reflection). b/c) Reprinted under the terms of Creative Commons Attribution NonCommercial-ShareAlike 4.0 International (CC BY-NC-SA 4.0) license.^[61,62] Copyright by the British Museum.

Although the effect was known at least since the 4th century, it took until the early 20th century to provide a scientific explanation. A fundamental prerequisite was the finding, that gold shows its ruby color only in the colloidal size regime.^[9,41] A theoretical approach to explain this effect was first derived by Maxwell Garnett whose equations were later solved analytically by Mie for spherical particles.^[8,63] By this, Mie rebutted an earlier theory of Ehrenhaft, who assumed the colloidal gold particles to be in resonant oscillation with the incident light.^[64] Interestingly, this misconception is not too far from the picture which is commonly used to describe localized surface plasmon resonances (LSPRs) occurring in these particles.

According to the free electron approximation (Drude model), the conduction electrons of a metal can move freely within a metallic body.^[65] An electromagnetic wave can excite the surface electrons of certain metal nanoparticles to resonant oscillations, which is known as LSPR (see **Figure 9**).^[66] The excitation of such plasmonic materials is accompanied by absorption and scattering of the incident radiation. For gold nanoparticles, for instance, the resonance frequency is in the visible wavelength range which results in intense colors. As shown for the Lycurgus Cup in Figure 8b, the absorption of green light gives rise to the ruby color of the transmitted light. *Vice versa*, without illumination from inside, the scattered light reveals the complementary green color (Figure 8c).

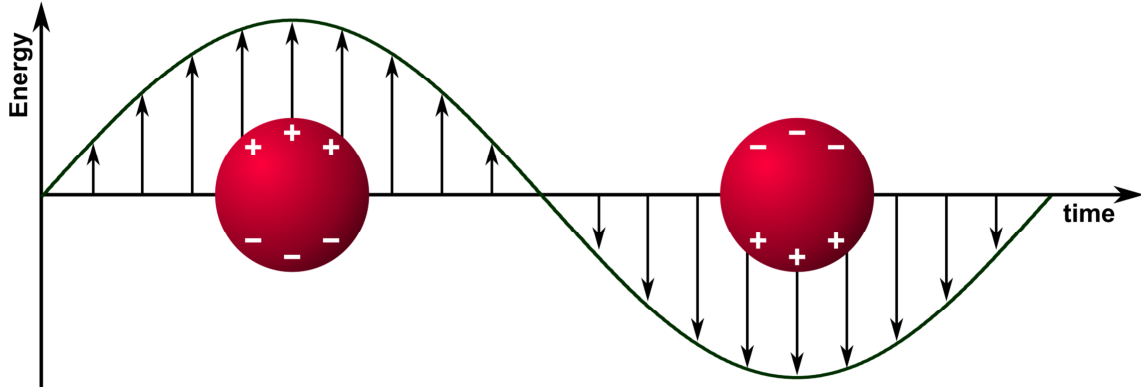


Figure 9. Schematic depiction of the localized surface plasmon resonance. The surface electrons of a metal particle are resonantly excited by the electric field of the incident radiation. A dipolar oscillation arises.

The movement of the surface electrons is confined by the geometry of the metal particle, which causes the resonance frequency to be influenced by its size and shape. The fully symmetric case, namely a sphere, gives rise to the polarization-independent fundamental modes, which is well described by Mie's theory. Small spherical particles ($2r < 25 \text{ nm}$)^[67] mainly support a dipolar mode, as depicted in Figure 9. Their dipole moment defines the response to the external field and is dependent on the polarizability a .^[11]

$$a = 4\pi R^3 \frac{\epsilon_m - \epsilon_d}{\epsilon_m + 2\epsilon_d} \quad (6)$$

Where ϵ_m and ϵ_d are the dielectric functions of the metal and the dielectric medium. A measure of the wavelength-dependent absorption and scattering is given by their cross-sections σ .^[11]

$$\sigma_{\text{abs}} = \frac{2\pi}{\lambda} \text{Im}(a) \quad (7)$$

$$\sigma_{\text{sca}} = \frac{8\pi^4}{3\lambda^4} |a|^2 \quad (8)$$

It follows that the absorption cross-section is proportional to R^3 , while the scattering

cross-section scales with R^6 . Consequently, smaller particles are dominated by absorption while scattering prevails for larger particles ($R > 15$ nm).^[68] Objects with dimensions smaller than 30 nm exhibit a negligible scattering contribution, which is a common threshold for single particle spectroscopy (see section 1.3.1).^[68] Another observation, following from the denominator of the polarizability, is the resonance condition: A minimum in $|\epsilon_m + 2\epsilon_d|$. The resonance position thus depends on the material itself, with the most common examples of plasmonic metals being gold, silver, and aluminum.^[69,70] Furthermore, it depends on the dielectric surrounding. There is a linear red-shift of the resonance wavelength λ_{\max} with increasing refractive index n of the medium.^[16] This phenomenon is frequently used in biosensing since organic molecules are likely to adsorb on the surface of metallic particles and induce local changes of the refractive index.^[71] Besides the influence of the dielectric constants, the particle diameter has a strong impact on λ_{\max} . With increasing size, the dipolar mode is shifted to longer wavelengths as the polarizability increases ($\sim R^3$). Link and El-Sayed have experimentally demonstrated such red-shift for gold spheres and reported a significant broadening of the plasmon bandwidth.^[67] The latter can be explained by the increased influence of retardation effects at larger particle sizes, as well as the superposition with higher order modes like quadrupolar oscillations.^[11,72] A further influence on the polarizability is given by the particle shape.^[73] For instance, if a sphere is elongated in one direction (spheroid), the LSPR becomes polarization-dependent.^[59] There are two extreme cases: a dipole orientation along the elongated axis or the perpendicular axis. The polarizability for the elongated case is higher, which results in a red-shift of λ_{\max} with respect to the spherical case. When going towards less symmetric cases, e.g. rod-shaped particles, two distinct modes can arise. They are commonly referred to as transversal (lower wavelength) and longitudinal (higher wavelength) resonance, as displayed in **Figure 10a**.^[74,75] Mock *et al.* have further studied the influence of particle shape on the spectral position of the resonance.^[76] A generally observed trend is a more pronounced red-shift for geometries with sharper edges.^[77,78]

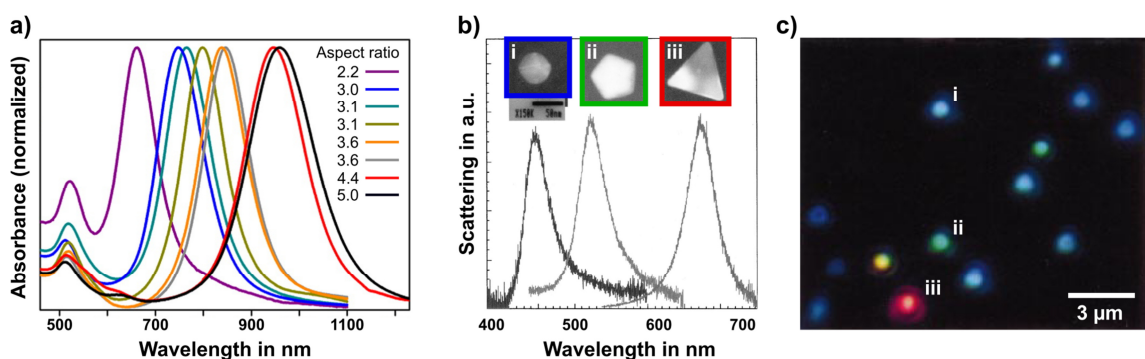


Figure 10. Influence of the particle shape on their optical properties. a) Absorbance spectra of gold nanorods with increasing aspect ratio. b) Scattering spectra of silver nanoparticles with different shapes (spherical, pentagonal, and triangular). c) Dark field micrograph of the respective particles. a) Adapted with permission.^[75] Copyright 2013 by the American Chemical Society. b/c) Adapted with permission.^[76] Copyright 2002 by AIP Publishing.

Due to their asymmetric shape, such structures leave the boundaries of Mie's theory and their optical properties cannot be described by analytical solutions.^[72] Different methods are required to predict the optical properties of these systems. In the last two decades, developments in the field of computing enabled numerical simulations to solve these questions. Finite difference methods (FDM) and finite element methods (FEM) are the bases for commercial simulation programs, *e.g.* Lumerical and COMSOL, which have been applied for this work. This allows predicting the optical properties of even sophisticated plasmonic structures. In order to prove the findings from optical simulations experimentally, a combination of analytical methods is required, which will be introduced in the following section.

1.3 Particle Characterization

This section will provide information on the fundamental measurement techniques used in this work. To describe the properties of plasmonic nanoparticles exhaustively, a combination of different optical and structural investigation methods is required. The optical investigation is covered through UV/vis, fluorescence, and scattering spectroscopy. For studying the particle geometry and surface topography, microscopy techniques were used. Transmission and scattering electron microscopy provide detailed information on the composition of the particles as well as their geometry, while atomic force microscopy is utilized for characterizing the topographic properties and particle distributions on substrates. To gain information on the colloidal properties of the applied dispersions, light scattering is used for determination of the hydrodynamic radius and the ζ -Potential.

1.3.1 Spectroscopy

Optical spectroscopy is one of the most common investigation techniques in chemistry. The chromatic dispersion of light has been known for thousands of years by the appearance of colorful arcs during rain showers. However, it took until the 17th century for the first scientific documentation of this effect, when Newton dispersed sunlight by using a pinhole and a glass prism.^[79] This basic principle is still applied for operation of modern spectrophotometers. As shown in **Figure 11**, light from a source, e.g. a halogen lamp, is reflected by a mirror towards a grating or prism, which acts as the wavelength dispersive element. The resulting angular dependence is caused either by refraction (prism) or by diffraction (grating). By rotation of this element, a narrow wavelength range is determined by means of a slit.

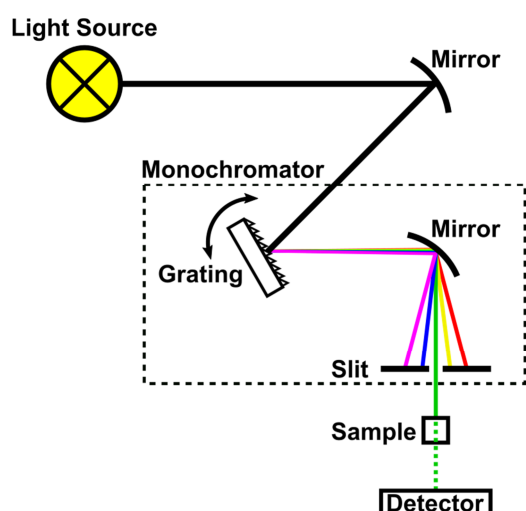


Figure 11. Schematic depiction of a spectrophotometer. Light is guided through a mirror system from the light source to a grating that leads to chromatic dispersion of the beam. A slit is applied to determine a narrow wavelength range. The unit containing the grating and the slit is thus called monochromator. The wavelength is tuned *via* rotation of the grating. After passing the sample, the transmitted light is collected by a detector.

As a result, monochromatic light passes the sample and is detected either by a charged coupled device (CCD) or by a photodiode. If no slit is used (polychromator), a diode array can be applied to capture the full spectrum without the requirement of a rotating grating.^[80]

When passing the sample, the incident light is attenuated. This attenuation is quantified by the negative common logarithm of the transmittance T_λ which compares the incident intensity I_0 to the intensity I of the transmitted light. The quantity is called absorbance A_λ whereas the term Extinction E is more common in German:^[80]

$$A_\lambda = -\lg\left(\frac{I}{I_0}\right) = -\lg T_\lambda \quad (9)$$

Although the absorbance is often confused with the absorptance (also abbreviated A), it is composed by processes of absorption, reflection, diffraction, and scattering. However, if diffraction and scattering are negligible, the wavelength-dependent absorbance can be used to determine the concentration c of absorbing substances *via* Beer-Lambert law:^[80]

$$A_\lambda = \varepsilon_\lambda \cdot c \cdot l \quad (10)$$

Where ε_λ is the molar attenuation coefficient and l is the path length, *i.e.*, the thickness of the sample. This linear dependence of the absorbance on the concentration could also be adapted for gold nanoparticle dispersions. As discussed by Scarabelli *et al.*, the absorbance of elemental gold at 400 nm^[81] can be utilized to determine the concentration of Au⁰ in nanoparticle dispersions if the scattering contribution is sufficiently low.^[82] It is to note that this empiric method has been applied for determination of stock concentrations in this work.

UV/vis spectroscopy is further used to gather information on the plasmonic properties of nanoparticle systems. As described above, LSPRs result in pronounced absorption and scattering which is strongly dependent on the material, size, shape, and dielectric surrounding of particles.^[11] Hence, if material, size, and shape are detected—for instance by the methods described in the following sections—conclusions can be drawn concerning the particle surrounding as well as their coupling behavior.

A powerful method for determining the optical properties of single particles is dark field microscopy, or more precisely, scattering spectroscopy. The fundamentals of this technique are displayed in **Figure 12a**. In contrast to bright field microscopy, a beam stop above the condenser blocks the center part of the beam, which results in a hollow cone illumination of the specimen. It is required that the numerical aperture (NA) of the condenser is higher than the NA of the objective, where $NA = n \cdot \sin\theta_{\text{obj}}$.^[83] With the refractive index n and θ_{obj} as the maximum half-angle of the cone, this condition means that the direct beam is not collected by the objective. Thus, only light that is scattered by the specimen can be detected. This leads to an inversion of the contrast and prevents common issues due to outshining of small objects known from bright field techniques.^[84]

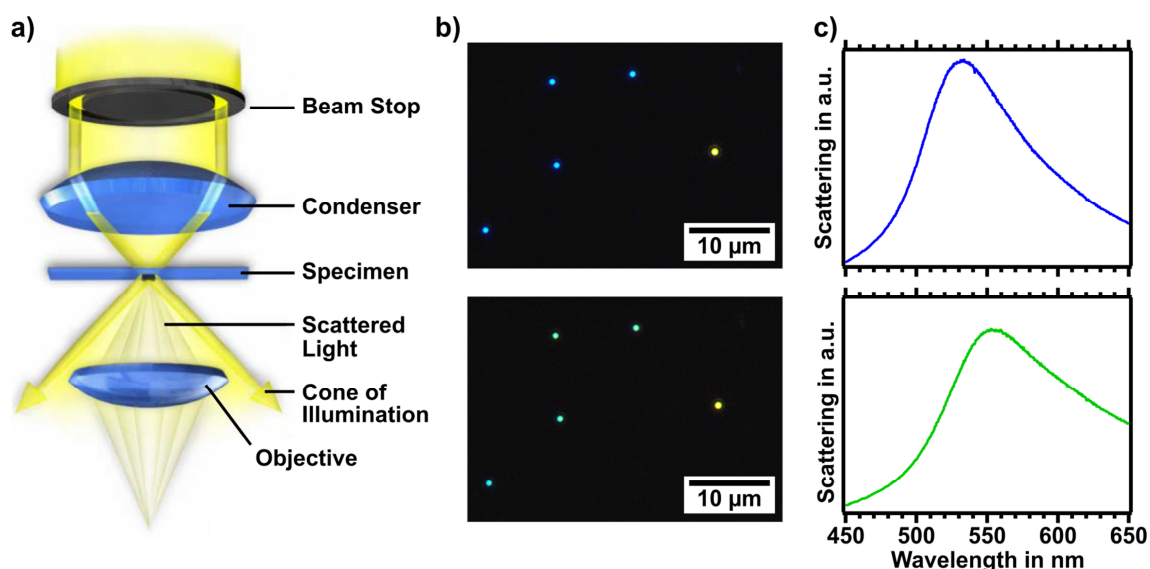


Figure 12. Dark field microscopy. a) Schematic depiction of the light path in a dark field microscope. The light is partially blocked by a beam stop before the condenser resulting in a hollow cone illumination. Only light scattered by the specimen enters the objective. b) Dark field image of silver nanocubes after a few minutes (top) and after a few hours (bottom) exposure to air. c) Respective scattering spectra before and after oxidation. a) Adapted with permission.^[84] Copyright 2002 by Wiley VCH. b/c) Credit for providing silver nanocubes goes to Martin Mayer and Anja Steiner.

The Abbe diffraction limit describes the minimum distance at which two objects can be distinguished from each other:^[83,85]

$$d_{\min} = \frac{\lambda}{2 \cdot \text{NA}} \quad (11)$$

However, it is possible to image objects that are significantly smaller than this limit. For plasmonic nanoparticles, the scattering contribution becomes significant at about 30 nm which enables single particle spectroscopy.^[68] Figure 12b shows two exemplary micrographs of silver cubes on a glass substrate. A distinct color of the objects is notable in the images (blue dots in the upper image whereas the lower one shows greenish dots). The scattered light of a single particle can be acquired by a spectrometer if the objects feature sufficient spacing ($> 3 \mu\text{m}$). The respective spectra are displayed in Figure 12c. In this case, the top row shows the silver particles directly after preparation of the sample while the lower row was measured after several hours of exposition to air. Oxidation of the silver cubes leads to rounding of the edges which results in a spectral red-shift of the LSPR and a respective change of the color.

This facile example demonstrates how simple kinetic reactions can be observed on the single particle level *via* dark field microscopy. Furthermore, from the position of the plasmonic scattering, conclusions can be drawn concerning the particle geometry. However, to provide comprehensive structural information, additional methods are required to be correlated with the single particle spectra.

1.3.2 Electron Microscopy

Conventional optical microscopy suffers mostly from its physical limitations due to the Abbe limit of diffraction. Particularly, it restricts the fundamental resolution to ~ 200 nm for visible light. A natural circumvention of this issue is the reduction of the applied wavelength. However, glass lenses (SiO_2) and common sample materials absorb strongly in the UV region. Thus, different techniques were required to facilitate illumination at low wavelengths. Shortly after de Broglie postulated, that all matter features a wave-like character, Thomson could prove this hypothesis, by demonstrating the scattering of electrons in 1927.^[86,87] The application of magnetic lenses allowed for construction of the first electron microscopes which surpassed the resolution of light microscopes in 1935.^[88] The fundamental strength of this method is provided by the de Broglie wavelength,^[89] which is defined by means of the Planck constant h and the momentum p :^[90]

$$\lambda = \frac{h}{p} = \frac{h}{m \cdot v} \quad (12)$$

With m being the mass, the wavelength λ depends on the velocity v of the electrons, which can be tuned by the accelerating voltage of an electron gun. For instance, a typical voltage of 100 kV results in a wavelength of 3.7 pm. This means, that the resolution of electron microscopes is limited by technical aspects (e.g. detectors and optical aberrations) rather than the underlying physics. There are two common variations of this technique: transmission electron microscopy (TEM) and scanning electron microscopy (SEM). They differ in their technical setup, sample preparation, and received information.^[91]

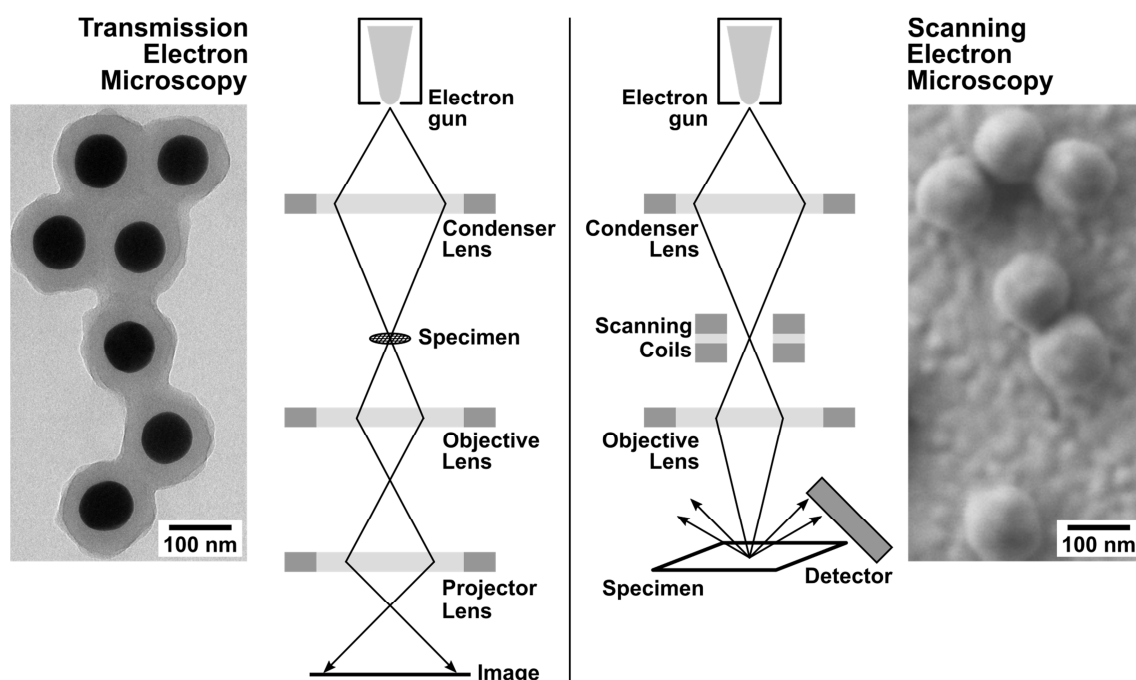


Figure 13. Electron microscopy. Left: Schematic depiction of a transmission electron microscope (TEM) with a respective image of Au-core/PANI-shell particles. Right: Schematic depiction of a scanning electron microscope (SEM) with a respective image of the same particles.

TEM is quite comparable to standard light microscopy. As shown in **Figure 13**, an electron beam, generated by the electron gun, is focused through a magnetic lens (condenser) and passes the sample. The transmitted beam is collected by an objective lens and focused at a fluorescent screen that visualizes the image. SEM could be largely compared to confocal laser scanning microscopy. Here, the focused beam is passing a scanning coil and then focused on the sample by the objective lens. The reflected beam (primary electrons) or the scattered beam (secondary electrons) is collected by the inlens or the secondary electron detector. The image is generated *via* scanning of the substrate and electronic composition of the intensity signals.

Both techniques utilize high vacuum, and thus, dried or frozen samples are commonly applied. Apart from this, the setups result in different requirements for the sample preparation. Due to the absorption of electrons by matter, TEM specimens need to be prepared sufficiently thin. Depending on the nature of the analyte, freestanding films or layers on top of carbon films are commonly prepared on copper grids. With respect to this work, dilute particle dispersions were typically drop-casted on copper grids with carbon films. During the measurement, the thermal stability of the samples has to be considered, *e.g.*, high illumination intensities can lead to melting of polymer coatings. For SEM, the sample thickness is almost irrelevant. Electrons are mostly scattered within a few nanometers of penetration depth. However, electrostatic charging of the samples can become an issue, as it leads to overexposure and blurring during the imaging process. To circumvent this effect, the samples can be sputtered with thin layers of conductive materials like Pt, Au, and carbon.^[91] In this work, particles on metal films, glass, and silicon were investigated, whereat the non-conductive samples were sputtered with platinum.

As can be observed from the micrographs in Figure 13, there are several differences regarding the accessible information from both methods. Due to the detection of a transmission signal, a single TEM image yields a 2D projection of the sample, which can provide information on the inner structure of a specimen. In the case of core-shell particles, there is a strong contrast between the two materials, because scattering and absorption are more pronounced for the gold core. Thus, precise data on core sizes and shell thicknesses can be extracted. However, since the specimens are specially prepared for microscopic investigation, no information is obtained on the final structure of the samples, like the particle distribution for instance. On the contrary, in SEM, the final samples can be directly applied for investigation. Due to the limited penetration depth of the electron beam, the received information related to the surface of the specimen. A 3D-impression is obtained because oblique areas and edges either lead to a larger surface area at which scattered electrons can exit the sample (bright areas) or they face away from the detector which leads to blocking of the scattered electrons (shadowing). Information on the surface topography and particle coverage can be received over large areas.^[91,92]

1.3.3 Atomic Force Microscopy

Atomic force microscopy (AFM), or scanning probe microscopy, was first introduced by Binnig *et al.* in 1986.^[93] The method is based on a technique that can be compared to a record player. A probe, which may feature a sharp tip, is located at the freestanding end of a cantilever. In imaging mode, the probe is systematically scanning a substrate, whereat the interactions between the probe and the surface deflect the cantilever. In contrast to a record player, the deflection is not detected by a piezoelectric translator but through a laser beam which is reflected on the backside of the cantilever (see **Figure 14a**). The signal of the reflected beam is detected by a quartered photodiode. Deflection of the cantilever is always caused by superposition of different interaction forces between the tip and the substrate. Depending on the imaging mode, the tip is in contact with the surface (contact mode), at a certain distance from the surface (non-contact mode), or in an intermittent contact (tapping modeTM). The influence of long range forces usually extends up to a distance of a few nanometers. Mainly, van der Waals forces (on the molecular level $\sim d^{-6}$), Coulomb interactions ($\sim d^{-2}$) and capillary forces play a role if the probe is not in contact with the surface of the sample.^[94] Long range interactions are of attractive nature if they are not dominated by repulsive electrostatic forces. Short range interactions feature Pauli repulsion, metallic adhesion^[95] and friction (due to movement of the probe) which are especially relevant when the probe is in contact with the surface.^[96,97]

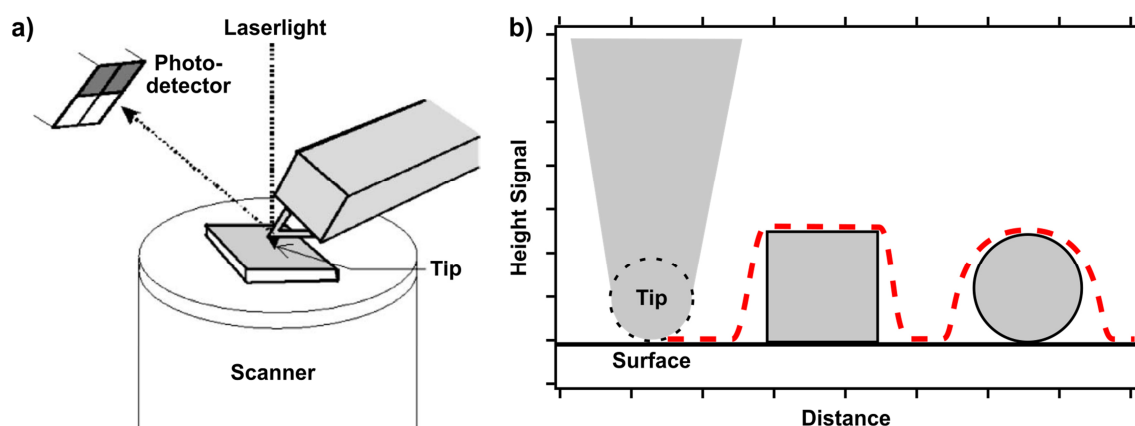


Figure 14. Atomic force microscopy for imaging purposes. a) Schematic depiction of the atomic force microscopy technique. A sharp tip, located at the freestanding end of a cantilever, is scanning a surface (here by moving the sample). Deflection of the cantilever is measured indirectly by detecting laserlight that is reflected at the backside of the cantilever and detected by a photodiode. b) Hypothetical height-distance curve for scanning of squared and round objects, showing the convolution due to the tip geometry. a) reprinted with permission.^[96] Copyright 2005 by Elsevier.

Commonly, three different methods of probing the surface are distinguished. It is important to mention that the resulting height profiles arise from superposition of the surface profile and the tip geometry as depicted in Figure 14b. This effect is called convolution and leads to an apparent smoothing and an increased width of objects with dimensions comparable to the tip radius. It is relevant for any surface probing method.

Scanning the substrate in close proximity to the surface is called contact mode. Deflection of the cantilever can be used to create a height profile directly from the detector signal (constant height mode). Alternatively, the deflection and therefore the interaction force can be kept constant by adjusting the z-position with a piezoelectric translator which is controlled by a feedback loop (constant force mode). However, the technique features two drawbacks caused by friction. While moving, the cantilever can twist due to forces that are not acting perpendicular to the surface. This can lead to perturbations in the detected signal. Moreover, abrasion of the probe can alter the contact geometry.

The non-contact mode can be used to overcome some issues of the contact mode measurements. In this technique, the cantilever is excited to oscillate close to its resonance frequency at a distance of a few nanometers from the surface. Long range attractive forces between the tip and the surface cause damping, which changes when the distance shifts. A feedback loop is used to keep the amplitude constant by variation of the z-piezo position. This in turn, is used to calculate a height profile. As the probe is not in direct contact with the sample, friction plays a minor role in this mode. However, weaker interaction forces in combination with stiffer cantilevers lead to reduction of the lateral resolution compared with contact mode.

The combination of both techniques leads to intermittent contact or so-called tapping modeTM. Similar to non-contact mode, the cantilever oscillates close to its resonance frequency but slightly taps the surface in this motion. This increases the lateral resolution due to stronger interaction forces but still minimizes the drawbacks caused by friction. Moreover, additional information about the surface can be achieved by observation of the vibrations' shifts in phase. The phase signal is sensitive to changes in adhesive forces and viscoelastic properties. Therefore, it is suited to determine material contrasts as in the example hard-core/soft-shell particles. The intermittent contact mode was applied throughout this work as it delivers the best compromise of lateral resolution and persistence of the scanning probe.^[97,98]

1.3.4 Light Scattering

Light scattering methods are commonly applied to gain information on particle sizes and the diffusion behavior of colloidal systems. Static light scattering can be applied for direct determination of particle size but is limited to monodisperse spherical systems. In contrast, dynamic light scattering provides the diffusion constant that can be utilized to calculate the hydrodynamic radius of the particles by applying the Stokes-Einstein equation. If an external field is applied to dispersions of charged colloidal particles, the scattering information can be used to determine the electrophoretic mobility, which leads to the ζ -Potential by means of the Smoluchowski approximation.^[48]

The interaction of light and matter results in different effects including absorption, reflection, and scattering. For light scattering measurements, elastic interactions are typically considered. The scattering center is regarded as an emitter of secondary waves which feature a different direction of propagation but the same phase and energy as the primary wave. The difference between both wave vectors (at an angle θ) is defined by the scattering vector \vec{q} :^[99]

$$|\vec{q}| = q = \frac{4\pi n}{\lambda} \cdot \sin \frac{\theta}{2} \quad (13)$$

The dynamic light scattering (DLS), or photon correlation spectroscopy, utilizes the fact that colloidal systems are subject to Brownian motion. Thus, fluctuations of the scattering intensity can be recorded with a photodetector and correlated against short time intervals. The operating principle of a DLS setup in the form of a ZetaSizer (Malvern) is depicted in Figure 15a.^[100] The time-dependent exponential decay of the intensity can be transformed into the time-dependent field autocorrelation function g^1 . Generally, larger particles move with a lower velocity which results in a slower decay of the autocorrelation as shown in Figure 15b.

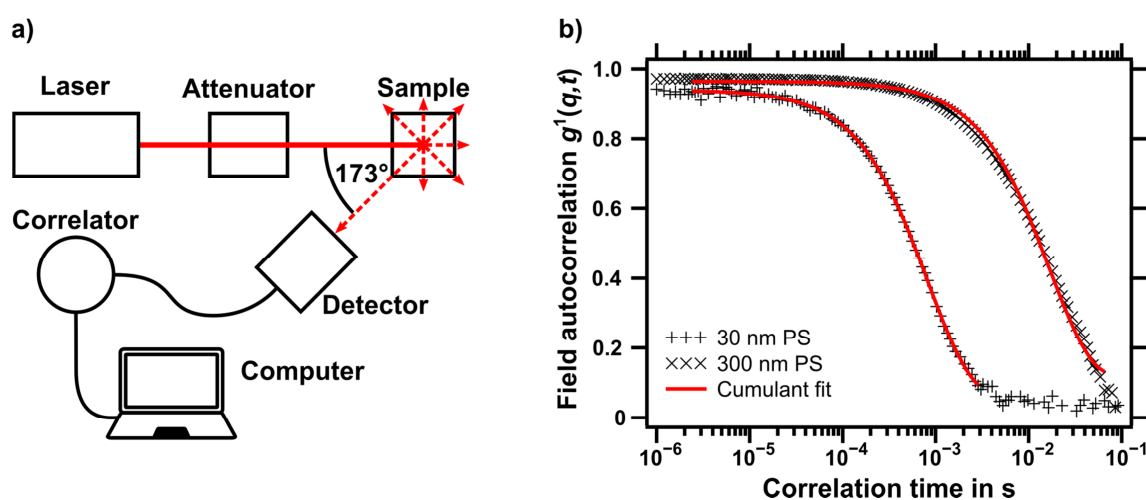


Figure 15. Dynamic Light Scattering. a) Schematic depiction of a DLS setup as applied in a ZetaSizer. A laser illuminates a dispersed sample and the scattered light is detected at an angle of 173° . The time-dependent intensity fluctuations are compared to the initial intensity by a hardware correlator and processed with a computer b) Field autocorrelation functions of 30 nm (+ marker) and 300 nm (× marker) polystyrene particles.

The decay can be described by two cumulants Γ_1 and Γ_2 , where Γ_1 corresponds to the average relaxation rate $\langle\Gamma\rangle$ and Γ_2 determines the polydispersity of the system. The most common methods for calculating the cumulants apply either a Taylor series or a Laplace transform (CONTIN algorithm).^[101] The diffusion coefficient D can be calculated as the quotient of the relaxation rate and the square value of the scattering vector:^[102]

$$D = -\frac{\langle\Gamma\rangle}{q^2} \quad (14)$$

As DLS is frequently used to determine sizes instead of the diffusion coefficient, the Stokes-Einstein is usually applied to calculate the hydrodynamic radius R_H of the particles:^[102]

$$D = \frac{k_B T}{6\pi\eta R_H} \quad (15)$$

Where k_B is the Boltzmann constant, T is the temperature, and η is the dynamic viscosity of the medium. It is important to bear in mind that the hydrodynamic radius includes the electric double layer of adsorbed ions influencing the diffusion coefficient. Thus, R_H is always larger than the actual size of colloidal particles but provides additional information on their behavior in the dispersed state. Because of that, the solvent conditions have to be taken into account for comparison of the hydrodynamic properties of different particle systems.

Light scattering can be further utilized to determine the surface charge of colloidal particles. Therefore, a potential can be applied to the dispersion, which results in electrophoresis. This movement of particles is detected by the scattering, which is applied to quantify their velocity v by means of the Doppler shift. The electrophoretic mobility μ_e is defined as the ratio of the velocity and the applied field E .^[48]

$$\mu_e = \frac{v}{E} \quad (16)$$

For colloidal systems, the electric double layer is thin compared to the size of a particle. If the dielectric constant ϵ of the sample is known, the ζ -potential can be calculated with the Smoluchowski approximation:^[48]

$$\zeta = \frac{\eta}{\epsilon \cdot \mu_e} \quad (17)$$

The described methods are powerful techniques to determine the properties of nanoparticles in dispersion. Namely, they indicate their hydrodynamic size in dependence on the solvent conditions and allow assessing their stability as well as their repulsive interactions *via* electrostatics. Hereby, fundamental information is received for the assembly of colloidal particles.

2 Coupling of Plasmonic Particles

This section deals with particles featuring anisotropic plasmonic properties in consequence of an inhomogeneous surrounding. These effects are usually induced by the presence of other particles or a substrate. The following questions will be answered:

- What happens if particles are adjacent to other plasmonic particles?
- What is the influence of the inter-particle distance and particle size?
- How can these effects be compared to particles on substrates?
- How can particles interact over long distances?

2.1 Inter-Particle Coupling

The interaction of metal nanoparticles with their surrounding is essential for their plasmonic properties. Since nanoparticles are rarely applied as homogeneously dispersed colloids, it is important to examine the behavior in an inhomogeneous surrounding. Particularly, this means the dielectric constants within a few nanometers distance of the particle surface are discontinuous. For insufficiently stabilized dispersions, the approach of a second particle is a likely case. A theoretical model describing the behavior of two plasmonic spheres in close proximity is given by the hybridization model shown in **Figure 16a**. In analogy to a chemical bonding, the particle dipoles hybridize. Here, bonding combinations feature a lower energy, while the antibonding ones possess a higher energy as compared to the isolated particles. These changes arise from the dipole interaction energy, which is negative in the case of bonding modes, and is dependent on the dipole separation ($\sim 1/d^3$).^[103]

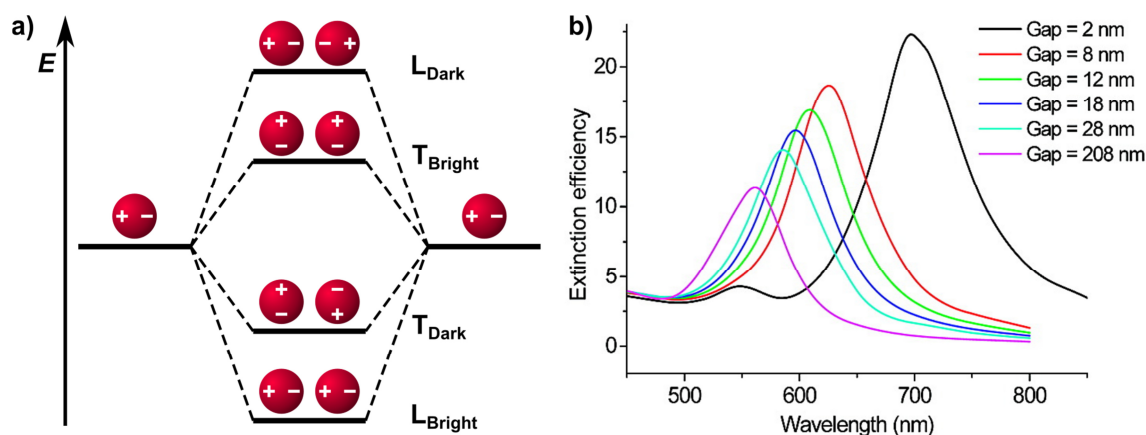


Figure 16. Inter-particle coupling. a) Hybridization model. b) Dependence of the extinction on the inter-particle distance. b) Reprinted with permission.^[104] Copyright 2007 by ACS Publications.

Although, this idealized model neglects retardation effects and multipole oscillations—and thus, underestimates plasmonic coupling at small distances—it can be applied to qualitatively describe the resonant properties of nanoparticles depending on their separation. The modes exhibiting a net dipole moment (here denoted as L_{Bright} and T_{Bright}) are typically radiating into the far field and thus called bright modes in contrast to the

dark modes.^[103,105] As the particles approach, the energetic difference increases. According to the discrete dipole approximation, there is a nonlinear transition for the longitudinal mode (L).^[106] Consequently, the LSPR peak red-shifts with decreasing inter-particle distance as shown in Figure 16b.^[104] This effect also explains the color transition of agglomerating nanosphere dispersions from red towards purple, which is visible by eye.

The addition of further particles in a chain-like configuration results in an additional red-shift of the resonance position as demonstrated by Barrow *et al.*^[107] In their study, the scattering of self-assembled gold nanoparticle chains of different length was investigated via dark field microscopy. As shown in Figure 17, the position shifts nonlinearly from 550 nm to 950 nm with increasing number of particles. In contrast to rod-shaped particles, this behavior does not proceed infinitely but reaches its maximum shift at about ten repeating units, which is known as infinite chain limit.^[108] This limit arises due to the limited polarizability of plasmonic particles, which ultimately leads to degeneration of the longitudinal mode.^[109]

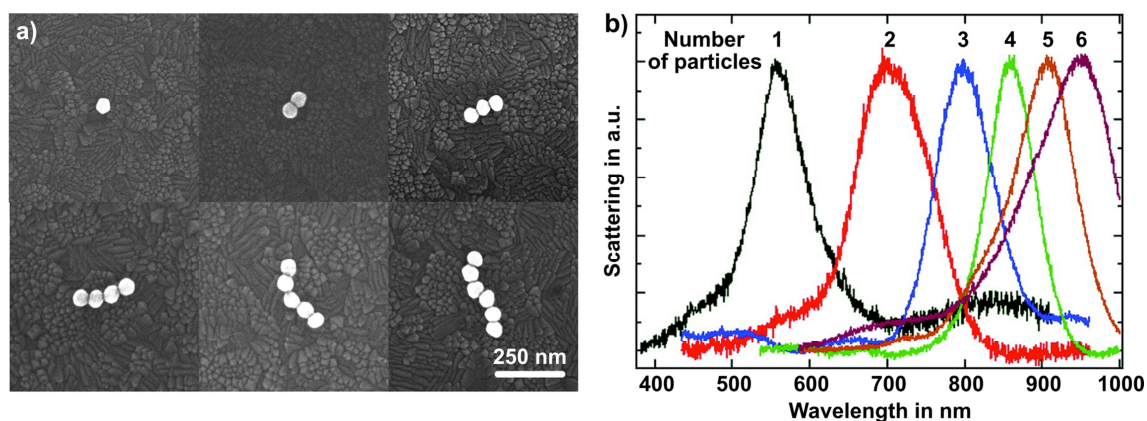


Figure 17. Dependence of the LSPR on length of particle chains. a) SEM images of plasmonic chains of gold nanospheres with different number of particles. b) Scattering spectra of the respective chains. Reprinted with permission.^[107] Copyright 2011 by ACS Publications.

The approach of a second particle is not strictly necessary to induce plasmonic coupling. Indeed, the presence of any interface in proximity to a plasmonic particle will lead to hybridization. For dielectric interfaces like glass, the energy difference is usually too low to be observed experimentally.^[110] On the contrary, plasmonic metal films can induce pronounced coupling. The mechanism can be considered in analogy to the hybridization model for identical particles (see Figure 18a). If a gold sphere is adjacent to a gold film, its dipole induces a corresponding mirror dipole in the film. Two binding modes emerge with the dipole orientation either perpendicular or parallel to the surface. In consequence of the plasmonic coupling, there is a strong enhancement of the electric field in the gap region. This enhancement is strongly dependent on the geometry of the plasmonic cavity. In the case of colloidal particles on planar surfaces, the coupling is more pronounced for larger particles.^[111] The relative intensity of the field can be

assessed by electromagnetic simulations. As displayed for a sphere in Figure 18b, the highest intensity is not located at the minimal gap distance for polarizations parallel to the surface. Due to the antiparallel dipole orientation (binding mode), the situation can be compared to a resonant circuit. The resulting magnetic field is a key feature for light manipulation through plasmonic metasurfaces, *i.e.*, subwavelength structured plasmonic surfaces,^[29] which will be further discussed in chapter V.

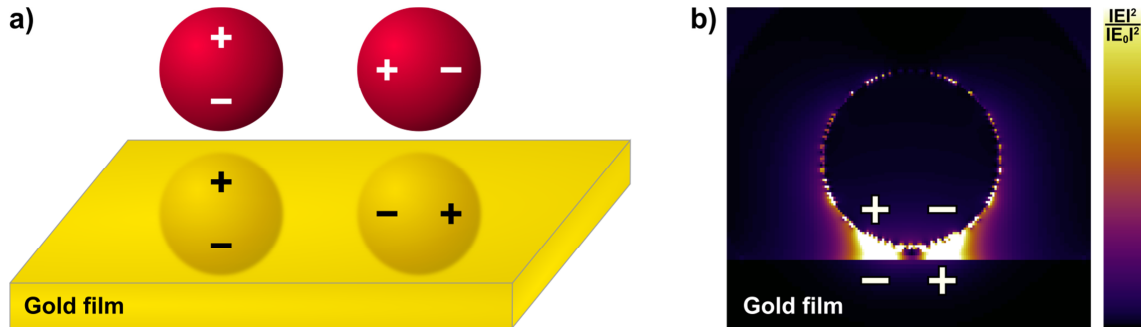


Figure 18. Coupling of plasmonic particles with a gold film. a) Schematic coupling of plasmonic particles (dipolar resonance) with their mirror charges either perpendicular (left) or parallel to the surface (right). b) Electric field enhancement (FDTD simulation) of an 80 nm gold particle in 5 nm distance to a gold mirror.

The coupling of plasmonic particles with metal films is of particular interest since these near-field effects result in modulation of the effective electric permittivity ϵ and the effective magnetic permeability μ , which gives rise to extraordinary properties in the far field. The intended macroscopic response is manifold: depending on the particular system, it could be lasing,^[26] negative refraction,^[112] fluorescence enhancement,^[113] or perfect absorption^[114] for instance. For the latter, different theories exist about the coupling mechanism resulting in the strong absorbance of particle-coated metallic films, which will be discussed in the following section.

2.2 Optical Absorbers

Film-coupled plasmonic systems usually involve metallic films that feature high reflectivity. Thus, it is important to know how coupled plasmonic particles potentially affect this property through near-field interactions. A popular application, utilizing the effects of plasmonic metasurfaces, was introduced by Landy *et al.* who created a near-perfect absorber in the microwave regime.^[115] This idea could be extended further towards optical and near-infrared wavelengths by applying plasmonic nanoparticles with respective LSPR positions.^[114,116-118] However, different approaches for electromagnetic wave absorbers have been studied to provide stealth technology since the 1940s.^[119] Examples of the resulting developments involve interference based technologies,^[120] semiconductor metasurfaces,^[121,122] and carbon nanotube arrays,^[123,124] which serve as near-perfect optical absorbers. Here, the focus will be on the comparison of plasmonic metasurfaces and interference based concepts.

The fundamental difference between both strategies is displayed in **Figure 19**. In both cases, a back reflector provides zero transmissivity. Thus, the absorptivity becomes $A_\lambda = 1 - R_\lambda$. Therefore, the reflectivity R_λ is required to converge zero for achieving perfect absorption. Metasurface approaches utilize the modulation of ϵ and μ to match the impedance z_1 of the surface with the impedance of free space z_0 as follows from the Fresnel equations at normal incidence:^[125]

$$R_\lambda = \left| \frac{z_1 - z_0}{z_1 + z_0} \right|^2 \quad (18)$$

Where $z = \sqrt{\mu/\epsilon}$. As a result, no reflection occurs at the interface between the metamaterial and free space (see Figure 19a). Since the metal substrate still exhibits back reflection, the overall structure will feature perfect absorbance only if sufficient thickness and losses are provided to fully attenuate the electromagnetic wave.

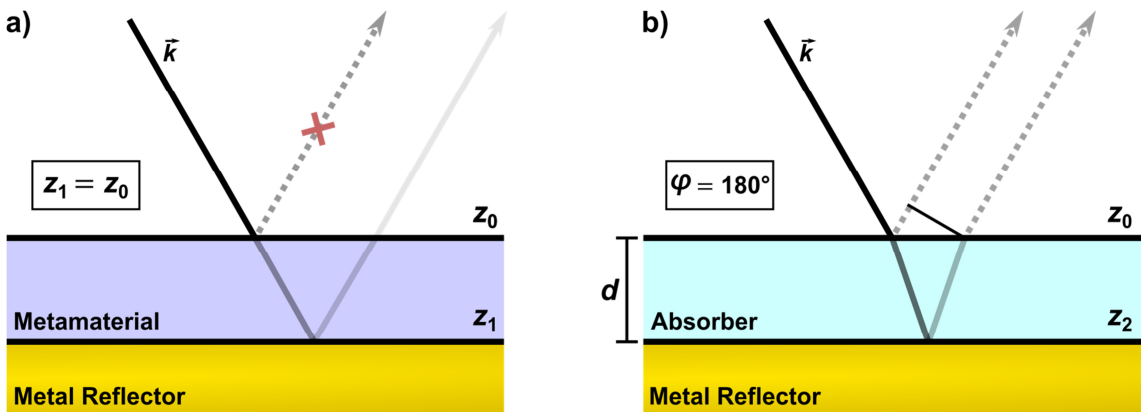


Figure 19. Strategies for near-perfect optical absorbers. a) Metamaterial absorbers combine impedance matching between free space and the metasurface with high losses within the plasmonic structure. As a result, there is no reflection at the surface and the incident light is almost completely absorbed. b) Interference is supported by a dielectric absorber on a metal reflector. A phase shift of 180° , between light that is reflected at the surface and light that is reflected by the metal film, leads to destructive interference.

A conceptually different strategy is the utilization of interference effects, as depicted in Figure 19b. Absorbing dielectric materials are applied to evoke a phase shift $\varphi = 180^\circ$ between waves that are reflected at free space/absorber interface and at the absorber/metal interface, which results in destructive interference. In contrast to conventional thin-film interference, the absorbing material results in rapid attenuation of light.^[120,126] For perfectly conducting substrates, the resonance condition is met at a thickness $d = \lambda/4n$. However, additional phase shifts can be introduced by applying substrates with finite optical conductivity, like gold for instance, which allows for thin layers on the order of a few nanometers ($d \ll \lambda/4n$).^[120]

Even though the strategies are fundamentally different, they may be difficult to distinguish—especially but not exclusively in non-ideal experimental setups. In this sense, typical metamaterial approaches comprise plasmonic particles^[127] or films^[128] that are coupled to a mirror and spaced by a dielectric material. Hereby, the prerequisites for interference effects as described in the above context are simultaneously provided. Thus, the isolated consideration of both effects is a subject of discussion. Indeed, theoretical considerations could show that certain metasurfaces support near-perfect absorption even without taking any magnetic responses into account.^[115,129,130]

To identify the nature of the absorption phenomena, oblique angles of incidence can be used, as they have an impact on the attenuation of the reflected light. Metasurface absorbers are typically efficient below 40° incidence but show significant increase of the reflectance above 60° incidence.^[114] This is due to the fact that the impedance matching condition is only valid for normal incidence.^[125] The absorbed wavelength position is robust, since it depends on the coupled plasmonic resonance. In the case of interference based concepts, an oblique angle results in alteration of the optical path difference. Thus, the efficiency of this type of absorbers also decreases with increasing angle of incidence. In addition, the wavelength, at which a phase shift of 180° occurs, changes. However, this influence is rather weak, since the phase accumulation by the optical path difference is low compared to the reflection phase change at the metal surface.^[120] More importantly, the amplitudes of the interfering waves can differ strongly for s- and p-polarized light, as follows from the Fresnel equations.^[131] In contrast to this, the absorption of metasurfaces is just weakly affected by polarization effects, which represents a major criterion to distinguish both effects experimentally.^[114,125]

2.3 Diffractive Coupling

While pronounced near-field resonance coupling only occurs at relatively small inter-particle distances on the order of the particle diameter or smaller, radiative coupling becomes relevant at distances that are several times larger than the particle size.^[132,133] Diffractive modes of ordered arrays of plasmonic NPs with wavelength-scale periodicity can mediate long-range radiative coupling. This coupling produces surface lattice resonances (SLRs) that strongly differ from the single particle resonance. SLR modes always arise at wavelengths slightly longer than the Bragg mode (λ_{Bragg}), *i.e.*, they appear at lower energies (see **Figure 20**).^[31,133,134] They are characterized by strong field enhancement and narrow bandwidths^[135] (long lifetimes), and thus, are promising for applications requiring coherence, *e.g.* lasing.^[136,137]

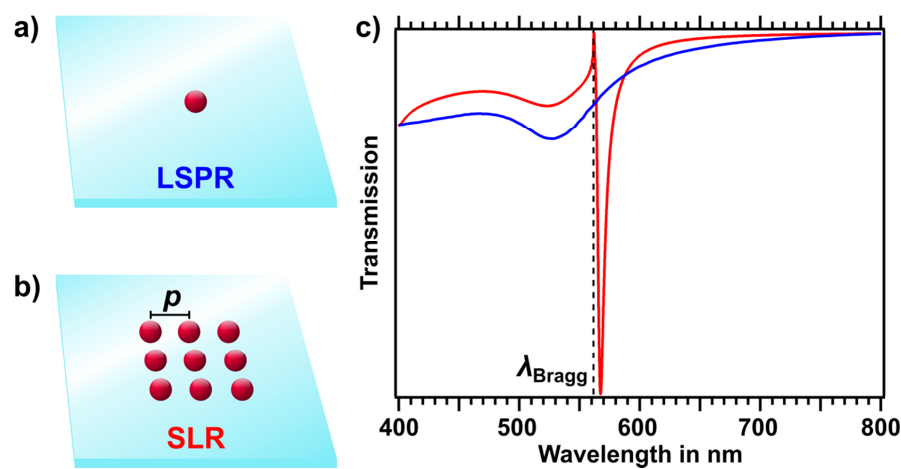


Figure 20. SLR versus LSPR. a) Schematic depiction of a single gold NP and b) an infinite square array of gold NPs with a periodicity p on glass. c) Simulated transmission spectra of a single NP (blue) and of the square array (red). The black dashed line indicates the position of the Bragg mode.

The excitation of particles with polarized light leads to a dipolar resonance that scatters perpendicular to the incident electric field as displayed in **Figure 21a**. Thus, diffractive coupling occurs always perpendicular to the polarization axis.^[138] The resulting SLR position depends strongly on the periodicity p of the lattice since this distance determines the spectral position of the Bragg mode ($\lambda_{\text{Bragg}} = n \cdot p$ for square lattices).^[139] Lattices that support SLRs are typically prepared by lithographic methods like electron beam lithography (EBL) and soft lithography. For example, Humphrey *et al.* prepared rectangular arrays of silver disks with a diameter of 120 nm and $p = 480$ nm *via* EBL.^[138] Such a square lattice (**Figure 21b**, blue frame) results in a SLR at 755 nm for both polarization axes (see **Figure 21c**). However, if the periodicity along the x-axis is increased or decreased, the spectral position changes for y-polarized light, as shown by the respective spectra.

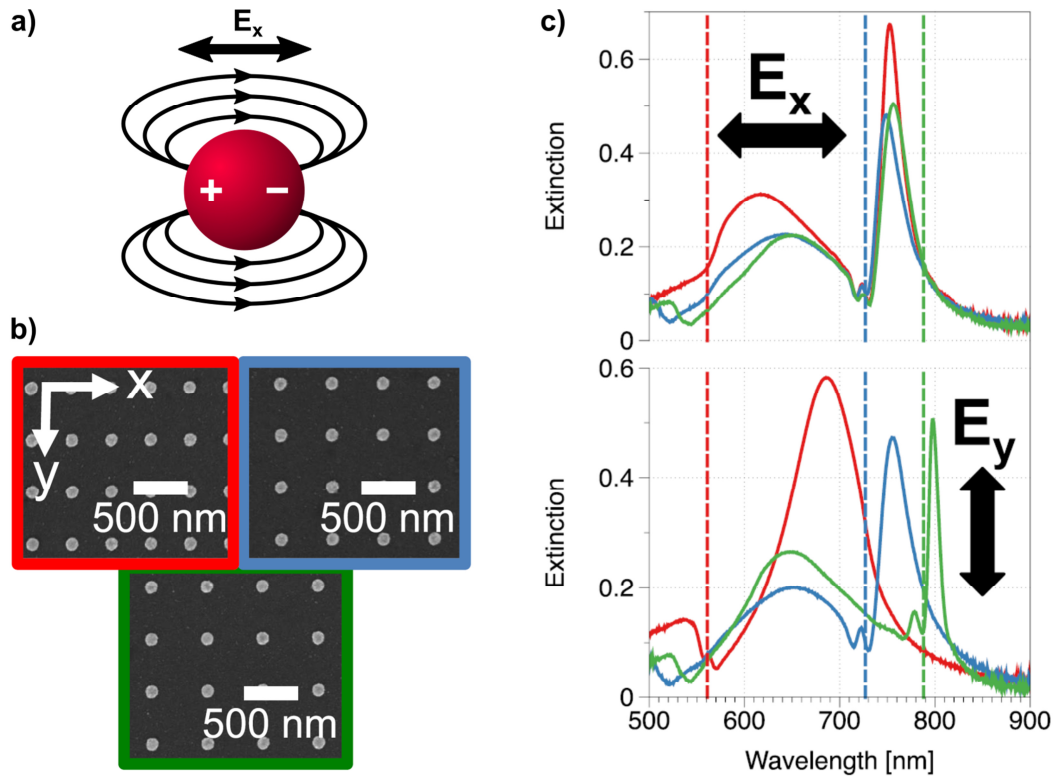


Figure 21. Diffraction Coupling. a) Schematic depiction of a plasmonic particle excited by an electric field E_x . The dipole orientation along the polarization axis results in perpendicular scattering. b) SEM images of 120 nm silver discs in a rectangular lattice with 420 nm periodicity along y -direction and variable periodicities (red = 370 nm, blue = 480 nm, green = 520 nm). c) Corresponding extinction at different polarizations E_x and E_y . b/c) Reprinted with permission.^[138] Copyright 2014 by the American Physical Society.

This example shows the sensitivity of SLRs to small changes in the lattice geometry. Since SLRs are linearly dependent on the periodicity, they are ideally suited to study the effects of mechanical deformations. This will be discussed as a perspective for tuning of coupled resonances in self-assembled plasmonic monolayers (see chapter VII). The controlled deformation of elastomer-supported superstructures will be examined regarding the manipulation of its spectral response by changing the plasmonic/diffractive coupling.

3 Plasmonic Core-Shell Systems

In fact, the vast majority of colloidal systems could be considered as core-shell systems. Most colloids carry layers of adsorbed molecules like stabilizing surfactants, polymers, or proteins on the particle surface. While there is no exact definition of core-shell particles, systems with irreversibly bound shells of at least a few nanometers thickness are typically considered as such. Here, two different types of core-shell particles will be distinguished by their shell's composition: inorganic and polymer shells (see **Figure 22**). Both materials deliver certain functionalities to the system, e.g. by providing surface charges. In the case of polymer shells, a special focus will be on responsive systems, *i.e.*, materials whose properties change in response to external triggers.

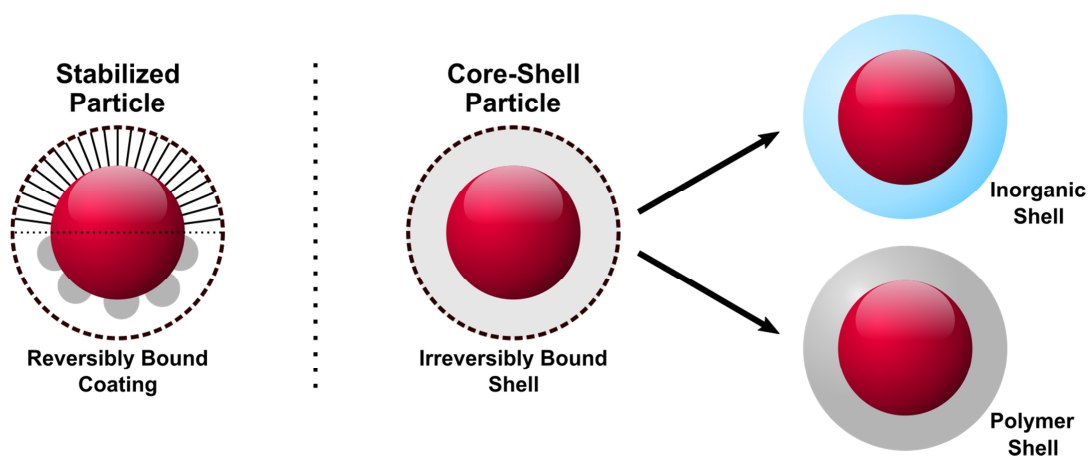


Figure 22. Classification of colloidal particles. In contrast to conventional stabilization with reversibly bound coatings, core-shell systems are irreversibly bound to the surface. Here, inorganic and polymer shell systems are distinguished.

3.1 Inorganic Shells

A common demand for shell materials is to provide stabilization of the core. This could be either colloidal or chemical stability. Plasmonic silver particles, for instance, are susceptible to oxidation at ambient conditions. Therefore, impermeable shells are required to protect the core from oxidizing agents without diminishing their plasmonic resonance. Common protective shell materials are noble metals like gold or metal oxides. However, the plasmonic properties only remain unaltered if the shells are sufficiently thin.^[140] Other plasmonic materials like copper or aluminum may form self-protective oxide layers^[141] but they are difficult to control and nanoparticles often tend to get fully oxidized.^[142,143]

A reliable method to create stable core-shell particles was obtained by applying shell materials that are known to form stable colloids themselves. Silica (SiO₂) is one of the most popular examples of such materials. It is capable of protecting a plasmonic core from chemical reaction and provides enhanced colloidal stability due to its surface chemistry. Pure SiO₂ particles feature strong surface charges as a consequence of the anionic polymerization or hydrolysis. Their ζ -potential is typically greater than -40 mV in

water (10 mM ionic strength at pH 7).^[144] Silica is especially versatile due to the accessibility for silane chemistry which facilitates the incorporation of functional molecules. A reaction scheme of the silica precipitation is displayed in **Figure 23a**. The Stöber process,^[145] applies tetraethyl orthosilicate (TEOS) dissolved in ethanol, which is hydrolyzed in presence of ammonia solution. At low silicate concentrations, subsequent condensation leads to formation of monodisperse silica nanoparticles. The reaction can be adapted for particle coatings by applying low TEOS concentrations with dilute aqueous dispersions with surfactants like CTAB.^[146] A TEM image of the resulting mesoporous silica and a schematic depiction of the core-shell structure are shown in **Figure 23b/c**.

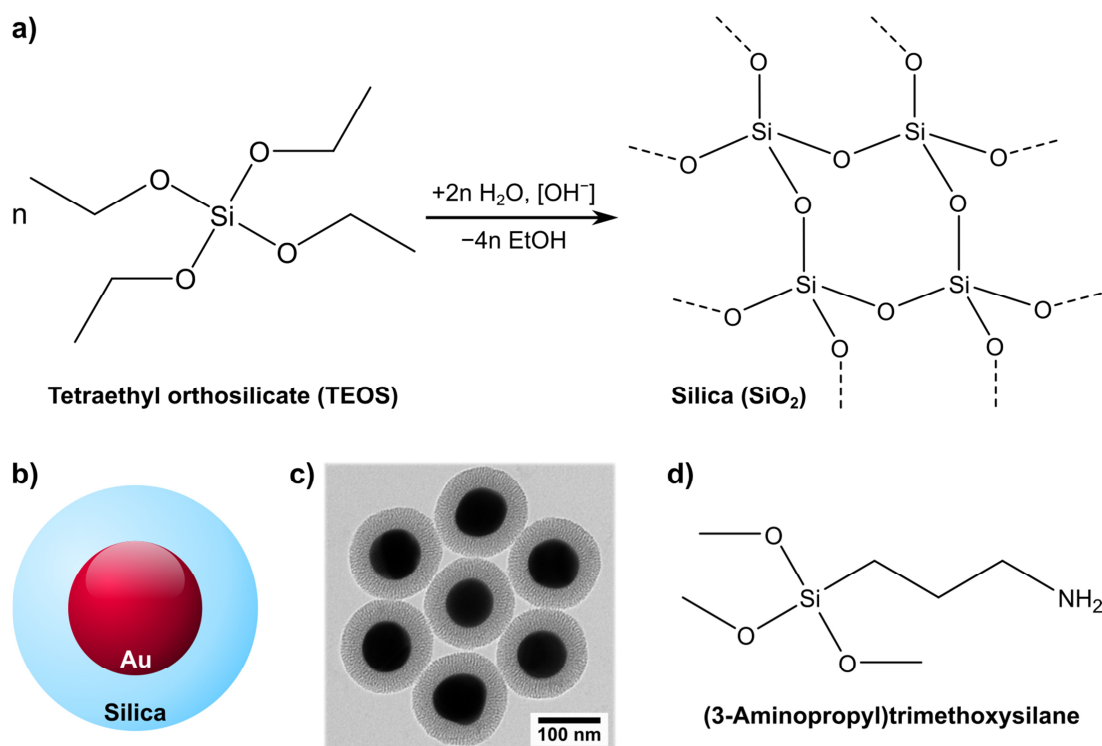


Figure 23. Silica particles. a) The chemical reaction of tetraethyl orthosilicate (TEOS) with water leads to formation of amorphous silica (SiO_2) under basic conditions. b) Schematic depiction of a Au-core/silica-shell particle. c) TEM image of these particles. d) Chemical structure of (3-Aminopropyl)trimethoxysilane.

Adding silanes with less than four alkoxy groups enables the incorporation of other molecules into the silica networks. Aminosilanes (see **Figure 23d**) are particularly suitable as they react with common anchoring groups like isothiocyanate, carboxyl, or *N*-hydroxysuccinimide. By that, fluorophores can be embedded into the shell, which is of interest due to resonance coupling with the plasmonic cores (see chapter IV). Different regions of the shells can be functionalized depending on whether the silane is added before, during, or after the shell formation. A surface functionalization with amine groups can be applied as a precursor to create additional shells^[147] that provide responsive properties to the system, as described in the following section.

3.2 Polymer Shells

A colloidal dispersion of polymer particles is called latex.^[43] Natural rubber can be seen as the archetype for this class of materials. Interestingly, Michael Faraday investigated its chemical composition during the same time period when Brownian motion was first described for small particles—though, neither the colloidal nor the polymeric nature of latex was known in the 1820s.^[42,148] However, it is this nature of macromolecules, which renders polymers as effective coating materials for plasmonic colloids.

There are two common approaches for receiving colloidal particles with polymer coatings: ligand exchange and precipitation polymerization. The former directly merges the desired coating material with the plasmonic cores. The stabilizing surfactant can be replaced if attractive interactions between the particle and the polymer are present. This gain in enthalpy and the gain in entropy, due to the exchange of multiple surfactant molecules for a single macromolecule, are the driving force for this process. However, this technique yields stable particles only for rather thin surface coatings well below 100 nm.^[149-151] In contrast, thick shells can be achieved through precipitation polymerization on colloidal particles.^[152] A prerequisite for this approach is the (partial) solubility of the monomer in the solvent while the polymer itself is insoluble. Examples of these substances are styrene, *N*-isopropylacrylamide (NIPAM), and aniline in water. During the polymerization process, the solubility of the oligomers decreases with increasing chain length. The presence of colloidal particles enables heterogeneous nucleation at their surface. Prior to the polymerization, the cores are commonly functionalized with molecules carrying vinyl groups.^[27,152] However, it is yet uncertain if these groups actually participate in the polymerization or if the colloidal stability of the cores is decreased and therefore they serve as seeds for nucleation.^[153] A reaction scheme for the polymerization of PNIPAM on gold nanoparticles is shown in **Figure 24**. Here, NIPAM is copolymerized with *N,N'*-methylenebisacrylamide (BIS) which carries two vinyl groups and therefore serves as a cross-linker. This results in irreversible formation of a polymer network around the gold core.

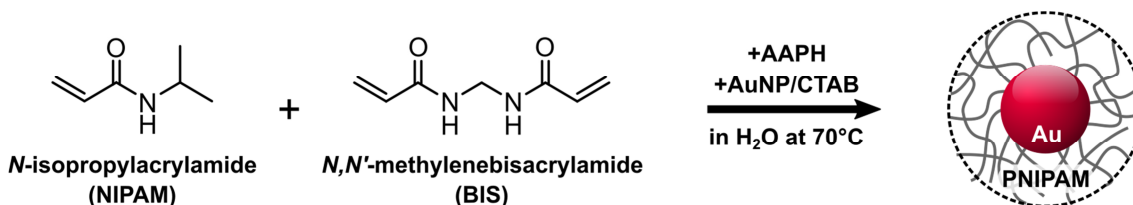


Figure 24. Synthesis of Au-core/PNIPAM-shell particles. Reaction scheme of *N*-isopropylacrylamide (NIPAM) with *N,N'*-methylenebisacrylamide in presence of gold nanoparticles initiated by 2,2'-azobis(2-methylpropionamide) dihydrochloride (AAPH). The reaction yields crosslinked PNIPAM microgel particles with gold cores.

Linear PNIPAM features a lower critical solution temperature (LCST) at about 32 °C (thus, it is typically polymerized at 70 °C to receive the precipitate). However, in the cross-linked state, the polymer is unable to dissolve in water. In turn, the network is swollen with water, classifying the material as a hydrogel.^[40] Since particles in the colloidal size

regime are formed, the system is further specified as a microgel.^[154] A characteristic swelling curve of Au-PNIPAM particles is shown in **Figure 25**. The temperature-dependent diameter is roughly described by a sigmoidal function. It is commonly designated as volume phase transition (VPT), where the inflection point (maximum of the first derivative) is the transition temperature.^[155] As noted in section 1.1, the interaction parameter χ crosses the value of 0.5 during that transition. This means, polymer-polymer interactions become energetically more favorable than polymer-solvent interactions. Water is repelled from the network, which results in a decreasing particle diameter. The VPT temperature is influenced by the LCST of the polymer itself and by the degree of crosslinking. Higher cross-linker content usually results in broader and less pronounced transition.

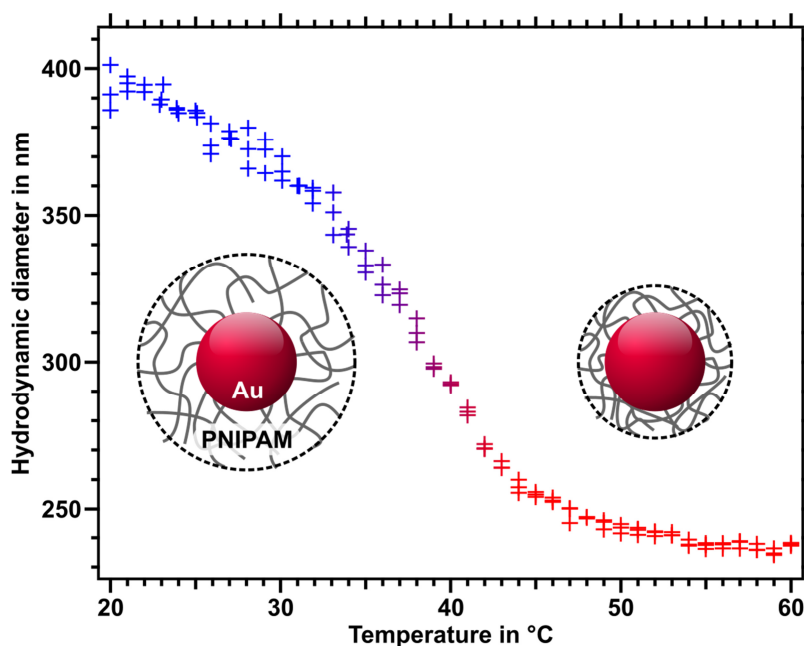


Figure 25. Swelling curve of Au-PNIPAM particles. Hydrodynamic diameter of the particles (10 mol% cross-linker) with 78 nm gold cores in dependence of the temperature.

PNIPAM, or other polymers featuring a VPT, may be applied as plasmonic nanoparticle coatings for different reasons. On the one hand, the overall size of the shell can be tuned easily by the monomer concentration during the synthesis. This is especially relevant if subsequent assembly steps are considered as it provides control over the inter-particle distances (see following section). Furthermore, the size and surface chemistry of microgel particles is nearly independent of the applied cores. On the other hand, the properties of the polymer shell directly influence the plasmonic properties of the core. As the LSPR is strongly dependent on the refractive index of the surrounding, the optical properties of a core-shell system change during the transition of the polymer.

Besides temperature induced volume changes of polymers, other triggers may be desired for changing the refractive index of the shells and the plasmonic properties of the system thereby. Polyaniline (PANI) is a pH- and redox-responsive polymer that can be tuned chemically or by applying a potential.^[58] It can be synthesized by oxidative polymerization in water under acidic conditions. Since the polymer is insoluble in water, it precipitates during the polymerization. By analogy with the microgel synthesis, the presence of gold nanoparticles in the reaction mixture results in the formation of core-shell particles. The chain growth of PANI is mostly linear (95%-98% substitution in para position).^[156] Hence, there is no cross-linking of the polymer shell. Attractive van der Waals forces between polymer chains evoke cohesion of the shell. The presence of surfactants like SDS is required to provide sufficient colloidal stability by introducing negative surface charges.^[157] The polymer features six different states of oxidation and protonation, which drastically alter its dielectric properties.^[158] The oxidation states are leucoemeraldine (reduced state), emeraldine (first oxidation), and pernigraniline (second oxidation), which are displayed in **Figure 26a**.^[156] The corresponding redox cycle is shown in Figure 26b.

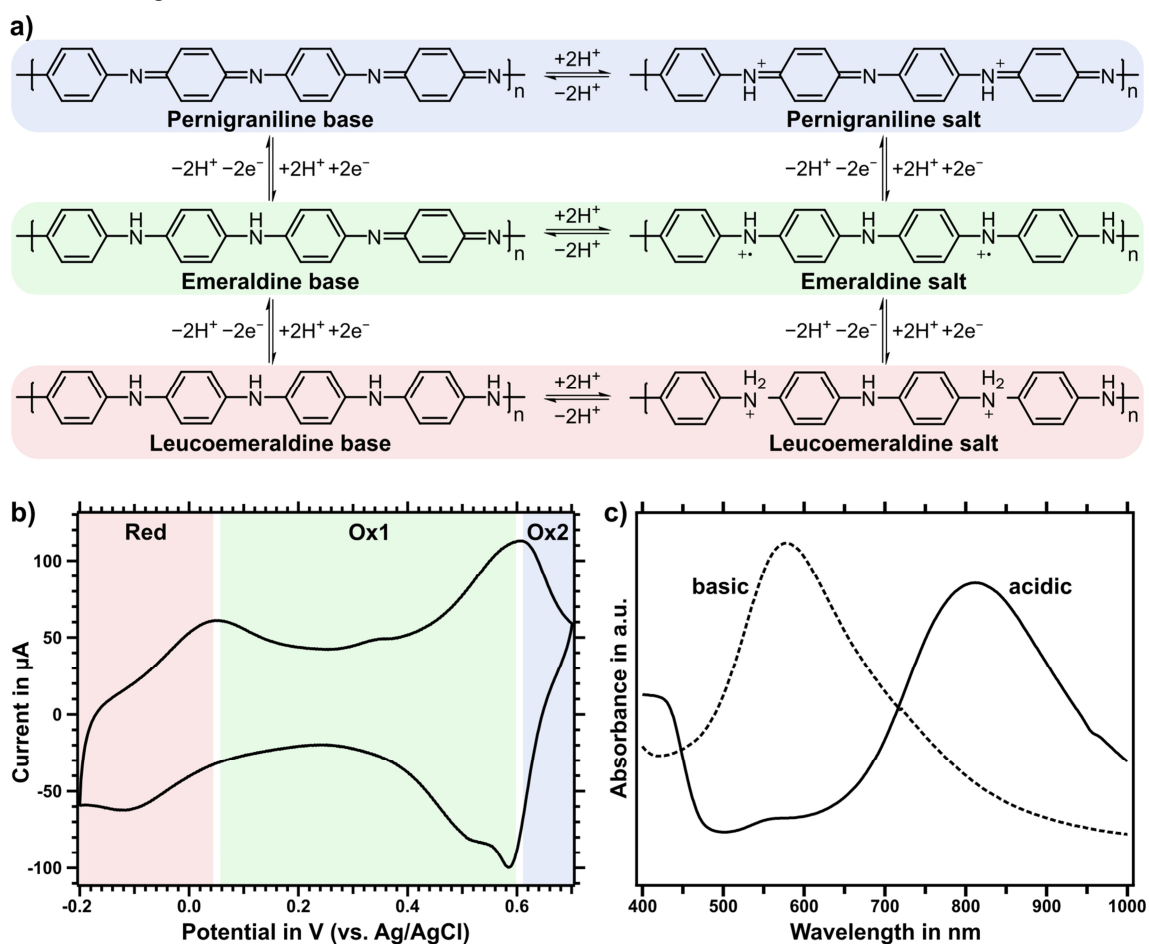


Figure 26. Redox and pH induced changes of Polyaniline. a) Chemical structure of polyaniline (PANI) in dependence on the oxidation state. The three states Leucoemeraldine (Reduced), Emeraldine (Oxidation 1), and Pernigraniline (Oxidation 2) can be distinguished in their protonated (salt) and deprotonated (base) form. b) Respective cyclic voltammetry measurement of Au-PANI on a gold electrode in a 3-electrode setup with platinum counter electrode and Ag/AgCl reference electrode. c) Absorbance spectra of dispersed PANI under acidic (HCl) and basic (NaOH) conditions. Adapted with permission.^[38] Copyright 2020 by the authors.

With each oxidation step, more benzoid groups are oxidized to quinoid ones. In consequence of these changes in the conjugated π -system, the absorption of the material is influenced. Colors ranging from yellow over green to blue/violet have been reported in literature.^[58] Therefore, the name of its most characteristic state results from its color: emeraldine. Figure 26c shows the absorbance spectra of emeraldine in acidic and basic conditions. The peak positions of the absorption bands at 810 nm and 570 nm are corresponding to a respective green and blue color of the dispersions. The protonated form of emeraldine is well known for its extraordinary conductivity in the order of 10^1 S/cm while the further oxidized state, pernigraniline, has a significantly lower conductivity ($<10^{-2}$ S/cm).^[156] The reduced leucoemeraldine, as well as the base forms, are considered non-conductive.^[159]

As the changes in color and conductivity hint, the dielectric constants of the polymer change in dependence on the oxidation and protonation state.^[158] Consequently, polyaniline can be applied as a shell material that influences the optical properties of a plasmonic system. The responsivity of the polymer is transferred to this system, which can be tuned by adjusting the pH or applying an electric potential.

4 Assembly of Colloidal Particles

Plasmonic coupling facilitates tuning of optical properties and new emergent effects, induced by functional shell materials. Besides coupling to a plasmonic mirror, the interaction of two or more particles can be utilized for these purposes. To obtain control over these interactions, it is required to arrange the particles at defined short distances (near-field coupling) or in evenly spaced lattices (long-range coupling). The arrangement can be achieved *via* colloidal assembly.

Colloidal self-assembly is a thermodynamically driven process resulting from the interplay of attractive (*e.g.* van der Waals forces, Coulomb attraction, and depletion forces) and repulsive interactions (*e.g.* Coulomb repulsion and steric repulsion). A straightforward interpretation of this technique is provided by interface-mediated assembly, which utilizes the surface-active behavior of colloidal particles to create hexagonal lattices at liquid interfaces. For further customization of the particle assembly, local energetic minima can be introduced by applying structured templates. Attractive electrostatic or capillary interactions direct the particles during the drying process. This technique is known as template-assisted assembly and leads to tailored particle deposition.^[160-162] To reach the energetic minima on the template, driving forces can be applied *via* confinement, convective flow, electric/magnetic fields, or templating molecules. Further control over the plasmonic coupling—even after the assembly step—can be provided by applying elastic templates. The received structures are referred to as mechano-tunable plasmonic arrays.

Sections 4.2 and 4.3 are adapted from the publication „Mechanotunable Plasmonic Properties of Colloidal Assemblies” by Yannic Brasse, Vaibhav Gupta, H. C. Tomohiro Schollbach, Matthias Karg, Tobias A. F. König, and Andreas Fery, Adv. Mater. Interfaces 2019, 1901678. Copyright by the authors. Adapted under the terms of the Creative Commons Attribution License (CC BY).

All paragraphs were written by me. Figures were adapted as indicated.

4.1 Interface-Mediated Assembly

The assembly of colloidal particles at interfaces is a straightforward method to produce particle arrays even at large scales. The prerequisite for applying this technique is the surface active behavior of particles. This effect has been observed already in the early 20th century for oil in water emulsions by Ramsden^[163] and Pickering.^[164] However, it took until the 1980s to exploit this effect for controlled particle assembly and to provide a theoretical description for the formation of these emulsions.^[165] As the process is thermodynamically driven, the assembly is accompanied by a reduction of the Gibbs energy. This energetic minimum emerges from the difference of the interfacial energy of the particle (p), dispersed in water (w) or oil (o), and the negative energy of the missing

interface between oil and water. The gain in energy is determined by the respective surface tensions γ and applies similarly for liquid/air interfaces:^[166]

$$\Delta E = -\frac{\pi r^2}{\gamma_{o,w}} \cdot \left(\gamma_{o,w} - |\gamma_{p,w} - \gamma_{p,o}| \right)^2 \quad (19)$$

Two trends can be deduced from this equation. First, the Gibbs energy decreases with the particle radius, and second, it is in a minimum if the wettability of the particles is similar in water and in oil ($\gamma_{p,w} = \gamma_{p,o}$). With respect to the interface-mediated assembly, this is of importance since the energy competes with the thermal energy of the system. Thus, the process is more favorable for large particles with equal wettability in both systems.

The forces affecting the particles at the interface are similar to the ones acting in a colloidal dispersion (see section 1.1). In addition to the short-range attractive (van der Waals) and intermediate-range repulsive (electrostatic and steric) interactions, long-range attraction through capillary forces has to be taken into account. At liquid/liquid interfaces, the capillary forces are comparably weak, which leads to formation of non-close-packed layers.^[167] In contrast, close-packed layers are often formed at air/liquid interfaces.^[168] Here, the interplay between capillary forces and repulsive interactions determines the quality of the formed monolayer. Sufficiently strong repulsion is required for the formation of ideally packed hexagonal lattices.^[160] There are various experimental methods to conduct the assembly of colloidal particles at interfaces. The classical approach is applying a Langmuir-Blodgett trough to push floating particles together at the interface, until a dense layer is formed.^[169] Though, this method is mostly suited if the particle interactions are dominated by repulsion.^[160]

Different methods can provide further control over the packing if the particles feature sufficient attractive interactions. For these, a second solvent is used to induce rapid spreading of the particles at the liquid/water interface, which is followed by formation of close-packed layers. The particle dispersion can be either injected into a liquid droplet^[170] or applied at the interface as introduced by Vogel *et al.* for polystyrene particles.^[171] This process is commonly assisted by surfactants like SDS to support the formation of dense layers. Core-shell particles like the introduced Au-PNIPAM system exhibit an exceptional behavior after the assembly step. Initially, the formed layer features inter-particle distances that match with the hydrodynamic diameter of the particles. However, since the PNIPAM shell is soft and deformable, the sum of inter-particle forces, polymer elasticity, and osmotic pressure results in expansion of the 2D lattice after time as depicted in **Figure 27a**. The hexagonal particle lattices can be transferred to hydrophilized glass slides by simply lifting them through the interface at a shallow angle. Hereby, the inter-particle spacing can be adjusted for the same type of particles through the dwell time (see **Figure 27c-d**).^[172]

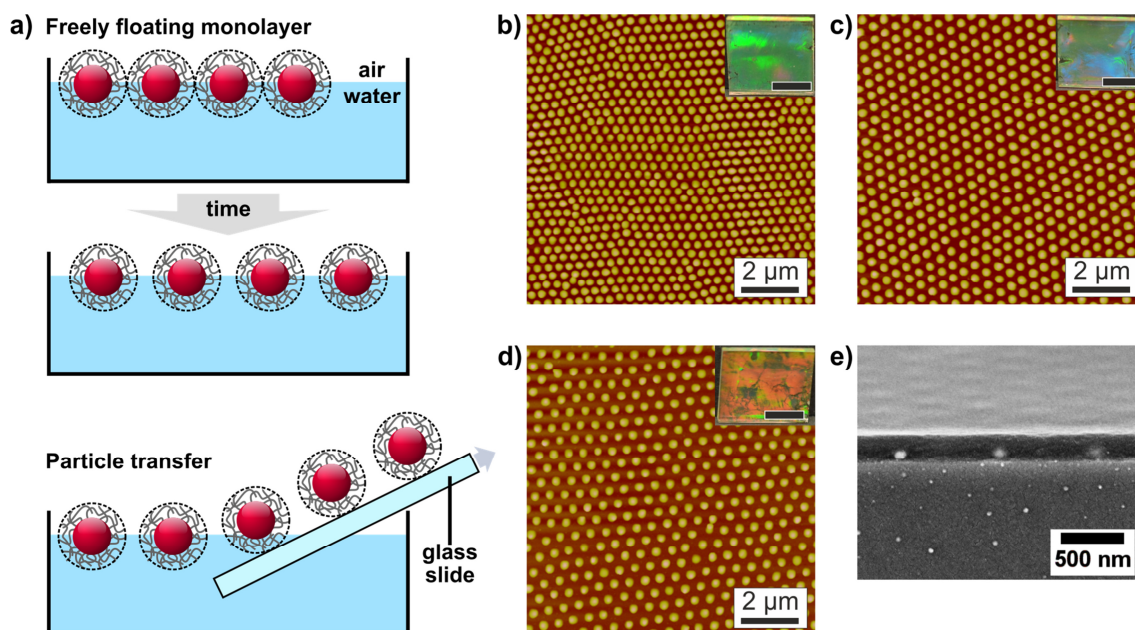


Figure 27. Preparation of monolayers via interface-mediated assembly. a) Schematic depiction of the process for fabricating self-assembled monolayers at an air/water interface and the subsequent transfer onto solid substrates after certain dwell-times. (b-d) $10 \times 10 \mu\text{m}^2$ AFM height profile images of monolayers of plasmonic core/shell particles on glass substrates that were withdrawn from the air/water interface after different dwell-times. Dwell-time and center-to-center distance increases from b) to d) with distances of $359 \pm 29 \text{ nm}$, $444 \pm 34 \text{ nm}$ and $527 \pm 28 \text{ nm}$. The insets show digital photographs of the corresponding coated glass slides. e) SEM side-view image of core/shell particles coated with an index-matching polymer layer. b-d) Adapted with permission.^[172] Copyright 2015 by Wiley-VCH. e) Adapted with permission.^[173] Copyright 2017 by Wiley-VCH.

The interface-mediated assembly of plasmonic particles is particularly convenient since objects with arbitrary shapes can be coated if the attractive interactions with the surface are sufficiently large. The resulting inter-particle spacing is primarily defined by the distances at the interface but can be influenced by the withdrawal of the substrate and the subsequent drying step.^[172] Control of the periodicity is especially relevant for plasmonic arrays featuring collective resonances as they are dependent on the quality of the lattice (see section 2.3). In the case of PNIPAM coated particles, additional polymer layers can be applied to create a homogeneous refractive index surrounding (see Figure 27e), which gives rise to SLRs.^[173]

4.2 Template-Assisted Assembly

The introduced interface-mediated assembly method is a powerful tool for creating hexagonally ordered arrays. Additionally, the stacking of these arrays further extends the range of accessible structures to more advanced ones like honeycomb or Moiré lattices. Furthermore, interface-mediated assembly can be used to create masks for metal deposition. However, while these methods provide a simple approach for large scale assemblies, they are also limited by their reliance on hexagonally ordered particles. Assemblies with a broader range of symmetries, more pronounced anisotropy or local variation of the packing can be achieved *via* template-assisted assembly.^[174]

Drop-casting and spin-coating are well known methods from thin-film preparation: A dissolved substance is deposited on a substrate by controlled evaporation of the solvent. This approach is also applicable for nanoparticle dispersions, resulting in the formation of close-packed particle monolayers for instance.^[56,175] The spin-coating process is influenced by a variety of interaction forces determining the deposition step. In dispersion, colloidally stable particles exhibit electrostatic and/or steric repulsion depending on their surface functionalization. During the drying process, the particles get confined in a thin liquid film in which capillary forces act between them. This interplay of attractive forces and repulsive interactions defines the resulting packing while the number of particles per area defines whether a sub-monolayer, a monolayer, or multilayers are formed. This layer formation is not only determined by the stock particle concentration and the wetting behavior on the substrate but also by the rotation speed, as the centrifugal forces influence the initial liquid film thickness.^[176]

Exchanging flat substrates for topographically structured templates gives access to particle arrays with a wide range of possible array geometries. In general, any nanostructured substrate—no matter whether fabricated *via* e-beam-,^[177] interference-,^[139] or soft-lithography^[178]—is applicable for template-assisted assembly. A simple and lithography-free method for creating templates is controlled surface wrinkling.^[179] Such structures are fabricated by deposition of a stiff material layer on top of an elastomer. As shown in **Figure 28a**, plasma treatment of polydimethylsiloxane (PDMS) results in the formation of a thin glassy layer with increased rigidity. The stiffness and thickness of this layer determine the wavelength and amplitude of the resulting sinusoidal wrinkles upon release.^[180,181]

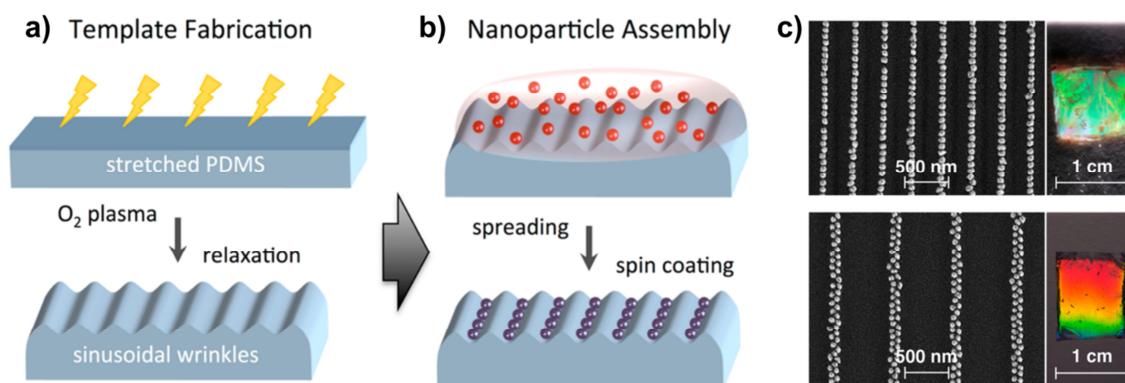


Figure 28. Template-assisted assembly on wrinkled surfaces. a) Schematic illustration of the preparation procedure for sinusoidal wrinkles by oxygen plasma treatment of stretched PDMS. b) Scheme of the particle assembly into linear structures *via* spin-coating. c) SEM images (left) and respective photographs (right) of gold nanoparticle lines prepared in wrinkles with different periodicities. Adapted with permission.^[108] Copyright 2014 by the American Chemical Society.

The spin-coating process is significantly altered by the presence of surface wrinkles. In the drying step, the varying liquid film thickness leads to confinement of the particles inside the wrinkles (see Figure 28b). The capillary forces acting during further drying result in the formation of close-packed particle chains. Depending on the topography, namely the amplitude and wavelength of the wrinkle, single or double lines are achieved, as displayed in Figure 28c.^[108]

The template-assisted approach can be further adapted in analogy to drop-casting. In this case, the nanostructured template does not serve as the substrate but is used to confine the particle dispersion in between the template and a flat surface (*e.g.* glass). During the evaporation process, the particles replicate the topographic features in accordance with the confinement. By applying colloids with hydrophilic functionalities featuring attractive interactions with the substrate, it has been shown that various geometries like pyramids,^[178] lines,^[182] cylinders, and donuts^[183] can be reproduced with this method.

The template-assisted methods discussed above are suitable for the realization of long-range ordered particle arrays. However, there are limitations regarding the preparation of single particle arrays. These can be overcome by utilizing assembly methods that allow for more control over the deposition step. Capillarity-assisted particle assembly (CAPA)^[184] utilizes a combination of pinning effects at the topographic features and convective particle flow for achieving such control.

The mechanism of particle assembly through drying of particle dispersions on flat substrates has been studied intensely by the group of Nagayama^[185,186] It was found that the increased solvent evaporation close to the three-phase contact line induces a convective flow of particles towards the contact line. This phenomenon is often referred to as the ‘coffee ring effect’ and can be utilized for particle assembly. The assembly processes based on convective flow have been foremost interpreted by Wolf and coworkers^[187,188] who refined the common dip-coating process. As shown in Figure 29a

(center right), a droplet containing dispersed particles is confined between the template and a glass slide. Nanoparticles accumulate at the meniscus as a result of the convective flow. By withdrawing the template, the meniscus is moved across the substrate leading to particle deposition in the grooves of the template. The parameters to control in these experiments are predominantly the movement speed, the substrate wetting (by surfactants), and the dew point. Two cases are distinguished for the assembly: the convective and the capillary regime. The convective assembly occurs at very low contact angles ($<20^\circ$) in which the particles are predominantly confined by a remaining thin solvent layer.^[187] This film forces them into the recesses during the evaporation, similar to the mechanism during spin-coating. Conversely, the capillary regime describes the assembly at comparably high contact angles ($>20^\circ$). The meniscus is not continuously moving but pinning at the topographical features. As a result, capillary forces drag particles into the recesses where they stay confined after unpinning. By rational design of the features, the orientation of anisotropic particles can be predefined. For instance, an energetic minimum can be reached by nanorods aligning parallel in rectangular grooves.^[177] By directing particles into accurate positions, this tightly controlled method also enables deposition of single particles in an array.^[189] The technique is applicable to various types of topographically structured templates, including elastomeric substrates.^[190] Thus, it is an excellent foundation for the preparation of mechano-tunable colloidal assemblies.

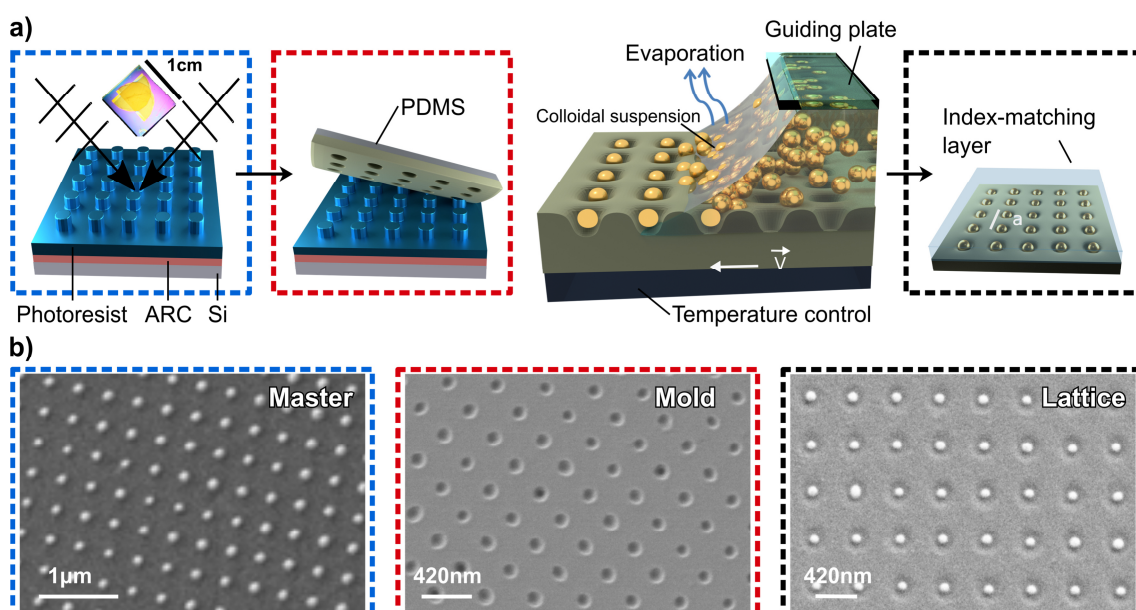


Figure 29. Capillarity-assisted particle assembly with soft-lithography templates. a) Scheme representing the fabrication of a stretchable 2D lattice using a combination of laser interference lithography with double exposure, soft molding with PDMS, and directed self-assembly of plasmonic nanoparticles. b) SEM images of the fabricated nanopillar master, its PDMS mold, and the 2D plasmonic lattice. Adapted with permission.^[139] Copyright 2019 by the American Chemical Society.

Suitable templates for colloidal assembly can be prepared by various methods of which laser interference lithography (LIL) should be highlighted.^[191] Figure 29a depicts the use of LIL in combination with CAPA to produce a plasmonic lattice. Gupta et al. employed

LIL to produce large-scale structures with nanometer precision at low cost as compared to e-beam lithography. Lloyd's mirror technique was used where a single coherent laser beam is converted into two coherent sources. Interference of the two beams occurred on a photosensitive material. By a second exposure with 90° rotation, a nanopillar structure was formed after curing (see Figure 29, blue frames). This master was replicated into a nanohole structure using PDMS (red frames). With this template, 80 nm diameter gold spheres were assembled in a square lattice of single nanoparticles as displayed by the black frames.

Aside from self-assembly methods based on evaporation, there are other methods that direct colloidal particles into defined geometries. For example, electrostatic interactions between charged nanoparticles and templates are applicable to create plasmonic particle arrays. These interactions can be triggered either by inducing charges chemically or electrically. The former of these methods requires chemical functionalization of the particles and the template. The latter assembles functionalized particles from a conductive medium on conductive templates. Realization of assembly *via* chemical interaction requires comparably low experimental effort with moderate control of the process. There are different ways to achieve chemical surface structuring based on microcontact printing or lithographic methods. Microcontact printing is an appealing method as it does not require specialized equipment. Hammond *et al.* have applied PDMS stamps from replica molding to print polyelectrolytes on top of a substrate.^[192] Depending on the pretreatment of the PDMS stamp, different printing patterns can be realized with a simple pillar structure. By changing the wettability, circles, rings, and dots could be printed. Using substrates with polyelectrolyte multilayers for the printing results in a charge contrast which induces selective attraction of charged colloidal particles by just immersing the templates in a dispersion (see **Figure 30a**).

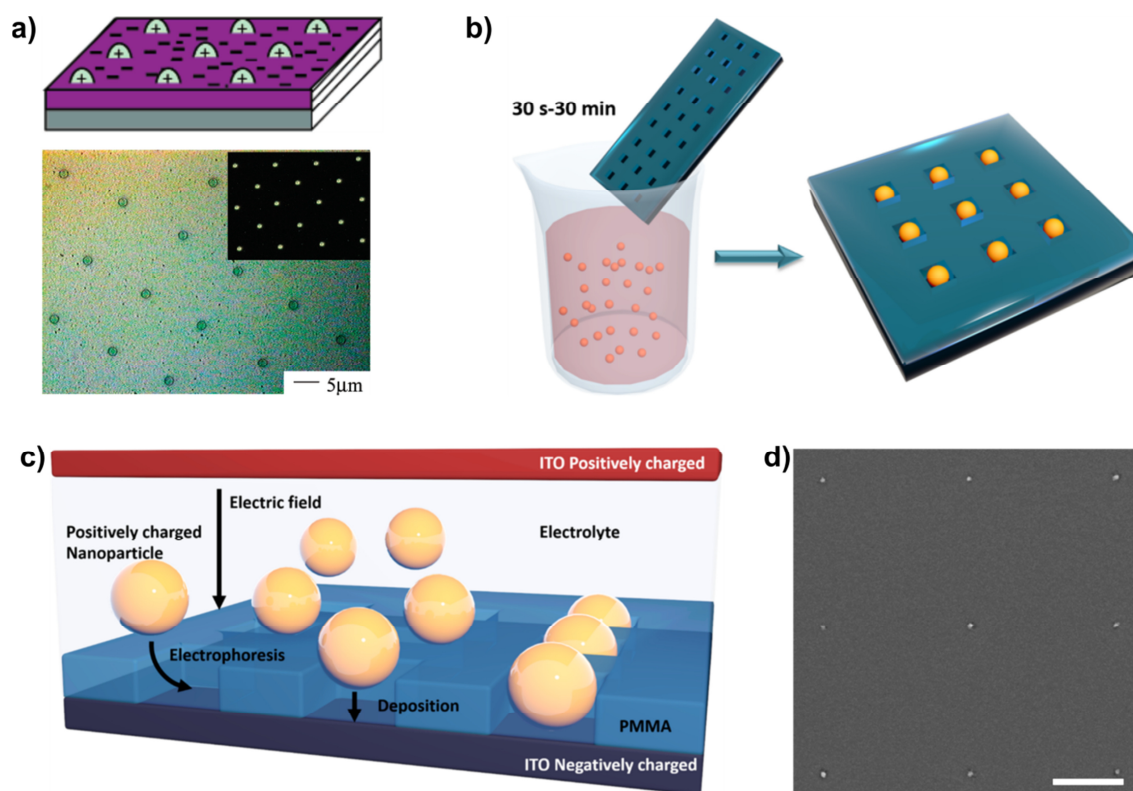


Figure 30. Particle assembly via electrostatic interactions. a) Schematic depiction of microcontact printed polyelectrolyte multilayers (top) and optical microscopy of polystyrene particles assembled on such printed substrates (bottom). b) Depiction of particle assembly by immersion of a nanostructured amine-functionalized glass in a colloidal gold dispersion. c) Schematic depiction of electrophoretic particle assembly on nanostructured ITO. d) SEM image of the resulting single particle assembly on ITO (Scale bar: 2 μm). a) Reprinted with permission.^[192] Copyright 2002 by the American Chemical Society. b) Reprinted with permission.^[193] Copyright 2018 by the American Chemical Society. c/d) Reprinted with permission.^[194] Copyright 2018 by the American Chemical Society.

The resolution with respect to the applicable feature size could be improved further by using lithographic templates since plasmonic colloids usually demand geometries in the nanometer regime for proper assembly. The group of Mulvaney utilized e-beam lithography to create spaced patterns with feature sizes of 80-300 nm. These wells were post-modified by silanization with amines.^[193] The resulting attractive interactions between the amine groups and the surface of gold nanoparticles enabled assembly of plasmonic particles by simple immersion into a colloidal dispersion. Due to the sufficiently small features, the deposition of either small clusters or single particles could be obtained.

The application of conductive substrates like nanostructured ITO enables further possibilities to assemble particles *via* charge interactions. Electrophoretic particle deposition (EPD) has been introduced as a tightly controlled method for single particle deposition that facilitates the orientation of anisotropic particles.^[194] Figure 30c depicts an electrophoretic cell used for the particle deposition. Applying a voltage to a colloidal dispersion leads to an attraction of the gold particles (functionalized with positively charged polyelectrolyte) by the negatively charged electrode. The dielectric PMMA coating screens the charges of the electrode which leads to selective deposition in the

uncoated areas. Compared to chemical methods, this process is more complex to apply but delivers direct control of the assembly through the electrolyte concentration and applied voltage. Utilization of anisotropic wells with similar particles like rods, for instance, results in further control on the orientation of particles. By that, the intrinsic polarization dependence of such plasmonic particles could be translated to the response of the array. Yet, EPD has not been shown on flexible substrates. However, this could be easily achieved *via* evaporation of thin metal layers^[195] or by conducting a wet transfer step of the assembled particles.^[108]

Different assembly methods have been introduced to achieve defined particle arrangements. These methods share comparably low experimental effort and good scalability, which makes them especially suitable for large scale applications and mechano-tunable plasmonics.

4.3 Mechano-Tunable Plasmonic Arrays

The optical response of periodic plasmonic particle arrays depends strongly on the lattice geometry and its periodicity. Thus, modulation of the inter-particle distances *via* changing the lattice constant as well as the lattice structure allows for tuning of the optical properties by influencing near-field and/or far-field electromagnetic coupling. Mechanical strain is a straight-forward and easily applicable method to achieve *in situ* tuning of the particle distances. Two boundary cases can be distinguished for such deformation: The isotropic strain leading to a uniform increase of all inter-particle distances and the uniaxial strain. Different scenarios for the structural response upon uniaxial strain are introduced in **Figure 31**. For elastomers, a deformation is typically accompanied by a transversal contraction, which leads to an increase of the inter-particle distance (a) along the stretching axis and a perpendicular reduction of the distance (b). The expression of this effect is defined by the ratio of the extended length ($\Delta l/l$) and the reduced thickness ($\Delta d/d$) as the Poisson's ratio ν :^[196]

$$\nu = - \frac{\Delta l/l}{\Delta d/d} \quad (20)$$

This effect can be utilized to create changes in the near-field coupling of non-periodic structures for instance (see Figure 31a). Hereby, a polarization-dependent optical response is generated. Deformation of 1D-periodic structures may further result in the tuning of optical waveguiding or perpendicular lattice coupling. 2D-periodic structures, as shown in Figure 31b, intrinsically feature polarization-dependent optical properties based on SLRs. More complex modulations could be achieved by using different matrix materials. For instance, colloidal membranes featuring pressure-sensitive molecular interactions would lead to nonlinear transitions.^[197]

In general, a mechanical strain enables the transition of the array geometry and its lattice modes thereby which will be covered in the following sections.

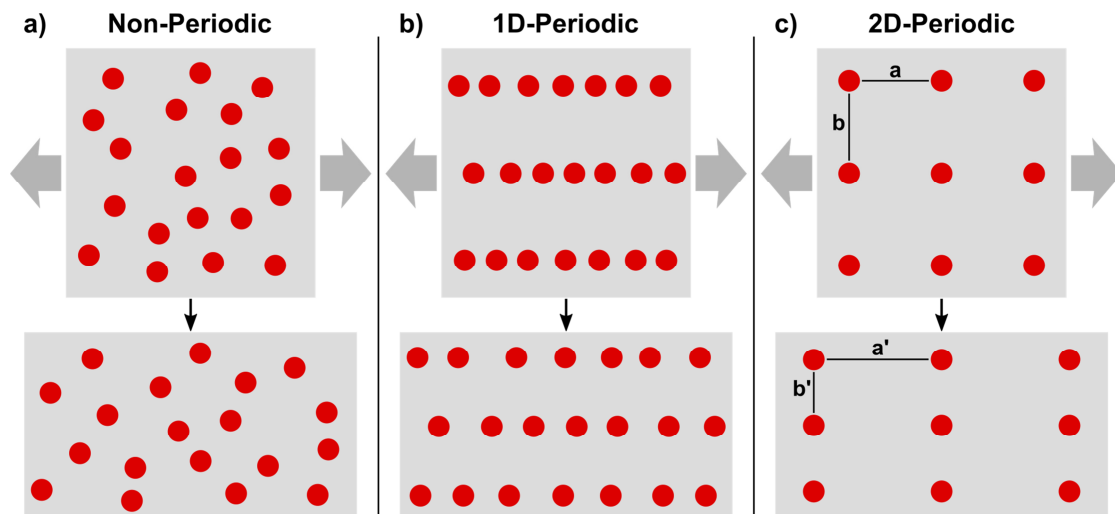


Figure 31. Substrate deformation upon uniaxial deformation depending on the array periodicity. a) For unordered particles. b) For a 1D-periodic lattice arranged along the strain direction. c) For a 2D-periodic lattice with symmetry axes parallel and perpendicular to the strain direction.

For achieving mechano-tunable optical properties, several requirements must be fulfilled: First, the optical feedback of the plasmonic particles needs to be maintained. Namely, the structures have to be exposed at the surface, or the substrate has to be transparent. Second, the substrate needs to be deformable. Ideally, it is an elastomer since this guarantees intrinsic reversibility of the tuning process. Bürgi et al. have demonstrated a facile method to create such mechano-tunable plasmonic structures by coating of PDMS with spherical gold nanoparticles.^[198] PDMS is a transparent elastomer with a Poisson's ratio close to 0.5, meaning that there is no volume change upon stretching. This, combined with possible deformations over 150% renders PDMS to an ideal substrate for mechano-tunable optical materials.^[199] In the case of randomly adsorbed gold spheres, stretching led to a change in inter-particle spacing. As shown in **Figure 32a**, the strain in x-direction induces an increased spacing along that axis while the transverse strain decreases the spacing along the y-axis. This is accompanied by a color transition from purple to blue, as shown in the photograph. The effect can be explained by arising inter-particle coupling as a consequence of the decreased spacing in y-direction.

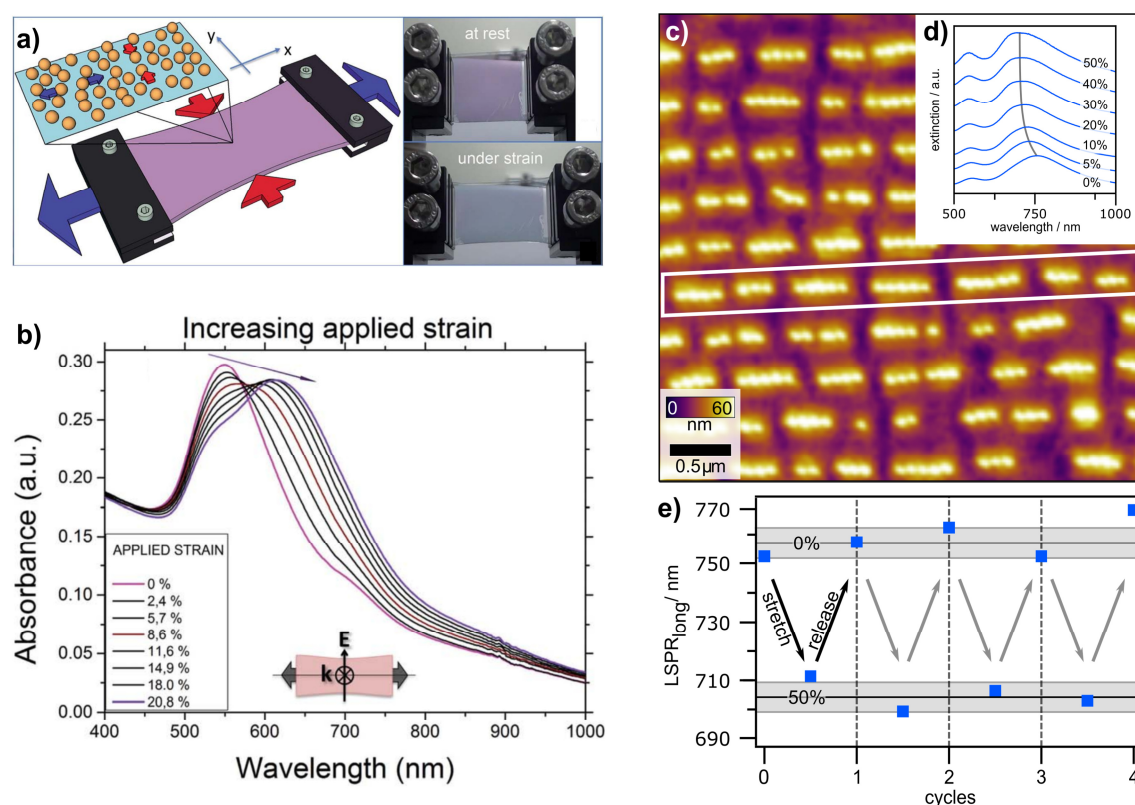
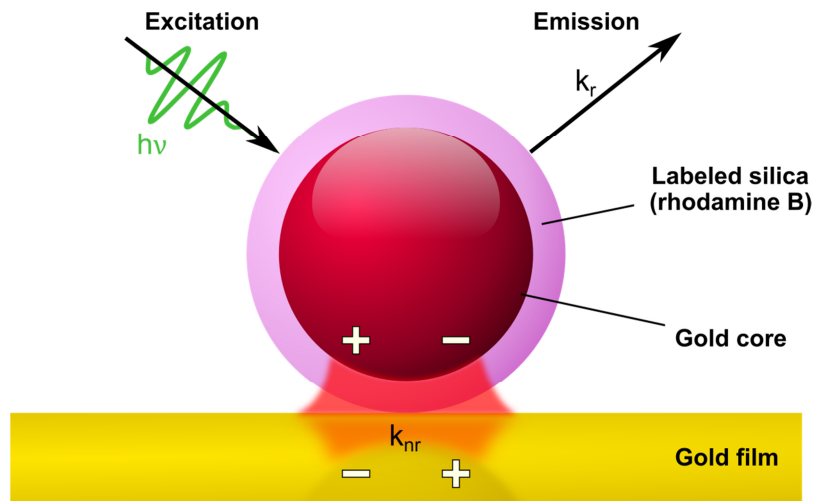


Figure 32. Mechano-tunable plasmonic response. a) Left: schematic depiction of the particle behavior on PDMS under uniaxial strain. Right: photograph of the respective sample at rest (top) and under strain (bottom). c) Particle lines on PDMS under 30% strain showing chain fragmentation. d) Respective UV/vis spectra between 0% and 50% strain. e) LSPR peak position over multiple cycles. a/b) Reprinted with permission.^[198] Copyright 2014 by the Royal Society of Chemistry. c-e) Adapted with permission.^[200] Copyright 2017 by the American Chemical Society.

The extinction spectra that are shown in Figure 32b reveal a red-shift of the absorbance maximum with an increasing strain related to near-field resonance coupling.^[104,107] The asymmetric peak results from a superposition of the coupling mode (excited by light polarized in the y-direction) and the uncoupled dipolar mode in the x-direction. This simple example shows that mechano-plasmonic tuning is achievable *via* facile methods. Yet, it features a polarization-dependent optical response which is of interest for strain sensing^[200] and color tuning.^[201]

For the realization of inverse tuning (spectroscopic blue-shift upon stretching), further requirements have to be met which cannot be delivered *via* random particle deposition. It is necessary that particles are plasmonically coupled along the stretching direction, but at the same time do not enter the coupling regime as a consequence of the transverse strain. A straightforward solution to this is the application of linear arrays. Based on the assembly in wrinkled structures (see section 4.2), Steiner et al. have applied particle lines to conduct mechano-plasmonic tuning (see Figure 32c).^[200] The applied spherical gold particles feature pronounced coupling along the lines with an absorbance maximum at around 760 nm, as shown in Figure 32d. A dipolar mode is visible at 550 nm as the perpendicular spacing is sufficiently large (>5 radii)^[132] to exclude perpendicular coupling (even in the stretched state). Stretching of the flat PDMS substrate results in an increase of the inter-particle distance (along strain direction) which evokes as an optical blue-shift of almost 50 nm. Interestingly, the lines do not elongate homogeneously but fragment into plasmonic oligomers, as displayed in Figure 32e. This is of special interest for energy transport (waveguiding)^[202-204] and sensing applications as these plasmonic oligomers are highly responsive to variations in the refractive index surrounding.^[205] Further relevance of such structures is found in the field of chiral plasmonics.^[206] As shown by the group of Kotov, lines of plasmonic colloids can be used for modulation of chiroptical activity *via* mechanical deformation.^[207,208] These structures are of potential interest for tunable nonlinear optics^[209] and optoelectronics.^[17]

IV Fluorescence in Colloidal Plasmonic Cavities



*This section is based on the publication “Single particle spectroscopy of radiative processes in colloid-to-film-coupled nanoantennas” by Max J. Schnepf, Yannic Brasse, Fabian R. Gößler, Anja Maria Steiner, Julian Obermeier, Markus Lippitz, Andreas Fery, and Tobias A. F. König (Z. Phys. Chem. **2018**, 232(9-11), 1593). Adapted with permission. Copyright 2019 by Walter de Gruyter GmbH.*

All figures and most paragraphs were modified and rewritten for this chapter. Max J. Schnepf and I contributed equally to the writing of the original manuscript. Anja Steiner prepared the gold nanoparticles. I conducted synthesis of labeled silica particles and fluorescent coating of gold particles. TEM, dark field microscopy, AFM, scattering spectroscopy, UV/vis spectroscopy, and bulk fluorescence measurements were performed by me. Max Schnepf carried out fluorescence intensity and lifetime measurements on substrate. Fabian R. Gößler conducted electromagnetic simulations and contributed to the discussion of the manuscript. Markus Lippitz and Julian Obermeier performed the single particle fluorescence spectroscopy. Andreas Fery and Tobias A.F. König were involved in the scientific coordination of the project, discussion of the physical background, and writing of the introduction.

Introduction

For the next generation of information and sensing technology, nanoscaled systems with high emission rates and short decay times must be integrated into scalable optical platforms. Quantum emitters, such as fluorophores or quantum dots, adjacent to metallic particles are attractive candidates for controlling and increasing the excitation and decay rates.^[210-213] Increasing the decay rate reduces the probability of photobleaching which results in more cycles of excitation and emission. Thus, it improves the detection limits *via* enhanced emission rates.^[212,214] Pioneering work from the group of Lakowicz studied the shortening of the lifetime and resulting fluorescent enhancement using assembled silver particles in proximity to fluorophores.^[215] Later, this relationship was investigated as a function of the distance between two metallic particles sandwiching a fluorophore.^[216] The spectral overlap between the localized surface plasmon resonance (LSPR) of the metallic particles and the fluorescence emission results in energy transfer as a consequence of near-field interactions.^[113,217,218] Thus, rational design of the plasmonic nanostructure is desired for optimization of these interactions in respect of the fluorescent decay rates. Wet chemical syntheses of metallic particles in colloidal systems features the required optical tunability and the combination with directed self-assembly provides additional scalability.^[161,219]

Using a particle-to-film coupled (nanoantenna) setup, Smith and coworkers have studied the electromagnetic enhancement *via* scattering spectroscopy.^[220] By introducing fluorophores in the gap region of such systems, strong enhancement of the emission rates can be realized; but it is still a matter of debate to which extent this process is limited by quenching through the metal. The Mikkelsen group tuned the distance between silver nanocubes and a metallic film to show enhancement of the spontaneous emission rate by a defined cavity.^[221] To unravel the mechanism of spontaneous emission in metallic systems, they noted that reliable and precise tuning of the plasmon resonance is required.

Here, the enhancement of spontaneous emission and significant reduction of decay rates is shown in a film-coupled plasmonic-core/fluorescent-shell system. In comparison to top-down lithographic methods, the colloidal synthesis and metallic film-coupled cavities are an inherently inexpensive and flexible platform for large-scale applications such as quantum information systems and ultralow-power switches.^[222,223]

Results and Discussion

To study the influence of plasmonic particles and cavities on the radiative properties of adjacent fluorophores, different particle systems have been synthesized. The plasmonic system consists of a spherical Au core (79 nm) with a thin, labeled silica shell (4 nm), as schematized in Figure 33a. The intended cavity is received by deposition of Au-core/fluorescent-shell particles on top of a gold film. In this setup, certain functionalities are associated with the different components: (1) The silica shell, labeled with rhodamine B, acts as a gain material. (2) The gold nanoparticle represents a nanoantenna due to the generation of a LSPR upon interaction with incident light. (3) The gold film serves as a plasmonic mirror in which opposing surface charges are induced. In this setup, the silica shell defines the dielectric spacing of 4 nm—building a plano-concave mode volume. To quantify the influence of plasmonics on the fluorescence properties, spherical silica particles (102 nm) with covalently bound rhodamine B were applied as a reference system (see Figure 33b).

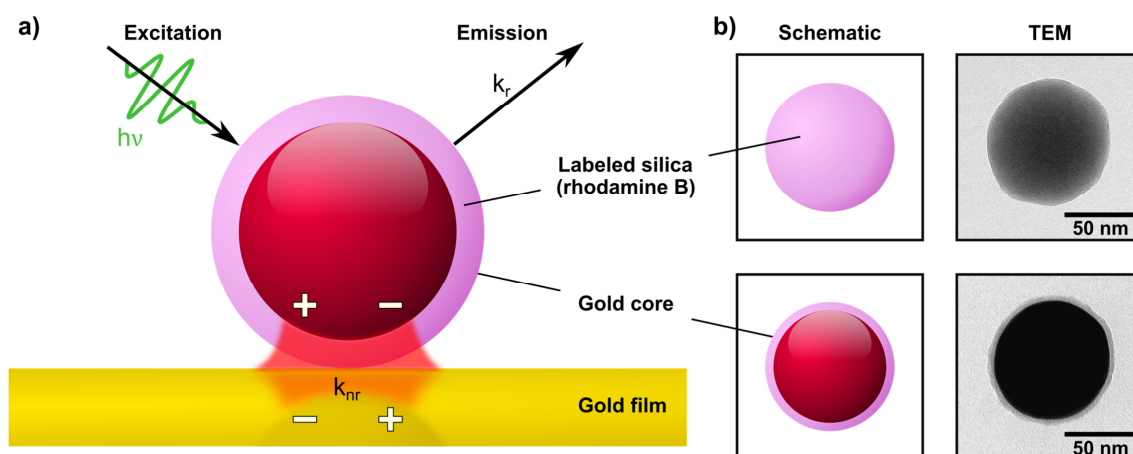


Figure 33. Concept of colloidal plasmonic nanoantenna for single particle spectroscopy. (a) Schematic depiction of the particle-to-film coupled nanocavity consisting of the colloidal building blocks (4 nm rhodamine B labeled silica shell and 79 nm gold nanoparticle core) on a gold film acting as a plasmonic mirror. Pulsed laser excitation at 506 nm induces rhodamine B emission at 580 nm, which energetically couples to the small mode volume between particle and film. The mode volume is highlighted by the red color.

The excitation with light that is absorbed by the dye leads to emission of photons (fluorescence) and non-radiative decay processes (conversion into heat). A convenient expression of the relationship between non-radiative (k_{nr}) and radiative decay (k_r) rates is given by the definition of the fluorescence lifetime $\tau_0 = (k_r + k_{nr})^{-1}$. It follows that a decreasing lifetime is accompanied by an increased radiative and/or non-radiative decay. In a classical fluorophore system, the quantum efficiency can be described as $QE_0 = k_r \tau_0$. Thus, the values of the quantum efficiency and the lifetime are coupled to each other: When the quantum efficiency is decreasing, the lifetime is also decreasing and *vice versa*. If a metallic interface is available, additional decay channels are enabled which makes the combination of high quantum efficiencies at short lifetime possible. The result is described as fluorescence enhancement.^[224]

To characterize the absorbance of the colloidal building blocks in detail, emission and scattering spectra were measured. **Figure 34a** shows the absorption and emission of rhodamine B doped silica particles in an aqueous dispersion. The absorption of these particles is calculated by subtracting the scattering contribution of the SiO_2 (isotropic scattering) and expresses a maximum at 555 nm. The emission of rhodamine B embedded in SiO_2 has its maximum at 570 nm. The scattering properties of the core-shell system are shown in **Figure 34b**. There is a 25 nm red-shift between particles deposited on glass (540 nm) and on a gold mirror (565 nm) as a consequence of plasmonic film-coupling. Still, both setups feature significant spectral overlap with the fluorescent dye since the plasmonic peak is sufficiently broad.

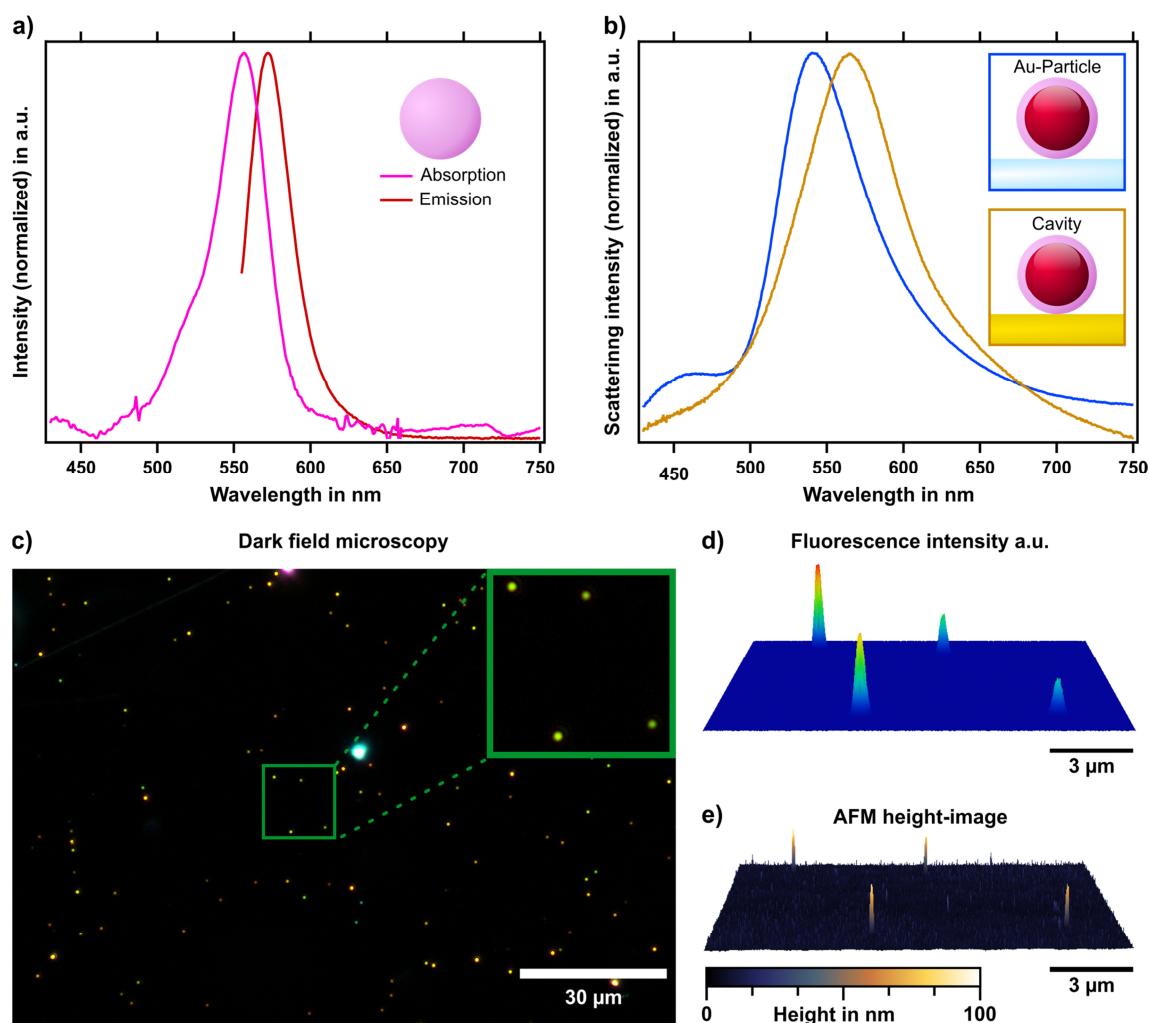


Figure 34. Optical properties of colloidal building blocks. a) Absorption (pink) and emission (red) of the rhodamine B doped silica particles in ethanol. b) Scattering spectra (averaged over 5 particles each) of the Au-core/fluorescent-shell particles on glass (blue) and gold (orange). c) Dark field micrograph of core-shell particles on a gold film. d) Fluorescence lifetime image and e) atomic force microscopy (AFM) image of the highlighted area in c.

Figure 34c shows a dark field micrograph of core-shell particles on a gold film. The four highlighted particles were correlated with regard to their fluorescence intensity (d) and height profile (e). Although the particles are monodisperse as generally proven by TEM

(see Appendix 1) and shown for the respective structures *via* SEM, there are slight changes in the color as well as the fluorescence intensity of these particles (see Appendix 2 for details). These can be explained by variations in the particle-to-film distance, which is reflected by their scattering spectra. Lower distances lead to stronger coupling and a stronger red-shift of the scattering peak.^[11] The particle-to-film distance is affected by two major variables: First, it is influenced by the stabilizing surfactant and capillary forces acting during the drying process. Second, it is determined by the silica shell thickness (4.0 ± 0.5 nm *via* TEM), which is adjusted through the chemical overgrowth process. Indeed, the scattering and fluorescence intensities change simultaneously which indicates an influence of the plasmonic cavity on the fluorescent properties.

To study the fluorescence emission spectroscopically, the fluorophore-plasmonic system was excited with a 506 nm pulsed laser in a confocal setup. **Figure 35** compares the relative fluorescence detection rates of four different setups created from labeled silica and core-shell particles on glass or gold substrates: a) the rhodamine B functionalized silica particle on a dielectric film as reference system (abbreviated as ‘reference’), b) the rhodamine B-functionalized silica particle coupled to metallic gold film (‘film’), c) the plasmonic-core and rhodamine B doped-shell coupled to dielectric film (‘particle’), and d) the core-shell nanoparticle coupled to metallic film (‘cavity’).

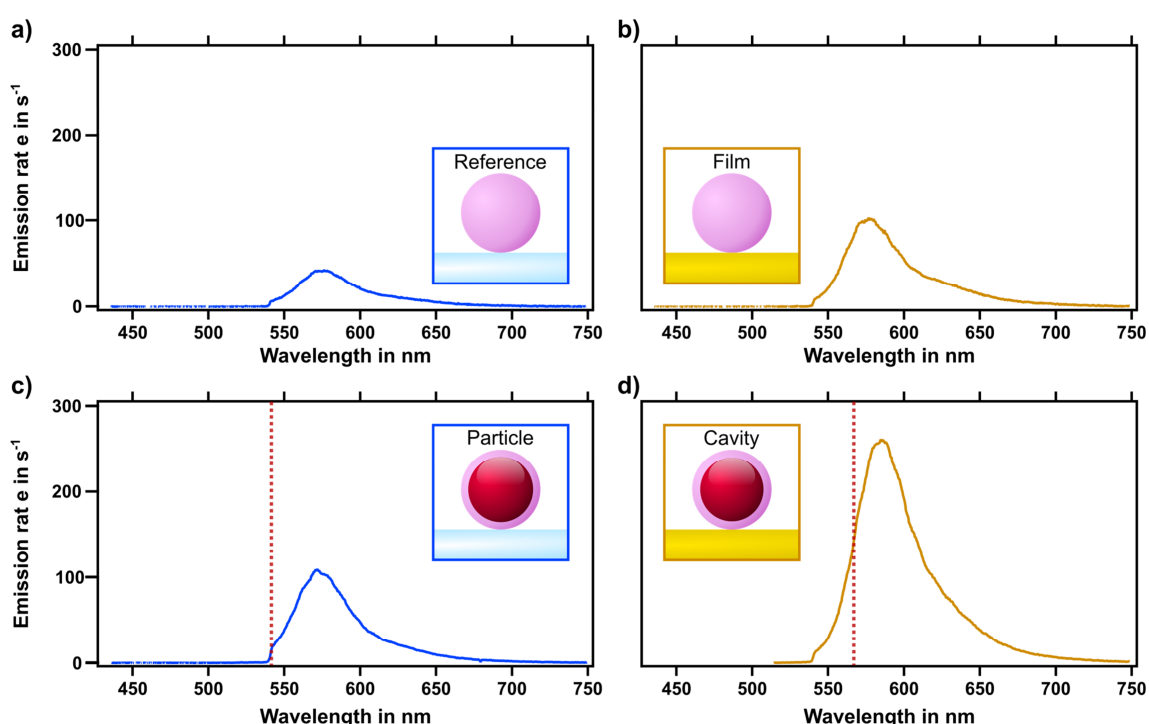


Figure 35. Fluorescence emission spectroscopy of four setups built from fluorescent colloids. Detection rates averaged over four fluorescence emission spectra (solid line) of rhodamine B labelled silica particles on (a) glass substrate (‘reference’) and (b) gold film (‘film’). Fluorescence response of a plasmonic-core and rhodamine B-shell system coupled to (c) glass substrate (‘particle’) and (d) gold film (‘cavity’). The respective plasmonic resonance position (maximum in scattering intensity) is indicated by the red dashed line.

As can be observed, the emission rate is more than doubled when one metallic interface is available ('film': factor 2.4, 'particle': factor 2.6), and once a second metallic interface is available (*i.e.*, the 'cavity'), the fluorescence intensity doubles again (factor 5.9 in comparison to the reference). In the case of the reference setup, the fluorescence intensity is linear proportional to the particle volume, *i.e.*, the amount of emitters. For the 'film' setup the relation is more complex since particles with a diameter of 102 ± 10 nm have regions which are strongly influenced by the gold-film and regions of almost no influence. It has to be taken into account that the effective number of fluorescent emitters is significantly reduced in the core-shell systems (excluded Volume of the plasmonic core). Normalizing for the amount of fluorophore per particle (Appendix 3), the fluorescence intensity of the 'cavity' is calculated to increase by a factor of 38 as compared to the reference, remains unaffected for all setups. The averaged quality factor, which is defined as the full width half maximum (FWHM) divided by the wavelength ($Q = \text{FWHM}/\lambda_{\text{max}}$), is 15.9 ± 0.4 for all systems. The continuity of the quality factor suggests that no inelastic processes (such as Raman-scattering) are involved.

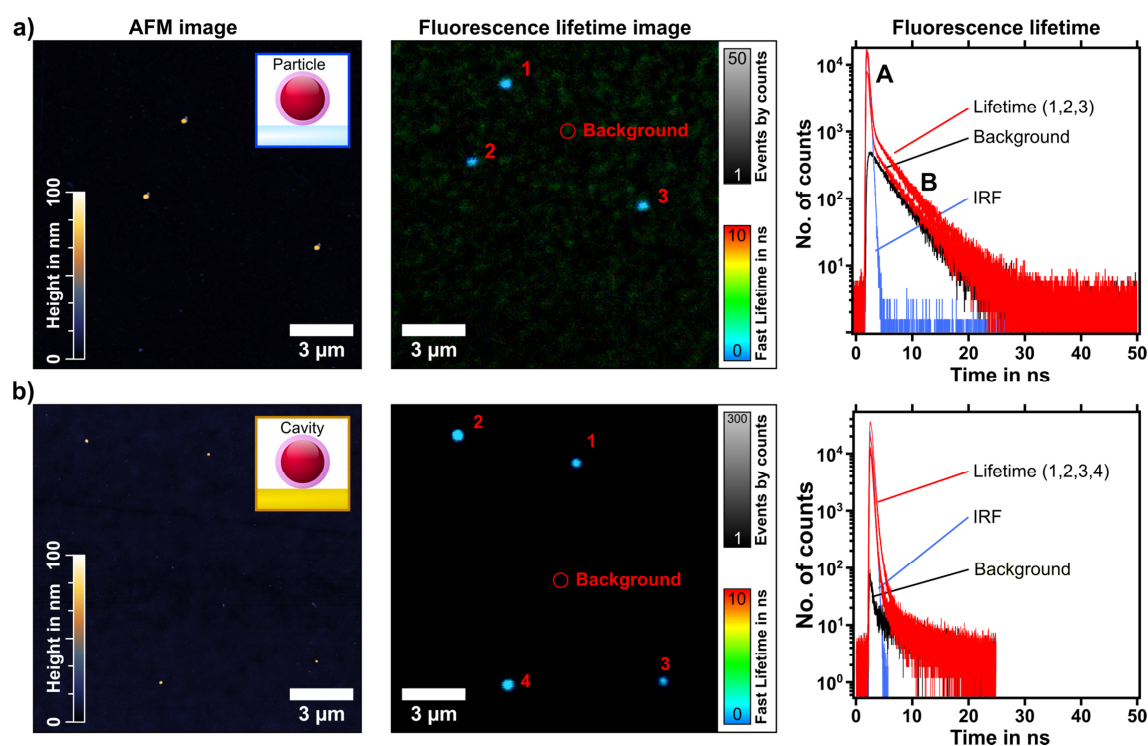


Figure 36. Fluorescence lifetime characterization of the 'particle' and 'cavity' setup. a) AFM image (left), fluorescence lifetime image (middle), and lifetime plot (right) for the 'particle' setup. b) Same items for the 'cavity' setup. Fluorescence lifetime decay is shown for the highlighted positions in the AFM/fluorescence images (red) and background (black). The instrument response function (IRF) is plotted in blue color.

For space and time correlated studies, the same fluorophore-plasmonic systems have been studied using fluorescence lifetime imaging methods (FLIM) and AFM to ensure single particles measurements (**Figure 36**). The fluorescent decay of several 'particle' and 'cavity' samples was studied similar to the previously introduced confocal

fluorescence emission spectroscopy. The lifetime is analyzed by using a pulsed laser at 506 nm combined with time-correlated single photon counting (TCSPC, details in experimental part).

The TCSPC reveals a difference in fluorescence lifetime when one or two metallic interfaces are available. For the ‘particle’ setup two decay times were observed: A fast ($\tau_A < 80$ ps) and a slow decay time ($\tau_B = 3.6 \pm 0.1$ ns). Comparing these decay times with the IRF and the background shows a superposition of an unresolvable fast decay time and a fluorescence decay time of unbound rhodamine B. The decay time of 3.6 ns in the background is in agreement with the lifetime which was measured for the reference (see Appendix 4).

It should be noted, that the illuminated spot size is 340 nm in diameter. The TCSPC detection counts of multiple ‘particle’ and ‘cavity’ samples vary by 26% and 44%, respectively. This behavior was also observed in the intensity of the emission spectra and can be attributed to the sensitivity of the fluorophore-plasmonic system.

At the ‘cavity’, there is a rapid decay ($\tau < 80$ ps) in fluorescence lifetime for all measured positions (Figure 36b). This characteristic decay time matches the IRF and the background signal but exceeds their intensity for several orders of magnitude. Therefore, the lifetime cannot be specified, except for noting that it is faster than 80 ps. Similar to the observation by fluorescence emission spectroscopy, the detected TCSPC counts almost triple (factor 2.7) when a second metallic interface is available.

By electromagnetic simulations, it is possible to conclude from the extinction cross-section of a plasmonic system on their radiative processes when a quantum emitter is available (see Appendix 5 for details). Hereby, the non-radiative and radiative decay for the four setups were calculated. It is shown that additional radiative decay channels, enabled by the presence of metal interfaces, lead to a significant increase of radiative decay as compared to the non-radiative. Consequently, the plasmonic cavity facilitates enhanced quantum efficiency while simultaneously reducing the fluorescence lifetime.^[224,225]

Conclusion

In this chapter, four different colloid-based systems were compared to study their radiative processes, namely, a classical fluorophore system, two systems with one metallic interface, and one system with two metallic interfaces. The observed trend is a significant increase of the fluorescence decay rates as soon as a metallic interface is available. The resulting emission rate is more than doubled, while it increases by a factor of six when a second metallic interface is introduced (plasmonic cavity). As supported by simulations, the increase of the radiative decay outweighs the non-radiative one.

In the growing field of metal-enhanced sensing, the distance control of plasmonic cavities that contain quantum emitters is crucial to study their coupling. Through this study, a colloidal gain material was presented that enables such control and can be applied easily in existing self-assembly methods.^[37,173,226]

Experimental Section

Particle synthesis. Fluorescence-labeled silane was produced by stirring a mixture of 6.0 mg rhodamine B isothiocyanate (11 μmol) and 17.72 μL 3-aminopropyltriethoxysilane (102 μmol) in 2 mL ethanol overnight. The synthesis of fluorescence-labeled silica particles is based on a modified protocol of the Stöber synthesis.^[145,227] 123 mL ethanol, 10.9 mL ammonium hydroxide solution (NH_4OH , 28%-30%) and the labeled silane solution were added to a 500 mL three-necked flask equipped with a reflux condenser. 5 mL tetraethoxy orthosilicate (TEOS, 22.56 mmol) in 20 mL ethanol were preheated and added to the three-necked flask at 50 °C under vigorous magnetic stirring. The stirring speed was reduced after 30 seconds, and the mixture was left for reaction overnight. The product was centrifuged at 8500 relative centrifugal force (rcf) for 30 minutes and redispersed in ethanol. Washing was repeated three times. The resulting particles size of 102.0 ± 9.8 nm was determined *via* transmission electron microscopy (TEM) statistics by evaluating the diameters of at least 100 particles.

Hexadecyltrimethylammonium chloride capped spherical gold nanoparticles were synthesized in a seeded growth process, as previously described.^[200] The resulting particles had a size of 78.6 ± 3.3 nm as determined by (TEM) statistics (at least 100 particles). An aqueous dispersion of these particles (0.66 mg gold) was centrifuged four times at 300 rcf for 30 min and redispersed in 10 mL of 1.1 mM hexadecyltrimethylammonium bromide aqueous solution. Prefunctionalization was conducted in a 25 mL glass vial under magnetic stirring at 30 °C by adding 1 μL of 3-mercaptopropyltrimethoxysilane, and 20 μL of NaOH (0.1 M) 3 h later. After 24 h of reaction time, the product was centrifuged as described above. Overcoating was initiated by adding 20 μL NaOH (0.1 M) to the particle dispersion in a glass vial under magnetic stirring at 30 °C. 40 min later, 10 μL of TEOS and 4 μL of the fluorescence-labeled silane solution (as described above) were added and left to react for 72 h. The final product was purified as described above. The doped silica shell thickness was quantified to be 4.0 ± 0.5 nm as determined by TEM statistics (at least 100 particles).

Substrate preparation. Smooth gold film substrates were produced by template stripping. A 34.2 ± 0.1 nm thick gold film was evaporated on an RCA SC1 cleaned^[228] silicon wafer without adhesive layer. Afterwards, 1.5×1.5 cm² glass slides were placed on top with 3 μL of NOA81 UV Curing Optical Adhesive and cured with an approximate energy exposure of 2 J/cm² from a hand-held UV light source followed by 12 h thermal curing at 50 °C. Finally, the glass slides were carefully stripped from the wafer using a scalpel, leaving the smooth gold film situated on top. The resulting gold films exhibited a root-mean-square (RMS) roughness of 0.4 nm and were spectrally transparent within a 400-750 nm optical window. Particle deposition was conducted *via* spin-coating of 60 μL diluted particle dispersion several weeks after synthesis on both glass slides and gold coated glass at 2000 revolutions per minute (rpm) for 2 min.

Characterization. Particles were analyzed by TEM using a Libra 120 (Carl Zeiss AG) operated with an acceleration voltage of 120 kV. Sizes were evaluated for at least 100 particles per sample. Scanning electron microscopy images were recorded on a NEON 40 (Carl Zeiss AG) microscope with an Everhart-Thornley detector.

Fluorescence lifetime images and time correlated single photon counting (TCSPC) measurements were acquired with an inverted confocal scanning microscope (MicroTime 200, PicoQuant, Germany) with a 100x air objective (UPLFLN, NA 0.9, Olympus, Japan), resulting in a focused laser spot with a diameter of 340 ± 4 nm for the laser configuration used. For excitation, a picosecond pulsed laser diode head (LDH-D-C-510, PicoQuant, Germany) with a center wavelength of 506 nm and a pulse width of 110 ps (full width at half maximum, FWHM), driven at repetition rates of 20 MHz, 30 MHz, and 40 MHz. For fluorescence collection, a dichroic mirror (ZT405-442/510rpc-UF3, Chroma, USA), a long pass filter with a cut-off below 519 nm (FF01-519/LP, Semrock, USA) and a single photon counting module (SPCM-AQRH, Excelitas, USA) were used. For evaluation of fluorescence lifetime images and TCSPC evaluation, SymphoTime64 2.1 was used. Fluorescence lifetime images were recorded at 0.2 μ W excitation power (before objective) and a dwell time of 2 ms per pixel. Single particle TCSPC experiments were performed at 0.2 μ W excitation power (before objective) and a measurement time of 60 s. The instrument response function (IRF) was collected at the same excitation conditions but in the absence of the 519 nm long pass filter and with 2 s integration time to reach similar counts as the fluorescent TCSPC measurements.

To obtain fluorescence spectra, the sample was excited by an optical parametric oscillator (APE OPO PP Auto FAN) with a center wavelength of 519 nm (15 nW excitation power) through an Olympus MPlanFLN 100x 0.9 BDP objective in reflection. The excitation and fluorescence signals were then separated with a dichroic mirror (RT532rdc-UF1, Chroma, USA). Residual energy at the excitation wavelength was removed with a long pass filter (532 LP Edge Basic, Semrock, USA). The spectra were acquired with a Princeton Instruments IsoPlane SCT320 spectrograph (150 g/mm grating, blaze 500 nm, center wavelength 700 nm) equipped with a PIXIS 400 eXcelon charged-coupled device (CCD) camera (Princeton Instruments). The spectra were corrected by subtracting dark spectra (*i.e.*, spectra recorded without laser excitation).

Single particle scattering spectroscopy was conducted on a Nikon Ti-U inverted microscope in transmission mode. The microscope was equipped with an IsoPlane-160 spectrometer and a PIXIS: 256 charged-coupled device (CCD) camera (Princeton Instruments). Measurements were performed with a darkfield condenser (air, NA 0.8 - 0.95) and a 60x air objective (CFI S Plan Fluor ELWD, NA 0.7, Nikon, Japan) under illumination with a 100 W halogen lamp. Spectra with 383 nm bandwidths were recorded for 30 s at 600 nm and 750 nm center wavelengths. These spectra were corrected by subtraction of the CCD's dark current and division by a reference spectrum (white light scattering) for polystyrene nanoparticles (hydrodynamic diameter $D_H = 450$ nm).

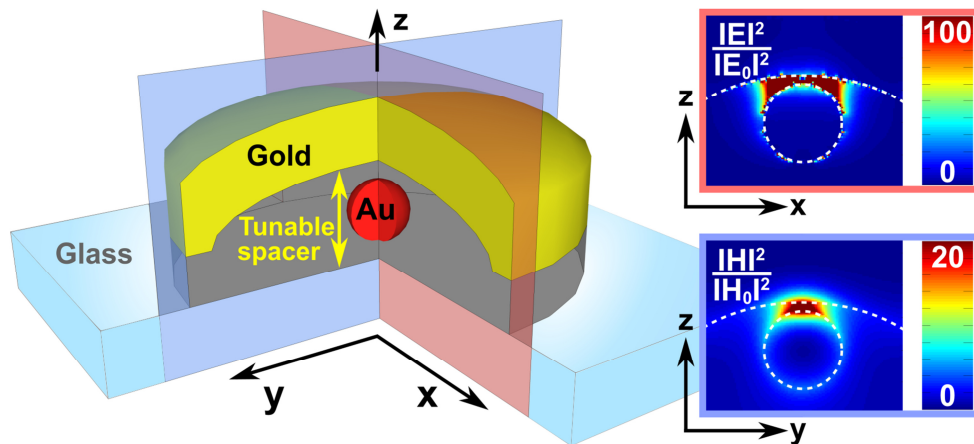
FDTD simulations. A commercial-grade simulator based on the finite-difference time-domain method was used to perform the calculations (Lumerical FDTD, version 8.16). For the simulation of the optical response, a total-field scattered-field source was used and the frequency points were set to be half the wavelength span. Monitor boxes (transmission monitors in all three principle directions) were used to obtain the optical responses of the system as well as the dipole power. For the dielectric properties of gold, data from Johnson and Christy^[229] was fitted using six coefficients with a RMS error of 0.2. For the silica shell, a fixed refractive index of 1.4 was chosen. The mesh size was set to 1 nm for the optical response simulations, and an additional mesh overlay of 0.5 nm was applied for calculations of the dipole and the induced fields. To determine the electric field and surface charge density, a model was simulated at the plasmonic mode frequency. In order to calculate the Purcell factor P and radiative decays, a dipole source was used with emission wavelengths between 400 nm and 800 nm and obtained P by the dipole source. All simulations reached an auto-shutoff of at least 10^{-7} before reaching 300 fs simulation time. For the best simulation stability, the mesh area was chosen to be at least 100 nm larger than the existing structure in all three principal directions.

Acknowledgements

Michael Goebel is acknowledged for assistance with SEM-related correlation. Discussion of the manuscript with Kenneth D. Harris from the National Research Council of Canada was highly appreciated. Thanks to Prof. Dr. Matthias Karg for discussion of the manuscript.

This project was financially supported by the Volkswagen Foundation through a Freigeist Fellowship to TAFK. YB acknowledges support through the elite study program Macromolecular Science by Elitenetzwerk Bayern and University of Bayreuth. The authors acknowledge the Deutsche Forschungsgemeinschaft (DFG) within the Cluster of Excellence 'Center for Advancing Electronics Dresden' (cfaed) for financial support.

V A Switchable Magnetic Library



This section is adapted from the publication “Magnetic and Electric Resonances in Particle-to-Film-Coupled Functional Nanostructures” by Yannic Brasse, Mareen B. Müller, Matthias Karg, Christian Kuttner, Tobias A. F. König, and Andreas Fery (ACS Applied Materials & Interfaces 2018, 10, 3133). Adapted with permission. Copyright 2018 by the American Chemical Society.

All figures and paragraphs were produced by me. Matthias Karg synthesized Au-PNIPAM particles that were deposited and overgrown by Mareen Müller. I conducted all measurements and swelling experiments on the samples. Simulations were performed by me under assistance of Tobias A. F. König and Christian Kuttner. Tobias A. F. König and Andreas Fery were involved in the scientific coordination of the project, discussion of the physical background, and writing of the introduction.

Introduction

Visible light can excite coherent oscillations of the free electrons in metallic nanoparticles. These localized surface plasmon resonances (LSPRs) can couple to adjacent metallic nanoparticles or surfaces, and this results in enhanced electromagnetic fields and scattering cross-sections.^[11] In the case of two coupling nanoparticles, the isolated plasmon resonance hybridizes into two resonances, an energetically lower (anti-symmetric) mode and a higher energy (symmetric) mode.^[105] Such systems have been studied extensively and are routinely referred to as “plasmon rulers” because of their high sensitivity for distance changes.^[104,230] In the case of coupling between a plasmonic particle and a metal film, the resulting mode is always anti-symmetric due to the different dispersion relations of the metallic nanoparticle and the metallic film.^[231] This type of optical nanocavity finds important applications in studies of strong-coupling regimes when, for instance, a quantum emitter is placed inside the gap region between the particle and the metal film.^[113,211] The plasmonic film-coupled resonance is also described as a magnetic mode, because surface charge is induced into the metallic film (*i.e.*, a plasmonic mirror) to oppose that of the charged nanoparticle and the resulting current flow causes a magnetic resonance (according to Ampère's circuital law).^[232] Consequently, these film-coupled nanoparticles find application in solar cells,^[14,233] nanophotonic devices,^[234] sensors,^[16] metasurfaces^[232,235] and photocatalysis.^[236,237] However, the scalability to large areas and tunability of the plasmonic resonance still remain challenging.

The issue of scalability can be addressed with colloidal self-assembly techniques. Tuning of distances between particle and film can be facilitated by introducing polymeric inter-layers. Responsive hydrogels such as poly(*N*-isopropylacrylamide) (PNIPAM) are well suited for this purpose, because they feature a temperature-dependent volume phase transition.^[238] Thin layers of linear PNIPAM have been used by Baumberg *et al.* to separate spherical gold nanoparticles from a gold film.^[239] Photothermal heating^[240] could be used for fast resonance shifting by variation of the film distance. However, randomly assembled gold colloids were applied in this approach and thus, coupling between particles could not be avoided. To prevent inter-particle coupling, hydrogel encapsulated nanoparticles were investigated by Fernández-Barbero *et al.*^[241] They deposited gold core/PNIPAM shell (Au-PNIPAM) colloids on a plasmonic mirror and observed large core-to-core separation (> 5 radii)^[132] and only short range order. By drying the hydrogel layer, spectroscopic shifts could be observed which were not present without the mirror. However, for a reliable screening of these resonances on the macroscopic scale, an efficient coupling between particles and film in terms of particle size and cavity geometry is important.^[176]

In this work, a field-enhancing macroscopic surface with isolated film-coupled nanoparticles in close proximity to a curved plasmonic mirror was studied. The framework of this functional structure is a hexagonally packed monolayer of gold nanoparticles that are well separated by hydrogel shells. With this setup particle-to-film

coupling (in-plane coupling) is solely achieved. The sufficiently large distance between the particles suppresses neighbor-to-neighbor coupling. In analogy to a previous work, an uniaxial gradient in particle size is created along the substrate by wet-chemical overgrowth of the gold cores.^[176] Finally, a plasmonic mirror is placed on top of the monolayer by evaporation of a thin gold film. By this approach, coupling can be tuned locally by controlled swelling of the hydrogel spacer. This cost-efficient and scalable approach targets functional metasurface applications, in which control of the magnetic and electrical resonances are crucial.

Results and Discussion

Fabrication of the functional nanostructure using a colloidal approach

The key element of the functional nanostructure is a substrate-supported plasmonic nanoparticle array, as previously introduced by us.^[176] Briefly, gold nanoparticles were formed using the Turkevich method,^[51] and from these nanoparticles, gold-core/PNIPAM-shell particles were synthesized by seeded precipitation polymerization.^[152,242] The gold cores have an average diameter of 15.4 ± 1.6 nm (determined by transmission electron microscopy, TEM; see Supporting Information, Appendix 6) while the core/shell system features a hydrodynamic diameter (D_h) of 253 nm in the swollen state (measured *via* dynamic light scattering, DLS, at 25 °C). The Au-PNIPAM colloids were spin-coated on cleaned glass slides from aqueous dispersion leading to the formation of a densely packed monolayer.^[56,243] In this process, the swollen particles are confined in a thin liquid film during spinning. While drying, attractive Van der Waals forces (mainly Keesom interactions) lead to attachment and spreading of the particles at the glass surface (see **Figure 37a**). A thermal annealing step was carried out to enhance attractive Van der Waals interactions between the glass substrate and the hydrogel corona. This step did not show significant changes in the particles' morphology. Due to the relatively thick PNIPAM shell, the gold nanoparticle cores are well separated in the monolayer with an average center-to-center spacing that is significantly larger than the limit for plasmonic near-field coupling (> 5 core radii).^[132] Additionally, spin-coating creates particle arrays with only short-range order and small single-crystalline domains of hexagonal order (**Figure 37a** and Appendix 7), which prevents the appearance of surface lattice resonance coupling.^[172,173]

Once the Au-PNIPAM array was formed, the Au-core size was subsequently increased *via* immersion of the substrates in a growth solution containing CTAB, ascorbic acid, and chloroauric acid. The autocatalytic reduction of Au^{+1} (formed by the reduction of Au^{+3} by ascorbic acid) at the gold particle surface leads to an increase in size while secondary nucleation is avoided.^[244] As previously shown, the duration of immersion in the solution regulates the particle growth. Removing the substrate from the solution stops the reaction, and further growth is inhibited. Consequently, the velocity of withdrawal was used to produce a gradient in core-size along the substrate which is here referred to as a plasmonic library (see **Figure 37b**).^[176] This library was coated with a gold film by physical vapor deposition (see **Figure 37c**). The thickness of the gold film was determined by spectroscopic ellipsometry (32.2 nm) and AFM cross-sections (34.1 ± 0.6 nm) using a reference gold film (Appendix 8 and Appendix 9). As will become evident in the following, resonance coupling between particles and the plasmonic mirror results in a uniaxially varying resonance enhancement due to the gradient in particle size.

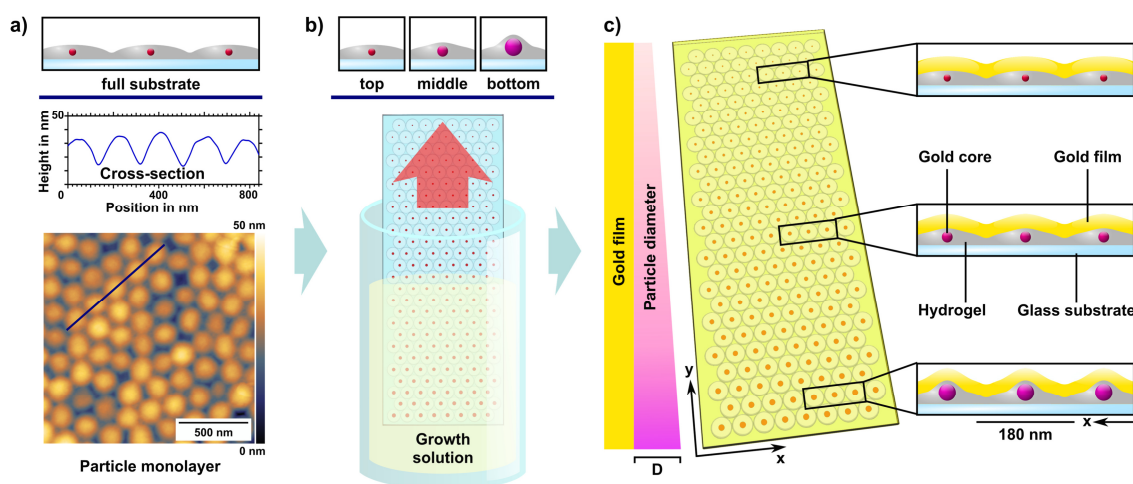


Figure 37. Fabrication of the functional nanostructure. a) AFM height image with cross-section of a monolayer film of Au-PNIPAM particles with 15 nm cores produced by spin-coating. b) Immersion of the substrate in a growth solution and slow withdrawal leads to a gradient of core diameters between 15 nm and 50 nm (plasmonic library). c) A gold film with a constant layer thickness of 34 nm is evaporated on top of the array. Insets show schematic cross-sections: A glass slide (blue) is coated with gold particles of various sizes (red) that are embedded in PNIPAM (grey) which is covered with a layer of gold (yellow).

Structural properties of the particle-to-film coupled nanostructure

In order to characterize the structure along the gradient, AFM height profiles were recorded at different positions. **Figure 38** shows exemplary AFM images (b) on three different spots in correlation to their schematic cross-sections (a). It shall be highlighted that these images were taken from the film-coupled nanostructure, *i.e.*, probing the topography of the gold mirror. By comparing against Figure 37a, it can be observed that the topography of the gold mirror follows that of the underlying Au-PNIPAM particle monolayer. The average center-to-center distance was found to be 183.1 ± 1.2 nm, as calculated by fast Fourier transform image analysis (see Appendix 10). This value is in accordance with the D_h of 253 nm, taking into account that DLS additionally considers diffuse electrolyte layers and that the particles are confined at the interface during the drying process. Comparing the AFM images from the different positions, an increase in peak-to-valley height difference is observed from top to bottom. This is related to the increase in gold particle size which was determined by evaluation of UV/vis extinction spectra, recorded prior to the deposition of the gold film (see following section). The plasmonic peak positions were correlated with the particle sizes, based on a calibration curve published in a previous work (see Appendix 11).^[176] A growth in diameter from initially 15.4 ± 1.6 nm (TEM) to 51.5 ± 2.2 nm (UV/vis) is concluded.

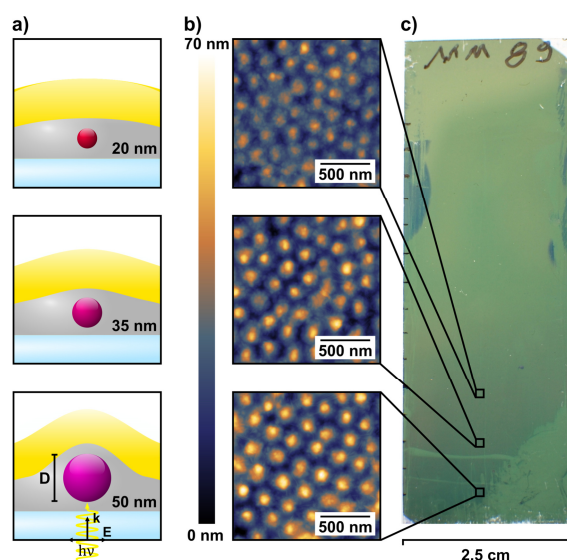


Figure 38. Optical appearance and structural properties of the functional array. a) Schematic depiction of the cross-section at different positions ($D = 20$ nm - 55 nm). Wave vector k and electric field vector E indicate the light path and polarization used for simulations. b) AFM height images at three different positions of the gold film on the same substrate. c) Photograph of the macroscopic substrate.

Optical properties by UV/vis spectroscopy and FDTD modelling

The UV/vis spectra recorded before gold-film coating are shown in **Figure 39a**. For every sample position, a single extinction band is observed, which is caused by the single particle LSPR.^[245] These peaks have a maximum at approximately 540 nm with a slight red-shift for increasing particle diameter. The peak intensity increases with increasing particle diameter. The bands can be assigned to dipolar modes (DM) due to the spherical shape of the cores, and their relatively small size prevents the occurrence of higher order modes.^[11] The evolution of the maximum position of the DM for increasing particle size is highlighted by the grey line.^[67] With increasing core size, a red-shift from 542.1 ± 1.5 nm to 550.2 ± 0.1 nm is observed, as expected by electromagnetic retardation.^[72,246]

After evaporation of a gold film of constant thickness on top of the plasmonic library, the optical properties of the sample change significantly. **Figure 38c** shows the optical appearance of the functional nanostructure on the macroscopic scale. The photograph was captured under backlight illumination and thus shows the transmission of light through the substrate. The characteristic green color can be attributed to the gold film and the sample becomes darker from top to bottom because of changes in absorbance. The corresponding UV/vis absorbance spectra are displayed in **Figure 39b**. In comparison to the pristine plasmonic library (without gold coating), two major trends are observed: First, the plasmon bands increase in intensity across the entire substrate, and second, the resonance peak shifts to longer wavelengths with increasing core diameter. This red-shift ($\Delta\lambda_{\max} = \lambda_{\text{CMmax}} - \lambda_{\text{DMmax}}$) is given by the difference of the peak wavelength for the isolated dipolar mode (DM, λ_{DMmax}) and the peak wavelength of the particle-to-film coupled mode (CM, λ_{CMmax}). **Figure 39c** shows $\Delta\lambda_{\max}$ plotted against the core diameter. A non-linear red-shift with increasing core size and a maximum red-shift of 44.3 ± 0.7 nm

is observed. Such behavior is explained by electromagnetic interactions of plasmonic particles with a metallic film. The dipolar oscillation of valence electrons in the particle induces mirror charges in the gold layer. Consequently, the resonance is coupled to its image in the plasmonic film. This leads to an energetically lower mode, *i.e.*, a higher resonance wavelength.^[113]

For a detailed study of the coupled plasmonic modes, FDTD simulations were conducted and correlated with the experimental findings. The model comprises a glass substrate (refractive index $n = 1.51$ at 589 nm) covered by an ellipsoidal polymer film ($n = 1.50$, see Appendix 12).^[247] A gold sphere of variable size ($D = 20$ nm - 55 nm) is embedded in the polymer and covered with a convex gold film (35 nm, $n = 0.27$) (see Appendix 13 and Appendix 14 for detailed description). Supported by AFM measurements, a cavity geometry with increasing curvature was included in the electromagnetic simulations.^[176] The electromagnetic modelling follows the experimentally observed trend and shows the particle-to-film coupling resonances in more detail (see Figure 39d). The extinction cross-section increases with increasing core diameter and the red-shift of the coupled mode is reproduced. A lower wavelength shoulder which is indicated in the experiment can be observed in the simulation at a particle diameter of 55 nm. This mode is also a dipolar mode, which is one order higher in comparison to the energetically lower DM.^[248] It appears to become more prominent due to the more pronounced red-shift of the superposing film-coupled mode.

In this fabrication approach, the hydrogel spacer thickness must be included in the considerations for electromagnetic modelling. By simulating various particle-to-film distances (see Appendix 15), decrease of the distance from 7.5 nm to 4 nm is estimated during the gold overgrowth. This finding is in accordance with the nature of the applied overgrowth process where the growing plasmonic core displaces the surrounding hydrogel shell.^[176] It results in thinning of the polymer layer which defines the particle-to-film spacing. This phenomenon, in turn, explains the non-linear red-shift of ΔCM_{max} (see Figure 39c) which is not solely described by the increasing particle size.

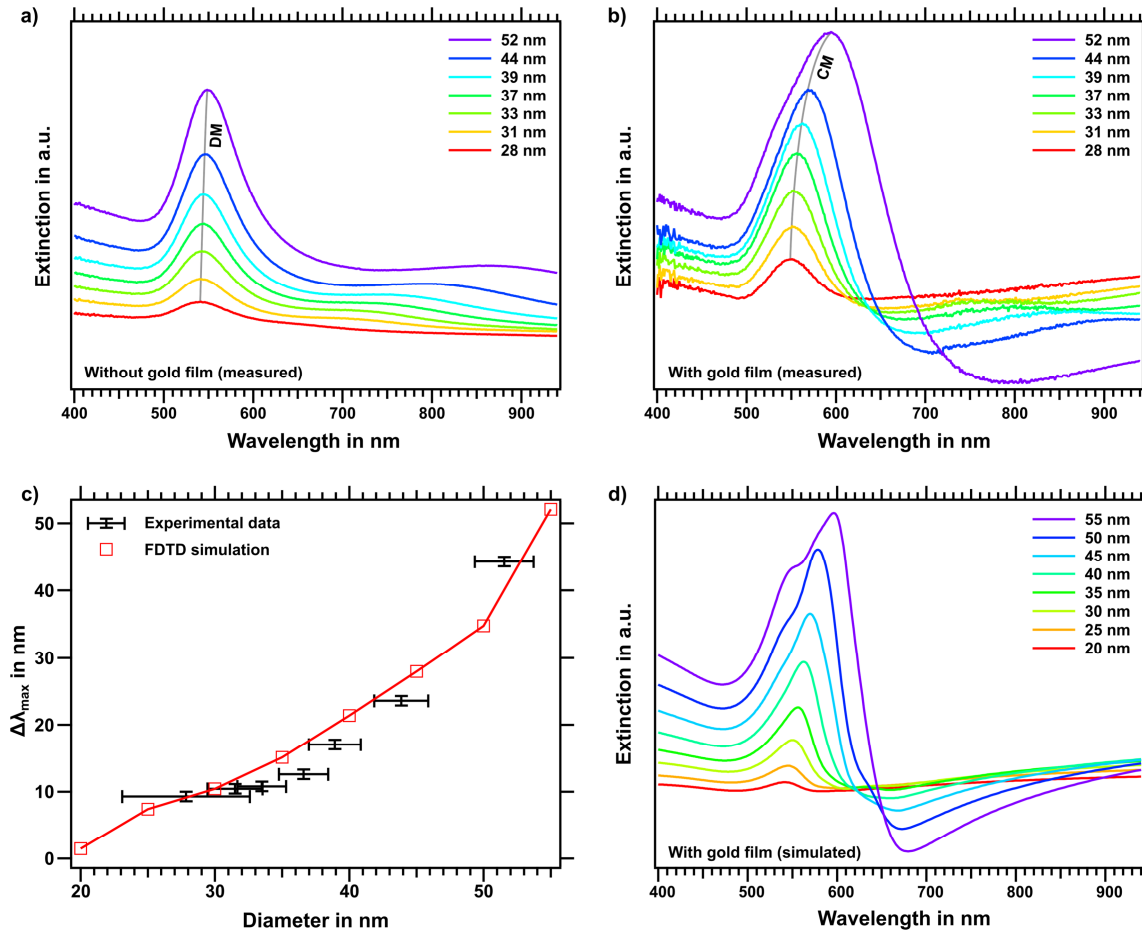


Figure 39. Spectroscopic response and electromagnetic modelling of the functional nanostructure. Experimental absorbance spectra for various particle sizes between 28 nm and 52 nm, a) without gold film and b) with gold film. Gray lines highlight the evolution of the resonance maxima of the corresponding dipolar modes (DM) and particle-to-film coupled modes (CM). c) Comparison of experimental and simulated peak shifts (CM with respect to DM) versus the gold particle diameter. The relative shift is defined as the difference of the plasmonic resonance peak in respect to the non-film-coupled setup. Experimental data are given as black symbols (including standard deviation). FDTD simulation is marked with red squares. Lines between points are guides to the eye. d) Simulated extinction cross-section in dependence of the wavelength, for particle diameters between 20 nm and 55 nm.

Effective permeability using S-parameter method

To identify the nature of the film-coupled nanoparticle mode, the effective refractive index is determined in terms of permeability (see **Figure 40**) and permittivity (see Appendix 16). For this purpose, the S-parameter method established by Smith *et al.*^[249] was applied, which is based on the phase related reflection and transmission in both z-directions of the sample (for more details, see experimental part). The electromagnetic response of two plasmonic particles in close proximity hybridizes into a symmetric and an anti-symmetric mode.^[105] Contrary to a particle-particle system, the dispersion relation of a particle-film system only allows the excitation of an anti-symmetric mode.^[231] The induction of opposing charges in the gold film results in a local enhancement of the magnetic field. Therefore, such anti-symmetric modes are often described as magnetic modes.^[226,232] A negative peak at the imaginary permeability without the gold film and a positive peak for the gold film-coupled setup is observed. The observed peak positions

correlate with the plasmonic resonances, as discussed above (Figure 39a/b). In Figure 40c/d, the real component of the permeability is plotted for the particle-only and particle-film simulations, respectively. In accordance to Kramers-Kronig relation,^[250,251] at the position of the resonance peak, the imaginary component shows a negative slope (without gold film) and the real component shows a corresponding positive slope (with film). These trends agree well with previous literature and indicate that the fabricated film-coupled system exhibits a magnetic mode.^[232]

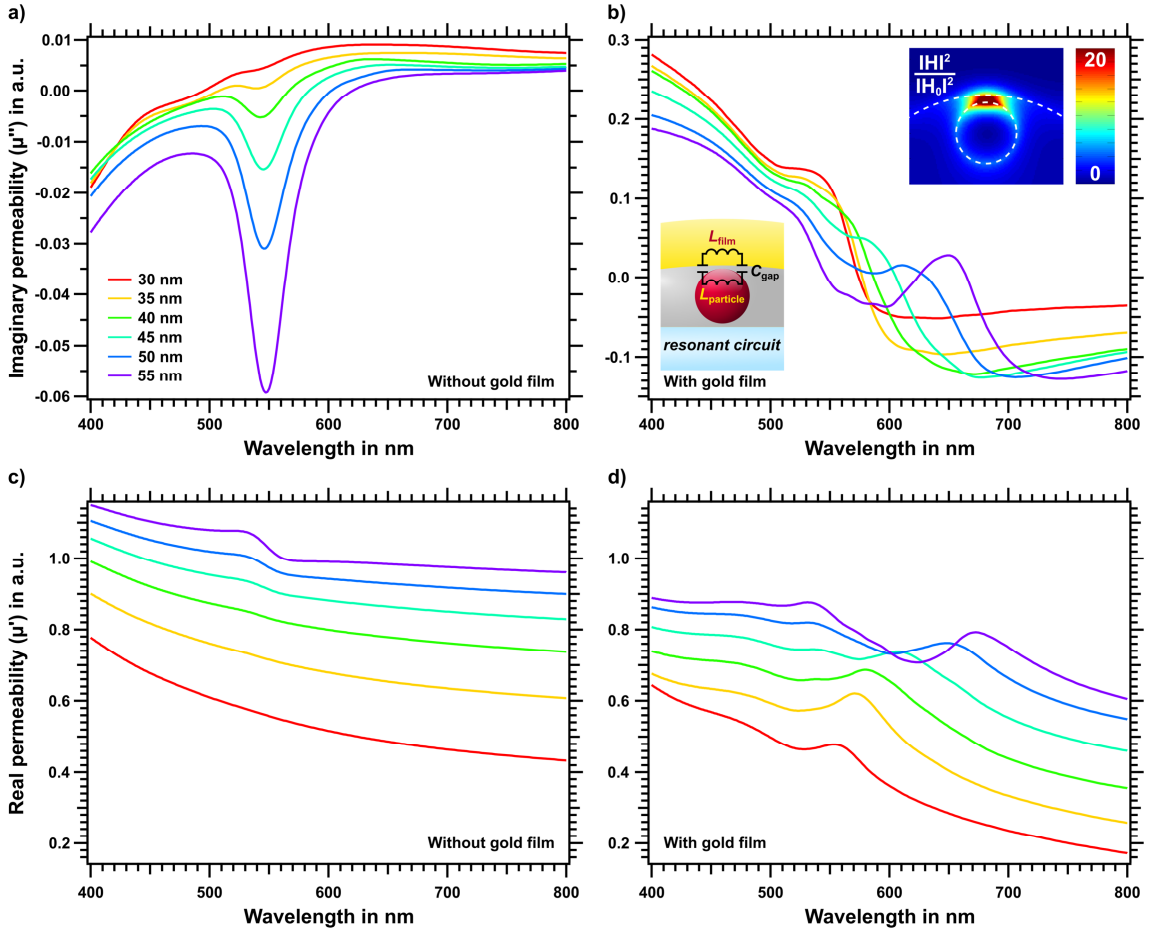


Figure 40. Effective permeability determined by the S-parameter method. Imaginary permeability a) of a gold nanoparticle and b) of a film-coupled nanoparticle, for various particle diameters. In c) and d), the corresponding real components of the permeability for the particle-only and particle-film systems are shown. The insets in b) represent the local magnetic field enhancement from numerical simulations and the corresponding resonant circuit.

The influences of particle diameter and particle-to-film distance on the magnetic resonance can be explained qualitatively with a resonant circuit (see inset in Figure 40b) and the corresponding equation^[235] for its resonance wavelength λ_0 :

$$\lambda_0 = 2\pi c \sqrt{\frac{L_{\text{particle}} + L_{\text{film}}}{1/C_{\text{gap}}}} \quad (21)$$

In this equation, c is the speed of light, and the remaining variables are the equivalent circuit parameters noted in the inset of Figure 40b. An increase in particle diameter

leads to a larger area of induced currents in the metal film. As a result, the capacitance (C_{gap}) and inductance (L_{particle} and L_{film}) increase, which in turn leads to a larger resonance wavelength λ_0 , *i.e.*, lower resonance energy. Experimentally, this was observed as the red-shift ($\Delta\lambda_{\text{max}}$) with increasing particle diameter. Similarly, a decrease in gap size (d_{gap}) between the particles and the gold mirror would cause an increase of C_{gap} resulting in an additional red-shift ($C_{\text{gap}} \sim 1/d_{\text{gap}}$). By determination of the permeability, the plasmonically induced resonance was identified as a magnetic mode. Because the fabrication process allows the particle diameter to be adjusted, tunability in both the strength and position of the plasmonic resonance is established in the particle-to-film coupled nanostructure.

Tunability of the functional nanostructure

To this point, the studies of the functional nanostructure were to dry conditions. Now, the sample behavior upon swelling of the PNIPAM hydrogel matrix by water will be addressed. Serpe *et al.*, have shown that swelling of a PNIPAM layer is maintained under thin metal films.^[252] Focusing the studies on film-coupled systems (43.5 ± 1.3 nm thickness *via* AFM) with 50 nm gold particles, two primary phenomena were observed upon immersion in water (see **Figure 41a**): First, a significant blue-shift of λ_{max} from 588.6 ± 0.5 nm to 550.2 ± 0.5 nm and second, narrowing of the resonance band by 23.9 ± 0.8 nm (full width at half maximum). This behavior takes place in a reversible manner over multiple cycles of swelling and drying. Explicitly, the plasmonic resonances in the dried and wet states are recalled without significant alterations or even damaging of the substrate (see Figure 41c and Appendix 17).

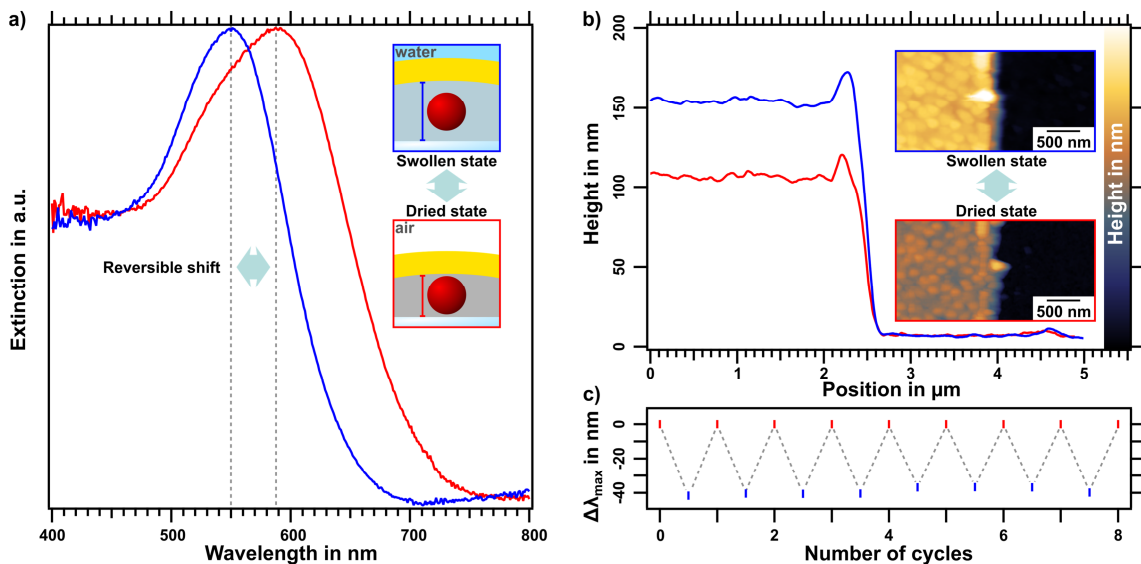


Figure 41. Spectral and structural changes of the film-coupled particle system by reversible swelling. a) Extinction spectra in dried (red) and swollen state (blue) with 50 nm gold cores. b) AFM cross-sections measured in air (red) and water (blue). Insets show the respective images. c) Relative peak shift over 8 cycles.

The pronounced shift is caused by swelling of the hydrogel matrix and the resulting changes in the coupling strength as proven in Appendix 18. There is an increase of the particle-to-film distance and a decrease of the effective refractive index in the gap between particles and the gold film due to the uptake of water. A decrease of the surrounding refractive index is known to narrow and blue-shift the extinction band of plasmonic particles. This behavior can be described by simulations in Appendix 15. Here, the position of λ_{\max} is shown in dependence of the dielectric surrounding (n between 1.50 and 1.33). These limiting values correspond to the indices of neat PNIPAM (dried state, see Appendix 12) and water (virtual swelling limit), respectively. In Appendix 19, λ_{\max} decreases linearly with decreasing refractive index at a constant gap size of $d_{\text{gap}} = 4.5$ nm, reaching a maximum shift of 28 nm. It is important to note that the effective refractive index depends on the degree of swelling (volume fraction of water) and is not likely to reach the value of pure water. Therefore, the 28 nm red-shift represents an upper bound for variation based solely on refractive index modulation. In order to account for the 38 nm shift that was observed experimentally, both the refractive index and physical dimensions of the particle/film gap are surmised to vary during the swelling process.

An AFM-based scratch test was performed to quantify the actual change in film height upon swelling by water. Figure 41b shows cross-sections and corresponding images of the surface measured in air (dry conditions) and in water (swollen state). The original thickness of the dried layer (Au-PNIPAM under gold film) is 98.5 ± 0.8 nm in the region of 50 nm sized gold particles. This is in agreement with the thickness of 94 nm that results from the FDTD model. Upon immersion in water, the height increases to 146.5 ± 1.0 nm which establishes the swelling capability of PNIPAM while isolated underneath a thin gold film. As a result, the particle-to-film distance increases while, at the same time, reducing the coupling strength between the dipole of the particle and its image in the metal film.^[231] Thus, a fully reversible switching between the strong and the weak coupling regime is achieved by infiltration of water.

Similarly, this behavior can be addressed by changing the relative humidity. A significant alteration of the spectroscopic response (7.3 ± 0.7 nm blue-shift) was observed by shifting from dry nitrogen atmosphere to 90% relative humidity (see Appendix 20). In the non-immersed state, the plasmon resonance is most sensitive to slight changes in spacing distance and refractive index because of the short particle-to-film distance (strong coupling regime). These changes occur by variation of the ambient humidity, which is a similar but less pronounced version of the transition induced by immersion in water. Hence, the system features additional sensitivity to relative humidity.

Conclusion

A monolayer of gold-core/PNIPAM-shell particles was assembled on a macroscopic substrate, and subsequent overgrowth of the cores resulted in a size gradient from 15.4 nm to 51.5 nm in diameter. These particles were coupled with a continuous 34.1 nm gold film, and extinction spectra were compared before and after coating. A significant red-shift of the plasmon resonance was observed, and this red-shift becomes more pronounced with increasing particle diameter, reaching up to 44.3 nm. The optical response was comprehensively studied by FDTD simulations, which show electromagnetic coupling between the plasmonic cores and gold film. It was observed that the decrease in particle-to-film distance (from 7.5 nm to 4 nm) that occurs during the overgrowth process influences the spectroscopic properties. Modeling of the effective permeability (by the S-parameter method) showed a magnetic character of the coupling mode, which increases with particle diameter. Swelling of the hydrogel spacer also reversibly modulates the plasmonic resonance, resulting in a maximum blue-shift of 38.4 nm in the case of 50 nm particle diameter. Such a shift is caused by changing both refractive index and particle-to film distance which was proven by FDTD simulations and AFM measurements.

The potential of the functional nanostructure lies in the following applications: (1) This approach makes the particle-to-film-coupled nanomaterial a cost-efficient screening platform, where a target molecule can be placed inside the cavity. By choosing a specific combination of particle diameter and spacer thickness, a spectral match between the target molecule and the film-coupled particle resonance can be obtained. (2) The electromagnetic modelling shows the potential of this platform as an optical metasurface, where the effective permittivity and permeability can be adjusted. (3) Finally, effective coupling of light to the functional nanostructure is shown, *i.e.*, field enhancements in the electric and magnetic modes, which can be used to study super absorber effects and hot electron injections.

Experimental Section

Materials. All chemicals were purchased from Sigma-Aldrich and used as received unless otherwise noted: Hydrogen peroxide solution (H_2O_2 , 30 wt%), ammonium hydroxide solution (NH_4OH , 28-30 wt%), gold(III) chloride hydrate ($\text{HAuCl}_4 \cdot 3\text{H}_2\text{O}$, $\geq 99.9\%$), cetyltrimethylammonium bromide (CTAB, $\geq 99.9\%$), ascorbic acid ($\geq 99.9\%$), *N*-isopropylacrylamide (NIPAM, 97%), *N,N'*-methylenebis(acrylamide) ($\geq 99.5\%$, Fluka), potassium peroxydisulfate ($\geq 99.0\%$, Fluka), trisodium citrate dihydrate ($\geq 99\%$), sodium dodecyl sulfate ($\geq 99.0\%$), and 3-butenylamine hydrochloride (97.0%). Water was purified using a Milli-Q system (Millipore), yielding a final resistivity of 18.2 M Ω cm.

Substrate preparation. Glass slides (Fisher Scientific, Premium microscope slides 12-544-4) were cleaned using RCA-1 solution ($\text{NH}_4\text{OH}/\text{H}_2\text{O}_2/\text{H}_2\text{O}$ in a ratio of 1:1:5 by volume) at 80 °C for 20 min.^[253] The cleaned glass slides were placed on a spin-coater (Model P6700, Specialty Coating Systems, Inc.) and coated with Au-PNIPAM particles (hydrodynamic diameter, $D_h = 253$ nm) prepared in a seeded precipitation polymerization, as previously described.^[242] In the spin-coating process, the Au-PNIPAM particles were dispensed from a 1 wt% aqueous solution (prepared from freeze-dried particles) onto a static substrate, followed by a 40 s acceleration from 0 to 1000 rpm, and an additional 90 s continuous rotation at 1000 rpm. The monolayer was annealed by placing the slide on a hot plate with a surface temperature of 91.0 ± 6.8 °C for 1 min. A dip-coater (DC/D/LM, KSV Instruments) was used for the gold overgrowth process. The growth solution was prepared by slowly adding 417 μL of HAuCl_4 solution (0.1 M) under vigorous stirring to 100 mL of CTAB solution (0.1 M), and after 5 min, 588 μL of a fresh solution of ascorbic acid (0.1 M) was added drop-wise under vigorous stirring.^[176] To form up to 50 nm sized gold cores, the substrate was dipped into the growth solution at 100 mm/min and retracted with exponentially decreasing speed. After growth, the substrate was washed twice by immersion in purified water at 29 °C, first for 20 min, then for 19 h. The sample and a cleaned reference slide were subsequently coated with a 35 nm gold film by physical vapor deposition in a BA510 system (Balzers, Lichtenstein). Vaporization was achieved by melting bulk gold with an electron beam at 10^{-6} mbar. The samples were placed 30 cm above the crucible, and the gold deposition rate was adjusted to 1 nm/s measured with a quartz oscillator.

Characterization. The initial Au-core/PNIPAM-shell particles were analyzed by transmission electron microscopy (TEM) using a FEI TF 20 operated with an acceleration voltage of 200 kV. The hydrodynamic diameter of the particles was determined by dynamic light scattering (DLS) at 25 °C, *i.e.*, in the swollen state of the PNIPAM shell. These DLS measurements were conducted with a standard goniometer setup (ALV, Langen, Germany). Measurements were performed at a constant scattering angle of 60°. A 632.8 nm HeNe laser (JDSU, USA) was used with a maximum output power of 35 mW as the light source. The sample temperature was regulated by a heat-controlled toluene refractive index matching/temperature bath. Multiple intensity-time autocorrelation functions were recorded and analyzed by inverse Laplace transformation using the

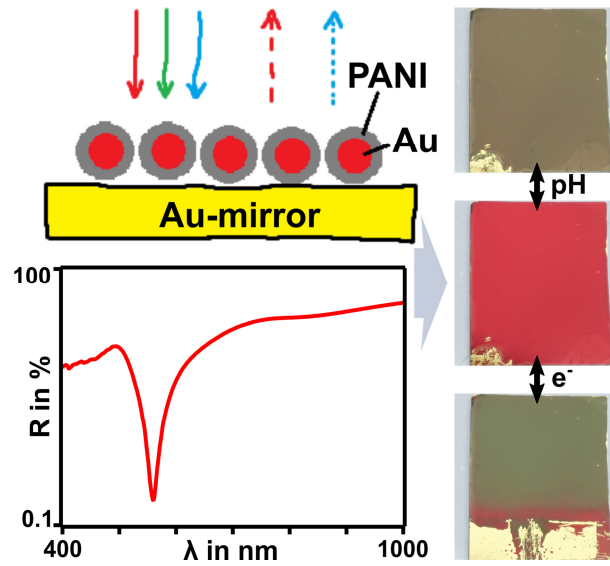
CONTIN algorithm.^[101] Atomic force microscopy (AFM) of particle layers was performed with a NanoWizard 4 NanoScience AFM (JPK Instruments) in intermittent contact mode. Spectroscopic ellipsometry on gold films was conducted with an RC2 ellipsometer (J.A. Woollam Co., Inc.) by measuring the full Müller matrix. The refractive index of dry PNIPAM was determined with a spectroscopic ellipsometer (M2000, J.A. Woollam Co., Inc.) in the wavelength range from 245 nm to 1600 nm (D2 and QTH lamps). Ellipsometric data from all samples were acquired at different angles of incidence (45° - 75° in steps of 5°). To specify the refractive index of all materials, a general oscillator layer model was used within the CompleteEASE software (Version 5.07). All modelling approximations were physically reasonable (parametrization to fulfill Kramers-Kronig relations^[250,251]) and showed mean square errors (MSEs) below five (PNIPAM) and seven (gold). UV/vis absorbance spectra were recorded in transmission before and after gold deposition with a Cary 5000 spectrometer (Agilent Technologies) using the Cary Universal Measurement Accessory (UMA) on a spot size of $2 \times 5 \text{ mm}^2$ (1° apertures). Transmission data were corrected against reference samples (glass slide and gold coated substrate). Swelling experiments of the PNIPAM shell in water were performed in a home-made 5 mm pathway liquid cell.

FDTD simulations. The optical responses in transmission and reflection at normal incidence were simulated using a commercial software package from Lumerical Solutions, Inc. (FDTD Solutions, Version 8.11.422). Periodic boundary conditions (BCs) were applied in lattice directions and a perfectly matched layer BC in the beam direction with a linearly polarized plane wave source. Nanoparticle diameters, periodicity, materials constants, and thickness were obtained from experimental studies. In the beam direction, the FDTD simulation total length was chosen to be $1.25 \mu\text{m}$ with transmission monitors located at both ends. The simulation setup was placed in the center of the FDTD simulations and the plane wave source was injected starting from the glass layer. For a broadband source simulation ($\lambda = 400 - 1000 \text{ nm}$), the FDTD software approximates the refractive indices of the materials using a polynomial function. All optical constants were estimated by curve fitting to a root mean square error below 0.21. For gold, the experimental data of Johnson and Christy were used.^[229] Zero-conformal-variant mesh refinement and an isotropic mesh overwrite region of 1 nm were used for the film-coupled nanoparticle setup. All simulations reached the auto shut-off level of 10^{-7} before reaching 1000 fs of simulation time. To determine the electric field distribution and surface charge densities, the model at the plasmonic mode frequency was simulated at a pulse length of 20 fs (optimized for long pulse length). To calculate the effective optical properties of film-coupled nanoparticles, S-parameter extraction analysis was used (Lumerical Solutions, Inc.).^[249] To retrieve the optical constants for the inhomogeneous asymmetric structure, the parameters S11 and S22 were calculated from simulations in forward and backward source directions, respectively, each at an automatic shut-off level of 10^{-7} .

Acknowledgements

This work was funded by the German Science Foundation within the SFB 840 and by the European Research Council under grant ERC-2012-StG 306686 (METAMECH: Template-assisted assembly of METAmaterials using MECHANical instabilities). The authors acknowledge the Cluster of Excellence Center for Advancing Electronics Dresden (cfaed). Y.B. acknowledges support through elite study program Macromolecular Science by Elitenetzwerk Bayern and University of Bayreuth. Klaus Müller from University of Bayreuth is acknowledged for vapor deposition of gold layer. Kenneth D. Harris is warmly acknowledged for English proofreading.

VI A Tunable Anti-Reflective Metasurface



This section is adapted from the publication “A Tunable Polymer-Metal Based Anti-Reflective Metasurface” by Yannic Brasse, Charlene Ng, Michele Magnozzi, Heyou Zhang, Paul Mulvaney, Andreas Fery, and Daniel E. Gómez, (*Macromol. Rapid Commun.* **2020**, *41*, 1900415). Adapted under the terms of the Creative Commons Attribution Non-Commercial License (CC BY-NC). Copyright 2019 by the authors.

All figures and paragraphs were produced by me. Gold particles were synthesized by Anja Steiner. Gold substrates were provided by Daniel E. Gómez while nanostructured ITO templates were provided by Heyou Zhang. I performed all particle functionalization, sample preparation, and measurements. Samples on gold substrates were prepared in the labs of Daniel E. Gómez at RMIT while samples on nanostructured ITO were prepared in the labs of Paul Mulvaney at the University of Melbourne. The calculation of the optical constants of polyaniline from spectroscopic ellipsometry was performed by Michele Magnozzi. COMSOL simulations were done by Heyou Zhang. Charlene Ng was involved in cyclic voltammetry measurements and their discussion. All authors contributed to the discussion and interpretation of the results. Paul Mulvaney, Charlene Ng, Andreas Fery, and Daniel E. Gómez were involved in the scientific coordination of this project.

Introduction

Surfaces with very low reflectivity are of great importance for a broad range of applications, such as anti-reflective coatings,^[4,254] optical resonators (lasers),^[255] or interferometers.^[256] Broadband absorbers are of particular interest since they can facilitate efficient conversion of solar energy through photovoltaics^[14,257] or photocatalysis.^[258-260] On the other hand, narrowband optical materials have also attracted significant attention as they can be utilized in sensing applications.^[22] Plasmonic metasurfaces are highly attractive materials because the absorbed wavelength can be finely tuned by adjusting their geometric structure. They also exhibit high sensitivity towards refractive index changes in the environment, which opens up a potential avenue for tunability.^[76,261] The group of Giessen has introduced such sensors based on metal-insulator-metal structures.^[22] By employing electron beam lithography (EBL), a gold nanodisc array featuring localized surface plasmon resonances can be fabricated on top of a gold mirror with a dielectric MgF₂ spacer sandwiched in between the nanodiscs and the mirror. The resulting plasmonic coupling enables tuning of the electric permittivity ϵ and magnetic permeability μ and leads to impedance matching between the structure and air. The device then features a minimum in the reflectance at the resonance frequency (THz range) that is sensitive to small refractive index changes.^[115,261]

More recently, colloidal particles have been utilized to create anti-reflective plasmonic metasurfaces.^[118,262] The colloidal approach offers scalability of the synthesis and allows different optical coatings to be incorporated, while maintaining precise control of the nanostructure and thus is especially appealing for large area applications.^[263] Mikkelsen *et al.* have tuned the resonance frequency of such surfaces in the visible region *via* random deposition of cubic silver nanoparticles onto a gold mirror.^[114] They achieved an absorbance of 99.7% at the resonance frequency, even at comparably low fill fractions of around 20% by area. Although the resonance frequency can be tailored through a variation of shape and size of the plasmonic nanoparticles, this involves strenuous preparation of different nanoparticles and *in situ* tuning is deemed impossible.

Contrarily, active tunability of the optical properties can be realized by integrating a switchable polymer layer as the spacer between plasmonic nanoparticles and a mirror. A change in the refractive index of such a layer can be triggered externally and used to alter both the plasmonic resonance frequency and optical impedance-matching condition. A suitable system for testing this concept has been introduced by Tsukruk *et al.*^[28,264] They investigated the electro-optical response of polyaniline coated silver cubes in dispersion and on transparent substrates. A strong influence of the polymer's complex refractive index on the localized surface plasmon resonance was demonstrated. Based on this system, Baumberg and coworkers also studied the influence of the polymer redox chemistry on (plasmonic) light scattering.^[265] Deposition of the particles on gold surfaces enabled tuning of the electrochromic properties while enhancing the plasmonic response. This is a promising route towards responsive nanoscale pixels. However, the influence of

the particle layers on the reflectivity of (metallic) surfaces was outside the scope of their investigations.

Here, a plasmonic metasurface based on polyaniline coated gold spheres is presented, which acts as a tunable, anti-reflective coating. By combining the polymer with gold nanocrystals, a scalable, wet-chemically synthesized material is created, providing pronounced narrowband extinction at optical frequencies. In contrast to previous works, this method provides *in situ* tunability of both the attenuation efficiency and the peak attenuation wavelength. This switchability is realized by utilizing the pH-responsive and electrochromic properties of the polyaniline corona. For further optimization of the anti-reflective metasurface, a facile assembly method is discussed to obtain precise control of the inter-particle distance.

Results and Discussion

Our approach to making tunable metasurfaces was based on using spherical gold nanoparticles^[200] coated with polyaniline (Au-PANI).^[28] Gold spheres with a diameter of 83.7 ± 2.8 nm were synthesized with a 31.5 ± 2.8 nm thick polyaniline shells (from TEM, see Figure 42a). The particles were deposited onto hydrophilized gold substrates *via* sedimentation yielding a sub-monolayer surface coverage with a homogeneous optical appearance at the macroscale as shown in Figure 42c (see Supporting Information for experimental details).

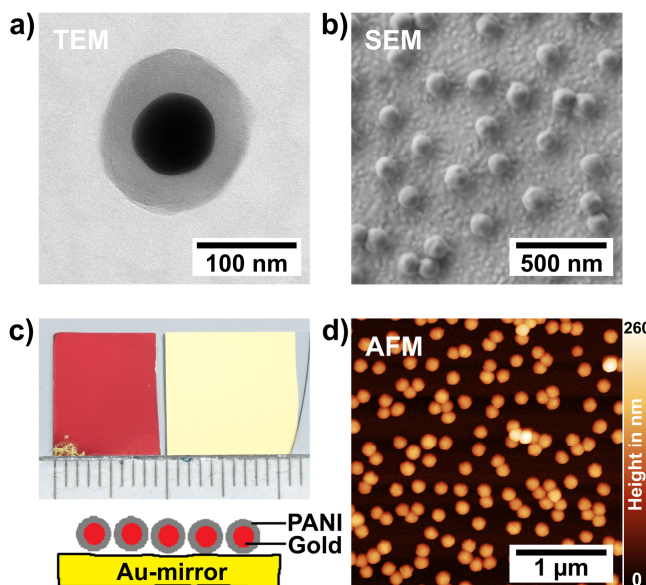


Figure 42. Surface structure of the tunable metasurface. a) TEM image of a single Au-PANI particle. b) SEM image of Au-PANI particles on a gold mirror. c) Top: photograph of the anti-reflective metasurface (consisting of Au-PANI on a gold mirror) and an Au-film reference under specular illumination (scale in mm). Bottom: a schematic cross-section of the sample. The structure is: 200 nm Au mirror, 32 nm PANI shell, 84 nm gold core d) AFM micrograph of the surface topography.

Depending on the applied concentration of the dispersed Au-PANI particles, the surface coverage was varied from $24\% \pm 1\%$ (see Figure 42) to $\sim 50\%$ (see Appendix 22). The visual appearance of the samples was strongly altered from the typical gold metallic reflection to an intense red color, as displayed in the photograph in Figure 42c. The film stability towards mechanical stress (e.g. wiping) was limited but the particle adhesion was sufficient to resist gas streaming, rinsing, and immersion into aqueous solutions.

The appearance of the samples can be easily explained by comparing the resulting optical spectra in Figure 43a. For characterization of the metasurface, UV/vis spectroscopy was performed at 10° specular reflectance angle and normalized to the reflectance of a pure gold film. In addition to the low reflectance below 500 nm caused by the interband transition of gold, there is a pronounced minimum at 550 nm. It corresponds to the peak position of the localized surface plasmon resonance (LSPR) and reaches a reflectance of just 1.5% with respect to the gold mirror. This attenuation of green light results in the observed red coloration of the sample. Furthermore, there is a

less pronounced band located at 800 nm which is attributed to the absorption of polyaniline in its emeraldine salt state (as synthesized).

It is hypothesized that the extraordinary low reflectance exhibited by these films can be attributed to a combination of plasmonic and interference effects. Namely, the key characteristic of the system is that optical phase shifts are induced by the polymer coated particles. Similar to the mechanism proposed by Chen *et al.*,^[129,130] the incident light (I) (see Figure 43b) encounters various interfaces through the overall structure. The three major components are: (II) the light which is directly reflected by the gold mirror, (III) the light transmitted by the polymer and scattered by the plasmonic particle, or (IV) scattered by the particle and then reflected by the mirror.^[266] As a consequence of passing the polymer and interacting with the plasmonic particle, III and IV are phase-shifted with regard to the reflected light (II). The resulting destructive interference contributes to additional attenuation of light and is responsible for the performance of the metamaterial as an antireflective coating.^[130] In contrast to coupling mechanisms as discussed by Peng *et al.*,^[265] the particle resonance is predominantly excited parallel to the surface (perpendicular k -vector), which results in comparably weak film-coupling at 32 nm film distance. However, alternative mechanisms based on plasmonic coupling are discussed in the supporting information (see Appendix 23).

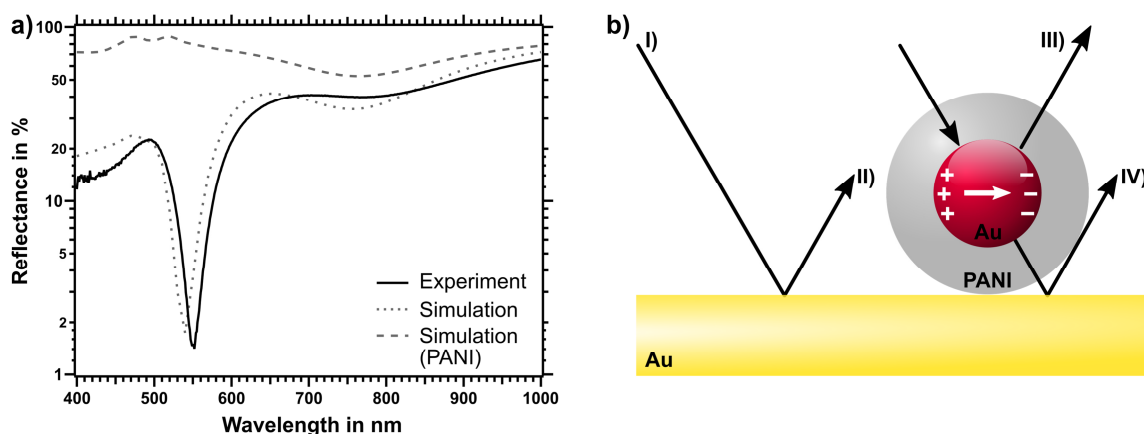


Figure 43. Optical properties of the metasurface. a) Typical specular reflectance spectrum of the anti-reflective surface (black line) together with COMSOL simulation of Au-PANI (dotted grey line) and pure PANI (dashed grey line), both normalized to the Au-film. b) Schematic depiction of the reflection and scattering events at the mirror and the particle, showing: (I) the incident light beam, (II) the light directly reflected by the mirror, (III) the light scattered by the particle, and (IV) the light which is scattered by the particle and then reflected by the mirror.

To qualitatively interpret the described interference effects with regard to their tunability, optical simulations based on the experimental parameters were conducted. Spectroscopic ellipsometry was applied to determine the optical properties of the polyaniline corona by extracting the wavelength-dependent complex refractive index (values of n and k) for the polymer (see Appendix 24). Based on these optical constants, COMSOL simulations were used to calculate the reflectance of a gold mirror covered with Au-PANI particles (see Appendix 25 for details). The dotted graph in Figure 43a shows the

simulated reflectance spectrum with an untreated PANI shell and 240 nm inter-particle distance (center-to-center). The features reproduce the experimental findings, including both the reflectance minimum at ~ 550 nm and the less-pronounced band at about 800 nm. As the localized surface plasmon peak position is strongly dependent on the refractive index of the surrounding medium, a shift is expected when the dielectric properties of the PANI layer change. Simulations based on the determined optical constants of NaOH-treated PANI are displayed in Appendix 26. Here, the reflectance minimum is redshifted by 20 nm as a consequence of the increased refractive index of the polymer.^[66,267] Interestingly, the minimum is less pronounced compared to that obtained for the untreated polymer. We deduce that the altered optical constants of PANI influence the phase shift of light interacting with the particle (compare the scattered light beams III and IV in Figure 43b). Consequently, destructive interference occurs to a lesser extent, which results in less attenuation of the reflected light.

For experimental demonstration of the proposed *in situ* switchability, the optical properties of the anti-reflective metasurfaces were modulated using two different triggers: pH and redox reactions. As displayed in Figure 44, immersion of the substrate in either HCl- or NaOH-containing aqueous solutions altered the optical appearance of the sample. Reflection of the surface changed from reddish (initial film and after HCl immersion) to a greenish color (after NaOH immersion). This was correlated to the spectral shifts shown in Figure 44a. Alternating color changes were induced by subsequent immersion into acidic and basic solutions with reflectance spectra collected after each step. The green curves depict the spectra after immersion into HCl while blue curves correspond to the spectra after immersion into NaOH. The green spectra exhibit a pronounced minimum at 550 nm with reflectance below 2% while an additional shoulder can be observed at around 800 nm. The blue spectra feature an increased reflectance of around 10% at the peak minimum, *i.e.*, a 5-fold increase. Furthermore, the band is redshifted to 570-585 nm and features a pronounced asymmetric, longer wavelength shoulder. The optical changes are associated with the changing chemistry of the polyaniline shell around the plasmonic particles. Under acidic conditions, polyaniline is in its protonated (doped) state referred to as emeraldine salt. Following immersion into a base, the emeraldine salt is deprotonated and is converted into its emeraldine base form, shown in Figure 44b. This transition is associated with several different changes to the polymer: i) A transition from a conductor to an insulator due to deprotonation (loss of the radical cation).^[58] ii) A shift of the main absorption band from 800 nm to 600 nm as displayed in Appendix 27 because of the changes in the π -electron system.^[268] iii) A change in refractive index (see Appendix 24). The shift of the reflectance minimum was reversible over multiple cycles, as displayed in Figure 44c. The slight deviations in the peak intensity and positions are attributed to chemical oxidation of the polymer, which will be discussed in the following section.

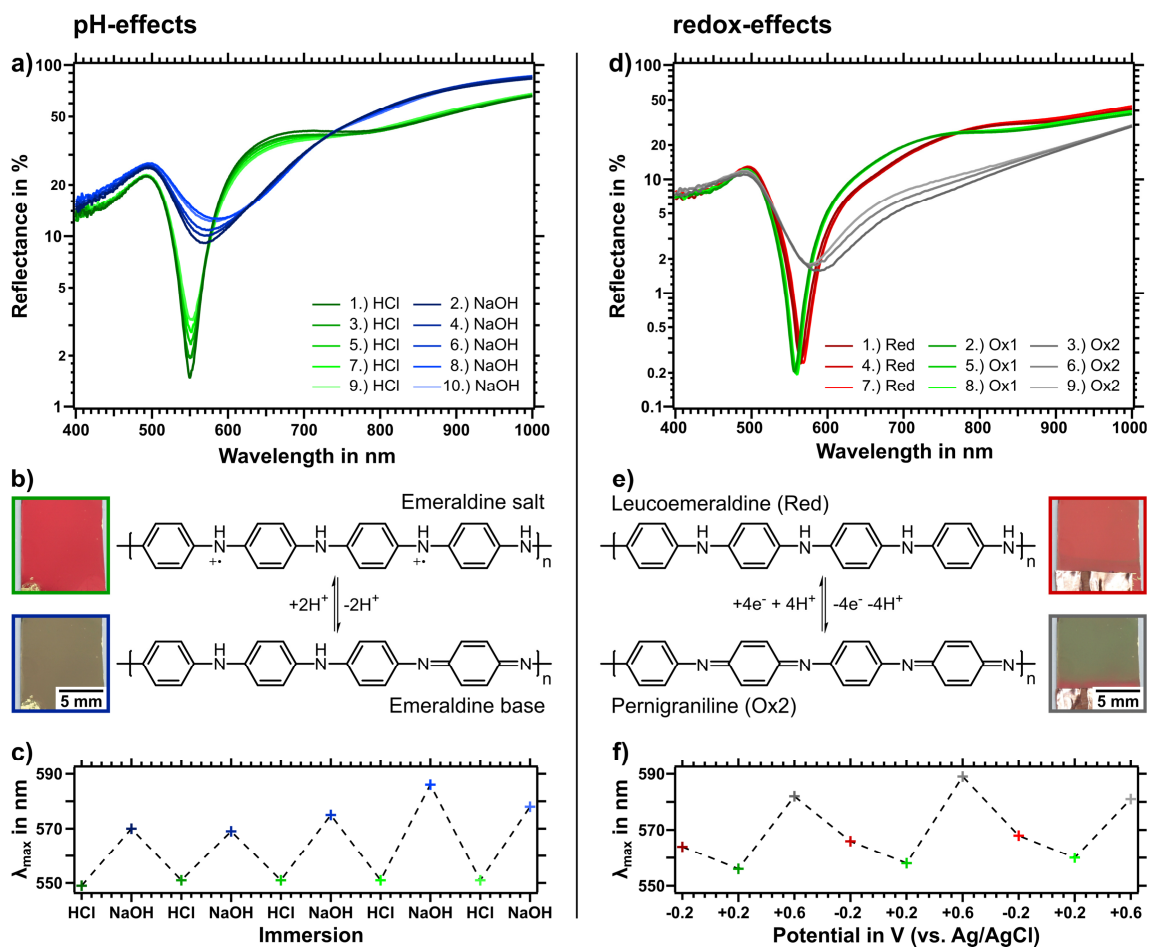


Figure 44. pH- and redox-dependent optical properties of the metasurface. a) Reflectance spectra of the surface after immersion into acidic (green) or basic (blue) solution. b) Structural formula of the protonated form (emeraldine salt) and deprotonated form (emeraldine base) of polyaniline together with respective photographs of the sample. c) Maximum peak positions of the reflectance spectra after immersion in HCl or NaOH for multiple cycles with dashed lines as a guide to the eye. d) Reflectance spectra of the tunable metasurface, after applying a reducing potential (red, -0.2 V vs. Ag/AgCl), an oxidizing potential (green, $+0.2$ V), and a strong oxidizing potential (blue, $+0.6$ V). e) Structural formula of the fully reduced leucoemeraldine base and the fully oxidized pernigraniline base forms of polyaniline, together with respective photographs of the sample. f) Maximum peak positions of the reflectance spectra after applying reducing (-0.2 V) or oxidizing ($+0.6$ V) potentials with dashed lines as guide to the eye.

Polyaniline is known to exhibit strongly potential-dependent optical spectra.^[27] In general, three states are distinguished, each featuring a protonated (salt) and a deprotonated (base) state.^[269] In the cyclic voltammetry data shown in Appendix 28, two oxidation peaks can be observed at $+0.05$ V and $+0.60$ V vs Ag/AgCl. The three different regions are attributed to the oxidation states Leucoemeraldine (here denoted as ‘Red’), Emeraldine (‘Ox1’) and Pernigraniline (‘Ox2’). The respective structural formulas are displayed in Figure 44b/e.

When the oxidation state is changed, the optical properties of the polymer are also altered. This can be observed in the reflectance spectra shown in Figure 44d. For this sample, the red curves (reduced state) exhibit a reflectance minimum of 0.25% at around 565 nm. When oxidized, the peak is blue-shifted by 10 nm after the first oxidation step (Ox1, green curves) and the reflectance slightly decreases to 0.15%. After the second

oxidation step, the reflectance is increased by a factor of 10 (to 1.5%) and it is further red-shifted by about 30 nm with respect to Ox1. At the same time, the full width half maximum (FWHM) is doubled and the peak features a pronounced shoulder at longer wavelengths. This results in visible changes to the optical appearance of the metasurface, as can be seen in the photographs in Figure 44e. The induced changes are again reversible, with only minor variations between each cycle. With regard to the performance as an anti-reflective coating, the attenuation of the reflected light is most efficient when the film is in the emeraldine salt state (Ox1), which corresponds to the as-synthesized state.

Based on the interference-related explanation of the extraordinarily low reflectance, it is assumed that the number of particles per area has a major impact on the efficiency of the metasurface. More precisely, the coverage determines the ratio of light which is directly reflected by the mirror (II) or which interacts with the particle (III and IV). Thus, an optimum (minimum reflection) is expected at a certain coverage, which is not necessarily the close-packed state.^[233] To target that coverage, optical simulation with systematic variation of the inter-particle distance d were conducted (see Appendix 29). The resulting reflectance minima with untreated PANI are displayed in Figure 45a. A global minimum is observed in this dataset: From that point, either reducing or increasing the separation leads to a less pronounced reflectance minimum. Thus, superposition of phase-shifted light evokes the most efficient, destructive interference at a particle distance of about 190 nm. This is also accounted by the deep red color in the CIE space (see Figure 45b).

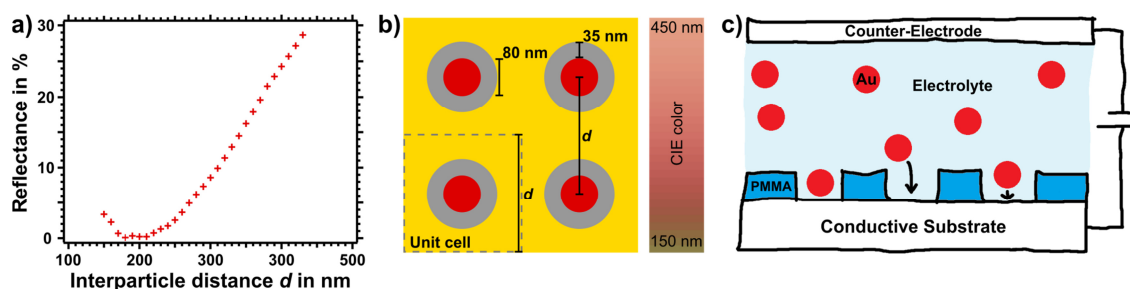


Figure 45. Optical simulations and particle assembly. a) Reflectance minima (red crosses) as a function of the particle separation, obtained from COMSOL simulations. b) Schematic depiction of the set-up used in the optical simulations showing the inter-particle distance D , the diameter of the particles (80 nm), the PANI shell thickness (35 nm), and the respective unit cell. Right: CIE color from the obtained spectra as a function of D (illuminated by standard D65 illumination). c) Schematic illustration of the electrophoretic particle deposition (EPD) system with gold nanoparticles on a substrate that has been nanostructured with poly(methyl methacrylate) (PMMA).

To achieve precise control of the inter-particle distance, which is necessary for optimal performance of the anti-reflective metasurface, electrophoretic particle deposition (EPD) was utilized as a route to receive well-defined nanoparticle assemblies.^[194] The mechanism displayed in Figure 45c employs the electrophoretic force between a nanostructured conductive substrate and a counter-electrode. The Au-PANI particles are attracted towards the exposed areas of the substrate. As a proof of concept, a positive

potential was applied to a nanostructured ITO substrate (see Appendix 30 for details). Due to the negative surface charge of the colloids (ζ -potential of -54 ± 7 mV), the particles were deposited in the cavities of the substrate. This resulted in assembly of Au-PANI particles in a square lattice as seen in the dark field micrograph in Appendix 30. For future work, utilization of nanostructured gold substrates (or other reflective surfaces) with small separation distances in the order of a few hundred nanometers will lead to significant improvements. This facile method enables the preparation of tunable metasurfaces with precise control of the inter-particle separation and thereby optimization of anti-reflective properties.

Conclusion

An *active* anti-reflective plasmonic metasurface was demonstrated. The wavelength at which anti-reflection occurs can increase by up to 30 nm as a result of an applied electric potential or a change in the pH of a surrounding solution. These spectral shifts were accompanied by an almost 10-fold modulation of the reflectance of the metasurface. The observed phenomena were interpreted with the aid of finite-element simulations and a simple interference description that accounts for the interaction of the metasurface with light. These metasurfaces were constructed with a redox-sensitive polymer (PANI) which enables further studies of photo-induced charge separation in plasmonic systems: a field of study with great potential for applications in photonic energy conversion, such as photocatalysis.

Experimental Section

Materials. All chemicals were used as received: cetyltrimethylammonium chloride (25 wt%, Sigma Aldrich), cetyltrimethylammonium bromide (CTAB, $\geq 99.9\%$, Merck), cetyltrimethylammonium chloride (CTAC, 25% in H₂O), sodium dodecyl sulfate (SDS, 99%, Fluka), aniline ($\geq 99.9\%$, Sigma Aldrich), hydrochloric acid (37%, VWR), ammonium persulfate (APS, $\geq 98\%$, Sigma Aldrich), Polyethylene imine (PEI, $M_w \sim 25000$, Aldrich). Water was purified with a Milli-Q system (Millipore), resulting in a resistivity of 18.2 M Ω cm.

Particle synthesis. Spherical Au particles were synthesized as described elsewhere.^[200] The resulting CTAC-coated particles had a diameter of 83.7 ± 2.8 nm. The product was purified by centrifugation at 400 rcf for 25 min and redispersing in 1.1 mM CTAB three times. The particle concentration was adjusted to 0.5-1.0 mg/mL in the last step. The aniline coating process was adapted from Jeon *et al.*^[28,264] Here, 1000 μ L Au particle dispersion, 4050 μ L H₂O, 600 mL Aniline (10 mM in H₂O), 500 μ L SDS (40 mM in H₂O) and 30 μ L HCl (1 M) were added to a 10 mL glass vial with a 20×7 mm² cylindrical stirring bar. The polymerization was initiated by adding 750 μ L APS (13.33 mM in H₂O) under vigorous stirring. The stirring speed was reduced to 130 rpm after 1 hour and the mixture was allowed to react for 24 hours. The product was centrifuged at 400 rcf for 40 minutes. The green supernatant was discarded and the purification was repeated 3 times after dispersing in 5 mM SDS.

Substrate preparation. Silicon wafers (p-type, Siebert Wafer, Germany) were coated with 200 nm Au by physical vapor deposition in a BA510 system (Balzers, Lichtenstein). Bulk gold is melted by an electron beam. Vapor deposition takes place at 10^{-6} mbar on silicon wafers placed 30 cm above the crucible. The deposition rate was adjusted to 1 nm/s measured by a quartz oscillator. The wafer was cut into pieces of 1.5×1.5 cm² and cleaned from silicon particles in a nitrogen stream. These substrates were hydrophilized by plasma cleaning (plasma technology GmbH, Germany) in 0.2 mbar air plasma for 5 minutes at 80 W. Subsequently, the freshly activated surfaces were immersed into PEI for at least 24 h. For each coating, 250 μ L of Au-PANI particles (0.5-0.25 mg/mL, 5 mM SDS) were diluted with 1000 μ L water and centrifuged at 400 rcf for 25 min. 1200 μ L of the supernatant were discarded and the pellet was redispersed in 2 mL water. The gold substrate was removed from the PEI solution, gently rinsed with water, dried in a nitrogen stream and directly immersed into the particle dispersion in a 15 mL centrifuge tube. The tube was stored in a tilted position (substrate angle $\sim 30^\circ$) for at least 48 h. After sedimentation of Au-PANI particles, the samples were removed from the dispersion, dipped in a water bath to remove excess particles, and dried in a nitrogen stream. Reference samples for determination of the optical properties of PANI were prepared by immersion of the gold-coated wafers in the reaction mixture for polymerization (see particle synthesis) but without adding gold nanoparticles.

Characterization. Reflectance spectra were collected with a Cary 5000 spectrophotometer (Agilent, USA) equipped with a universal measurement accessory (UMA). Spectra were measured in a wavelength range from 350 nm - 1400 nm with a sample angle between 5° and 85° in steps of 5°. All spectra were normalized to their respective substrates (gold or silicon). Reflectance spectra with values <1% were smoothed with a binomial smooth algorithm.

Acknowledgements

This work was supported by the 'Bayreuth-Melbourne Colloid/Polymer Network' with funding from the German Academic Exchange Service 'DAAD'. The authors acknowledge the Cluster of Excellence Center for Advancing Electronics Dresden (cfaed). The authors thank Anja Steiner for providing gold nanoparticles and Inga Melnyk for conducting SEM measurements. Y.B. acknowledges support through elite study program Macromolecular Science by Elitenetzwerk Bayern and the University of Bayreuth. C.N. is supported by the Alexander von Humboldt Foundation as a Postdoctoral Fellow. P.M. thanks the ARC for support through grant CE170100026. D.G. acknowledges the ARC for support *via* a Future Fellowship grant FT140100514.

VII Perspective: Mechano-Tunable Plasmonic Lattices

The results presented in this chapter are partially based on collaborations with the groups of Prof. Matthias Karg (Universität Düsseldorf) and Dr. Tobias König (IPF Dresden). Preparation of samples for structural investigation, embedding of hexagonally packed lattices in elastomers, and the displayed measurements were performed by me. Hexagonal gold nanoparticle assemblies that exhibit surface lattice resonances were prepared by Ekaterina Ponomareva (Karg group) while square lattices were prepared by Vaibhav Gupta (König group).

Introduction

Nanoparticles featuring localized surface plasmon resonances (LSPRs) are applied in the fields of photonics, sensing, and catalysis, because they exhibit strong optical absorption and localized enhancement of electromagnetic fields. However, they suffer from broad bandwidths due to resonance damping. This issue can be overcome by arranging plasmonic particles into lattices. Coupling of localized resonances with diffractive modes leads to surface lattice resonances (SLRs) that feature strong absorbance and narrow spectral linewidths due to low losses and long lifetimes.^[270] Plasmonic lattices are commonly prepared by lithographic methods like e-beam lithography (EBL).^[138] However, less complex and more cost-efficient methods are available *via* colloidal self-assembly.^[139,173] Providing sufficient inter-particle spacing is a major concern in colloidal approaches since the resonance wavelength is linked to the Bragg condition ($\lambda \sim n \cdot p$).^[271] A convenient approach is given by using core-shell particles to adjust the periodicity directly. Au-PNIPAM particles are utilized to form hexagonally packed lattices *via* interface-mediated assembly and can be transferred to solid substrates. To match the Bragg mode with the LSPR, the periodicity can be altered by the shell thickness and by the dwell time during the assembly process.^[172]

In situ tunability is a common request for optical devices, which can be complied by making the periodicity of plasmonic lattices adjustable. To achieve this, transparent elastomer substrates can be applied, as reported by Odom and coworkers.^[272] They proved tuning of the SLR position by applying uniaxial strain to a square lattice of lithographically prepared gold nanocylinders. In this chapter, the capabilities of hexagonal gold nanoparticle lattices, prepared *via* colloidal self-assembly, are examined. The arrays could be attached to the interface of polydimethylsiloxane (PDMS) slabs or embedded within the transparent material. This approach may allow for surface sensing of catalytic reactions on the one hand and enables strain sensing on the other hand. A special focus is on the underlying geometric peculiarities of the hexagonal symmetry and the resulting SLR behavior under uniaxial strain.

Preliminary Results and Discussion

Mechano-tunable gold nanoparticle lattices were prepared by embedding of hexagonally packed gold spheres in PDMS. The preparation is visualized in **Figure 46**. Au-PNIPAM particles were floated at the air/water interface by applying the particles from an ethanol-water mixture to a water bath. Evaporation of ethanol led to rapid formation of hexagonally packed layer as displayed in Figure 46b. The layers could be transferred by using solid substrates. Due to a strong adhesion between the PNIPAM shell and the applied polystyrene substrates, the shell had to be removed for transferring the gold cores to elastomer substrates. Therefore, the samples were treated with oxygen plasma, which led to decomposition of the PNIPAM shell as shown in Appendix 31. The gold cores could be embedded in PDMS by allowing the precursor mixture to harden on top of the coverslips. After peel-off, matching of the refractive index was achieved by adding a second layer of PDMS. This resulted in homogeneous embedding of gold particles in a transparent elastomer matrix, as displayed in Figure 46c.

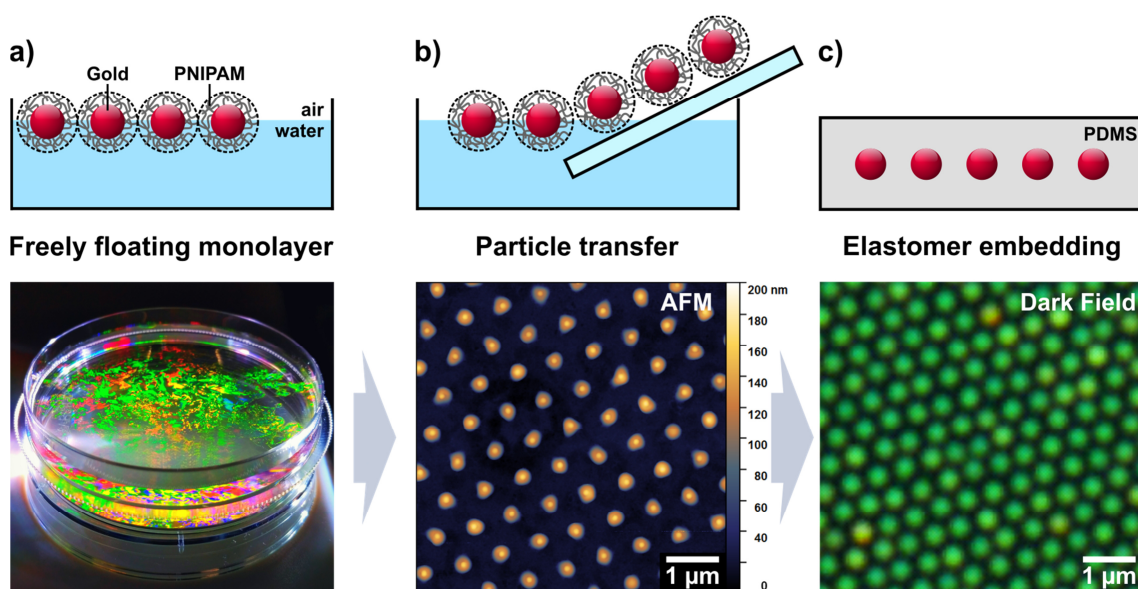


Figure 46. Preparation of mechano-tunable plasmonic lattices. a) Schematic depiction and photograph of the assembly of Au-PNIPAM particles at the air-water interface. b) Illustration of the monolayer transfer on a glass slide with a respective AFM image of the monolayer. c) Schematic depiction of particles embedded in PDMS and a respective dark field micrograph.

To study the structural behavior of embedded gold particles under strain, dark field microscopy was conducted for samples with large inter-particle spacings. Two extreme cases were investigated: one where the lattice's symmetry axis is parallel to the strain direction and another where these are perpendicular to each other. As can be observed in **Figure 47**, the gold particles nicely follow the strain field. Namely, the inter-particle distances increase homogeneously along the strain direction, while a perpendicular contraction is observed. This results in the formation of a rhombic lattice with either a compressed or an elongated unit cell (compare top row *versus* bottom row). The preservation of a defined lattice geometry is supported by the clear signals in the fast

Fourier transform (FFT). A particularly interesting case is represented by the parallel orientation at 40% strain (see Figure 47c, top row). The initial hexagonal lattice is transformed into a square lattice, which is calculated to occur at 39.2% strain for PDMS (Poisson's ratio $\nu \approx 0.5$, see Appendix 32).^[199]

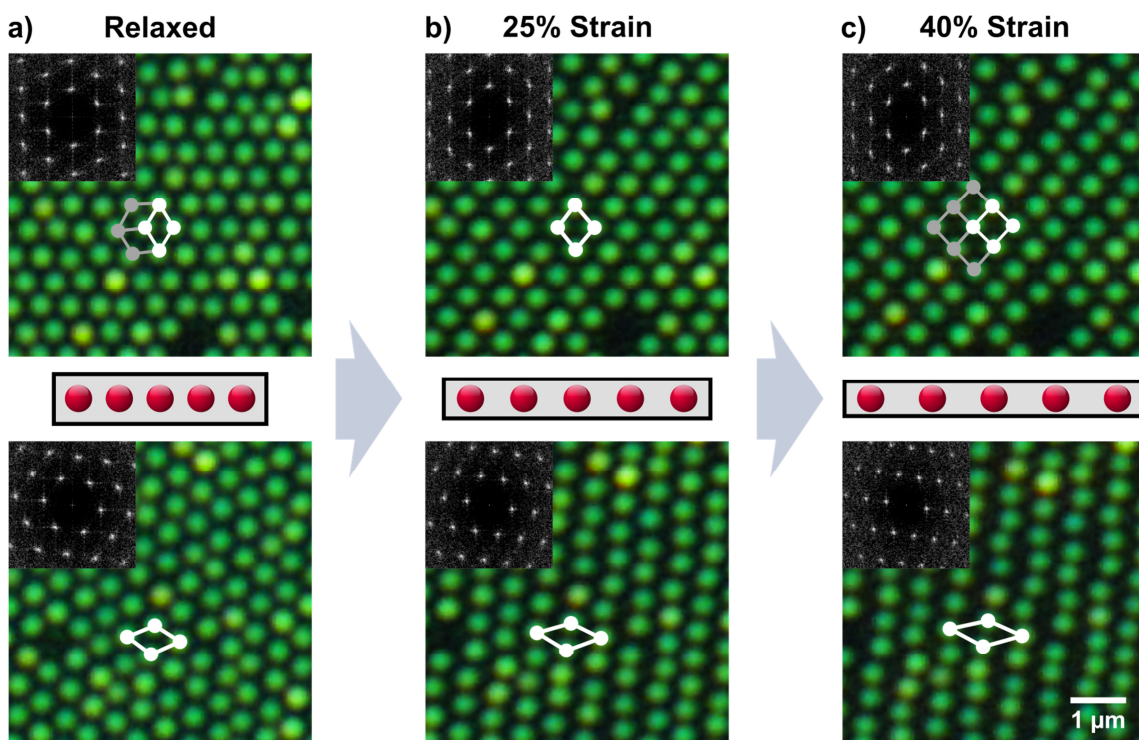


Figure 47. Stretching behavior of a gold nanoparticle lattice embedded in PDMS. Dark field micrographs of a hexagonal gold nanoparticle lattice a) in the relaxed state, b) at 25% strain, and c) at 40% strain. The top row corresponds to a lattice symmetry axis parallel to the strain direction while the bottom row features a symmetry axis almost perpendicular to the strain direction. Insets show the respective fast Fourier transform (FFT) of the images.

In consequence of the stretching, the inter-planar distances d change (where d is the 2D-analogue the distance between two lattice planes, see Figure 48), and thus, the Bragg condition is altered. In contrast to square lattices, where only two distances have to be taken into account, three different distance vectors need to be considered for hexagonal lattices under strain. Thus, a splitting into three SLR signals is expected. More specifically, this is valid if the lattice is oriented neither parallel nor perpendicular to the strain direction, as depicted in Figure 48a. Here, the deformation of a 15° tilted hexagonal lattice is displayed, which transforms into an oblique lattice upon stretching. The corresponding absorbance spectrum of the gold nanoparticle lattice with 516 ± 45 nm spacing (arranged *via* CAPA) exhibits a pronounced SLR at about 645 nm without strain. After stretching by 20%, the peak splits into three equally less pronounced signals, whereat one stays at the same location (D_1), another shifts to 620 nm (D_2), and the third shifts to 700 nm (D_3). These changes could be explained by the different inter-planar distances shown in the schematic. d_1 stays constant while d_2 decreases and d_3 increases, which entails the according changes to the SLR peak positions. This behavior could be

interpreted as superposition of the resonances, which initially represent a degenerate mode ($D_1+D_2+D_3$). The annulment of the degeneracy *via* stretching evokes splitting into three individual resonances featuring an apparent decrease of the signal intensity. Further strain results in shifting of the longer wavelength peak out of the measurement range while the shorter wavelength peak red-shifts linearly. A similar behavior can be observed for square lattices as well (see Figure 48b). The PDMS-embedded gold nanoparticles (arranged *via* interface-mediated assembly) with 440 nm spacing exhibit a SLR peak at about 660 nm, which splits into two distinct peaks upon stretching. The orientation of the lattice along the strain direction results in transition into a rectangular lattice, where d_1 is higher and d_2 is lower than the initial inter-planar distance. This gives rise to a linearly red-shifting resonance and a linearly blue-shifting resonance with increasing strain.

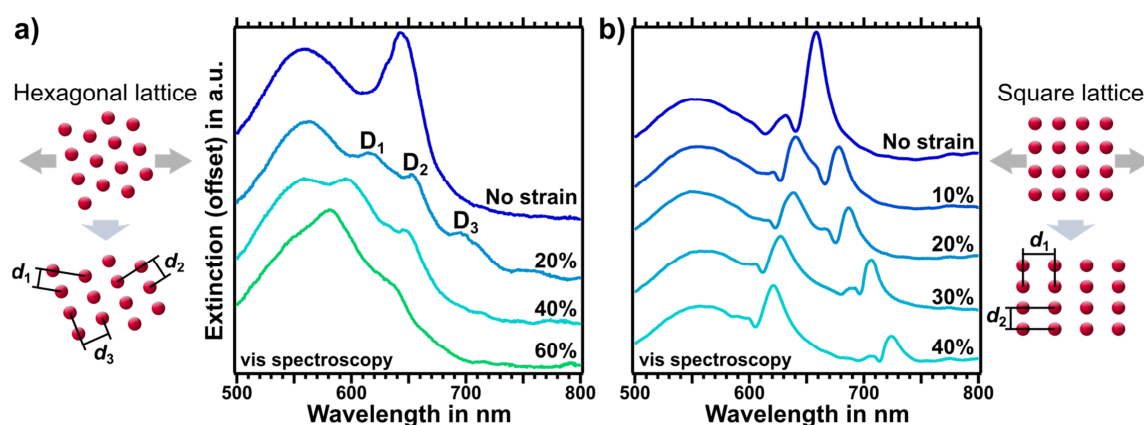


Figure 48. Optical transition of mechano-tunable plasmonic lattices under strain. a) Schematic depiction of the structural transition of a 15° tilted hexagonal lattice under uniaxial strain and respective vis-spectra at 0%, 20%, 40%, and 60% strain. b) Vis-spectra of a square lattice at 0%, 10%, 20%, 30%, and 40% and a corresponding schematic depiction of a square lattice under uniaxial strain. b) Adapted under the terms of the ACS AutorChoice usage agreement.^[139] Copyright 2019 by the American Chemical Society.

Conclusion

The introduced gold nanoparticle lattices feature SLRs that are characterized by narrow linewidths and high intensities. Tuning of the resonance position was achieved *via* mechanical deformation. As the optical response towards strain is linear, mechano-tunable plasmonic lattices could be applied as strain sensors over a broad range of deformation. A major benefit is provided by the microscopically detectable feedback, which enables even highly localized sensing. The combination with optical gain materials also facilitates the application for tunable lasing. Furthermore, the utilization of only partially embedded gold nanoparticles allows for application as chemical sensors. Catalytic reactions at the gold surface could be followed due to the local refractive index changes. For initially index-matched conditions, these changes would lead to a strong impact on the SLR. The resulting sensitivities are proposed to be superior to established plasmonic sensors due to the detection of more pronounced and narrow-band features.

„Der Mensch an sich selbst, insofern er sich seiner gesunden Sinne bedient,
ist der größte und genaueste physikalische Apparat, den es geben kann“

Johann Wolfgang Goethe

References

- [1] M. Loos, "Chapter 1 - Nanoscience and Nanotechnology", in *Carbon Nanotube Reinforced Composites*, William Andrew Publishing, Oxford, 2015.
- [2] H. Koinig, *Metallkeramik*, Verlag Neuer Merkur, 2003.
- [3] C. W. W. Ostwald, *Grundriss der kolloidchemie*, Steinkopf Verlag, 1909.
- [4] S. Kinoshita, S. Yoshioka, J. Miyazaki, *Reports on Progress in Physics* 2008, 71, 076401.
- [5] I. Newton, *Opticks: or, a treatise of the reflexions, refractions, inflexions and colours of light*, Royal Society of London, 1704.
- [6] B. Jirgensons, M. Straumanis, *Kurzes Lehrbuch der Kolloidchemie*, J.F. Bergmann-Verlag, 1949.
- [7] L. Rayleigh, *The London, Edinburgh, and Dublin Philosophical Magazine and Journal of Science* 1899, 47, 375.
- [8] G. Mie, *Annalen der Physik* 1908, 330, 377.
- [9] M. Faraday, *Philosophical Transactions of the Royal Society of London* 1857, 147, 145.
- [10] P. P. von Weimarn, *Zeitschrift für Chemie und Industrie der Kolloide* 1912, 11, 65.
- [11] Y. Sonnefraud, A. Leen Koh, D. W. McComb, S. A. Maier, *Laser & Photonics Reviews* 2012, 6, 277.
- [12] This image was originally posted to Flickr by optick at <https://www.flickr.com/photos/50206319@N00/112909824>. It was reviewed on 17 June 2010 by FlickreviewR and was confirmed to be licensed under the terms of the cc-by-sa-2.0.
- [13] C. Novo, A. M. Funston, P. Mulvaney, *Nature Nanotechnology* 2008, 3, 598.
- [14] H. A. Atwater, A. Polman, *Nature Materials* 2010, 9, 205.
- [15] K. Saha, S. S. Agasti, C. Kim, X. Li, V. M. Rotello, *Chemical Reviews* 2012, 112, 2739.
- [16] J. N. Anker, W. P. Hall, O. Lyandres, N. C. Shah, J. Zhao, R. P. Van Duyne, *Nature Materials* 2008, 7, 442.
- [17] Y. Yang, R. C. da Costa, M. J. Fuchter, A. J. Campbell, *Nature Photonics* 2013, 7, 634.
- [18] P. Mühlischlegel, H.-J. Eisler, O. J. F. Martin, B. Hecht, D. W. Pohl, *Science* 2005, 308, 1607.
- [19] N. Liu, H. Giessen, *Angewandte Chemie International Edition* 2010, 49, 9838.
- [20] W. Cai, V. Shalaev, *Optical Metamaterials: Fundamentals and Applications*, Springer New York, 2009.
- [21] D. R. Smith, W. J. Padilla, D. C. Vier, S. C. Nemat-Nasser, S. Schultz, *Physical Review Letters* 2000, 84, 4184.
- [22] N. Liu, M. Mesch, T. Weiss, M. Hentschel, H. Giessen, *Nano Letters* 2010, 10, 2342.
- [23] N. Liu, H. Guo, L. Fu, S. Kaiser, H. Schweizer, H. Giessen, *Nature Materials* 2008, 7, 31.
- [24] Q. Liang, T. Wang, Z. Lu, Q. Sun, Y. Fu, W. Yu, *Advanced Optical Materials* 2013, 1, 43.
- [25] J. A. Fan, C. Wu, K. Bao, J. Bao, R. Bardhan, N. J. Halas, V. N. Manoharan, P. Nordlander, G. Shvets, F. Capasso, *Science* 2010, 328, 1135.
- [26] M. A. Noginoy, G. Zhu, A. M. Belgrave, R. Bakker, V. M. Shalaev, E. E. Narimanov, S. Stout, E. Herz, T. Suteewong, U. Wiesner, *Nature* 2009, 460, 1110.

- [27] R. Contreras-Cáceres, A. Sánchez-Iglesias, M. Karg, I. Pastoriza-Santos, J. Pérez-Juste, J. Pacifico, T. Hellweg, A. Fernández-Barbero, L. M. Liz-Marzán, *Advanced Materials* **2008**, *20*, 1666.
- [28] J.-W. Jeon, P. A. Ledin, J. A. Geldmeier, J. F. Ponder, M. A. Mahmoud, M. El-Sayed, J. R. Reynolds, V. V. Tsukruk, *Chemistry of Materials* **2016**, *28*, 2868.
- [29] A. Pors, S. I. Bozhevolnyi, *Opt. Express* **2013**, *21*, 27438.
- [30] C. Cherqui, M. R. Bourgeois, D. Wang, G. C. Schatz, *Accounts of Chemical Research* **2019**, *52*, 2548.
- [31] D. Wang, A. Yang, A. J. Hryn, G. C. Schatz, T. W. Odom, *ACS Photonics* **2015**, *2*, 1789.
- [32] V. G. Kravets, F. Schedin, A. N. Grigorenko, *Physical Review Letters* **2008**, *101*, 087403.
- [33] F. Huang, J. J. Baumberg, *Nano Letters* **2010**, *10*, 1787.
- [34] D. Wang, W. Wang, M. P. Knudson, G. C. Schatz, T. W. Odom, *Chemical Reviews* **2018**, *118*, 2865.
- [35] V. G. Kravets, A. V. Kabashin, W. L. Barnes, A. N. Grigorenko, *Chemical Reviews* **2018**, *118*, 5912.
- [36] J. Schnepf Max, Y. Brasse, R. Goßler Fabian, M. Steiner Anja, J. Obermeier, M. Lippitz, A. Fery, A. F. König Tobias, *Zeitschrift für Physikalische Chemie* **2018**, *232*, 1593.
- [37] Y. Brasse, M. B. Müller, M. Karg, C. Kuttner, T. A. F. König, A. Fery, *ACS Applied Materials & Interfaces* **2018**, *10*, 3133.
- [38] Y. Brasse, C. Ng, M. Magnozzi, H. Zhang, P. Mulvaney, A. Fery, D. E. Gómez, *Macromolecular Rapid Communications* **2020**, *41*, 1900415.
- [39] T. Graham, *Philosophical Transactions of the Royal Society of London* **1861**, *151*, 183.
- [40] IUPAC. Compendium of Chemical Terminology, 2nd ed. (the "Gold Book"). Compiled by A. D. McNaught and A. Wilkinson. Blackwell Scientific Publications, Oxford (1997). Online version (2019-) created by S. J. Chalk. ISBN 0-9678550-9-8. <https://doi.org/10.1351/goldbook>.
- [41] H. Siedentopf, R. Zsigmondy, *Annalen der Physik* **1902**, *315*, 1.
- [42] R. Brown, *The Philosophical Magazine* **1828**, *4*, 161.
- [43] J. Keddie, A. F. Routh, *Fundamentals of Latex Film Formation: Processes and Properties*, Springer Netherlands, **2010**.
- [44] B. Derjaguin, L. Landau, *Progress in Surface Science* **1993**, *43*, 30.
- [45] E. J. W. Verwey, J. T. G. Overbeek, *Journal of Colloid Science* **1955**, *10*, 224
- [46] H. J. Butt, K. Graf, M. Kappl, *Physics and Chemistry of Interfaces*, Wiley, **2013**.
- [47] J. N. Israelachvili, "11 - Contrasts between Intermolecular, Interparticle, and Intersurface Forces", in *Intermolecular and Surface Forces (Third Edition)*, Academic Press, San Diego, **2011**.
- [48] S. Bhattacharjee, *Journal of Controlled Release* **2016**, *235*, 337.
- [49] L. L. Schramm, *Emulsions, Foams, and Suspensions: Fundamentals and Applications*, Wiley, **2006**.
- [50] J. Lyklema, *Fundamentals of Interface and Colloid Science: Solid-Liquid Interfaces*, Elsevier Science, **1995**.
- [51] J. Turkevich, P. C. Stevenson, J. Hillier, *Discussions of the Faraday Society* **1951**, *11*, 55.
- [52] P. J. Flory, *The Journal of Chemical Physics* **1941**, *9*, 660.
- [53] M. L. Huggins, *The Journal of Chemical Physics* **1941**, *9*, 440.

- [54] R. A. Orwoll, P. A. Arnold, "Polymer-Solvent Interaction Parameter χ ", in *Physical Properties of Polymers Handbook*, Springer New York, New York, NY, **2007**.
- [55] R. H. Pelton, P. Chibante, *Colloids and Surfaces* **1986**, *20*, 247.
- [56] S. Schmidt, H. Motschmann, T. Hellweg, R. von Klitzing, *Polymer* **2008**, *49*, 749.
- [57] A. B. R. Mayer, J. E. Mark, *Journal of Macromolecular Science, Part A* **1997**, *34*, 2151.
- [58] W.-S. Huang, B. D. Humphrey, A. G. MacDiarmid, *Journal of the Chemical Society, Faraday Transactions 1: Physical Chemistry in Condensed Phases* **1986**, *82*, 2385.
- [59] A. Trügler, *Optical Properties of Metallic Nanoparticles: Basic Principles and Simulation*, Springer International Publishing, **2016**.
- [60] "Chapter 16 - Nanoeffects in Ancient Technology and Art and in Space", in *Fundamentals and Applications of Nano Silicon in Plasmonics and Fullerenes*, Elsevier, **2018**.
- [61] The Lycurgus Cup 1958,1202.1, AN106680001 https://research.britishmuseum.org/collectionimages/AN01066/AN01066800_001_l.jpg, Accessed on 03.12.2019.
- [62] The Lycurgus Cup, 1958,1202.1, AN1066672001 https://research.britishmuseum.org/collectionimages/AN01066/AN01066672_001_l.jpg, Accessed on 03.12.2019.
- [63] J. C. M. Garnett, J. Larmor, *Philosophical Transactions of the Royal Society of London. Series A, Containing Papers of a Mathematical or Physical Character* **1904**, *203*, 385.
- [64] F. Ehrenhaft, *Annalen der Physik* **1903**, *316*, 489.
- [65] P. Drude, *Annalen der Physik* **1900**, *306*, 566.
- [66] K. A. Willets, R. P. V. Duyne, *Annual Review of Physical Chemistry* **2007**, *58*, 267.
- [67] S. Link, M. A. El-Sayed, *The Journal of Physical Chemistry B* **1999**, *103*, 4212.
- [68] Sönnichsen, C. (2001). *Plasmons in metal nanostructures* (Dissertation, Physik). Ludwig-Maximilians-Universität München.
- [69] E. J. Zeman, G. C. Schatz, *The Journal of Physical Chemistry* **1987**, *91*, 634.
- [70] W. L. Barnes, A. Dereux, T. W. Ebbesen, *Nature* **2003**, *424*, 824.
- [71] A. J. Haes, L. Chang, W. L. Klein, R. P. Van Duyne, *Journal of the American Chemical Society* **2005**, *127*, 2264.
- [72] U. Kreibig, M. Vollmer, *Optical Properties of Metal Clusters*, Springer Berlin Heidelberg, **2013**.
- [73] W. A. Murray, W. L. Barnes, *Advanced Materials* **2007**, *19*, 3771.
- [74] C. J. Murphy, A. M. Gole, S. E. Hunyadi, C. J. Orendorff, *Inorganic Chemistry* **2006**, *45*, 7544.
- [75] X. Ye, C. Zheng, J. Chen, Y. Gao, C. B. Murray, *Nano Letters* **2013**, *13*, 765.
- [76] J. J. Mock, M. Barbic, D. R. Smith, D. A. Schultz, S. Schultz, *The Journal of Chemical Physics* **2002**, *116*, 6755.
- [77] E. Galati, M. Tebbe, A. Querejeta-Fernández, H. L. Xin, O. Gang, E. B. Zhulina, E. Kumacheva, *ACS Nano* **2017**, *11*, 4995.
- [78] A. M. Steiner, M. Mayer, D. Schletz, D. Wolf, P. Formanek, R. Hübner, M. Dulle, S. Förster, T. A. F. König, A. Fery, *Chemistry of Materials* **2019**, *31*, 2822.
- [79] I. Newton, *Philosophical Transactions of the Royal Society of London* **1671**, *6*, 3075.
- [80] N. V. Tkachenko, *Optical Spectroscopy: Methods and Instrumentations*, Elsevier Science, **2006**.
- [81] O. Loebich, *Gold Bulletin* **1972**, *5*, 2.

- [82] L. Scarabelli, A. Sánchez-Iglesias, J. Pérez-Juste, L. M. Liz-Marzán, *The Journal of Physical Chemistry Letters* **2015**, *6*, 4270.
- [83] Finder, C. (2005). *Optische Beobachtung von oberflächengebundenen und frei beweglichen Nanopartikeln* (Dissertation, Physikalische Chemie). Universität Duisburg-Essen.
- [84] M. W. Davidson, M. Abramowitz, "Optical Microscopy", in *Encyclopedia of Imaging Science and Technology*, Wiley VCH, **2002**.
- [85] E. Abbe, *Archiv für Mikroskopische Anatomie* **1873**, *9*, 413.
- [86] L. de Broglie, *Foundations of Physics* **1970**, *1*, 5.
- [87] C. Davisson, L. H. Germer, *Physical Review* **1927**, *30*, 705.
- [88] "Transmission Electron Microscopy: Fundamentals of Methods and Instrumentation", in *Electron Microscopy of Polymers*, Springer Berlin Heidelberg, Berlin, Heidelberg, **2008**.
- [89] L. De Broglie, *Nature* **1923**, *112*, 540.
- [90] E. H. Wichmann, *Quantenphysik*, Vieweg+Teubner Verlag, **2013**.
- [91] G. H. Michler, *Electron Microscopy of Polymers*, Springer Berlin Heidelberg, **2008**.
- [92] D. B. Williams, C. B. Carter, *Transmission Electron Microscopy: A Textbook for Materials Science*, Springer, **2009**.
- [93] G. Binnig, C. F. Quate, C. Gerber, *Physical Review Letters* **1986**, *56*, 930.
- [94] J. N. Israelachvili, "6 - Van der Waals Forces", in *Intermolecular and Surface Forces (Third Edition)*, Academic Press, San Diego, **2011**.
- [95] A. Banerjea, J. R. Smith, J. Ferrante, *Journal of Physics: Condensed Matter* **1990**, *2*, 8841.
- [96] H.-J. Butt, B. Cappella, M. Kappl, *Surface Science Reports* **2005**, *59*, 1.
- [97] H. Takano, J. R. Kenseth, S.-S. Wong, J. C. O'Brien, M. D. Porter, *Chemical Reviews* **1999**, *99*, 2845.
- [98] N. Jalili, K. Laxminarayana, *Mechatronics* **2004**, *14*, 907.
- [99] B. J. Berne, R. Pecora, *Dynamic Light Scattering: With Applications to Chemistry, Biology, and Physics*, Dover Publications, **2000**.
- [100] B. Saha, J. Mukhopadhyay, R. Johnson, *Particulate Science and Technology* **2012**, *30*.
- [101] S. W. Provencher, *Computer Physics Communications* **1982**, *27*, 229.
- [102] J. Stetefeld, S. A. McKenna, T. R. Patel, *Biophysical Reviews* **2016**, *8*, 409.
- [103] P. Nordlander, C. Oubre, E. Prodan, K. Li, M. I. Stockman, *Nano Letters* **2004**, *4*, 899.
- [104] P. K. Jain, W. Huang, M. A. El-Sayed, *Nano Letters* **2007**, *7*, 2080.
- [105] V. Myroshnychenko, J. Rodriguez-Fernandez, I. Pastoriza-Santos, A. M. Funston, C. Novo, P. Mulvaney, L. M. Liz-Marzán, F. J. Garcia de Abajo, *Chemical Society Reviews* **2008**, *37*, 1792.
- [106] L. Gunnarsson, T. Rindzevicius, J. Prikulis, B. Kasemo, M. Käll, S. Zou, G. C. Schatz, *The Journal of Physical Chemistry B* **2005**, *109*, 1079.
- [107] S. J. Barrow, A. M. Funston, D. E. Gómez, T. J. Davis, P. Mulvaney, *Nano Letters* **2011**, *11*, 4180.
- [108] C. Hanske, M. Tebbe, C. Kuttner, V. Bieber, V. V. Tsukruk, M. Chanana, T. A. F. König, A. Fery, *Nano Letters* **2014**, *14*, 6863.
- [109] M. Mayer, P. L. Potapov, D. Pohl, A. M. Steiner, J. Schultz, B. Rellinghaus, A. Lubk, T. A. F. König, A. Fery, *Nano Letters* **2019**, *19*, 3854.
- [110] H. Chen, T. Ming, S. Zhang, Z. Jin, B. Yang, J. Wang, *ACS Nano* **2011**, *5*, 4865.
- [111] H. Chen, L. Shao, T. Ming, K. C. Woo, Y. C. Man, J. Wang, H.-Q. Lin, *ACS Nano* **2011**, *5*, 6754.

- [112] D. R. Smith, J. B. Pendry, M. C. K. Wiltshire, *Science* **2004**, *305*, 788.
- [113] R. Chikkaraddy, B. de Nijs, F. Benz, S. J. Barrow, O. A. Scherman, E. Rosta, A. Demetriadou, P. Fox, O. Hess, J. J. Baumberg, *Nature* **2016**, *535*, 127.
- [114] G. M. Akselrod, J. Huang, T. B. Hoang, P. T. Bowen, L. Su, D. R. Smith, M. H. Mikkelsen, *Advanced Materials* **2015**, *27*, 8028.
- [115] N. I. Landy, S. Sajuyigbe, J. J. Mock, D. R. Smith, W. J. Padilla, *Physical Review Letters* **2008**, *100*, 207402.
- [116] M. K. Hedayati, M. Javaherirahim, B. Mozooni, R. Abdelaziz, A. Tavassolizadeh, V. S. K. Chakravadhanula, V. Zaporozhchenko, T. Strunkus, F. Faupel, M. Elbahri, *Advanced Materials* **2011**, *23*, 5410.
- [117] F. Pourcin, C. A. Reynaud, M. Carlberg, J. L. Rouzo, D. Duché, J.-J. Simon, L. Escoubas, R.-M. Sauvage, G. Berginc, O. Margeat, J. Ackermann, *Langmuir* **2019**, *35*, 2179.
- [118] Q. Shi, T. U. Connell, Q. Xiao, A. S. R. Chesman, W. Cheng, A. Roberts, T. J. Davis, D. E. Gómez, *ACS Photonics* **2019**, *6*, 314.
- [119] B. A. Munk, *Frequency Selective Surfaces: Theory and Design*, Wiley, **2005**.
- [120] M. A. Kats, R. Blanchard, P. Genevet, F. Capasso, *Nature Materials* **2013**, *12*, 20.
- [121] J. Zhu, Z. Yu, G. F. Burkhard, C.-M. Hsu, S. T. Connor, Y. Xu, Q. Wang, M. McGehee, S. Fan, Y. Cui, *Nano Letters* **2009**, *9*, 279.
- [122] K. X. Wang, Z. Yu, V. Liu, Y. Cui, S. Fan, *Nano Letters* **2012**, *12*, 1616.
- [123] K. Mizuno, J. Ishii, H. Kishida, Y. Hayamizu, S. Yasuda, D. N. Futaba, M. Yumura, K. Hata, *Proceedings of the National Academy of Sciences* **2009**, *106*, 6044.
- [124] J. Lehman, A. Sanders, L. Hanssen, B. Wilthan, J. Zeng, C. Jensen, *Nano Letters* **2010**, *10*, 3261.
- [125] C. M. Watts, X. Liu, W. J. Padilla, *Advanced Materials* **2012**, *24*, OP98.
- [126] S. Shu, Z. Li, Y. Y. Li, *Opt. Express* **2013**, *21*, 25307.
- [127] T. U. Connell, G. O. Bonin, C. D. Easton, E. Della Gaspera, A. S. R. Chesman, T. J. Davis, D. E. Gómez, *ACS Applied Energy Materials* **2019**, *2*, 1155.
- [128] M. Yan, *Journal of Optics* **2013**, *15*, 025006.
- [129] H.-T. Chen, J. Zhou, J. F. O'Hara, F. Chen, A. K. Azad, A. J. Taylor, *Physical Review Letters* **2010**, *105*, 073901.
- [130] H.-T. Chen, *Opt. Express* **2012**, *20*, 7165.
- [131] W. Demtröder, *Experimentalphysik 2: Elektrizität und Optik*, Springer Berlin Heidelberg, **2008**.
- [132] S. K. Ghosh, T. Pal, *Chemical Reviews* **2007**, *107*, 4797.
- [133] B. Auguie, W. L. Barnes, *Physical Review Letters* **2008**, *101*, 143902.
- [134] S. Zou, N. Janel, G. C. Schatz, *The Journal of Chemical Physics* **2004**, *120*, 10871.
- [135] B. D. Thackray, P. A. Thomas, G. H. Auton, F. J. Rodriguez, O. P. Marshall, V. G. Kravets, A. N. Grigorenko, *Nano Letters* **2015**, *15*, 3519.
- [136] W. Wang, M. Ramezani, A. I. Väkeväinen, P. Törmä, J. G. Rivas, T. W. Odom, *Materials Today* **2018**, *21*, 303.
- [137] W. Zhou, M. Dridi, J. Y. Suh, C. H. Kim, D. T. Co, M. R. Wasielewski, G. C. Schatz, T. W. Odom, *Nature Nanotechnology* **2013**, *8*, 506.
- [138] A. D. Humphrey, W. L. Barnes, *Physical Review B* **2014**, *90*, 075404.
- [139] V. Gupta, P. T. Probst, F. R. Goßler, A. M. Steiner, J. Schubert, Y. Brasse, T. A. F. König, A. Fery, *ACS Applied Materials & Interfaces* **2019**, *11*, 28189.
- [140] M. Mayer, A. M. Steiner, F. Röder, P. Formanek, T. A. F. König, A. Fery, *Angewandte Chemie International Edition* **2017**, *56*, 15866.
- [141] Y. Chen, X. Xin, N. Zhang, Y.-J. Xu, *Particle & Particle Systems Characterization* **2017**, *34*, 1600357.

- [142] V. Canalejas-Tejero, S. Herranz, A. Bellingham, M. C. Moreno-Bondi, C. A. Barrios, *ACS Applied Materials & Interfaces* **2014**, *6*, 1005.
- [143] C. Hou, M. Zhang, T. Kasama, C. Engelbrekt, L. Zhang, H. Wang, Q. Chi, *Advanced Materials* **2016**, *28*, 4097.
- [144] P. Leroy, N. Devau, A. Revil, M. Bizi, *Journal of Colloid and Interface Science* **2013**, *410*, 81.
- [145] W. Stöber, A. Fink, E. Bohn, *Journal of Colloid and Interface Science* **1968**, *26*, 62.
- [146] W.-C. Wu, J. B. Tracy, *Chemistry of Materials* **2015**, *27*, 2888.
- [147] S. Wu, J. Kaiser, M. Drechsler, M. Ballauff, Y. Lu, *Colloid and Polymer Science* **2013**, *291*, 231.
- [148] American Chemical Society National Historic Chemical Landmarks. U.S. Synthetic Rubber Program., <http://www.acs.org/content/acs/en/education/whatischemistry/landmarks/syntheticrubber.html>, Accessed on 06.12.2019.
- [149] "Macromolecular Decoration of Nanoparticles for Guiding Self-Assembly in 2D and 3D", in *Macromolecular Self-assembly*.
- [150] Y. Kang, T. A. Taton, *Macromolecules* **2005**, *38*, 6115.
- [151] D. Li, Q. He, J. Li, *Advances in Colloid and Interface Science* **2009**, *149*, 28.
- [152] M. Karg, S. Jaber, T. Hellweg, P. Mulvaney, *Langmuir* **2011**, *27*, 820.
- [153] R. Contreras-Cáceres, I. Pastoriza-Santos, R. A. Alvarez-Puebla, J. Pérez-Juste, A. Fernández-Barbero, L. M. Liz-Marzán, *Chemistry - A European Journal* **2010**, *16*, 9462.
- [154] M. Antonietti, "Microgels", in *Encyclopedia of Materials: Science and Technology*, Elsevier, Oxford, **2001**.
- [155] S. Höfl, L. Zitzler, T. Hellweg, S. Herminghaus, F. Mugele, *Polymer* **2007**, *48*, 245.
- [156] I. Y. Sapurina, M. A. Shishov, "Oxidative Polymerization of Aniline: Molecular Synthesis of Polyaniline and the Formation of Supramolecular Structures", in *New Polymers for Special Applications*, Intech Open, **2012**.
- [157] N. Jiang, L. Shao, J. Wang, *Advanced Materials* **2014**, *26*, 3282.
- [158] L. Yong-yao, M. Dang, G. Ke-cheng, Z. Gui-ping, *Acta Physica Sinica (Overseas Edition)* **1993**, *2*, 816.
- [159] Y. Harima, R. Patil, K. Yamashita, N. Yamamoto, S. Ito, A. Kitani, *Chemical Physics Letters* **2001**, *345*, 239.
- [160] N. Vogel, M. Retsch, C.-A. Fustin, A. del Campo, U. Jonas, *Chemical Reviews* **2015**, *115*, 6265.
- [161] M. Grzelczak, J. Vermant, E. M. Furst, L. M. Liz-Marzán, *ACS Nano* **2010**, *4*, 3591.
- [162] J. N. Israelachvili, "Chapter 22 - Dynamic Biointeractions", in *Intermolecular and Surface Forces (Third Edition)*, Academic Press, San Diego, **2011**.
- [163] W. Ramsden, F. Gotch, *Proceedings of the Royal Society of London* **1904**, *72*, 156.
- [164] S. U. Pickering, *Journal of the Chemical Society, Transactions* **1907**, *91*, 2001.
- [165] P. Pieranski, *Physical Review Letters* **1980**, *45*, 569.
- [166] A. Böker, J. He, T. Emrick, T. P. Russell, *Soft Matter* **2007**, *3*, 1231.
- [167] L. Isa, K. Kumar, M. Müller, J. Grolig, M. Textor, E. Reimhult, *ACS Nano* **2010**, *4*, 5665.
- [168] S. M. Weekes, F. Y. Ogrin, W. A. Murray, P. S. Keatley, *Langmuir* **2007**, *23*, 1057.
- [169] K.-U. Fulda, B. Tieke, *Advanced Materials* **1994**, *6*, 288.
- [170] Z. Dai, Y. Li, G. Duan, L. Jia, W. Cai, *ACS Nano* **2012**, *6*, 6706.

- [171] N. Vogel, S. Goerres, K. Landfester, C. K. Weiss, *Macromolecular Chemistry and Physics* **2011**, *212*, 1719.
- [172] K. Volk, J. P. S. Fitzgerald, M. Retsch, M. Karg, *Advanced Materials* **2015**, *27*, 7332.
- [173] K. Volk, J. P. S. Fitzgerald, P. Ruckdeschel, M. Retsch, T. A. F. König, M. Karg, *Advanced Optical Materials* **2017**, 1600971.
- [174] Y. Yin, Y. Lu, B. Gates, Y. Xia, *Journal of the American Chemical Society* **2001**, *123*, 8718.
- [175] A. Burmistrova, R. von Klitzing, *Journal of Materials Chemistry* **2010**, *20*, 3502.
- [176] M. B. Müller, C. Kuttner, T. A. F. König, V. V. Tsukruk, S. Förster, M. Karg, A. Fery, *ACS Nano* **2014**, *8*, 9410.
- [177] V. Flauraud, M. Mastrangeli, G. D. Bernasconi, J. Butet, D. T. L. Alexander, E. Shahrabi, O. J. F. Martin, J. Brugger, *Nature Nanotechnology* **2016**, *12*, 73.
- [178] C. Hanske, G. González-Rubio, C. Hamon, P. Formentín, E. Modin, A. Chuvilin, A. Guerrero-Martínez, L. F. Marsal, L. M. Liz-Marzán, *The Journal of Physical Chemistry C* **2017**, *121*, 10899.
- [179] C. Lu, H. Möhwald, A. Fery, *Soft Matter* **2007**, *3*, 1530.
- [180] N. Bowden, W. T. S. Huck, K. E. Paul, G. M. Whitesides, *Applied Physics Letters* **1999**, *75*, 2557.
- [181] B. A. Glatz, A. Fery, *Soft Matter* **2019**, *15*, 65.
- [182] A. Schweikart, A. Fortini, A. Wittemann, M. Schmidt, A. Fery, *Soft Matter* **2010**, *6*, 5860.
- [183] M. Tebbe, S. Lentz, L. Guerrini, A. Fery, R. A. Alvarez-Puebla, N. Pazos-Perez, *Nanoscale* **2016**, *8*, 12702.
- [184] S. Ni, J. Leemann, I. Buttinoni, L. Isa, H. Wolf, *Science Advances* **2016**, *2*, e1501779.
- [185] E. Adachi, A. S. Dimitrov, K. Nagayama, *Langmuir* **1995**, *11*, 1057.
- [186] A. S. Dimitrov, K. Nagayama, *Langmuir* **1996**, *12*, 1303.
- [187] L. Malaquin, T. Kraus, H. Schmid, E. Delamarche, H. Wolf, *Langmuir* **2007**, *23*, 11513.
- [188] T. Kraus, L. Malaquin, H. Schmid, W. Riess, N. D. Spencer, H. Wolf, *Nature Nanotechnology* **2007**, *2*, 570.
- [189] T. Kraus, L. Malaquin, E. Delamarche, H. Schmid, N. D. Spencer, H. Wolf, *Advanced Materials* **2005**, *17*, 2438.
- [190] A. Rey, G. Billardon, E. Lörtscher, K. Moth-Poulsen, N. Stuhr-Hansen, H. Wolf, T. Bjørnholm, A. Stemmer, H. Riel, *Nanoscale* **2013**, *5*, 8680.
- [191] J.-H. Seo, J. H. Park, S.-I. Kim, B. J. Park, Z. Ma, J. Choi, B.-K. Ju, *Journal of Nanoscience and Nanotechnology* **2014**, *14*, 1521.
- [192] H. Zheng, M. F. Rubner, P. T. Hammond, *Langmuir* **2002**, *18*, 4505.
- [193] C. Kinnear, J. Cadusch, H. Zhang, J. Lu, T. D. James, A. Roberts, P. Mulvaney, *Langmuir* **2018**, *34*, 7355.
- [194] H. Zhang, J. Cadusch, C. Kinnear, T. James, A. Roberts, P. Mulvaney, *ACS Nano* **2018**, *12*, 7529.
- [195] S. P. Lacour, S. Wagner, Z. Huang, Z. Suo, *Applied Physics Letters* **2003**, *82*, 2404.
- [196] D. Meschede, C. Gerthsen, *Gerthsen Physik*, Springer Berlin Heidelberg, **2013**.
- [197] J. P. Coelho, M. J. Mayoral, L. Camacho, M. T. Martín-Romero, G. Tardajos, I. López-Montero, E. Sanz, D. Ávila-Brandé, J. J. Giner-Casares, G. Fernández, A. Guerrero-Martínez, *Journal of the American Chemical Society* **2017**, *139*, 1120.

- [198] U. Cataldi, R. Caputo, Y. Kurylyak, G. Klein, M. Chekini, C. Umeton, T. Bürgi, *Journal of Materials Chemistry C* **2014**, *2*, 7927.
- [199] I. D. Johnston, D. K. McCluskey, C. K. L. Tan, M. C. Tracey, *Journal of Micromechanics and Microengineering* **2014**, *24*, 035017.
- [200] A. M. Steiner, M. Mayer, M. Seuss, S. Nikolov, K. D. Harris, A. Alexeev, C. Kuttner, T. A. F. König, A. Fery, *ACS Nano* **2017**, *11*, 8871.
- [201] M. L. Tseng, J. Yang, M. Semmlinger, C. Zhang, P. Nordlander, N. J. Halas, *Nano Letters* **2017**, *17*, 6034.
- [202] D. Solis, B. Willingham, S. L. Nauert, L. S. Slaughter, J. Olson, P. Swanglap, A. Paul, W.-S. Chang, S. Link, *Nano Letters* **2012**, *12*, 1349.
- [203] S. J. Barrow, D. Rossouw, A. M. Funston, G. A. Botton, P. Mulvaney, *Nano Letters* **2014**, *14*, 3799.
- [204] S. A. Maier, P. G. Kik, H. A. Atwater, S. Meltzer, E. Harel, B. E. Koel, A. A. G. Requicha, *Nature Materials* **2003**, *2*, 229.
- [205] H. Wang, *Scientific Reports* **2018**, *8*, 9589.
- [206] A. Guerrero-Martínez, B. Auguie, J. L. Alonso-Gómez, Z. Džolić, S. Gómez-Graña, M. Žinić, M. M. Cid, L. M. Liz-Marzán, *Angewandte Chemie International Edition* **2011**, *50*, 5499.
- [207] Y. Kim, B. Yeom, O. Arteaga, S. Jo Yoo, S.-G. Lee, J.-G. Kim, N. A. Kotov, *Nature Materials* **2016**, *15*, 461.
- [208] W. J. Choi, G. Cheng, Z. Huang, S. Zhang, T. B. Norris, N. A. Kotov, *Nature Materials* **2019**, *18*, 820.
- [209] M. Kauranen, A. V. Zayats, *Nature Photonics* **2012**, *6*, 737.
- [210] K. J. Russell, T.-L. Liu, S. Cui, E. L. Hu, *Nature Photonics* **2012**, *6*, 459.
- [211] G. M. Akselrod, C. Argyropoulos, T. B. Hoang, C. Ciraci, C. Fang, J. Huang, D. R. Smith, M. H. Mikkelsen, *Nature Photonics* **2014**, *8*, 835.
- [212] P. Anger, P. Bharadwaj, L. Novotny, *Physical Review Letters* **2006**, *96*, 113002.
- [213] H. Li, C.-Y. Chen, X. Wei, W. Qiang, Z. Li, Q. Cheng, D. Xu, *Analytical Chemistry* **2012**, *84*, 8656.
- [214] Q.-C. Sun, H. Mundoor, J. C. Ribot, V. Singh, I. I. Smalyukh, P. Nagpal, *Nano Letters* **2014**, *14*, 101.
- [215] J. Zhang, Y. Fu, M. H. Chowdhury, J. R. Lakowicz, *Nano Letters* **2007**, *7*, 2101.
- [216] A. Bek, R. Jansen, M. Ringler, S. Mayilo, T. A. Klar, J. Feldmann, *Nano Letters* **2008**, *8*, 485.
- [217] K. Matsuzaki, S. Vassant, H.-W. Liu, A. Dutschke, B. Hoffmann, X. Chen, S. Christiansen, M. R. Buck, J. A. Hollingsworth, S. Götzinger, V. Sandoghdar, *Scientific Reports* **2017**, *7*, 42307.
- [218] R. Chikkaraddy, V. A. Turek, N. Kongsuwan, F. Benz, C. Carnegie, T. van de Goor, B. de Nijs, A. Demetriadou, O. Hess, U. F. Keyser, J. J. Baumberg, *Nano Letters* **2018**, *18*, 405.
- [219] M. Rycenga, C. M. Cobley, J. Zeng, W. Li, C. H. Moran, Q. Zhang, D. Qin, Y. Xia, *Chemical Reviews* **2011**, *111*, 3669.
- [220] C. Ciraci, R. T. Hill, J. J. Mock, Y. Urzhumov, A. I. Fernández-Domínguez, S. A. Maier, J. B. Pendry, A. Chilkoti, D. R. Smith, *Science* **2012**, *337*, 1072.
- [221] A. Rose, T. B. Hoang, F. McGuire, J. J. Mock, C. Ciraci, D. R. Smith, M. H. Mikkelsen, *Nano Letters* **2014**, *14*, 4797.
- [222] J. B. Lassiter, F. McGuire, J. J. Mock, C. Ciraci, R. T. Hill, B. J. Wiley, A. Chilkoti, D. R. Smith, *Nano Letters* **2013**, *13*, 5866.
- [223] G. Di Martino, S. Tappertzhofen, S. Hofmann, J. Baumberg, *Small* **2016**, *12*, 1334.
- [224] T. Soller, M. Ringler, M. Wunderlich, T. A. Klar, J. Feldmann, H. P. Josel, Y. Markert, A. Nichtl, K. Kürzinger, *Nano Letters* **2007**, *7*, 1941.

References

- [225] A. Raevskaya, V. Lesnyak, D. Haubold, V. Dzhagan, O. Stroyuk, N. Gaponik, D. R. T. Zahn, A. Eychmüller, *The Journal of Physical Chemistry C* **2017**, *121*, 9032.
- [226] M. Mayer, M. Tebbe, C. Kuttner, M. J. Schnepf, T. A. F. König, A. Fery, *Faraday Discussions* **2016**, *191*, 159.
- [227] A. Rauh, M. Rey, L. Barbera, M. Zanini, M. Karg, L. Isa, *Soft Matter* **2017**, *13*, 158.
- [228] W. Kern, *Journal of the Electrochemical Society* **1990**, *137*, 1887.
- [229] P. B. Johnson, R. W. Christy, *Physical Review B* **1972**, *6*, 4370.
- [230] C. Sönnichsen, B. M. Reinhard, J. Liphardt, A. P. Alivisatos, *Nature Biotechnology* **2005**, *23*, 741.
- [231] G. Lévêque, O. J. F. Martin, *Opt. Express* **2006**, *14*, 9971.
- [232] G. Dolling, C. Enkrich, M. Wegener, J. F. Zhou, C. M. Soukoulis, S. Linden, *Opt. Lett.* **2005**, *30*, 3198.
- [233] M. Karg, T. A. F. König, M. Retsch, C. Stelling, P. M. Reichstein, T. Honold, M. Thelakkat, A. Fery, *Materials Today* **2015**, *18*, 185.
- [234] A. G. Brolo, *Nature Photonics* **2012**, *6*, 709.
- [235] H. Wang, K. O’Dea, L. Wang, *Opt. Lett.* **2014**, *39*, 1457.
- [236] B. Dong, Y. Fang, X. Chen, H. Xu, M. Sun, *Langmuir* **2011**, *27*, 10677.
- [237] C. Ng, J. J. Cadusch, S. Dligatch, A. Roberts, T. J. Davis, P. Mulvaney, D. E. Gómez, *ACS Nano* **2016**, *10*, 4704.
- [238] T. Ding, A. W. Rudrum, L. O. Herrmann, V. Turek, J. J. Baumberg, *Nanoscale* **2016**, *8*, 15864.
- [239] T. Ding, C. Rüttiger, X. Zheng, F. Benz, H. Ohadi, G. A. E. Vandenbosch, V. V. Moshchalkov, M. Gallei, J. J. Baumberg, *Advanced Optical Materials* **2016**, *4*, 877.
- [240] T. Ding, V. K. Valev, A. R. Salmon, C. J. Forman, S. K. Smoukov, O. A. Scherman, D. Frenkel, J. J. Baumberg, *Proceedings of the National Academy of Sciences* **2016**, *113*, 5503.
- [241] J. Clara-Rahola, R. Contreras-Caceres, B. Sierra-Martin, A. Maldonado-Valdivia, M. Hund, A. Fery, T. Hellweg, A. Fernandez-Barbero, *Colloids and Surfaces A: Physicochemical and Engineering Aspects* **2014**, *463*, 18.
- [242] A. Rauh, T. Honold, M. Karg, *Colloid and Polymer Science* **2016**, *294*, 37.
- [243] A. Burmistrova, R. von Klitzing, *Journal of Materials Chemistry* **2010**, *20*, 3502.
- [244] T. Honold, K. Volk, A. Rauh, J. P. S. Fitzgerald, M. Karg, *Journal of Materials Chemistry C* **2015**, *3*, 11449.
- [245] K. A. Willets, R. P. Van Duyne, *Annual Review of Physical Chemistry* **2007**, *58*, 267.
- [246] C. Sönnichsen, T. Franzl, T. Wilk, G. v. Plessen, J. Feldmann, *New Journal of Physics* **2002**, *4*, 93.
- [247] V. Nerapusri, J. L. Keddie, B. Vincent, I. A. Bushnak, *Langmuir* **2006**, *22*, 5036.
- [248] Colloidal Approach of Local and Propagating Magnetic Modes for Optical Metamaterials on the Macroscopic Area
- [249] D. R. Smith, D. C. Vier, T. Koschny, C. M. Soukoulis, *Physical Review E* **2005**, *71*, 036617.
- [250] R. d. L. Kronig, *J. Opt. Soc. Am.* **1926**, *12*, 547.
- [251] La diffusion de la lumière par les atomes
- [252] C. D. Sorrell, M. C. D. Carter, M. J. Serpe, *Advanced Functional Materials* **2011**, *21*, 425.
- [253] W. Kern, *RCA Review* **1970**, *31*, 187.

- [254] H. K. Raut, V. A. Ganesh, A. S. Nair, S. Ramakrishna, *Energy & Environmental Science* **2011**, *4*, 3779.
- [255] I. M. Thomas, *Appl. Opt.* **1986**, *25*, 1481.
- [256] X. Zeng, Y. Gao, H. Hu, D. Ji, Q. Gan, F. Bartoli, *Journal of Applied Physics* **2013**, *113*, 133102.
- [257] C. Hägglund, S. P. Apell, *The Journal of Physical Chemistry Letters* **2012**, *3*, 1275.
- [258] H. Robotjazi, S. M. Bahauddin, C. Doiron, I. Thomann, *Nano Letters* **2015**, *15*, 6155.
- [259] C. Ng, L. Wesemann, E. Panchenko, J. Song, T. J. Davis, A. Roberts, D. E. Gómez, *Advanced Optical Materials* **2019**, *7*, 1801660.
- [260] C. Clavero, *Nature Photonics* **2014**, *8*, 95.
- [261] J. J. Mock, D. R. Smith, S. Schultz, *Nano Letters* **2003**, *3*, 485.
- [262] X. Liu, X. Jia, M. Fischer, Z. Huang, D. R. Smith, *Nano Letters* **2018**, *18*, 6181.
- [263] M. Mayer, M. J. Schnepf, T. A. F. König, A. Fery, *Advanced Optical Materials* **2019**, *7*, 1800564.
- [264] J.-W. Jeon, J. Zhou, J. A. Geldmeier, J. F. Ponder, M. A. Mahmoud, M. El-Sayed, J. R. Reynolds, V. V. Tsukruk, *Chemistry of Materials* **2016**, *28*, 7551.
- [265] J. Peng, H.-H. Jeong, Q. Lin, S. Cormier, H.-L. Liang, M. F. L. De Volder, S. Vignolini, J. J. Baumberg, *Science Advances* **2019**, *5*, eaaw2205.
- [266] Plasmonic particle-on-film nanocavities: a versatile platform for plasmon-enhanced spectroscopy and photochemistry
- [267] H. A. Al-Attar, Q. H. Al-Alawina, A. P. Monkman, *Thin Solid Films* **2003**, *429*, 286.
- [268] W. S. Huang, A. G. MacDiarmid, *Polymer* **1993**, *34*, 1833.
- [269] J. Anthony Smith, M. Josowicz, J. Janata, *Physical Chemistry Chemical Physics* **2005**, *7*, 3614.
- [270] A. Yang, A. J. Hryn, M. R. Bourgeois, W. K. Lee, J. Hu, G. C. Schatz, T. W. Odom, *P Natl Acad Sci USA* **2016**, *113*, 14201.
- [271] K. Volk, J. P. S. Fitzgerald, M. Karg, *ACS Applied Materials & Interfaces* **2019**, *11*, 16096.
- [272] D. Wang, M. R. Bourgeois, W.-K. Lee, R. Li, D. Trivedi, M. P. Knudson, W. Wang, G. C. Schatz, T. W. Odom, *Nano Letters* **2018**, *18*, 4549.

Appendix

Appendix 1: TEM images of fluorescence labeled nanoparticles

The structure of pure silica particles and gold-core/silica-shell particles can be compared *via* TEM (see Figure A1). The material contrast between gold and silica allows for exact determination of the shell thickness in the core-shell particles.

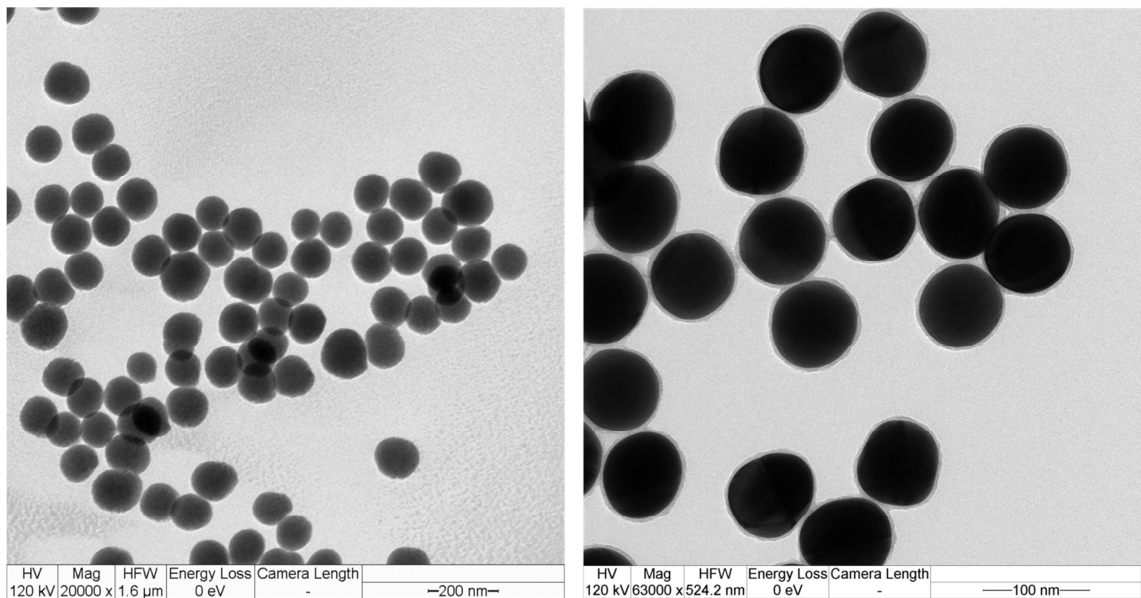


Figure A1. TEM images of the doped silica particles without (left) and with (right) plasmonic cores.

Appendix 2: Correlation of scattering, fluorescence, and morphology

To provide an in-depth investigation of the plasmonic cavities presented in Figure 35, the plasmonic scattering was correlated to the fluorescence emission, AFM, and SEM. For this purpose, the same particles were first investigated regarding their plasmonic properties *via* dark field microscopy and spectroscopy. Second, they were analyzed concerning their emission properties by FLIM, TCSPC and emission spectroscopy. Finally, their morphology was measured with AFM and SEM.

It is to note that the intensities of the fluorescent spectra are not comparable due to bleaching during TCSPC measurements and optimization during spectral collection. Therefore, fluorescence intensity of the four particles was compared using TCSPC measurements which were performed before spectral collection. Integrating the particle response in the FLIM measurements reveals following intensities:

Table A1. TCSPC counts of correlated cavities.

Object	Top left	Top right	Bottom left	Bottom right
TCSPC counts	235.273	93.039	206.776	71.404

These intensities are related to the maximum scattering intensity in the respective dark field spectra (see Figure A2). The ‘top left’ particle shows the highest scattering intensity as well as the highest fluorescence intensity. Accordingly, the ‘bottom right’ particle shows the lowest fluorescence and lowest scattering intensity. The other two particles match this observation.

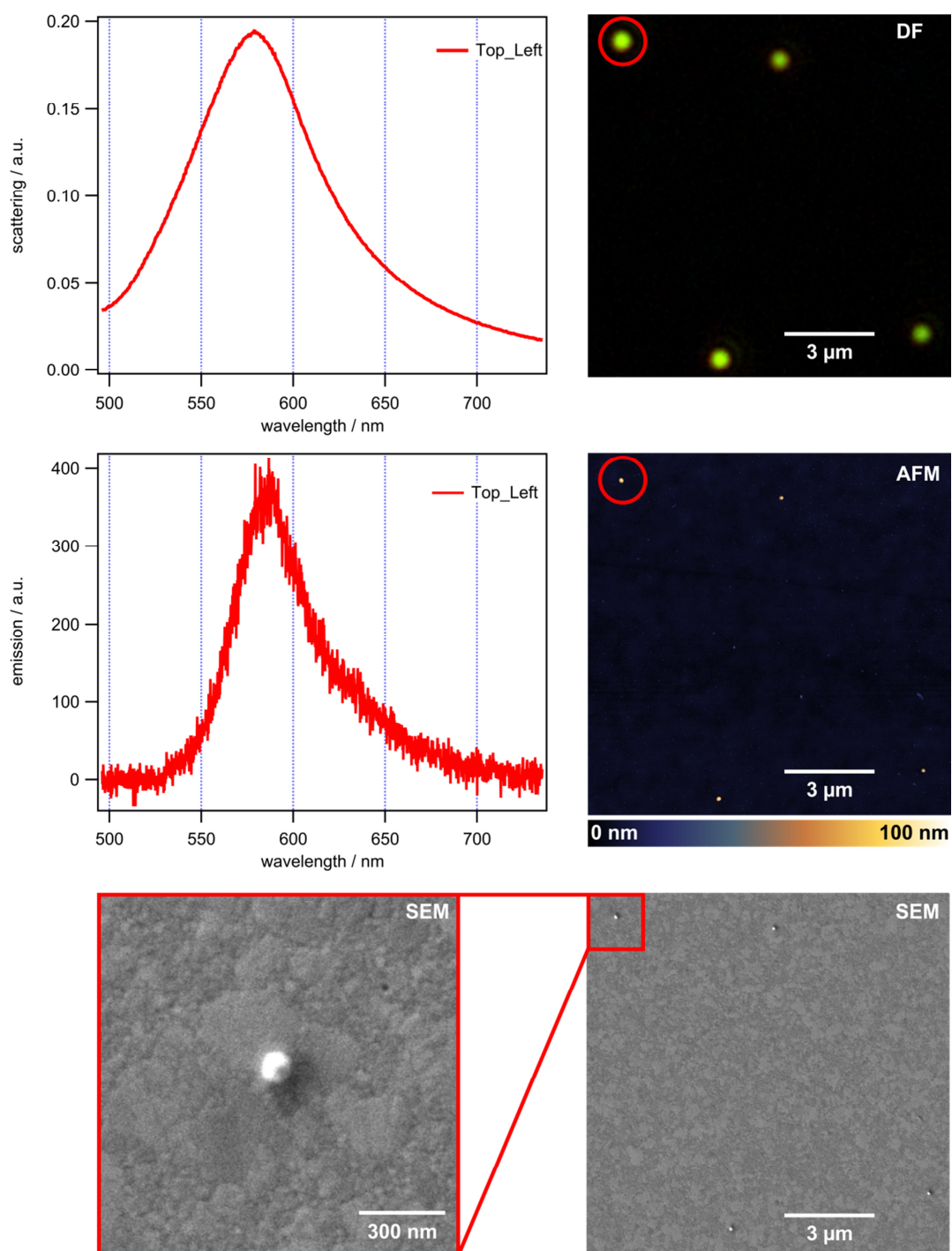


Figure A2. Correlation of darkfield spectroscopy and imaging (top left and right), fluorescence spectroscopy (middle left), AFM (middle right) as well as SEM (bottom).

Appendix 3: Calculation of the particle volume and fluorescence intensity

The molar ratio of TEOS and dye molecules were the same in both, the silica particle and the core-shell particle synthesis. Thus, the amount of fluorophore is considered to be proportional to the volume of SiO₂.

The calculated values in Table A2 leads to a volume ratio of 6.4 : 1. Regarding an increase of the fluorescence intensity by a factor of 5.9 ('cavity' setup respective the 'reference' setup), the normalized fluorescence intensity increases by $6.4 \times 5.9 = 37.8$.

Table A2. Comparison of the silica volume in silica particles and core-shell particles.

	Labeled Silica Particle (102 nm)	Labeled Core-Shell Particle (87 nm with 79 nm core)
Total Volume in nm ³	555647	344791
Excluded Volume (core) in nm ³	0	258155
Labeled Silica Volume in nm ³	555647	86636
Volume Ratio	6.4	1

Appendix 4: Fluorescence lifetime of rhodamine B labeled Au-silica particles
Evaluation of the fluorescence lifetimes for the ‘reference’ and the ‘film’ setup (Figure A3) setup show comparable lifetimes and decay rates.

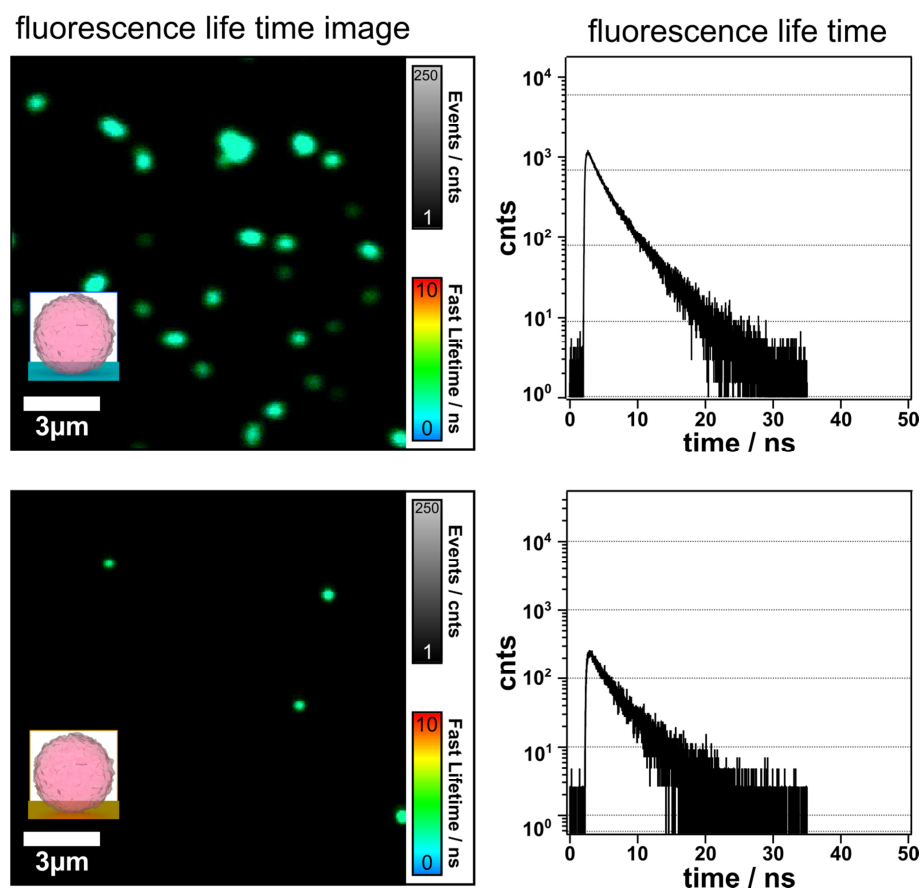


Figure A3. Fluorescence lifetime images (left) and respective TCSPC curves of the ‘reference’ setup (top) and the ‘film’ setup (bottom)

Appendix 5: Radiative and non-radiative processes in fluorescent nanoparticles

In order to describe the nanoantenna system, a convenient expression of the relationship between non-radiative (k_{nr}) and radiative decay (k_r) is given by the definitions of quantum efficiency ($QE_0 = k_r \tau_0$) and fluorescence lifetime ($\tau_0 = (k_r + k_{nr})^{-1}$). In the case of a fluorophore in vicinity of a metallic surface (index m) the definition for quantum efficiency and fluorescence lifetime can be extended by introducing an altered radiative decay rate $k_{m,r}$ as well as an additional non-radiative decay rate $k_{m,nr}$ thus becoming $QE_0 = (k_{m,r}) \tau_m$ and $\tau_m = (k_{m,r} + k_{m,nr} + k_{nr})^{-1}$.^a

FDTD simulations were used to describe the radiative processes of the fluorophore-plasmonic system. First, to study the interaction of light (plane wave source) with the various systems, the absorption and scattering cross-section efficiency were applied (Figure A4a). It is observed that the absorption is about four times greater than of the scattering cross-section, which is reasonable for the applied particle size and particle-to-film distance.^b The observed peaks and shoulders correlate with the corresponding plasmonic modes, namely a dipole resonance (for the ‘particle’ setup) as well as a lower and a higher order dipolar cavity resonance (in the ‘cavity’ setup). Surface charge calculations were used to identify the cavity modes. The extinction cross-section of the ‘film’ setup corresponds to the typical absorbance of a gold film.^c

Second, the Jablonski diagram correlates the calculated extinction cross-section efficiency with the radiative process (Figure A4b).^d Starting from a classical fluorophore system, the Jablonski diagram is extended to the fluorophore-plasmonic system. In the setup without metal (‘reference’ setup), the excited fluorophore decays with a non-radiative decay rate (k_{nr}) and a radiative decay rate (k_r), respectively. Once a metallic interface is added to the system, the absorption and scattering cross-section efficiency results in an increased coupling rate (arrow thickness represent increased coupling rates) and an increased decay rate ($k_{m,r}$). This behavior is reasonable due to the fluorophore induced plasmon oscillations, which result in an increased radiation to the far field.^e

Third, FDTD simulations were applied with a dipole source to distinguish between the non-radiative and radiative decay rates of the fluorophore-plasmonic system (Figure A4c). For all setups, the dipole source is located inside the cavity with an electric field vector perpendicular to the film. To fully explain the radiative processes, a dipole source was chosen with an excitation wavelength between 400 nm and 800 nm as well as a sweep of 40 narrow-bandwidth dipole sources with center wavelengths covering the same wavelength domain (Figure A11). The ideal case of a dipole orientation perpendicular to the cavity was assumed for the decay rates to obtain the highest

^a T. Soller, M. Ringle, M. Wunderlich, T. A. Klar, J. Feldmann, H. P. Josel, Y. Markert, A. Nichtl, K. Kürzinger, *Nano Letters* **2007**, *7*, 1941.

^b V. Myroshnychenko, J. Rodriguez-Fernandez, I. Pastoriza-Santos, A. M. Funston, C. Novo, P. Mulvaney, L. M. Liz-Marzan, F. Garcia de Abajo, *Chemical Society Reviews* **2008**, *37*, 1792.

^c P. B. Johnson, R. W. Christy, *Physical Review B* **1972**, *6*, 4370.

^d A. Jablonski, *Nature* **1933**, *131*, 839.

^e J. R. Lakowicz, Y. Fu, *Laser & Photonics Reviews* **2009**, *3*, 221.

coupling interactions for each system. In all setups, the radiative process are altered by the metallic interfaces. For the ‘cavity’, the absorption at the plasmonic resonances correlates with the non-radiative decay. The same signature is observed for the scattering cross-section and the radiative decay, which is increased significantly compared to the “particle” (120-fold) and the “film” setup (530-fold). It is also notable that for the uncoupled systems, the radiative decay rates correlate directly with the corresponding plasmon resonance position. However, in the cavity system, the radiative decay rate enhancement is red-shifted by 50 nm in respect to the plasmon resonance. More available metallic interfaces result in higher absorption/non-radiative decay and higher scattering/radiative decay. Based on the calculations for non-radiative and radiative decay rates, the reduction of lifetime can be comprehended, which is defined as the inverse sum of non-radiative and radiative decay rates. The calculated quantum efficiency revealed that in a fluorophore-plasmonic system the lifetime is shortened while the quantum efficiency is increased. For application where coherent coupling is crucial, the Purcell factor was determined, which shows an enhanced spontaneous emission ($P_{\text{cavity}} \approx 40,000$ and $P_{\text{particle}} \approx 20,000$) at the plasmonic cavity resonance wavelength.

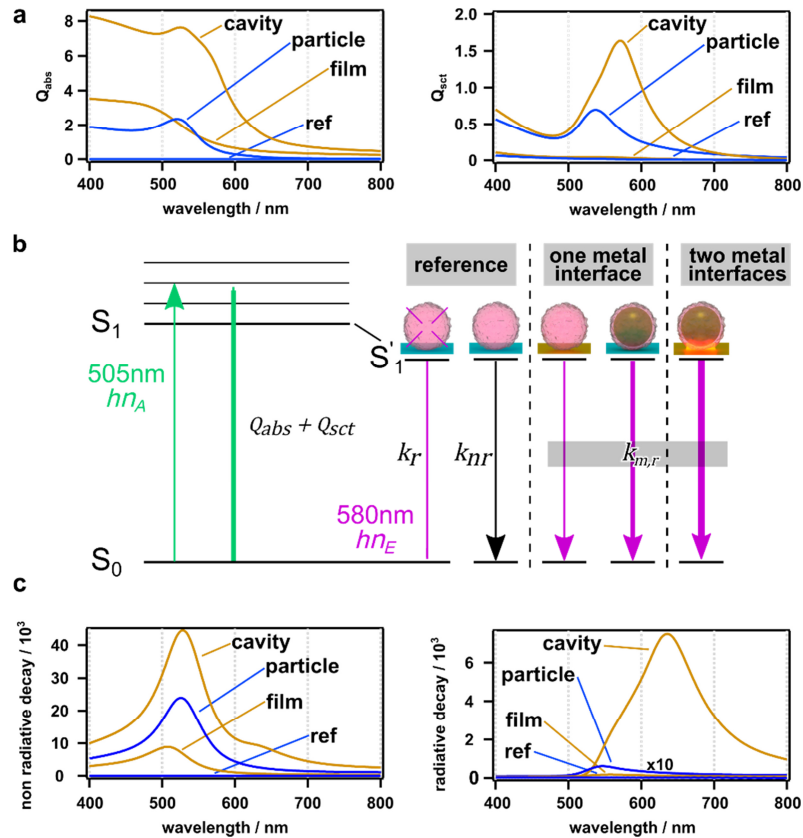


Figure A4. Radiative processes of colloidal film-coupled nanoantennas supported by FDTD simulations and Jablonski diagram: (a) FDTD simulated absorption and scattering cross-section efficiency (Q) for various systems. (b) Jablonski diagram including fluorophore absorption ($h\nu_A$), absorption and scattering cross-section efficiency (Q) from ground state (S_0) to excited states (S_1) and radiative, non-radiative decay rates (k) as well as additional decay rate k_m for various metallic setups. (c) Simulated non-radiative and radiative decay rates for various setups. Labels for the colloidal building blocks and systems: rhodamine B particle on a dielectric film (‘reference’ setup), rhodamine B coupled to metallic film (‘film’), plasmonic-core and rhodamine B-shell coupled to dielectric film (‘particle’) and metallic film (‘cavity’).

Appendix 6: TEM on the particle system

Transmission electron microscopy was performed to provide better insight to the particle system. PNIPAM particles of 180 nm (dried state) with 15 nm sized gold cores are displayed in Figure A5.

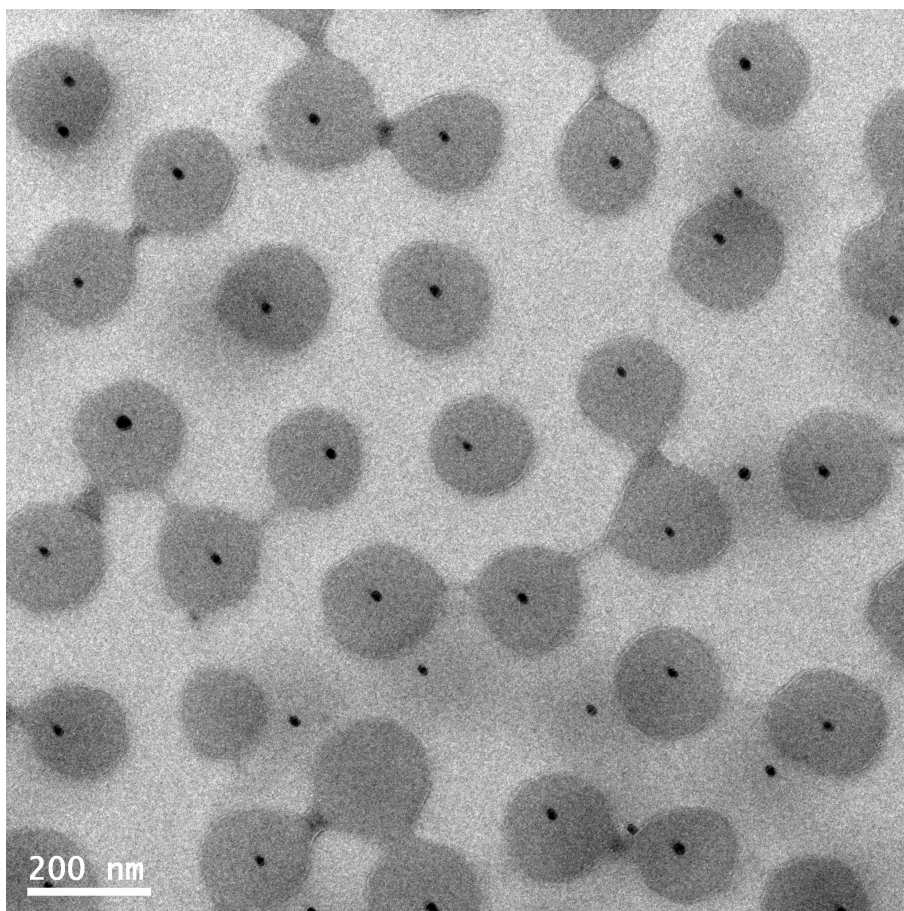


Figure A5. TEM image of Au-PNIPAM particles

Appendix 7: Atomic force microscopy on spin-coated samples

Atomic force microscopy was conducted on a spin-coated microscope slide to give an impression of the Au-PNIPAM particle monolayer that is formed (see Figure A6).

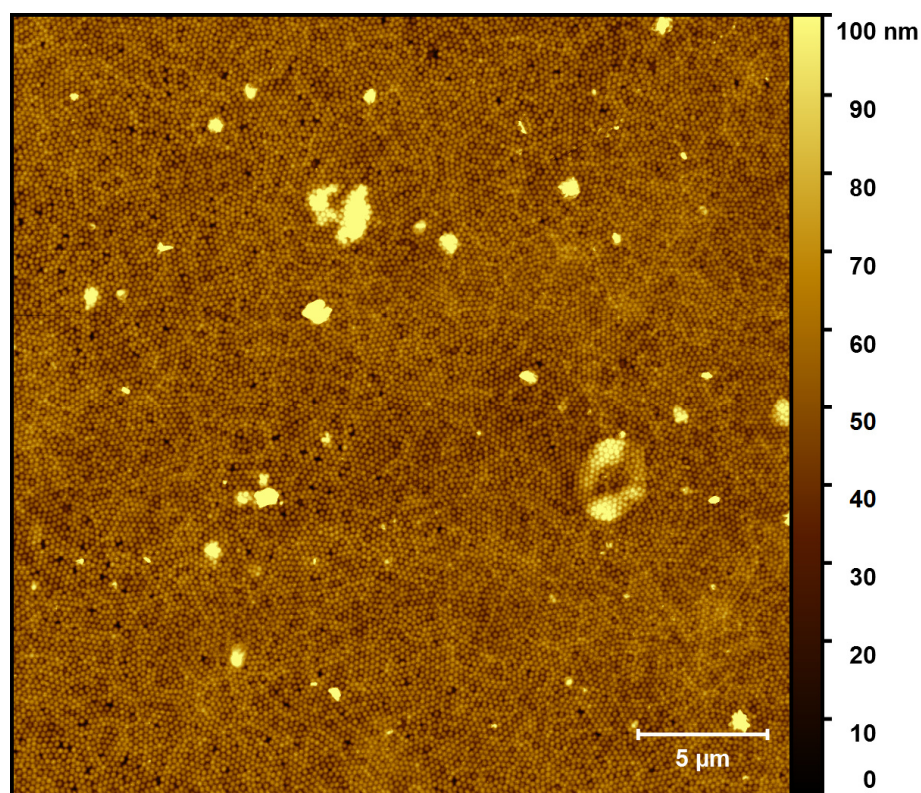


Figure A6. AFM image of a spin-coated monolayer of Au-PNIPAM particles on a microscope slide

Appendix 8: Spectroscopic ellipsometry for determination of the gold layer thickness

The layer thickness of the reference gold film was determined from ellipsometry data (see Figure A7). For this, the Mueller-matrix elements were measured at various angles (45° - 75° in steps of 5°). Results were modelled within CompleteEASE™ software (Version 5.07) by a layer of Au (optical constants from thin film - KK oscillator fit) on a microscope slide (optical constants fit to Cauchy). Optical constants were taken from the CompleteEASE™ material library. Fitting of the gold-layer resulted in a thickness of 32.2 nm with an MSE of 7.

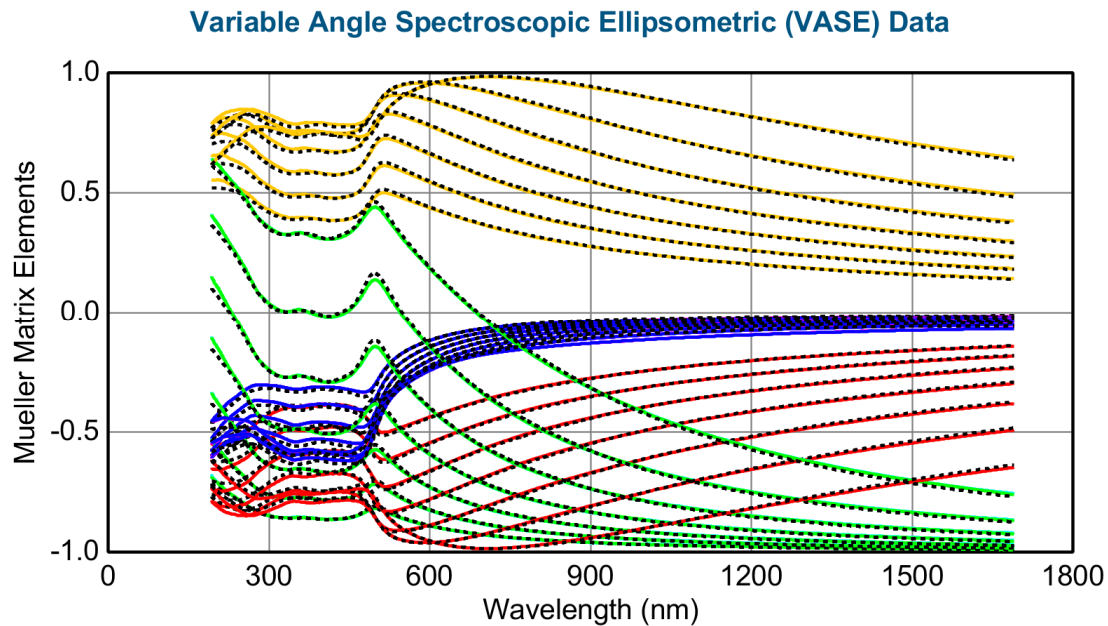


Figure A7. Müller Matrix Elements M34 (orange), M44 (green), M21 (blue) and M43 (red) with curve fits (dotted black) at 45° - 75° measurement angle.

Appendix 9: AFM investigation for gold-layer thickness determination

A spot on the reference sample, where the gold film has been blown off with a nitrogen stream, was used for investigation in AFM (see Figure A8). The edge was measured at three different positions to determine the average height of the gold film. Extraction of the cross-sections and height determination was conducted as shown below.

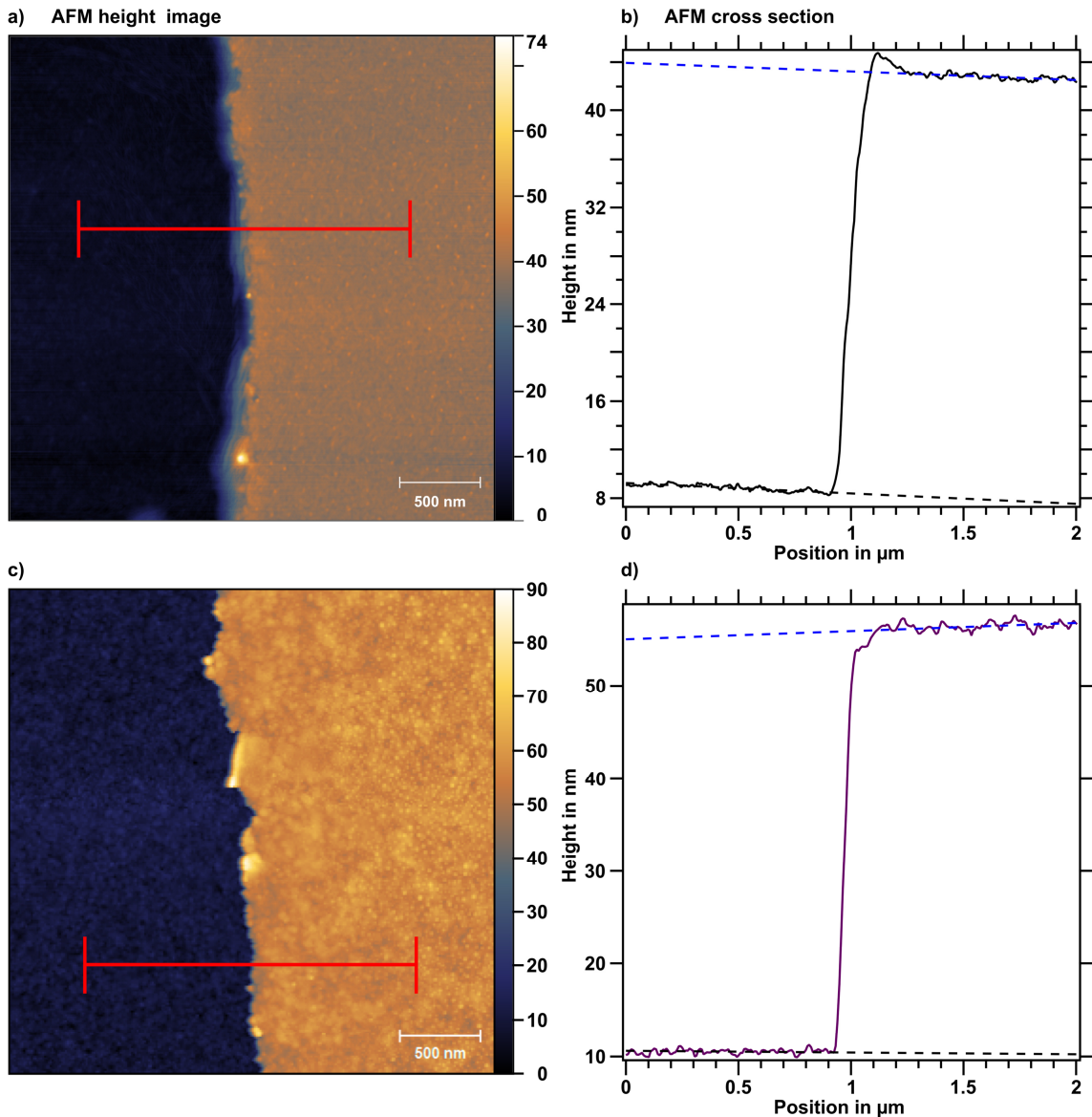


Figure A8. Extraction of the gold-layer thickness. a/c) AFM height images of a defect in the reference gold films. b/d) Cross-sections of the region marked in the image with fits for the glass substrate (dotted black) and the metal surface (dotted blue) which were used for determination of the height. Upper row presents reference gold film for the gradient studies. Lower row shows reference gold film for the sample used in swelling experiments (refer to Figure 5 in main text).

Appendix 10: Center-to-center distance determination via FFT

The center-to-center distance of Au-PNIPAM particle monolayer was determined on basis of AFM measurements (see Figure A9). A fast Fourier transform was made from the resulting image. A radial cross-section was used to fit the grey level peak position and calculate back from pixels to the particle distance in nanometers.

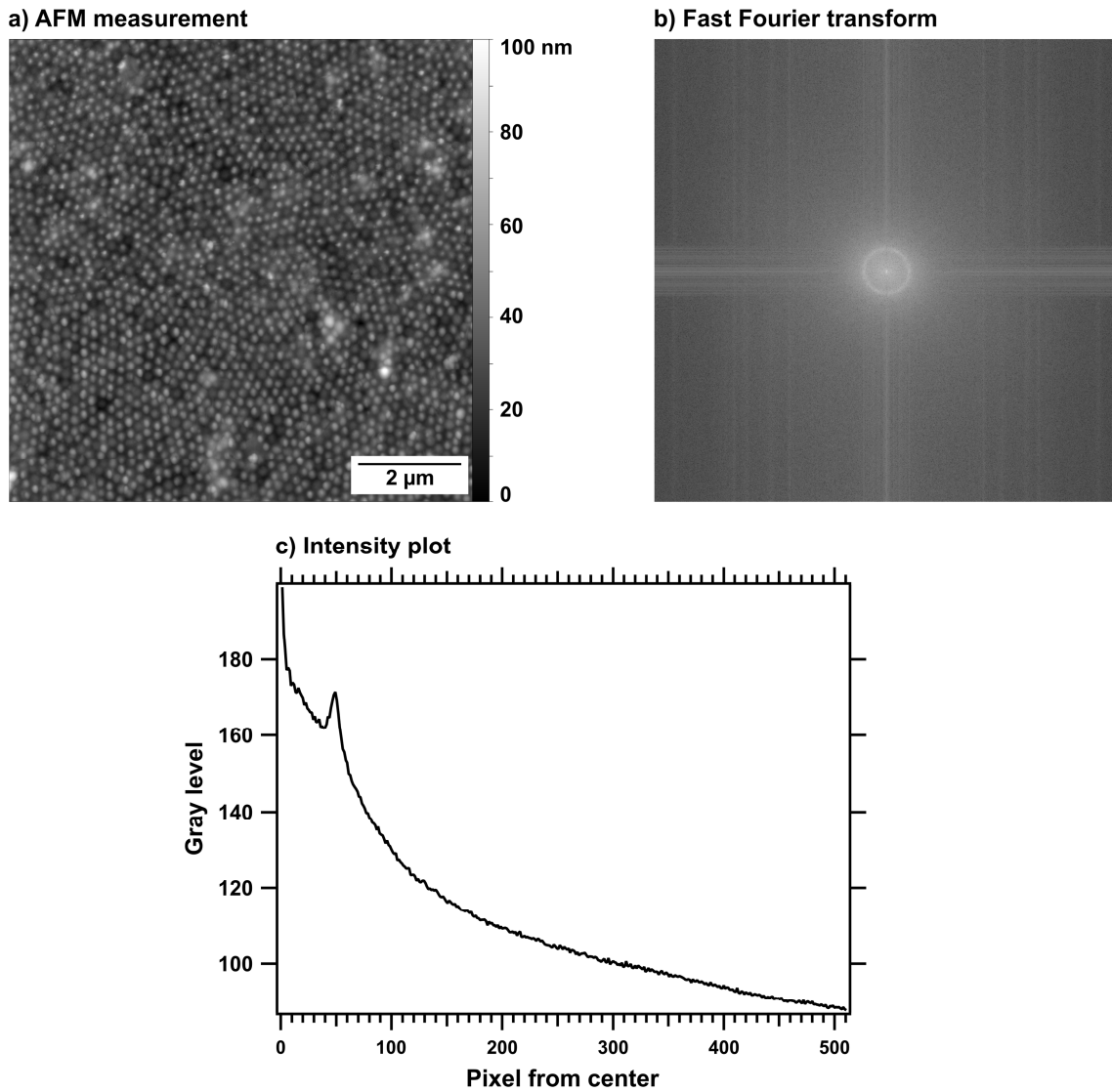


Figure A9. Determination of the center-to-center distance. a) AFM height image of the particle monolayer. b) Fast Fourier transform of the AFM image. c) Radial cross-section of the FFT plotting gray level *versus* distance in pixel from the center.

Appendix 11: Calculation of gold core sizes

The gold core sizes were calculated on basis of a previous investigation which compared their diameters to the location of the LSPR (Figure A10). The fit function shown below was used to determine the actual particle diameters.

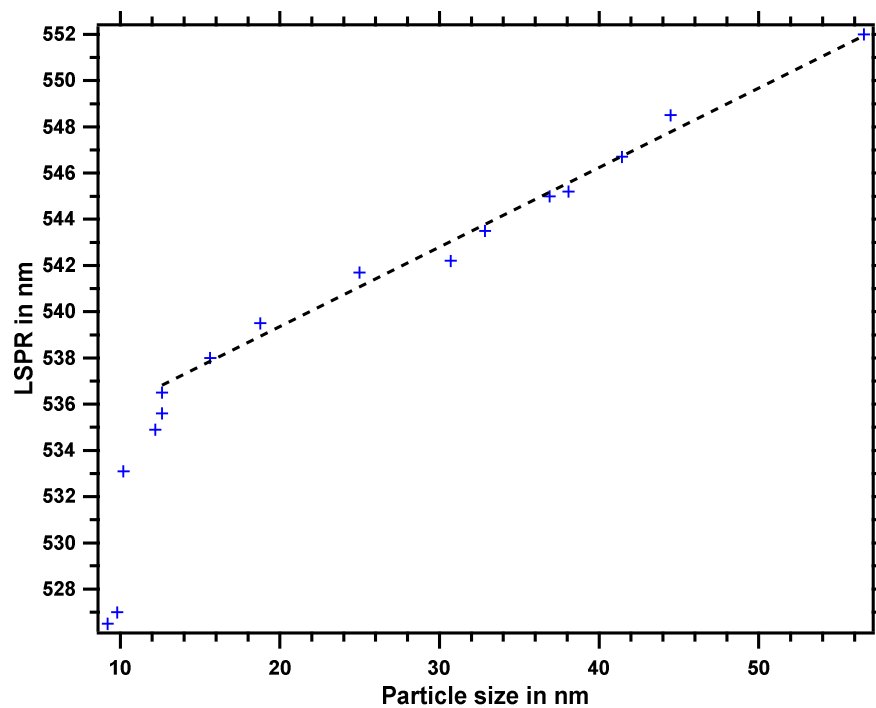


Figure A10. Position of the LSPR in dependence of the gold core diameter. Dashed black line represents linear fit (neglecting first 5 data points).

Appendix 12: Determination of the refractive index for PNIPAM

Ellipsometric data of a 125 nm PNIPAM layer on a silicon wafer (see Figure A11) were measured with a M2000 spectroscopic ellipsometer (J.A. Woollam Co.). To specify the refractive index of PNIPAM, a general oscillator layer model was used within the CompleteEASE software (Version 5.07). All modelling approximations were physically reasonable (parametrization to fulfill Kramers-Kronig relations) and showed a low mean square error ($MSE < 5$).

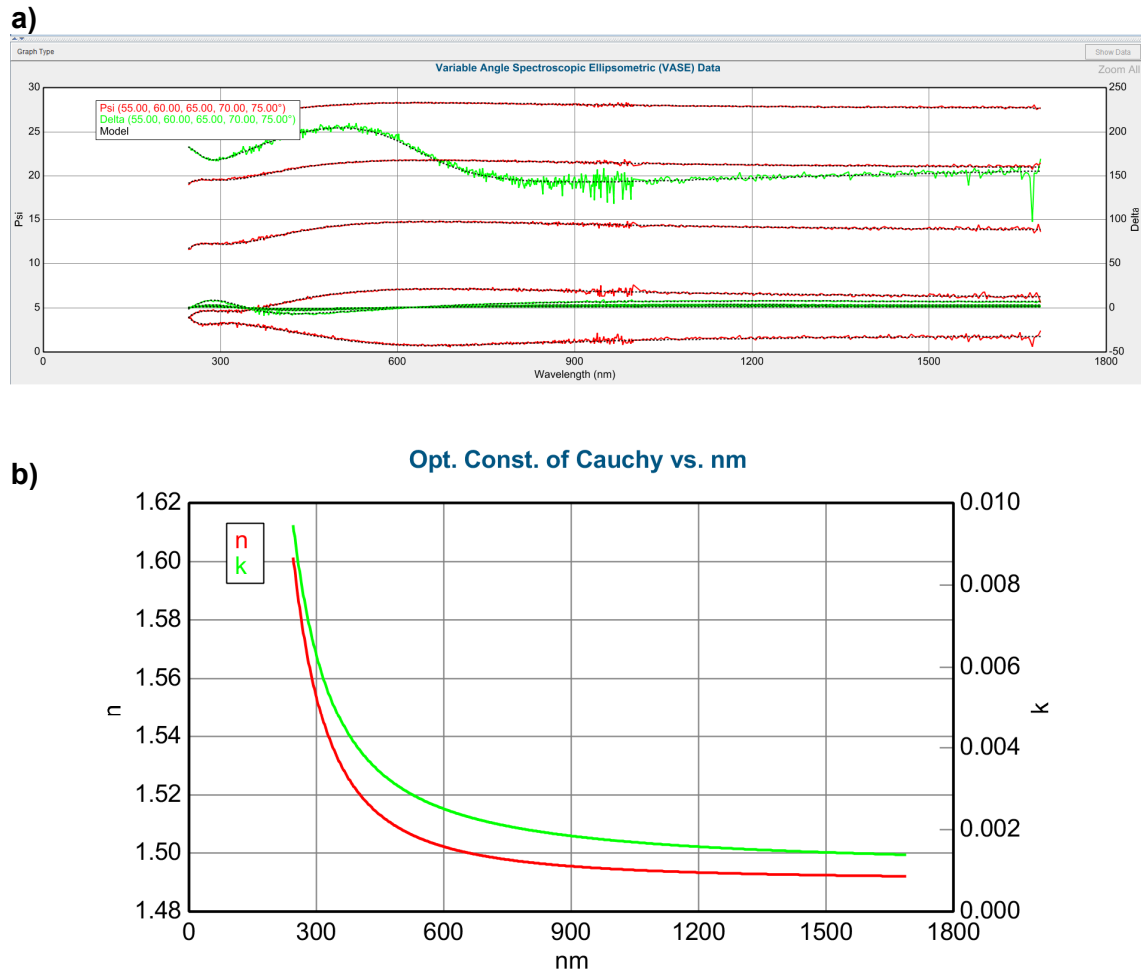


Figure A11. Determination of the refractive index for PNIPAM. a) Ellipsometric (psi/delta) spectra (red/green lines) at five different angles with Cauchy fit (dotted black). b) Wavelength-dependent refractive index (n , red line) and extinction coefficient (k , green line) yielded from Cauchy fit.

Appendix 13: Additional FDTD setup information

Simulations were performed on basis of a model as shown in Figure A12. The PNIPAM layer was determined as an ellipsoid with radius $R_{xy} = 130$ nm and $R_z = D_{\text{sphere}} + 2d$ (where d_{gap} is the particle-to-film distance). The covering gold layer featured a constant layer thickness of 35 nm. An initial spacing (d_{gap}) of 7.5 nm was estimated from AFM measurements. The decrease of d_{gap} (see Table A3) was concluded from simulations given in Appendix 15.

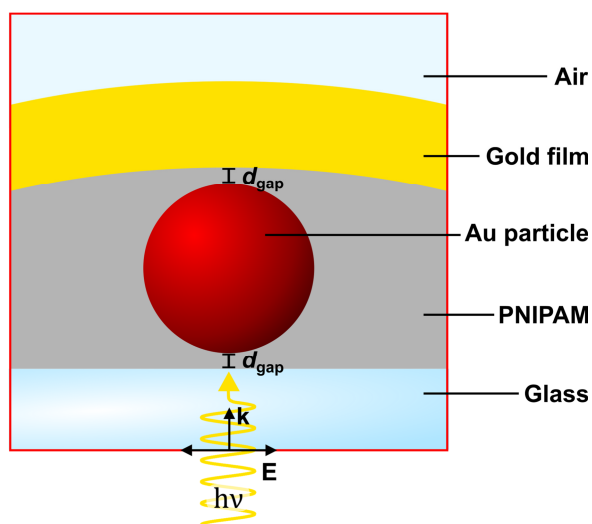


Figure A12. Schematic depiction of the FDTD model.

Table A3. Parameter sweep of particle and layer thicknesses

D_{sphere} in nm	PNIPAM spacing d_{gap} in nm	Gold layer thickness in nm
20	7.5	35
25	7.0	35
30	6.5	35
35	6.0	35
40	5.5	35
45	5.0	35
50	4.5	35
55	4.0	35

Appendix 14: FDTD simulations for comparison of curved/ flat gold film geometry

To determine the influence of the curvature, FDTD simulations were performed with curved gold film geometry (see Figure A10a) and flat geometry (b). In comparison to the maximum resonance position in the curved setup (596 nm at 55 nm particle), the maximum is at significantly lower wavelength (582 nm). Thus, a curved geometry promotes the particle-to-film coupling is concluded.

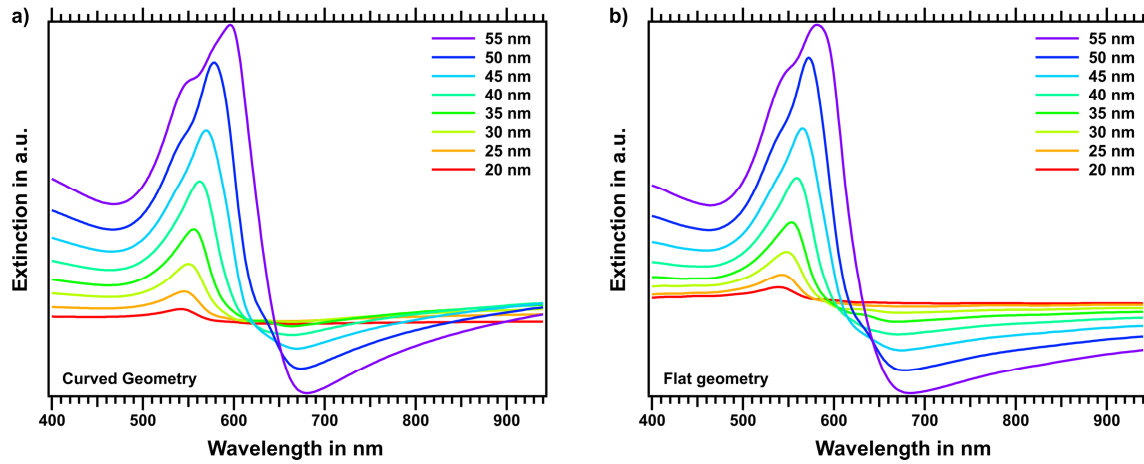


Figure A13. Simulated extinction cross-sections of the film-coupled array a) with a curved gold film and b) with a flat film geometry (b).

Appendix 15: Simulation with variable particle-to-film distances

Figure A14 shows results from FDTD simulations of $\Delta\lambda_{\max}$ in dependence of the particle-to-film distance. A Setup with constant spacing of 7.5 nm (upward triangle) or 4.0 nm (downward triangle) yields in values above and below the experimental data, respectively. However, a variation of the particle-to-film distance from 7.5 nm to 4.0 nm results in coincidence of FDTD simulations and experimental results. Hereby, the observed non-linear shift of λ_{\max} , which is not solely caused by increase of the gold core diameter, can be explained.

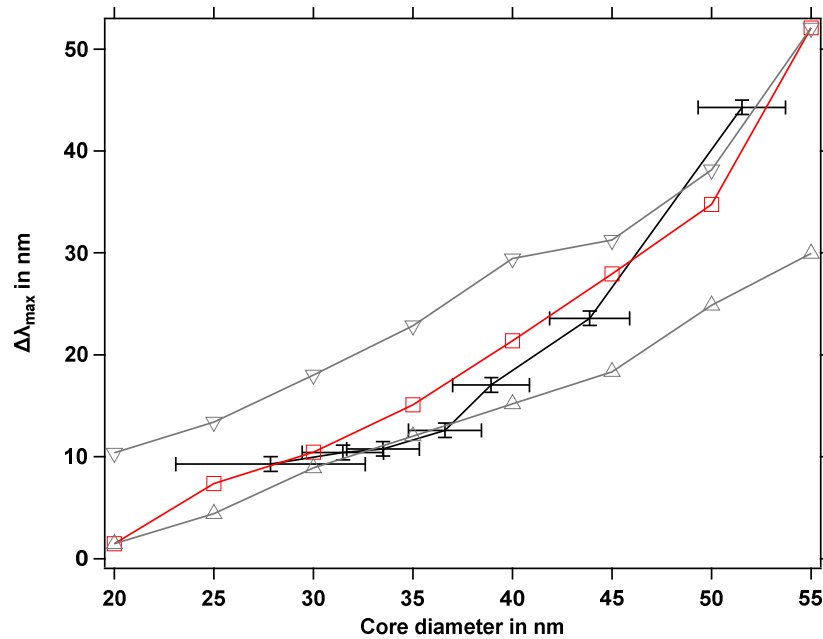


Figure A14. Comparison of experimental and simulated peak shifts *versus* the gold particle diameter. The relative shift is defined as the difference of the plasmonic resonance peak in respect to the non-film-coupled setup. Experimental data are given as black markers (including standard deviation). FDTD simulation at varying particle-to-film distances is marked with red circles. Gray triangles show simulations for 7.5 nm (upward triangle) and 4.0 nm (downward triangle) distances. Lines between points are guides to the eye.

Appendix 16: Effective permittivity using S-parameter method

The S-parameter method established by Smith *et al.* was used to determine the effective permittivity as shown in Figure A15.

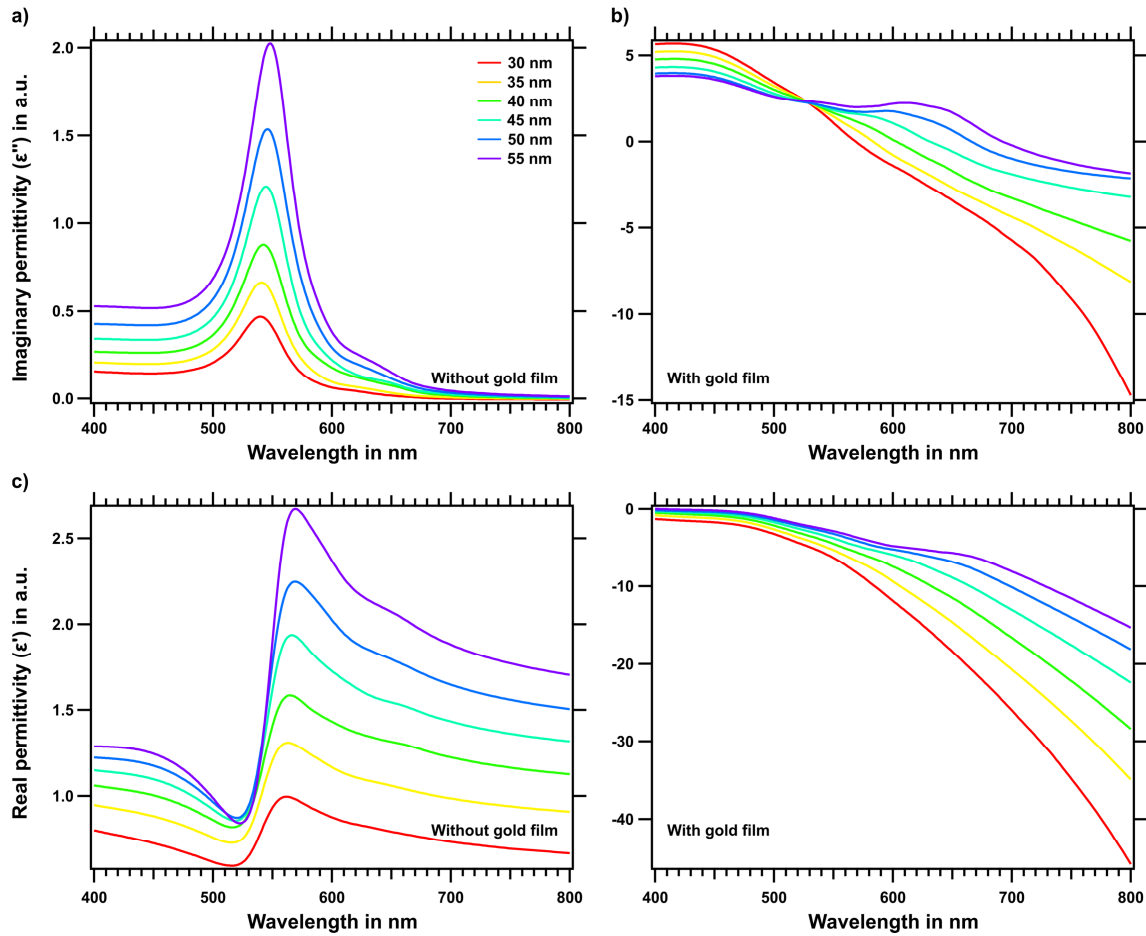


Figure A15. Effective permittivity determined by the S-parameter method. Imaginary permittivity a) for a gold nanoparticle and b) for a film-coupled nanoparticle at various particle diameter. Corresponding real parts are shown in c) and d), respectively. Pink solid line represents literature value of gold obtained from Johnson and Christy.

Appendix 17: Large scale microscopy image in the swelling region

Repeated swelling and drying of the substrate does not lead to damaging (e.g. cracking) of the nanostructure as shown in Figure A16.

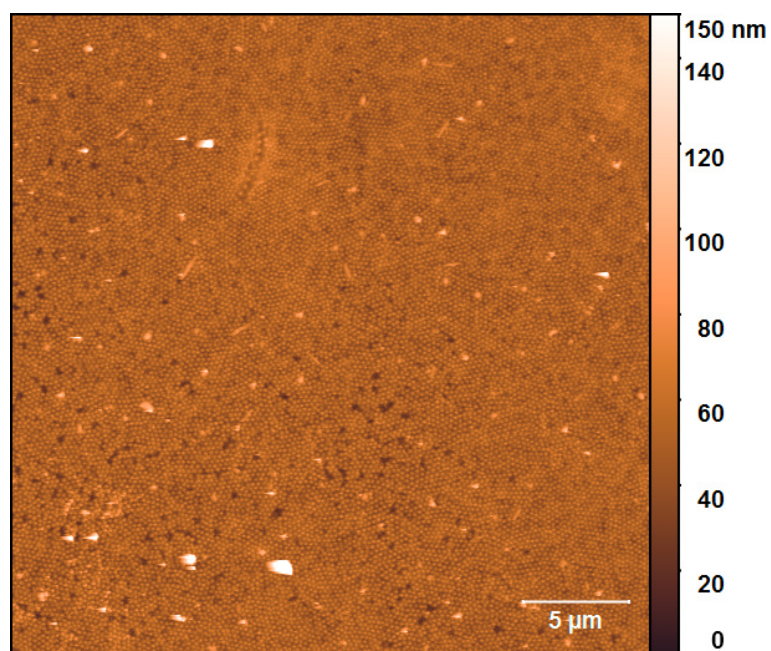


Figure A16. AFM image of the functional nanostructure after multiple cycles of swelling and drying.

Appendix 18: Comparison of the swelling behavior without and with gold film

To emphasize the pronounced resonance shift upon swelling being attributed to the plasmonic film-coupling, UV/vis spectra of the plasmonic library (without gold film) and the film-coupled system (with gold film) are shown in Figure A17. Spectra in the dried state (red) and immersed state (blue) are compared for both, the plasmonic library (56 nm particles) and the film-coupled system (region of 50 nm particles).

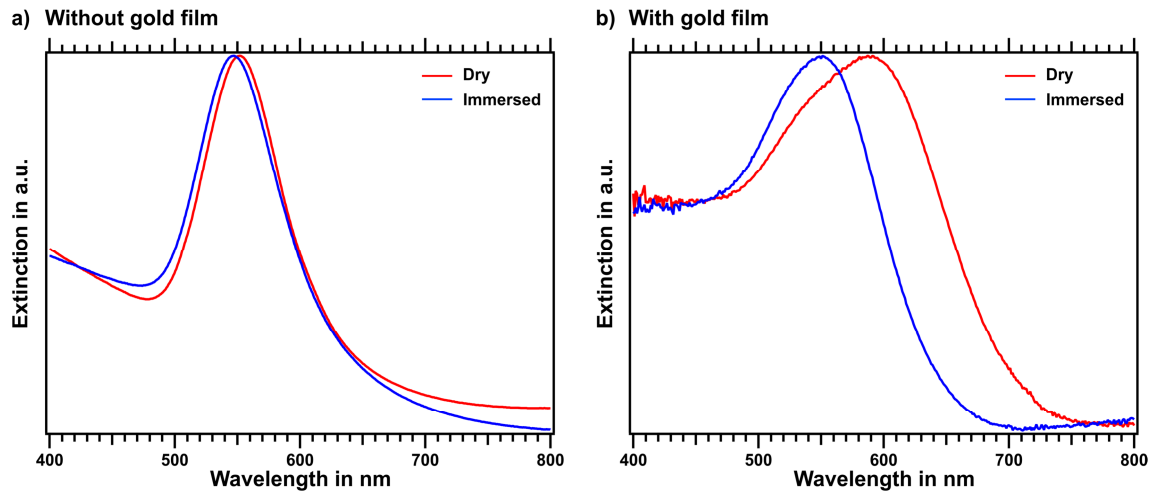


Figure A17. UV/vis spectra of the particle array a) without and b) with gold film in dried state (red) and immersed state (blue).

Appendix 19: Simulation of LSPR peak position in dependence of the refractive index
 Changing the refractive index of the PNIPAM spacer layer from dried ($n = 1.5$) to the swollen state ($n = 1.33$) results in a linear decrease of λ_{\max} at constant spacing $d_{\text{gap}} = 4$ nm (see Figure A10). The refractive index boundaries result from dry polymer (see Appendix 5) and the virtual swelling limit (n of water). However, the actual refractive index is determined *via* the volume fraction (Φ) of the swollen polymer according to Maxwell Garnett (with refractive indices of polymer (n_p) and water (n_w), respectively):^a

$$n_{\text{eff}} = \sqrt{1 + \frac{3\Phi}{\left(\frac{n_p^2 + n_w^2}{n_w^2 - n_p^2}\right) - \Phi}}$$

Hence, the refractive index is not likely to reach the value of pure water (1.33) but rather 1.42-1.46.^b Moreover, the experimental shift to 550 nm is not even reached if water is assumed as spacing material. By comparing the setup without a gold film, two differences reveal: λ_{\max} is lower and the refractive index dependence is weaker (lower slope). Both effects are caused by the nature of plasmonic coupling. It is also observed that λ_{\max} of the non-coupled system is slightly below the measured value. Thus, a weakly coupled plasmonic resonance can be assumed upon immersion of the substrate.

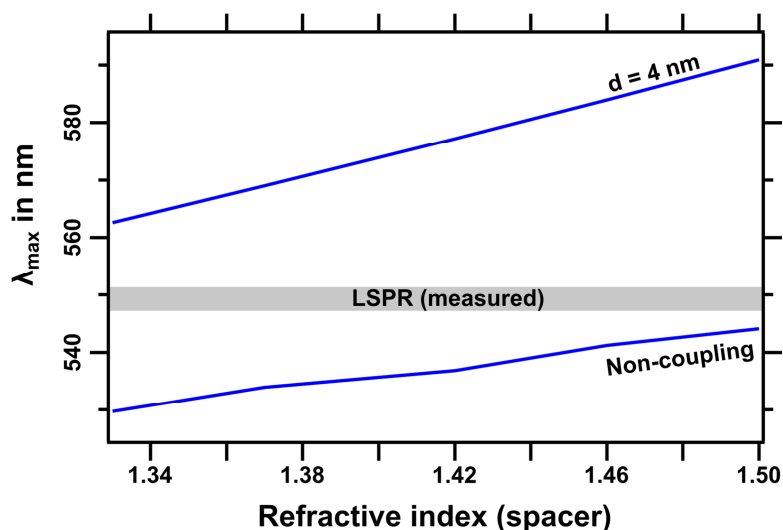


Figure A18. LSPR peak position in dependence of the effective refractive index of the gap for a constant gap size (particle-to-film distance) as a result from FDTD simulations (blue). The measured position of the plasmon resonance in the immersed state is highlighted in gray.

^a A. Albersdörfer, *Über das Quellverhalten und die viskoelastischen Eigenschaften ultradünner, festkörpergestützter Polyelektrolytfilme*, Herbert Utz Verlag 1999, Chapter 6, p. 58.

^b M. B. Müller, C. Kuttner, T. A. F. König, V. V. Tsukruk, S. Förster, M. Karg, A. Fery, *ACS Nano* 2014, 8, 9410.

Appendix 20: UV/vis-spectroscopy of the functional nanostructure at different humidity

The sample was investigated *via* UV/vis spectroscopy under variation of the humidity (see Figure A19). For this purpose, a home-made humidity cell was flushed with nitrogen (dry and 90% relative humidity, respectively) for one hour before measuring the absorbance spectra.

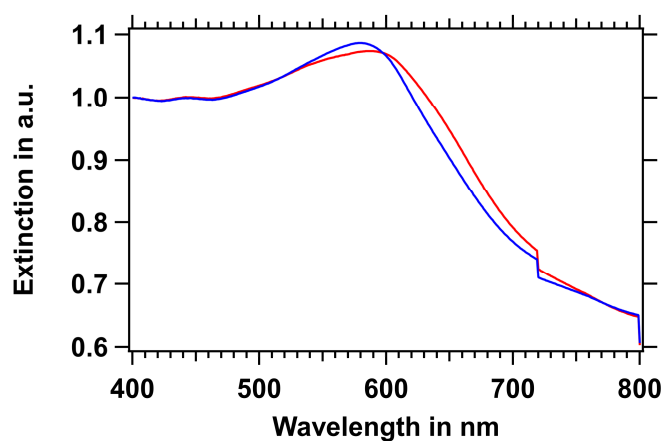


Figure A19. UV/vis spectra of the functional nanostructure (50 nm sized cores) in dry nitrogen (red) and with nitrogen atmosphere at 90% relative humidity (blue).

Appendix 21: UV/vis-spectroscopy of the nanostructure in water at different temperatures

To determine the temperature induced changes in the coupling resonance, the sample was investigated with UV/vis spectroscopy at 25 °C and 50 °C. Spectra were recorded in the region of 50 nm sized particles. The results are displayed in Figure A20a. At 25 °C the sample features an extinction maximum at 556 nm. An increase of the temperature to 50 °C results in a red-shift the maximum position by 1 while increasing the bandwidth by 5 nm. Since these changes are not significant, tunability *via* changing the temperature could not be reported. This is caused by two effects: During growth of the gold particles, the PNIPAM corona is displaced by the growing core. The resulting compression of the hydrogel in proximity to the gold core leads to a dielectric surrounding that is already similar to the collapsed polymer (by temperature induced volume phase transition). Thus, the temperature induced effect is weak in this system. Another factor is the swelling itself. It leads to a strong increase in the particle-to-film distance. The system is shifted out of the strong coupling regime which reduces its sensitivity against small changes in the spacing distance as caused by the thermal collapse (see Figure A20b).

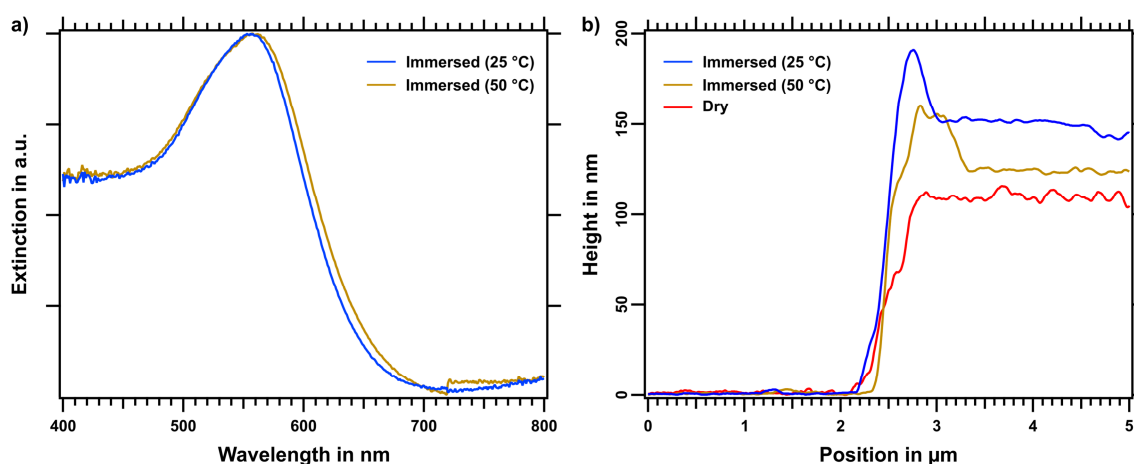


Figure A20. a) UV/vis spectra of the functional substrate immersed in water at 25 °C (blue) and 50 °C (ochre). b) AFM cross-section profile of the same substrate immersed in water at 25 °C (blue), at 50 °C (ochre) and in the dried state (red).

Appendix 22: Surface topography

The coverage of gold-coated silicon wafers with Au-PANI particles can be varied by applying different particle and surfactant concentrations. In Figure A21, two examples are shown with moderate (left) and low (right) concentration of SDS in the deposition step.

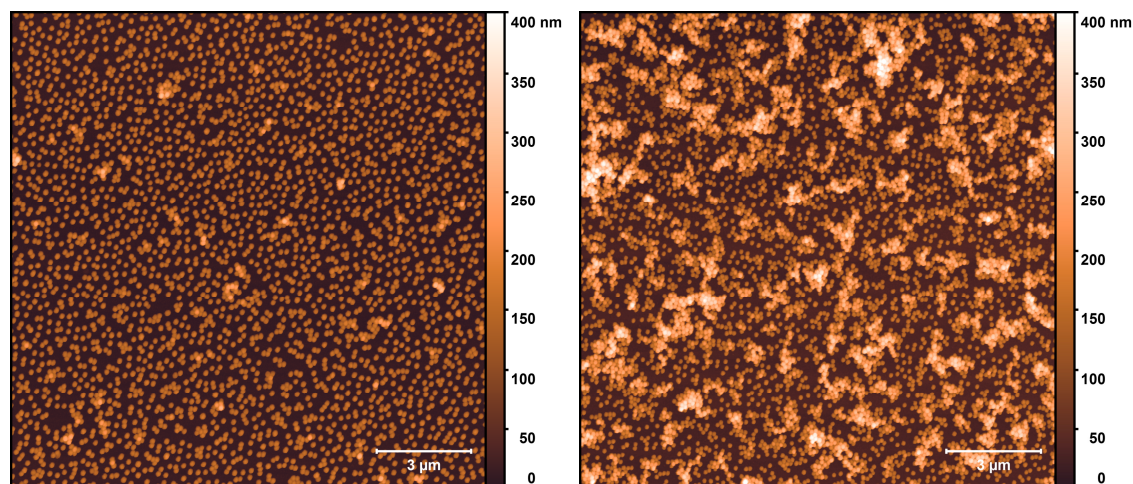


Figure A21. AFM micrographs of Au-PANI particles on gold surfaces with different 24% coverage (left) and 53% coverage (right).

Appendix 23: Anti-reflective surface: observations and mechanism

Typically, the characteristics of plasmonic metasurfaces can be explained *via* coupling between the particle dipoles and their images in a plasmonic mirror, e.g. an Au-film. The electric and magnetic response of this coupled mode then leads to an impedance matching between two media, resulting in enhanced absorption at the resonance frequency of the plasmonic nanoparticles.^a However, in this case this is not a valid explanation as the particle-to-film distance contributed by the PANI layer (32 nm) is too large to induce such a significant magnetic resonance. Furthermore, the effect can also be observed when a non-plasmonic substrate (silicon wafer, see Figure A22) is utilized instead of a gold mirror, which rules out the commonly reported plasmonic coupling effects.

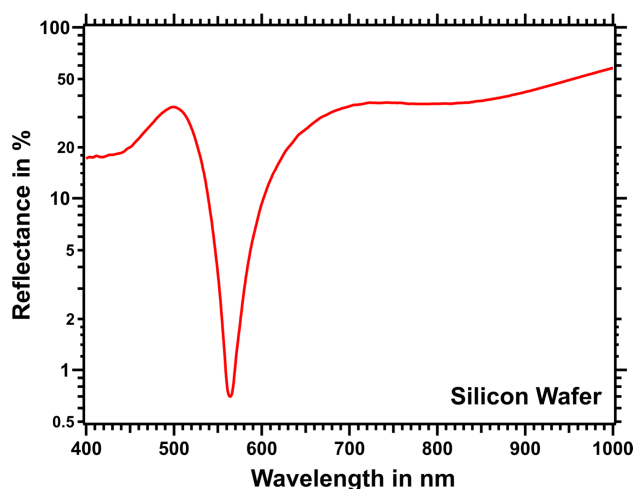


Figure A22. Reflectance spectrum of a silicon wafer coated with Au-PANI particles.

^a G. M. Akselrod, J. Huang, T. B. Hoang, P. T. Bowen, L. Su, D. R. Smith, M. H. Mikkelsen, *Advanced Materials* **2015**, *27*, 8028.

N. Liu, M. Mesch, T. Weiss, M. Hentschel, H. Giessen, *Nano Letters* **2010**, *10*, 2342.

J. J. Baumberg, J. Aizpurua, M. H. Mikkelsen, D. R. Smith, *Nature Materials* **2019**, *18*, 668.

N. I. Landy, S. Sajuyigbe, J. J. Mock, D. R. Smith, W. J. Padilla, *Physical Review Letters* **2008**, *100*, 207402.

Appendix 24: Ellipsometry and modelling of optical data

Spectroscopic ellipsometry of chemically synthesized polyaniline films on gold-coated wafers was conducted with an RC2 ellipsometer (J.A. Woollam Co., Inc.) by measuring the full Müller matrix. Collection angles were tuned from 45° to 60° in steps of 5° . The results, displayed as Ψ - and Δ -spectra, are shown in Figure A23 and Figure A24.

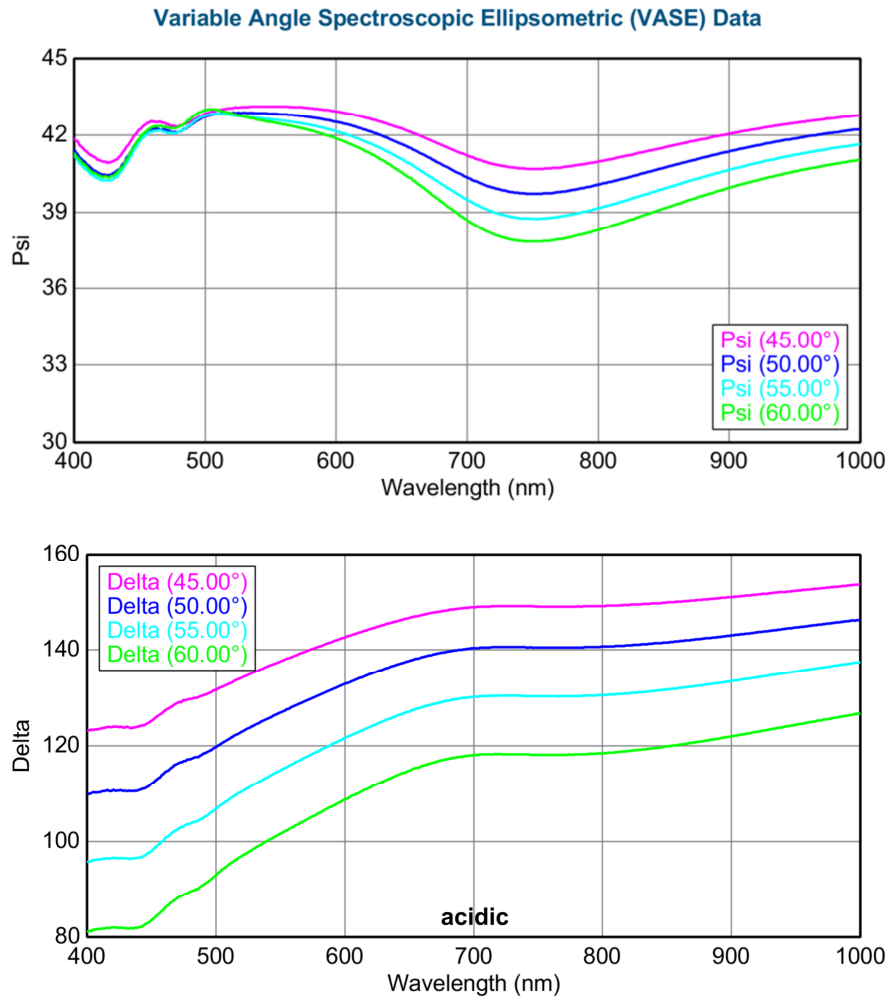


Figure A23. Ψ - and Δ -spectra of a PANI film on a gold-coated wafer after immersion in acidic solution.

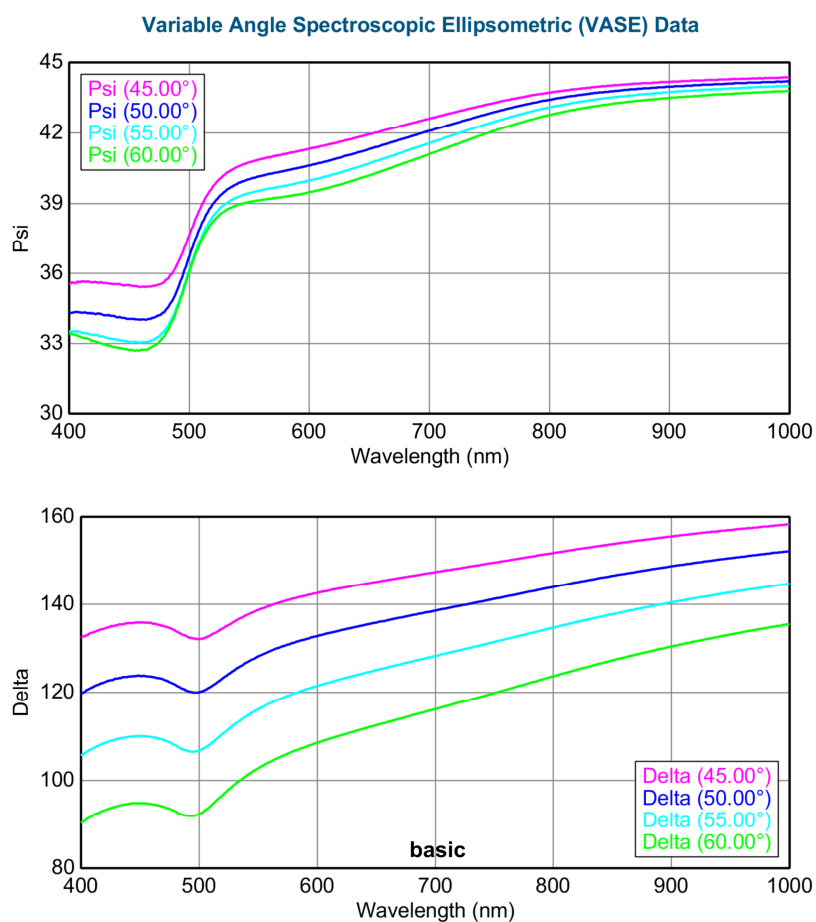


Figure A24. Ψ - and Δ -spectra of a PANI film on a gold-coated wafer after immersion in basic solution.

A PANI-film thickness of 55.5 ± 7.1 nm (protonated state) and 35.9 ± 9.1 nm (deprotonated state) was determined by evaluation of AFM cross-section profiles at five different position on the sample. The changing film thickness with differences in the order of 30% was expected from the literature.^b The height data were used to model the optical properties and hereby extract the optical constants.

^b C. Barbero, R. Kötz, *J. Electrochem. Soc.* **1994**, *141*, 859.

The optical properties (ϵ_1/ϵ_2 and n/k from these) of PANI were obtained from the analysis of SE data (see Figure A25). In the model used for such analysis, the dielectric functions of both substrate and PANI were fitted with B-splines. The fitting of the model parameters to the experimental data took place in two separate steps, as customary for film-on-a-substrate systems. First, the optical properties of the bare substrate were determined by fitting the corresponding SE data with a B-spline. Then, the same procedure was applied to characterize PANI, having fixed the properties of the substrate to the values found in the first step. The experimental data were fitted considering three angles of incidence simultaneously (50° , 55° , 60°). The quality of the fittings was always high, as indicated by the low values of MSE (<2.5). The calculated optical properties of both PANI and the substrate are Kramers-Kronig consistent, as guaranteed by the "KK mode" built in the CompleteEASE 5.11f software.

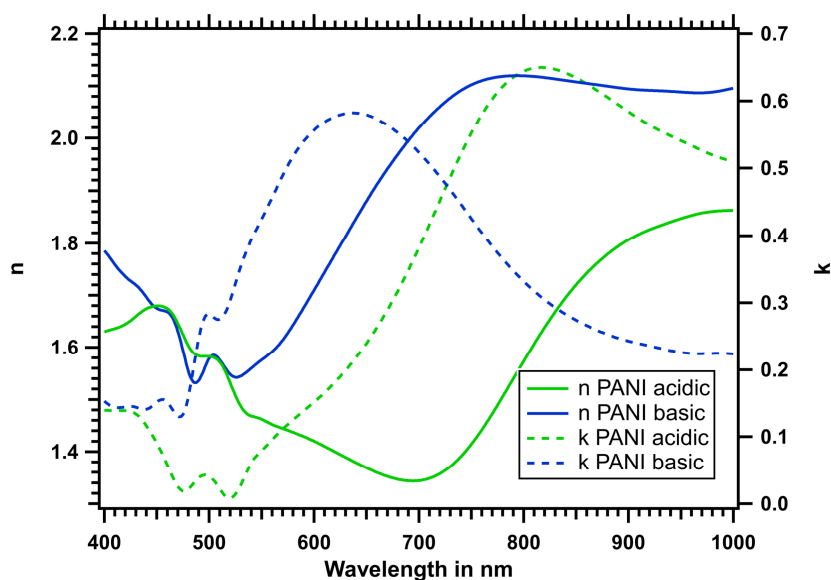


Figure A25. Optical constants (n and k extracted from ellipsometric data) of a PANI film after treatment in acidic (green) and basic (blue) conditions.

Appendix 25: COMSOL Simulations

The simulations of reflectance, transmittance and absorbance of the Au-nanoparticle / PANI / Au-film structure were performed using the finite element method in COMSOL Multiphysics package with Wave Optic model, Electromagnetic Waves, Frequency Domain. The geometry was designed in 3D with a two ports model (Figure A26). The periodic boundary condition is given to the opposite face boundaries along x- and y-axis to simulate the nanoparticle square array structure. The amplitude of electric field from incident port was set to 1 V/m as a normalized value for further simulations. The thickness of the gold mirror was set according to experimental value as 200 nm, and the diameter of gold nanoparticle was set as 80 nm. The refractive index (dielectric permittivity) of gold was imported based on a previous report (Johnson and Christy).^c The PANI shell around the gold nanoparticle was set with thickness of 35 nm and the wavelength-dependent refractive index (n and k) of PANI was imported from the analysis of SE spectra, described in Appendix 24. The environment above the particle-thin film (wave incident side) structure was set as air with refractive index $n = 1$ and the environment below the thin film structure was set as glass with refractive index $n = 1.5$. The mesh size of particle-thin film structure was set with minimum of 1 nm to maximum of 30 nm and the mesh size of air and glass was set as with minimum of 2 nm to maximum of 60 nm. The periodicity (D) of the particle-thin film structure array was simulated from 150 nm to 450 nm with 10 nm step. The range of spectrum was simulation from 370 nm to 1000 nm with 10 nm step for each array periodicity. The resulting electric field and scattering parameter were further converted to reflectance according to a previous report.^d

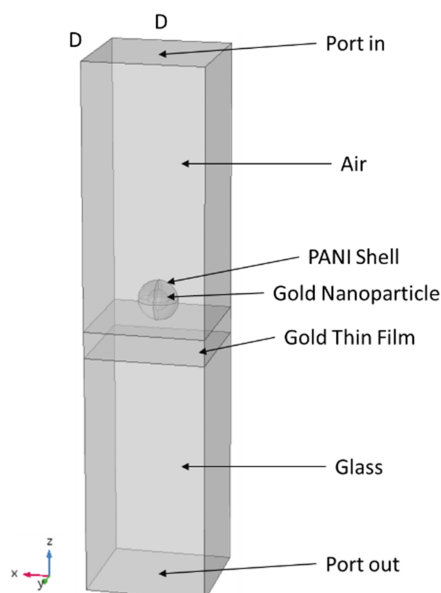


Figure A26. Geometry of the simulation model.

^c P. B. Johnson, R.-W. Christy, *Phys. Rev. B* **1972**, *6*, 4370.

^d K. Kurokawa, *IEEE Trans. Microwave Theory Tech.* **1965**, *13*, 194.

Appendix 26: Optical simulations of the metasurface with HCl- and NaOH-treated polyaniline

COMSOL simulations were conducted with the optical datasets of untreated (HCl) and NaOH-treated polyaniline (Appendix 24). The inter-particle distance (d) in the simulation displayed in Figure A27a was set to 240 nm while the thickness of the shell was set to 35 nm (HCl) and 25 nm (NaOH) as deduced from the thickness measurement on the reference film. When changing the optical properties of the shell from protonated to deprotonated PANI, major changes were observed in the optical data. The reflectance minimum is red-shifted by about 20 nm and its intensity increased by a factor of 5 (The changes are primarily attributed to the changing optical constants of PANI rather than the layer thickness as revealed by simulations with the same thickness). Simulations of particles without gold cores (dashed lines) show that the polymer is not directly contributing to the extraordinary low reflectance of the metasurface.

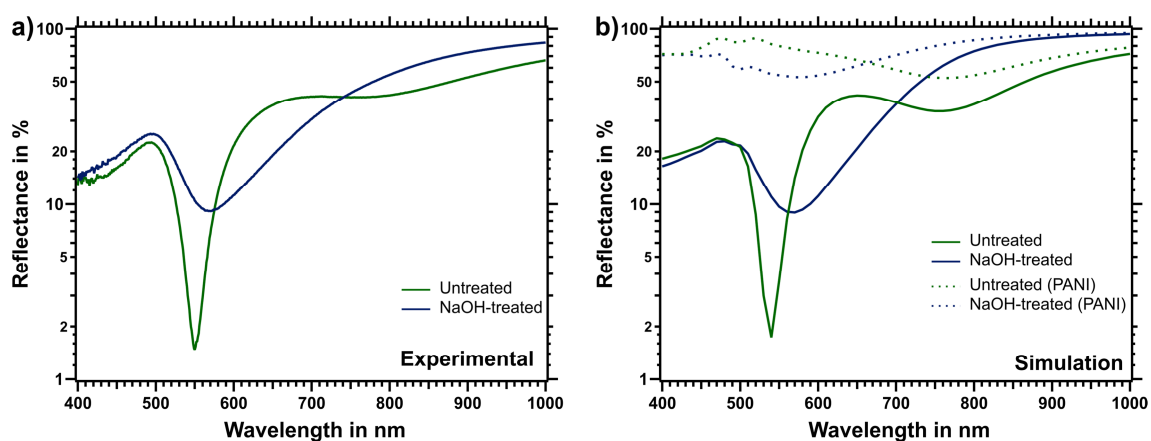


Figure A27. a) Measured reflectance spectra of Au-PANI particles on a gold mirror in the untreated (green) and NaOH-treated (blue) state. b) Simulated reflectance spectra with optical constants of protonated (green) and deprotonated (blue) polyaniline. Dashed lines indicate simulations of pure PANI particles.

Appendix 27: Absorbance spectra of dispersed polyaniline

The dispersion with pure PANI, namely the supernatant after centrifugation of Au-PANI particles, was investigated by absorbance spectroscopy. Therefore, the dispersion was measured in acidic (HCl) conditions directly after centrifugation (see Figure A28, green curve) and after addition of excess NaOH (basic, blue curve).

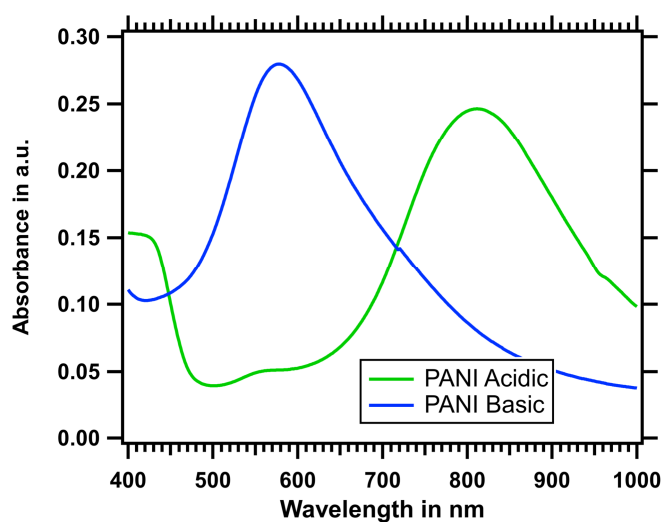


Figure A28. Absorbance spectra of PANI in aqueous dispersion under acidic (HCl, green) and basic (NaOH, blue) conditions.

Appendix 28: Cyclic voltammetry of Au-PANI

Cyclic voltammetry of the metasurface was measured in a 3-electrode-setup with a Pt counter-electrode, an Ag/AgCl reference-electrode and Au-PANI coated gold film as working-electrode. 0.5 M NaCl with 1 mM HCl and 1 mM SDS were used as electrolyte. The cycling speed was set to 50 mV/s. The resulting measurement of the second cycle is displayed in Figure A29. Two oxidation peaks can be observed at +0.05 V and +0.60 V while the respective reduction minima are shifted to lower potentials due to scan-rate-dependent hysteresis.^e Based on this, three different regions are attributed to the oxidation states Leucoemeraldine (here denoted as 'Red'), Emeraldine ('Ox1') and Pernigraniline ('Ox2').

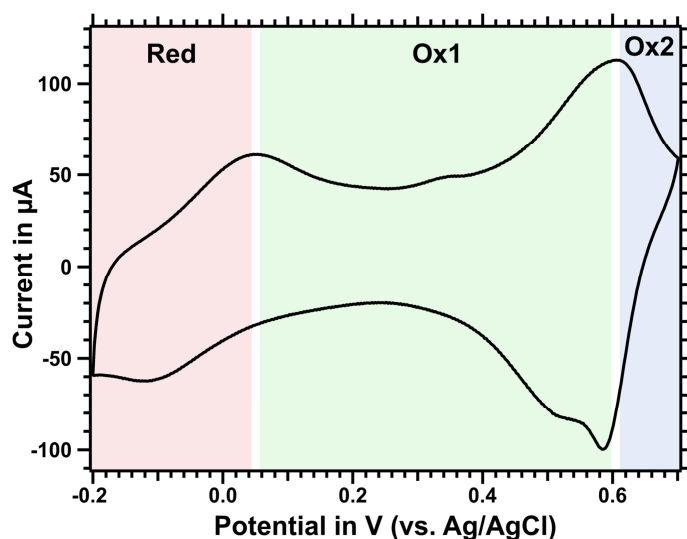


Figure A29. Cyclic voltammetry measurement of the tunable metasurface in a 3-electrode setup with platinum counter electrode and Ag/AgCl reference electrode.

^e A. J. Bard, L. R. Faulkner, *Electrochemical Methods: Fundamentals and Applications*, 2nd Edition, Wiley, New York 2001.

Appendix 29: Optical simulations with changing inter-particle distance D

The anti-reflective properties of the metasurface are strongly distance-dependent. Therefore, the reflectance spectra were simulated while changing the particle separation from 450 nm to 150 nm. The resulting spectra with separations below 400 nm are displayed in Figure A30a/b. The respective CIE colors are shown in c/d. According to the most pronounced minima at about 190 nm, the CIE plot shows the most intense (darkest) coloration. Although, the particles with NaOH treated polymer appear to be less efficiently at higher separation distances (e.g. 240 nm, compare Figure A27), it exhibits excellent performance as a broadband antireflective coating at lower distances (190 nm).

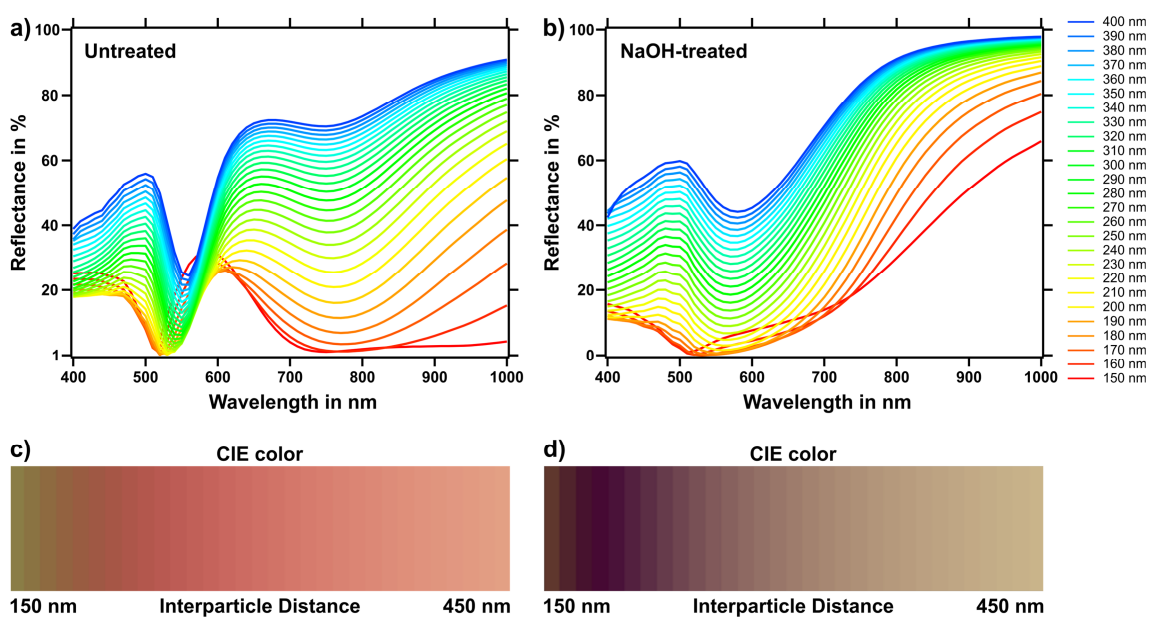


Figure A30. a) Simulated spectra with optical data of untreated (protonated) polyaniline. b) Simulated spectra with optical data of NaOH-treated (deprotonated) polyaniline. c/d) Respective CIE colors based on the simulated spectra.

Appendix 30: Electrophoretic particle deposition

Electrophoretic particle deposition (EPD) was conducted in a homemade cell. ITO with a nanostructured PMMA layer featuring square holes (arrays with well sizes between 50 nm and 500 nm in a separation of 5 μm) was electrically connected to a potentiostat with copper tape and aluminum cables. Together with the Tantalum counter-electrode, the substrate was mounted to a 3D-printed holder (see Figure A31a). The holder defines 2 mm spacing between the electrodes on a 5 \times 5 mm² area. This volume was filled with a dispersion of 40 $\mu\text{g}/\text{mL}$ particles in 0.2 mM SDS + 1 mM NaCl. Particle deposition was conducted by applying +4.5 V for 3 s. The sample was rinsed with water and dried in a nitrogen stream before analysis. The resulting particle assembly was characterized *via* dark field microscopy and atomic force microscopy. Satisfactory assembly was achieved in arrays with 100-300 nm sized wells, exemplarily shown for 270 nm and 310 nm wells (see Figure A31b/c). Future work will be conducted for optimization towards single particle deposition.

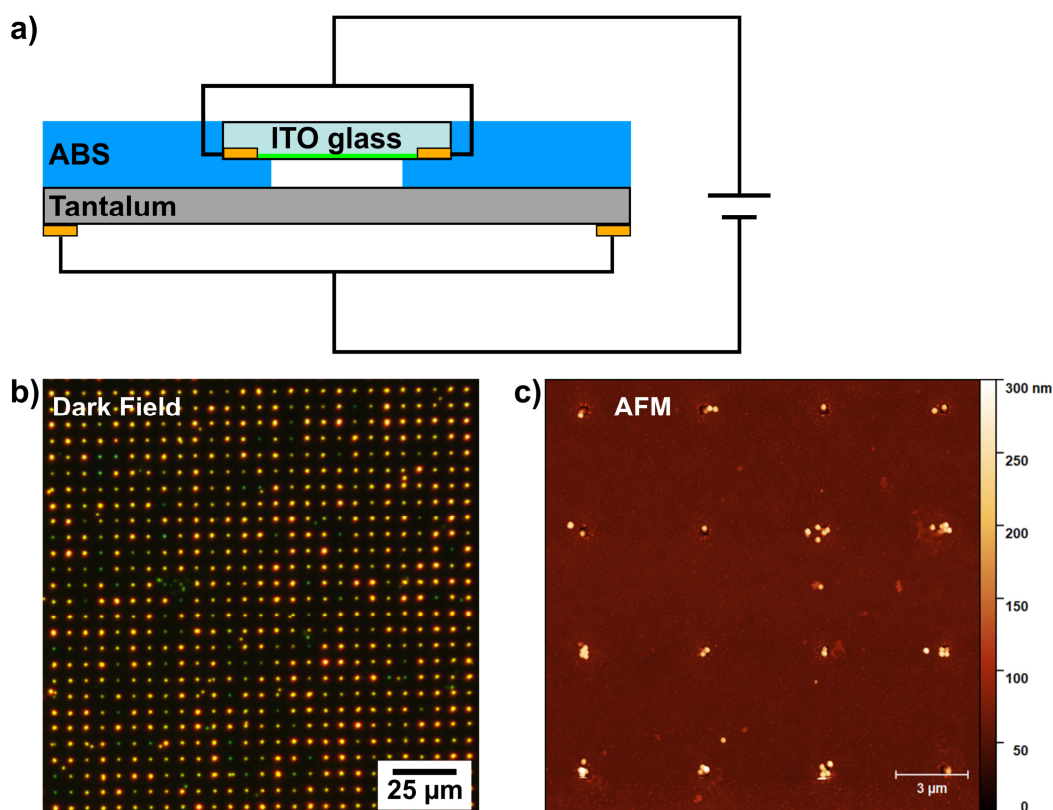


Figure A31. a) Schematic depiction of the experimental setup. b) Dark field micrograph of the obtained assembly in 270 nm square features. c) AFM image of the assembly in 310 nm features.

Appendix 31: PDMS embedding of Au-PNIPAM particles

Monolayers of Au-PNIPAM on polystyrene coverslips were treated with oxygen plasma at 800 W with 40 sccm O₂ flow for 60 seconds (MicroSys apparatus, Roth & Rau AG, Germany). The plasma etching process can be followed by comparison of the AFM images displayed in Figure A32 representing similar particles at different treatment times on glass substrates.

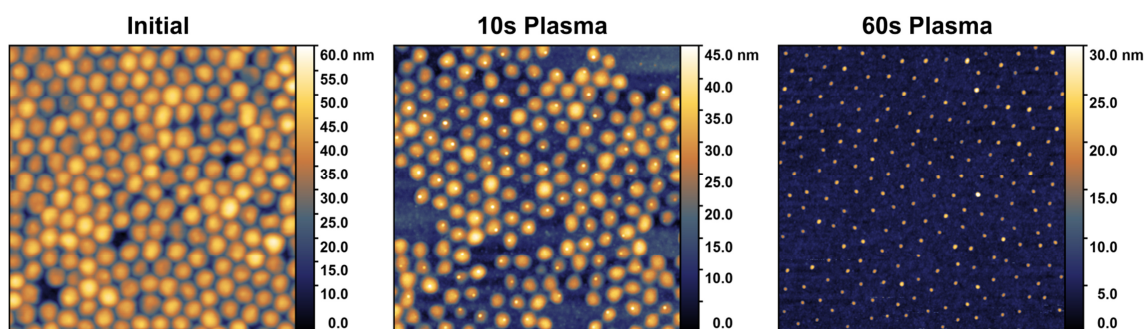


Figure A32. AFM images of Au-PNIPAM particles after preparation (left), after 10 s plasma treatment, and after 60 s plasma treatment.

The particles could be embedded in PDMS (Sylgard 184, Dow Chemical, USA) by pouring the precursor on top of plasma treated polystyrene coverslips. After hardening on the elastomer (80 °C for 4 h), the AFM investigation (see Figure A33) revealed that gold particles are partially embedded at the interface.

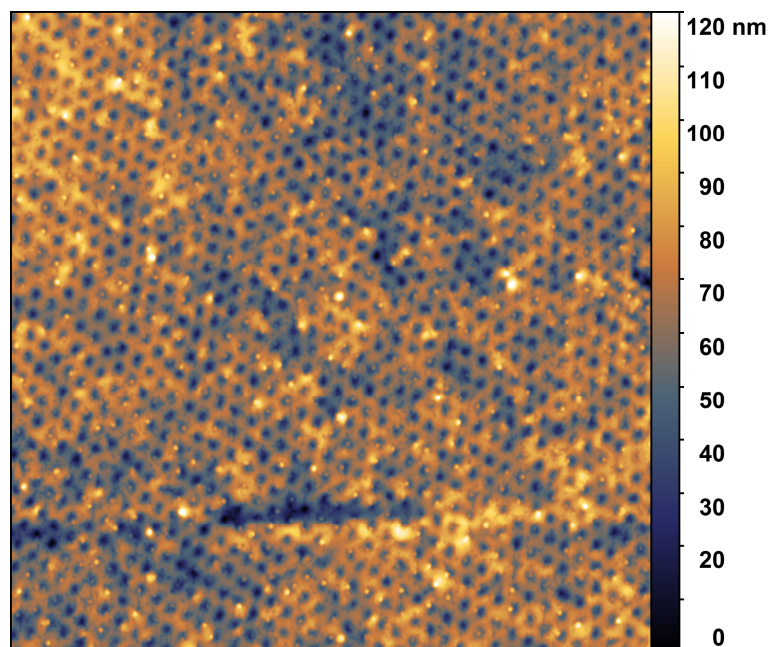


Figure A33. AFM image of a PDMS slab with embedded gold nanoparticles.

Appendix 32: Calculation of the required strain for transition into square lattice

In Figure A34, the unit cell of a hexagonal lattice is displayed. The transition into a square lattice *via* stretching along d (including perpendicular strain along h) is visualized by the grey square.

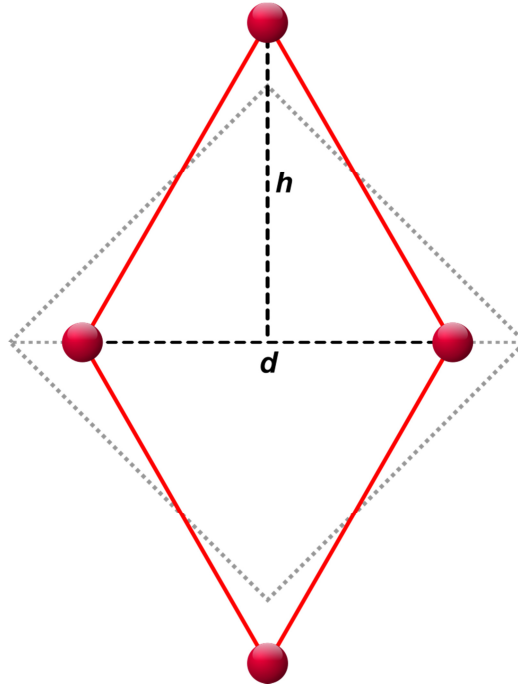


Figure A34. Unit cell of a hexagonal lattice (red) with the length of an equilateral triangle d and its height h . Dashed grey lines indicate the transition into a square lattice upon uniaxial deformation in an ideal elastomer.

The condition for this transition is given by:

$$h = \frac{1}{2}d$$

The length of h and d upon stretching can be written as:

$$h_{\text{initial}} + h_{\text{initial}} \cdot \Delta h/h = \frac{1}{2} \cdot (d_{\text{initial}} + d_{\text{initial}} \cdot \Delta d/d)$$

Since the unit cell is composed of two equilateral triangles, h_{initial} is defined as:

$$h_{\text{initial}} = \sin(60^\circ) \cdot d_{\text{initial}} = 0.866 \cdot d_{\text{initial}}$$

With the Poisson ratio for PDMS being:

$$\nu = -\frac{\Delta h/h}{\Delta d/d} = 0.5$$

The equation can be solved:

$$0.866 d_{\text{initial}} + 0.866 d_{\text{initial}} \cdot 0.5 \Delta d/d = 0.5 d_{\text{initial}} + 0.5 d_{\text{initial}} \cdot \Delta d/d$$

$$\Delta d/d = 0.3923$$

As a result, the transition of a hexagonal lattice into a square lattice is achieved upon stretching by 39.2%.

Danksagung

Zunächst möchte ich meinem Doktorvater **Andreas Fery** dafür danken, dass er mir die Möglichkeit gab bei ihm zu promovieren. Das Arbeiten mit dir und deiner Gruppe hat mir in der Tat einiges an Freude bereitet und ich danke dir, dass du das für mich richtige Maß aus langer Leine und Daumenschrauben gefunden hast, damit ich meine Promotion mit einem guten Gefühl abschließen kann. Außerdem bedanke ich mich bei meinem Co-Betreuer **Tobias König**, der mich vor allem in der Findungsphase dieser Arbeit und meiner Anfangszeit am Institut unterstützt hat. Weiterhin danke ich der gesamten **AG-Fery**. Ihr seid ja, ehrlich gesagt, der Hauptgrund weshalb es mich nach Dresden gezogen hat. Danke für die schönen letzten vier Jahre!

Ein besonderer Dank gilt natürlich meiner Frau **Inga**, die auch, und vor allem dann, für mich da war, wenn es einmal nicht ideal lief. Außerdem hat sie die Schreibphase dieser Arbeit mindestens um Wochen verkürzt, indem sie einen Männerschnupfen immer sofort als solchen erkannte und dann entsprechend gewissenhaft behandelte. Weiterer Dank gilt meiner **Familie**, die mich mental immer unterstützte und mir den Rücken stärkte—ja Papa, ich bin noch dran am Schreiben, aber das dauert halt—and ja ich weiß, dass du vermutlich der einzige bist, der das hier liest ;-). Ein großer Dank geht auch an meine Freunde, die eben das tun was gute Freunde tun. Danke an **Martin, Max, Fabi, Daniel** und **Maxer** für die Gelegenheit sich in die Welt von Pen and Paper einzufinden, um mir so die Möglichkeit zu geben meine Freizeit mit noch mehr Nerdkram zu füllen. Danke an **Bernhard, Anja**, Maxer und Martin dafür, dass wir das Bouldern nicht haben sein lassen, und ich so zumindest fast wöchentlich dazu gekommen bin Sport zu machen. Danke auch an meine Bürokollegen **Dana, Jonas, Fabi, Martin** und **Anja** mit denen es in der ‚Kariesgarage‘ nie langweilig wurde (auch wenn das manchmal bedeutet, dass keiner arbeiten konnte und ab vier Uhr Bier getrunken werden musste).

Außerdem möchte ich allen Coautoren und Kooperationspartnern danken, die indirekt an dieser Arbeit mitgewirkt haben (lest halt die Arbeit für eine vollständige Liste). Besonderer Dank gilt hier meinen Gastgebern **Paul Mulvaney** und **Daniel Gómez**, die mir einen fantastischen Aufenthalt in Australien ermöglichten und damit obendrein auch noch die Zielgerade für die Promotion geebnet haben. Vielen Dank hier auch an **Heyou**, der mir in Pauls Labor immer mit Rat und Tat zur Seite stand Danke außerdem an **Katja**, ohne die Australien vermutlich ein gutes Stück langweiliger gewesen wäre, und ohne die diese Arbeit keinen Ausblick haben würde. Vielen Dank auch an **Matthias Karg**, der das Verbrechen begangen hat, mich für die physikalische Chemie zu begeistern und mich darin auch weiterhin zu unterstützen. In diesem Sinne auch Danke an **Mareen**, die mich zur PC II in Bayreuth brachte. Ein großer Dank geht an **Michele**, der mir zeigte, dass es sehr viel Spaß machen kann, mit bisher unbekanntem Leuten im Labor zusammen zu arbeiten, und der nicht müde wird über fachliche Fragestellungen nachzudenken.

Zuletzt danke ich natürlich allen Lektoren dieser Arbeit. Ohne **Charlene, Tony, Martin, Max, Anja, Jonas** und **Inga** wäre hier wohl noch einiges an Stuss zu finden gewesen.

Versicherung und Erklärung

Hiermit versichere ich, dass ich die vorliegende Arbeit ohne unzulässige Hilfe Dritter und ohne Benutzung anderer als der angegebenen Hilfsmittel angefertigt habe; die aus fremden Quellen direkt oder indirekt übernommenen Gedanken sind als solche kenntlich gemacht. Die Arbeit wurde bisher weder im Inland noch im Ausland in gleicher oder ähnlicher Form einer anderen Prüfungsbehörde vorgelegt.

Die vorliegende Arbeit wurde im Zeitraum von Dezember 2015 bis Februar 2020 am Leibniz-Institut für Polymerforschung Dresden e.V. unter der Betreuung von Prof. Andreas Fery (betreuender Hochschullehrer) und Dr. Tobias König (betreuender Young Investigator) durchgeführt.

Datum, Unterschrift